Spin orbit torque measurements in Pt-based heavy metal/ferromagnetic heterostructures with in-plane magnetic anisotropy

Alexandru Vladimir Trifu

Communauté
UNIVERSITÉ Grenoble Alpes

THÈSE

Pour obtenir le grade de

DOCTEUR DE LA COMMUNAUTÉ UNIVERSITÉ GRENOBLE ALPES

Spécialité : **Nanophysique**

Arrêté ministériel : 25 mai 2016

Présentée par

Alexandru Vladimir TRIFU

Thèse dirigée par **Giles GAUDIN, Directeur de Recherche, CNRS/ SPINTEC**, et
Codirigée par **Ioan Mihai MIRON, Chargé de Recherche, CNRS/SPINTEC**

préparée au sein du **Laboratoire SPINTEC**, GRENOBLE
dans **l'École Doctorale de Physique**

Mesures de Couples de Spin Orbite dans des heterostructures métal lourde /ferromagnet a base de Pt, avec anisotropie magnétique planaire

Thèse soutenue publiquement le **16/06/2017**,
devant le jury composé de:

M. Jan VOGEL
Directeur de Recherche, Institut Néel, CNRS - France, Président
M. Pietro GAMBARDELLA
Professeur, ETH Zürich - Suisse, Rapporteur
M. Sayeef SALAHUDDIN
Professeur, University of California, Berkeley - USA, Rapporteur
M. Juan Carlos ROJAS-SANCHEZ
Charge de Recherche, Institut Jean Lamour, CNRS - France, Examinateur
M. Mihai GABOR
Maître de Conférence, Université Technique de Cluj-Napoca - Roumanie, Examinateur
M. Mairbek CHSHIEV
Professeur, Université Grenoble Alpes - France, Examinateur

Acknowledgements

My first acknowledgements go towards my two supervisors, Gilles Gaudin and Mihai Miron, who mentored me and guided my work during the last four years. Gilles and Mihai have been the most amazing supervisors a PhD student can wish for. Exceedingly patient, always finding the time to answer my questions, no matter how trivial. They have taught me how to be a scientist, how to be rigorous in my work and most of all how to value the path taken and not just the end result. I want to thank Gilles for his calm, his patience, his fairness and for his constructive criticism regarding every presentation, abstract or in general any piece of writing that I made. I want to thank Mihai for sharing with me his passion for science and research, and most of all for his ability to instill this passion in others around him (me, in this case). I am thankful for all the conferences you paid for, for having faith in my ability to represent SPINTEC, and for always making sure that we, your students, always got the right exposure for our work. Working with Gilles and Mihai teaches you how to combine rigorous measurements and nanofabrication techniques, with epoxy, hand-cut copper pads and wiring, and duct tape. It teaches you that the lack of expensive equipment should not deter you from doing physics. They are, simply put, formidable and inspiring!

Thank you for the daily help, your confidence and encouragement and for always knowing how to lift my morale whenever my confidence failed. Equally, thank you for the life lessons you both shared with me at the end of my PhD. At the end, I am also grateful for the friendship that has formed and that I wish will last. I wouldn't have been here without your help.

I would also like to extend my thanks to the members of the Jury, M. Jan Vogel, the Jury president, M. Pietro Gambardella and M. Sayeef Salahuddin, the two referents, M. Juan Carlos Rojas-Sanchez, M. Mihai Gabor and M. Mairbek Chshiev, examiners. I would like to thank them for honoring me with their presence at my defense, their interest in my work, for the time they took to examine my manuscript, their questions and encouragements.

I am further extending my thanks to the Nanoscience Foundation, for making it possible for me to follow my passion by financing my PhD studies.

I want to extend a special thanks to Marc Drouard, for his help with LabVIEW and SOT measurements, that he offered at the expense of his “writing time” at the beginning of my thesis. Next, to Jay Nath, for his extensive help in the cleanroom, and most importantly for the time-consuming sample patterning and measurements done on my behalf at the end of my thesis when my “experimental privileges” expired, that at times were done at the expense of his own immediate goals. Also important are the improvements to the nanofabrication process brought by Jay Nath and Thomas Brächer. Thanks to Kevin Garello and Can Onur Avci for their invaluable advice regarding the measurements and data analysis. Thanks to Alexandre Mouillon for his streamlining of the measurement program.

A big acknowledgement to Stéphane Auffret, for his daily help with wafer deposition, especially for the many “last minute” requests, and for trainings; Isabele Joumard for her continuous involvement and assistance in improving existing, and developing new experimental setups, as well as for providing trainings; Nathalie Lamard for her help in the cleanroom and getting me started with sample fabrication.

I also want to extend my thanks to all the SOTs group, for their help, answering my questions and all the interaction and group meetings we had. Thanks to Olivier Boulle, Liliana Buda-Prejbeanu, Safeer CK, Emily Jué, Alexandre Lopez and Claire Hamelin.

I want to thank to everyone at SPINTEC laboratory, for all their understanding and sympathy and for all the good moments spent with them during the past four years, since the beginning of my masters’ internship and throughout my thesis.

I also want to thank the entire PTA technical team, for their support and trainings on all the cleanroom equipment. Thanks to Thierry Chevolleau, Christophe Lemonias, Jean-Luc Thomassin, Nicolas Chaix, Marlène Terrier, Thibault Haccart and Frédéric Gustavo.

A big “thank you” also to Rachel Mauduit, Catherine Broisin and Sandra Ingrassia for their help in all the administrative processes that I had to complete during my PhD, for their efficiency and for their patience.

Thanks to all my friends from the lab (yes, PhD students have friends too). Thanks to Magali, Mathieu, Paulo, Lamprini, Cécile, Guillaume, Thomas B, Mélissa, Haozhe, Dali…

As well to my friends outside the lab. Thanks to Ioan, Alex and Dan, for all the good times, all the late night video games and most of all for their friendship, advice and moral support.

Hopefully, I did not forget anyone.

Last but not least, I also want to thank my family. To my incredible parents, for their sacrifices and understanding, for believing in me and for all the moral and financial support during my many years of study.

To my wife, Cristina, for always being by my side, for her understanding and patience regarding all the late night “writing sessions” and for all the many times I have been way to absorbed by my work... which I will probably do again.

Table of Contents

1 General Introduction

Moore's law is based on empirical observation and states that every two years approximately, the number of transistors in dense integrated circuits doubles. This trend has held up well in the past several decades (1970s and onwards). However, the continuous miniaturization of transistors brings about a significant increase in leakage current, which increases the stand-by power consumption. This energy loss has become a major problem in microelectronics during the last several years, making the development of new technologies more difficult. One of the solutions that can address this issue is to place non-volatile memory elements inside the chip, that retain the configuration of the transistor during power-off and allow to restore it at power-on.

Here is where MRAMs (Magnetic Random Access Memories) based on STT (Spin Transfer Torque) and SOT (Spin Orbit Torque) come into play. STT-MRAMs have been identified by the ITRS as a promising candidate for the implementation of new non-volatile memory and logic devices that can offer high-speeds, high density, scalability and low power consumption. The electric current drives the magnetization switching of a free ferromagnetic layer by transferring angular momentum from an adjacent ferromagnet [1]. STT-based memory elements are two terminal devices in which the "pillar" shape defines both the "read" and the "write" current paths. Independent optimization of the reading and writing parameters is therefore difficult, while the large writing current density injected through the tunnel barrier causes its accelerated aging, particularly for fast switching. Recent demonstrations of magnetization switching induced by in-plane current injection in heavy metal (HM)/ferromagnet (FM) heterostructures have drawn increasing attention to spin-torques based on orbital-to-spin momentum transfer induced by Spin Hall and interfacial effects (SOTs).

Unlike STT-MRAM, the in-plane current injection geometry of SOT-MRAM allows for a three-terminal device which decouples the "read" and "write" mechanisms, allowing the independent tuning of reading and writing parameters. However, an essential first step in order to control and optimize the SOTs for any kind of application, is to better understand their origin. The origin of the SOTs remains one of the most important unanswered questions to date. While some experimental studies suggest a SHE (Spin Hall Effect)-only model for the

SOTs, others point towards a combined contribution of the bulk (SHE) and interface (Rashba Effect and Interfacial SHE). At the same time, many studies start with a SHE only hypothesis and do not consider interfacial effects. Furthermore, there are not so many systematic studies on the effects of interfaces. This thesis tries to fill in this gap, by providing a systematic study on the effects of interfaces on the SOTs, in NM/FM/HM multilayers with in-Plane magnetic anisotropy. Since by simply measuring the SOTs we have no means of distinguishing between bulk and interface effects as sources of SOTs, in this thesis we explored three avenues:

i. First, we aimed to change the interface/bulk effect ratio by modifying the thickness of the HM layer;
ii. Second, we explored different HM/FM/NM combinations, in order to study different interfaces;
iii. We changed the properties of the interfaces either by growing epitaxial/textured HM layers or by oxidation.

The thesis is structured in seven chapters. The first chapter of this manuscript gives a short, general introduction about the scientific context and the objectives of this thesis.

The second chapter is dedicated to introducing the theoretical concepts needed to understand the context and the results presented in this thesis. We begin by introducing the concepts of STT, Spin Orbit Interaction (SOI) and SOT. After giving a qualitative picture of the Spin Orbit Torques, the focus shifts towards exploring the two mechanisms that can potentially be responsible for the generation of the SOTs, namely the Rashba Effect (interface) and the Spin Hall Effect (bulk). These two mechanisms are representative for the interface vs. bulk debate over the origin of the SOTs.

In the third chapter of this manuscript, our goal is to give an overview of the current directions in the quantitative analysis of the SOTs. Its purpose is not to give an exhaustive review of the work done in this field, but to emphasize the most significant results in the context of this thesis. We briefly talk about Magnetization Switching and current induced Domain Wall motion, before discussing the first experimental observations of SOT. In this chapter, we also outline the most important question that this manuscript tries to address, namely what is the origin of the SOTs: bulk or interface? Finally, we discuss some experimental methods dedicated to the quantitative analysis of the SOTs themselves, their amplitude, symmetry and most importantly, their origin.

The goal of the fourth chapter is to provide an in-depth description of the measurement technique used for the SOT measurements, namely Harmonic Analysis of the Hall voltage. We then describe the data analysis process used to accurately calculate the Damping-Like and Field-Like effective fields from the measured data, in an independent manner. We also consider additional contributions to the measured signal (such as from the Oersted field and the Anomalous Nernst Effect (ANE), for example) that greatly influence SOT measurements. A way of taking such effects into account is provided. Finally, this chapter also contains a presentation of the sample preparation process and a description of the measurements setup and its specific difficulties.

The fifth chapter is dedicated to the presentation and discussion of the experimental results. In the first part of the chapter, we consider the influence of the thickness of a Pt layer on the amplitude of the SOTs, in $MgO/FeCoB_{(20)}/Pt_{(10\text{-}100)}$, $Pt_{(10\text{-}40)}/Co_{(20)}/Al_{(20)}$, $Pt_{(30)}/Co_{(20)}/Pt_{(10\text{-}40)}$, $Ta_{(30)}/Cu_{(10)}/Co_{(20)}/Pt_{(10\text{-}40)}$ and $Ta_{(30)}/Cu_{(10)}/CoFeB_{(20)}/Pt_{(10\text{-}40)}$ multilayers. This way, we are able to study different bulk/interface effects ratio, as well as different interfaces. We compare the experimental results to a SHE-only model of the SOTs, and then to a model that takes into account interfacial contributions. In the second part of the chapter, we investigate the influence of the crystallographic structure of the interface on the amplitude of the SOTs. For this purpose, we grew epitaxial/textured Pt layer with [001] and [111] interfaces, and coupled them with Co and CoFeB. This part of our study has been done in collaboration with the Technical University of Cluj-Napoca, Romania. In the third part of the chapter, we complete our study of interfaces in $Ta_{(30)}/Cu_{(10)}/Co_{(20)}/Pt_{(10\text{-}40)}$ multilayers, by further modifying the properties of the interface through oxidation. We then follow the evolution of the Damping-Like effective field as a function of Pt thickness (and indirectly, as a function of the degree of oxidation).

Finally, the sixth chapter sums up the general conclusions and perspectives of the experimental work presented in this thesis.

Additionally, the seventh chapter contains supplementary information concerning the characterization of the magnetic properties of our sample systems.

2 Theoretical considerations

2.1 Spin Transfer Torques

Since their theoretical prediction in 1996 by Berger [2] and Slonczewski [3], Spin Transfer Torques (STTs) have attracted increased attention from the research community because they provided the first means of manipulating the magnetization of ferromagnetic materials without the need of an external magnetic field. This makes it easier to control the magnetization in magnetoelectric devices. Most importantly, they allow the reversing of the magnetization solely by current injection.

STTs arise from spin currents. Just like an electric current being created by a flow of electric charges, a spin current is created by a flow of spins and carries spin angular momentum.

The electron possesses both charge and spin, but under normal circumstances the spins of the conduction electrons are randomly oriented, so there is no net spin current associated to an electric current. However, because of the existence of the spin, electrons can interact with ferromagnetic materials in interesting ways. By means of the exchange interaction, if an electric current passes through a ferromagnetic layer, the spins of the conduction electrons interact with the localized magnetization so as to realign themselves parallel to its direction. As a result, the transmitted current becomes spin polarized, a process also known as spin filtering. If this spin polarized current is filtered again through another ferromagnetic layer, whose magnetization is not parallel with the polarization direction, the conduction electrons spins will again realign themselves with the local magnetization, and, in the process, they transfer spin angular momentum to the magnetization [1], [4], [5]. As the magnetization of the ferromagnetic layer changes the spin polarization of the current, it exerts a torque on the conduction electrons' spins. By conservation of angular momentum, a change in the spins angular momentum direction leads to an equal and opposite torque on the magnetization of the ferromagnet [1], [4], [5]. Such a situation is encountered in spin valves and tunnel junctions, where a non-magnetic or tunnel barrier is sandwiched in between two ferromagnetic layers.

A similar situation occurs when a spin polarized current passes through a structure with a non-uniform spatial distribution of the magnetization, such as a magnetic Domain Wall (DW), skyrmion, etc. Here, the spins of the conduction electrons will rotate to follow the local

magnetization. The direction of their spin angular momentum will therefore change as a function of position [1].

Remark

A magnetic Domain Wall (DW) is the transition zone between two magnetic domains, in which the magnetization changes its orientation from one easy axis to another. The length over which the magnetization reversal occurs defines the width of the DW, $\boldsymbol{\Delta}$. In a thin film, the width of the domain wall is decided by the competition between the exchange and anisotropy energies. It can be written as $\boldsymbol{\Delta = \sqrt{A_{ex}/K_0}}$, where $\boldsymbol{A_{ex}}$ is the exchange coefficient and $\boldsymbol{K_0}$ is the anisotropy constant (see section 2.2.3). The exchange interaction favors wide DWs while the anisotropy favors narrow DWs [6], [7]. DW can be classified depending on the axis of rotation of the magnetization. Figure 2.1 shows a schematic of two common DW configurations for thin films with perpendicular magnetic anisotropy (PMA): the Bloch Wall, where the rotation axis lies in the plane created by the magnetization of the two domains, and the Neel Wall, where the rotation axis is perpendicular to said plane. In thin films with in-plane magnetic anisotropy, DWs can have more complicated structures, such as vortex or transverse walls [8].

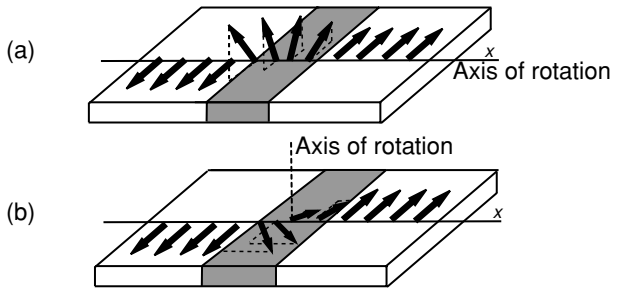

Figure 2.1: Schematic showing a Bloch DW (a) and a Neel DW (b). The shaded area represents the width of the DW. From [7].

The spin angular momentum transfer from the conduction electrons to the magnetization is the source of the STTs. According to [1], [5], [9], in the case of a NM/FM multilayered structure, there are three mechanisms by which the spin angular momentum transfer occurs: (1) spin-dependent scattering at the interface between the FM and the NM material, (2) rotation of the transmitted and reflected spins, and (3) spin precession in the FM.

The first mechanism is due to the exchange interaction in the ferromagnetic material. The magnetization of the FM material defines a quantification axis. As such, any incident spin orientation can be expressed as a linear combination of spin "Up" and spin "Down" components. Because of the exchange interaction the density of states at the Fermi level for the "Up" and "Down" spin states is different [10], [11]. In consequence, the transmission and reflection coefficients at the interface are different for the two spin states. The incident spin state will be partially transmitted and partially reflected and a spin filtering effect appears [3].

In the ideal case, only the spin component parallel to the magnetization of the ferromagnet will be transmitted and the transverse component is absorbed at the interfaces creating a torque on the magnetization of the ferromagnet (Figure 2.2). In reality not all the transversal component is absorbed at the interface. The remaining part is further diminished by the other two mechanisms [1], [3], [5], [9].

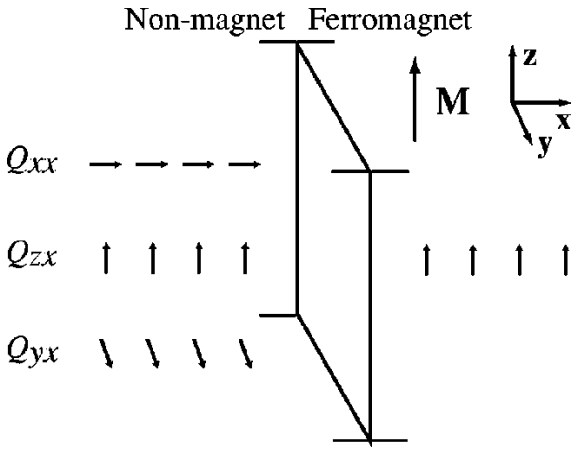

Figure 2.2: Spin current scattering at the interface, showing longitudinal, Q_{zx} and transverse components Q_{xx}, Q_{yx}. The longitudinal component is transmitted and the transverse components are absorbed at the interface. From [5].

The second mechanism consists of a rotation of the incident spin upon transmission or reflection at the interface [5]. Because the transmission and reflection coefficients depend on the wave vector, $\vec{k}$, of the incident electron, the magnitude of this rotation will also depend on $\vec{k}$. Different spin rotation means different transverse spin component being transmitted or reflected. When we consider all the electrons' spins at the Fermi level these transverse components cancel each other out, which greatly diminishes the reflected part of the transverse component.

In the third mechanism, "Up" and "Down" spins transmitted inside the ferromagnetic material have different kinetic energies corresponding to different wave vectors, k. This

means that each spin will have a different precession frequency around the direction of the magnetization. When we consider all the spins at the Fermi level, the precessions are out of phase with each other, therefore the transverse component cancels out over a distance of a few lattice constants [1], [5], [9]. The transmitted transverse component is absorbed over a few lattice constants.

Since the transverse component of the spin current is largely absorbed by the ferromagnet close to the interface, over a few lattice constants, it is safe to consider that the STT acting on the magnetization is proportional to the transverse component of the incident spin current. These same mechanisms also lead to the transfer of angular momentum to the magnetization of a ferromagnetic layer in the case of the Spin Orbit Torques (SOTs) which we will discuss later.

STTs therefore arise when the flow of spin current through our device has sources and sinks of spin angular momentum. There are two components of the STTs: i) an adiabatic torque ($\vec{T}_A$) [12] and ii) a non-adiabatic torque ($\vec{T}_{NA}$) [13]–[15].

For a system with PMA, $\vec{T}_A$ describes the fact that the spins align perfectly (adiabatic regime) with $\vec{M}$. For a current perpendicular to the DW, it is oriented out-of-plane, and it has opposite directions for up/down and down/up domains. It is equivalent to an effective field, $\vec{H}_A$, oriented along the hard magnetization axis. $\vec{T}_A$ is also named Damping-Like torque or Slonczewski-Like torque.

$\vec{T}_{NA}$ consists of deviations from the adiabatic regime and it is orthogonal to $\vec{T}_A$ and $\vec{M}$. It is equivalent to an effective field, $\vec{H}_{NA}$, oriented along the easy magnetization axis (for a system with PMA).

Figure 2.3 shows a schematic representation of current induced STTs.

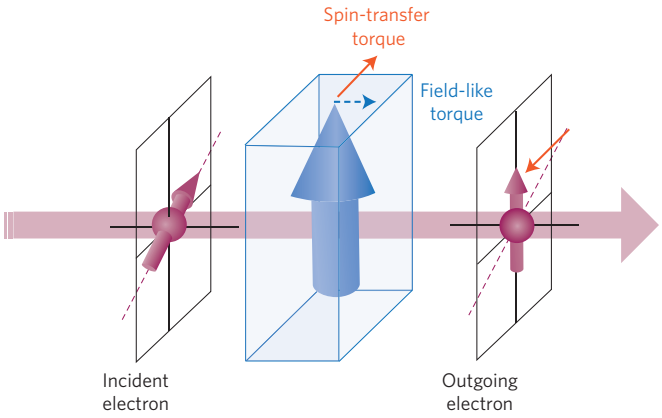

Figure 2.3: Schematic of current induced Spin Transfer Torques (STTs): When a spin-polarized current enters a ferromagnetic layer, the incident spins interact with the local magnetization and realign themselves along its direction. As a consequence, torques are created both on the incident spins as well as on the magnetization: one torque in the plane of the spins called Damping-Like torque, and one torque perpendicular to this plane called field-like torque. From [4].

There are various consequences of the STTs on the magnetization dynamics. First, STTs can lead to magnetic domain wall motion. This was theoretically predicted by L. Berger [16]. In his theory, he suggested that electrons passing through a DW can create a torque which moves the DW along the electron flow (opposite to the current direction). A first experimental proof is found in [17].

Second, depending on the amplitude of the current and external applied magnetic fields, STTs can excite steady-state precession or magnetization switching from one magnetic orientation to another [1], [18] (Figure 2.4).

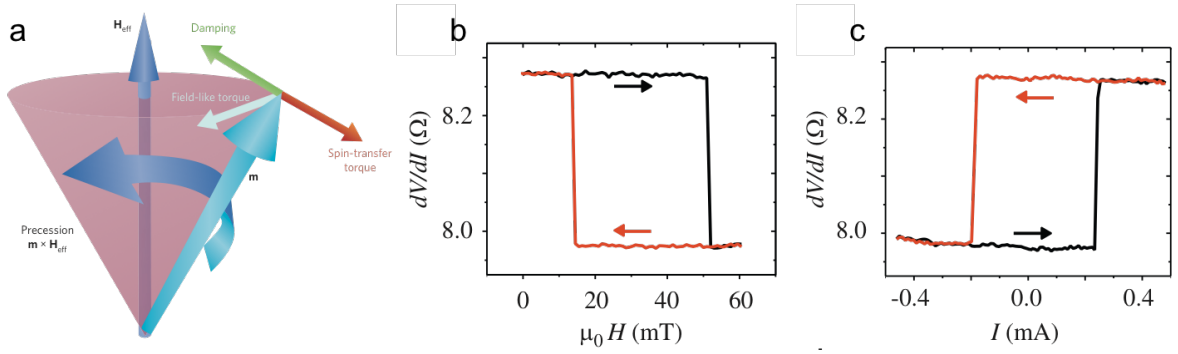

Figure 2.4: STT induced magnetization dynamics: (a) steady state precession around an effective field $\vec{H}_{eff}$ direction, showing the dissipative damping torque (green), the spin transfer torque (red) and the field-like torque (light blue) [4]. (b) magnetic field driven switching of a $Ni_{81}Fe_{19}$(20nm)/Cu(12nm)/$Ni_{81}Fe_{19}$(4.5nm) nanopillar device. (c) STT driven switching of the same device with a constant bias field.

2.2 Spin Orbit Interaction

As we have seen in the previous section, in the case of the STTs the system requires a source of spin angular momentum, i.e. a spin reservoir. This is indeed achieved by the presence of a polarizer (essentially an additional magnetic layer) or a magnetization gradient, $\nabla\vec{M}$, such as a Domain Wall (DW). More recently however, another mechanism of transferring spin angular momentum to the magnetization, from the crystal lattice via the Spin-Orbit Interaction (SOI), has been proposed [19]–[23]. This effect, known as Spin Orbit Torque (SOT), is created by the flow of an electric current in metallic samples with Structural Inversion Asymmetry (SIA). It is a strong effect, present both in Ferromagnetic materials (FM) as well as in semiconductor ones, that can be tuned by means of material and device engineering.

2.2.1 Spin Orbit Interaction Energy

Let's look first at the SOI. It couples the spin angular momentum, $\vec{s}$, with the orbital angular momentum, $\vec{l}$, into the total angular momentum, $\vec{j} = \vec{s} + \vec{l}$. For a system with more than one electron the coupling between spin and orbital angular momenta is written as $\vec{J} = \vec{S} + \vec{L}$ (Russell – Saunders coupling), where $\vec{S} = \sum_i \vec{s}_i$ and $\vec{L} = \sum_i \vec{l}_i$ [7].

In a classical picture, we can calculate the SOI energy as the interaction energy between the spin and the magnetic field at the center of a current loop which represents the orbital momentum, Figure 2.5 [24]:

$$E = -\vec{m}_s \vec{H}_{orb} = -m_s H_{orb} \cos\theta$$

Equation 2.1

where $\vec{m}_s$ is the spin magnetic moment:

$$\vec{m}_s = -\frac{2\mu_B \vec{s}}{\hbar} = -\frac{e\mu_0 \vec{S}}{m_e}$$

Equation 2.2

$\vec{H}_{orb}$ is the magnetic field created by a current I flowing in a loop of radius r:

$$\vec{H}_{orb} = \frac{I}{2r}$$

Equation 2.3

and e is the electron charge, m_e the electron mass, μ_0 the vacuum magnetic permeability.

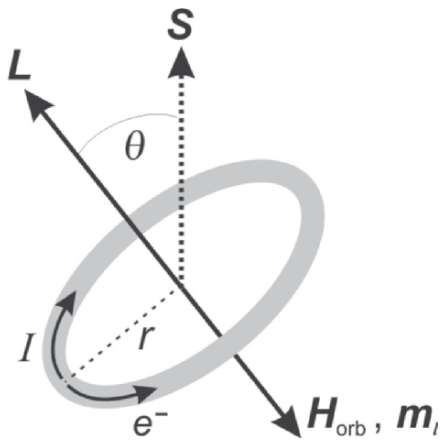

Figure 2.5: Calculating the Spin-Orbit Interaction energy as the interaction energy between the spin and the magnetic field created at the center of the current loop. $\vec{L}$ and $\vec{S}$ are the orbital and spin angular momenta. From [24].

Knowing the classical relations $m = \mu_0 IS$ and $\vec{m} = -\frac{e\mu_0}{2m_e}\vec{L}$ we find the link between $\vec{H}_{orb}$, the orbital magnetic moment, $\vec{m}_l$, and the angular momentum, $\vec{L}$ [7], [24], [25]:

$$\vec{H}_{orb} = \frac{\vec{m}_l}{2\pi\mu_0 r^3} = -\frac{e\vec{L}}{4\pi m_e r^3}$$

Equation 2.4

We can now rewrite the SOI energy as:

$$E = -\vec{m}_s\vec{H}_{orb} = -\frac{e^2}{4\pi\varepsilon_0 m_e^2 c^2 r^3}\vec{L}\vec{S}$$

Equation 2.5

where $-e$ is the electron's charge, and $\mu_0 = \frac{1}{\varepsilon_0 c^2}$.

$\vec{H}_{orb}$ is the magnetic field experienced by the electron in its own frame of reference, and it can be referred to as the "Spin-Orbit" field, $\vec{H}_{SO}$.

2.2.2 Spin Orbit Interaction Hamiltonian

The Spin-Orbit Hamiltonian that corresponds to the SOI is [26]:

$$\mathcal{H}_{SO} = -\vec{m}\vec{B}_{SO}$$

Equation 2.6

It takes into account the magnetic field, $\vec{B}$, experienced by the electron in its own frame of reference as it moves in the electric field, $\vec{E}$, of the nucleus, $\vec{B} = \frac{\vec{v}\times\vec{E}}{c^2}$ [10]. This field must be

corrected by a factor $\frac{1}{2}$, due to the non-inertial nature of the electrons reference frame [27], a correction known as "Thomas precession"[24]:

$$\vec{B} = \frac{\vec{v}\times\vec{E}}{2c^2}$$

Equation 2.7

Using the same transformation to write $\vec{B}_{SO} = \vec{B}$ and substituting in the equation of the Hamiltonian, we have:

$$\mathcal{H}_{SO} = -\vec{m}\vec{B}_{SO} = \frac{ge\hbar}{4m_e c^2}\left(\vec{v}\times\vec{E}\right)\cdot\vec{S} = \frac{ge}{4c^2}\left(\vec{k}\times\vec{E}\right)\cdot\vec{S}$$

Equation 2.8

where $\vec{m} = -g\mu_B\vec{s}$, $\mu_B = \frac{e\hbar}{2m_e}$, $\vec{E}$ is the electric field created by the crystal lattice and $\vec{k}$ is the electron's wave vector. As a consequence, the interaction between the electron's spin with this magnetic field is an interaction with the crystal lattice. This interaction will depend on the electron's trajectory, connecting the orbital degrees of freedom of the electron with the spin degree of freedom.

2.2.3 Magnetocrystalline anisotropy

An important consequence of the SOI is the magnetocrystalline anisotropy. In a ferromagnetic material, the total energy depends on the orientation of the magnetization with respect to the crystal structure. Due to the SOI, the spin angular momentum is coupled to the orbital angular momentum and their two relative orientations are linked. Because of the Coulomb interaction between the electron orbitals associated to the magnetization (3d and 4f) and the crystal field created by the periodic potential of the crystal lattice, not all orientations of are equally energetically favorable (Figure 2.6) [24], [28].

The energy corresponding to this effect is called the magnetocrystalline anisotropy energy, E_A. In order to minimize the magnetocrystalline anisotropy energy, the magnetization will prefer energetically favorable orientations, along certain crystallographic directions called easy magnetization axes. For example, Fe with a bcc crystal structure has three <100> easy axes, Co with a hcp structure has one, [001], and Ni with a fcc structure has four <111> axes [7]. Figure 2.6 (c) illustrates all three situations.

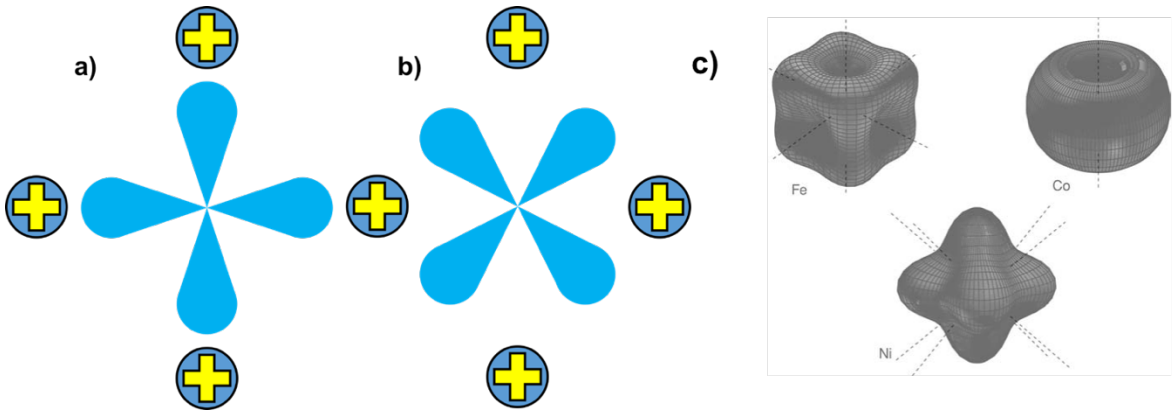

Figure 2.6: Schematic representation of the orientation of a 3d orbital inside the crystal field created by a periodic potential. Blue lobes represent negatively charged electronic orbitals, while the circles represent positively charged atoms of the crystal structure. In this case, the orientation in (a) is more energetically favorable than the one in (b). (c) Magnetocrystalline anisotropy energy surfaces for Fe, Co and Ni, showing the easy magnetization axes in each case. From [7].

Generally, when expressing the anisotropy energy, for a system with uniaxial symmetry, we can consider only a second-order uniaxial energy as:

$$E_A = K_u \sin^2 \theta$$

Equation 2.9

where θ is the angle between the magnetization orientation and the crystallographic easy magnetization axis and K_u is the anisotropy constant of the material. The anisotropy energy is therefore minimized when $\theta = 0°$ or $\theta = 180°$, i.e. the magnetization is aligned either parallel or antiparallel with the easy axis.

In the case of materials for which the orbital quantum number is zero, $\vec{L} = 0$, such is the case for materials with half-filled valence shells (Gd^{3+}, Fe^{3+}, Mn^{2+}, …), the charge distribution of the magnetic atom has a spherical symmetry. In this situation, all orbital momentum orientations have the same energy and the magnetocrystalline anisotropy is zero[1].

When the orbital quantum number is non zero, $\vec{L} \neq 0$, the situation changes. In the case of 4f rare earths, the SOI is stronger than the crystal field, and the relevant operator is the total angular momentum $\vec{J} = \vec{S} + \vec{L}$. The crystal field lifts the degeneracy of the fundamental state $(2J + 1)$ and the different orientations of the total angular momentum no longer have the same energy, resulting in high anisotropy constants. For 3d transition metals with localized orbitals, the SOI is small compared to the crystal field and the angular

[1] Magnetocrystalline anisotropy is zero only to first order perturbation. Higher order terms that are non-zero can appear, but their anisotropy constants are usually very small.

momentum is oftentimes “quenched”. The anisotropy constants in this case are small (see Table 1).

Material	Symmetry	K (first order) $[Jm^{-3}]$
Fe	bcc	$4.8 \cdot 10^4$
Ni	fcc	$-4.5 \cdot 10^3$
Co	hcp	$4.1 \cdot 10^5$
$Ni_{80}Fe_{20}$ (Permalloy)	fcc	$4 \cdot 10^2$
Sm_2Co_{17}	hcp	$3.3 \cdot 10^6$
$SmCo_5$	hcp	$17 \cdot 10^6$
$Nd_2Fe_{14}B$	tetragonal	$5 \cdot 10^6$

Table 1: Anisotropy constants at room temperature for several FM materials. FM based on 3f rare earth have significantly higher anisotropy constants than FM based on 3d transition metals.

The reason that the crystal field is stronger than the SOI for 3d transition metals while the opposite is true for 4f rare earths can be qualitatively understood by looking at their respective electronic configurations. In the case of 3d transition metals, the 3d electrons in the valence shell are the also outermost electrons of the atom and are strongly affected by the crystal field created by neighboring charges, therefore the crystal field is stronger than the SOI, resulting in lower magnetocrystalline anisotropy. In the case of 4f rare earths, the 4f electrons in the valence shell are shielded by the 5s and 5p electrons and are thus isolated from the surrounding crystal field. The crystal field in this case is weaker than the SOI, resulting in higher magnetocrystalline anisotropy.

When studying thin films, such is our case, we need to take into account another effect. At the surface of a thin film the symmetry of the crystal field changes with respect to the bulk, by losing the translational symmetry. L. Neel proposed in 1954 that this change in symmetry results in an additional term to the magnetocrystalline anisotropy. We will refer to this term as interface magnetic anisotropy. Being an interface effect, it becomes smaller as the thickness of the thin film increases, being negligible for thicknesses beyond a few nanometers. Taking the interface anisotropy into account, we can write the total anisotropy constant as:

$$K_u = K_{eff} = K_V + \frac{2K_S}{t}$$

Equation 2.10

where K_V is the volume anisotropy constant, K_S is the surface anisotropy constant and t is the thickness of our film. Equation 2.10 also gives us a means of estimating the two constants, by performing measurements as a function of film thickness and looking at the slope and intercept of a K_{eff} vs. $\frac{1}{t}$ plot. The most important consequence of the surface anisotropy, comes in the form of Perpendicular Magnetic Anisotropy (PMA), when K_S is the dominant term and favors a magnetization easy axis along the normal to the surface of the film.

The magnetocrystalline anisotropy appears therefore as the cumulated effect of crystal field and SOI, on each magnetic atom. Its effect is to align the magnetization along the easy magnetization axes. To take its effect into consideration, when studying the magnetization dynamics, we consider an equivalent effective magnetic field, $\vec{H}_A$, as the anisotropy field. The anisotropy field is the magnetic field needed to saturate the magnetization along a hard axis, and it is given by:

$$\vec{H}_A = \frac{2K_{eff}}{\mu_0 M_S}$$

Equation 2.11

2.2.4 Spin Orbit Interaction and Structural Inversion Asymmetry

According to Equation 2.8, the energy levels of the electron state are degenerate, corresponding to each of the spin states. Such a spin degeneracy of an electron state comes from time and space inversion symmetries [29]. For the time inversion symmetry, the eigenvalues of the electron states must satisfy the relation (Kramers degeneracy[2] [30]):

$$E_{\uparrow}(\vec{k}) = E_{\downarrow}(-\vec{k})$$

Equation 2.12

and for the space inversion symmetry:

$$E_{\uparrow}(\vec{k}) = E_{\uparrow}(-\vec{k})$$

Equation 2.13

where $\vec{k}$ is the electrons wave vector and ↑↓ are the up/down spin states [29].

[2] In quantum mechanics, the Kramers degeneracy theorem states that for every energy eigenstate of a time-reversal symmetric system with half-integer total spin, there is at least one more eigenstate with the same energy. In other words, every energy level is at least doubly degenerate if it has half-integer spin.

The expression of the SO Hamiltonian shows that the SOI has time reversal symmetry. Therefore, in a system with both time and space inversion symmetry, for zero applied magnetic field, $\vec{B} = 0$, the eigenvalues of the electron states will satisfy the relation [26], [29]:

$$E_{\uparrow}(\vec{k}) = E_{\downarrow}(\vec{k})$$

Equation 2.14

However, if the system in question does not have space inversion symmetry, i.e. the crystal potential through which the conduction electrons move is asymmetric, the spin degeneracy is removed, and the only relation that needs to be satisfied by the eigenvalues is the time reversal symmetry, $E_{\uparrow}(\vec{k}) = E_{\downarrow}(-\vec{k})$. In this situation we have a $\vec{k}$-dependent spin-splitting of the electron bands, $E_{\uparrow}(\vec{k})$ and $E_{\downarrow}(\vec{k})$ [26], [29]. In thin film heterostructures, the lifting of the spin degeneracy can come from bulk inversion asymmetry (BIA), such as the zinc blende structure [31], or from Structural Inversion Asymmetry (SIA) [32]. The latter is the case of multilayer heterostructures with dissimilar interfaces that create SIA along the normal to the surface. The SOI Hamiltonian for a SIA heterostructure consisting of a metal layer deposited in between different interfaces can be expressed as [26]:

$$\mathcal{H}_{SO} = \alpha(\vec{k}\times\hat{z})\vec{\sigma}$$

Equation 2.15

where $\hat{z}$ is the unit vector normal to the surface (SIA direction) and α is a material dependent constant proportional to the strength of the SOI.

An important consequence of the lifting of the spin degeneracy is that the correlation between the electrons wavevector, $\vec{k}$, and the spin leads to a net out of equilibrium spin polarization when an electric current is passed through our system [26]. It is this spin polarization, created by means of the SOI, that allows us to control the magnetization's direction, by interacting with the magnetization of an adjacent ferromagnetic (FM) layer. Like in the case of the STT, discussed in 2.1, the FM layer absorbs the perpendicular component of the SOI induced spin polarization at the interface [26], [33], [34]. Spin angular momentum transfer occurs by the same three mechanisms: (1) spin-dependent scattering at the interface between the FM and the NM material, (2) rotation of the transmitted and reflected spins, and (3) spin precession in the FM [1], [5], [9].

The ensemble of torques, created by this spin polarized current, that act on the magnetization is what we will later call Spin Orbit Torques (SOTs) due to their origin.

SOI is thus essential in our study of SOTs. Apart from what has been discussed here so far, SOI has many other important consequences such as damping and fine structure splitting of single atoms [7], [24], [25], and it is also responsible for physical phenomena such as the Anomalous Hall Effect (AHE), Spin Hall Effect (SHE), etc.

2.3 Spin Orbit Torques

The SOTs are fundamentally different from the STTs. Although they make use of spin polarized currents, they rely on strong SOI, intrinsic to the atomic structure of a material[3]. SOTs arise from angular momentum transfer to the magnetization from the crystal lattice and do not require magnetic textures or other sources of spin angular momentum. It is in recent years that current induced SOTs have been predicted in FM [21], [22], [35] and experimentally proven [19], [23].

In this section, we will discuss about how the SOTs are being generated, how they manifest, their differences with respect to the STTs and explain some of the more pressing questions regarding their origin.

2.3.1 Qualitative picture of the Spin Orbit Torques

For the existence of SOTs, there are two general requirements: large SOI and Structural Inversion Asymmetry (SIA). For this reason, most samples intended for the study of SOTs are Heavy Metal (HM) / Ferromagnetic (FM) / Non-magnetic (NM) multilayers. Here, the HM provides the SOI and, by sandwiching the FM layer between dissimilar interfaces, we provide the SIA along the normal direction to the sample plane, which we will designate as the $\hat{z}$ axis. It has been theoretically predicted [21], [35], [36] and experimentally observed [19], [20], [23], [37] that when we inject an in-plane electric current in such a structure, we will have angular momentum transfer from the crystal lattice to the magnetization, $\vec{M}$, of the ferromagnetic layer (Figure 2.7).

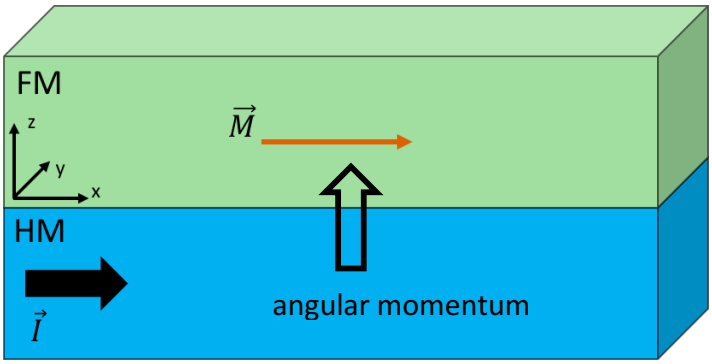

Figure 2.7: Schematic of a Heavy Metal / Ferromagnet heterostructure, showing current injection and magnetization direction, angular momentum transfer direction from the HM to the FM as well as the relevant reference frame. $\vec{M}$ is the magnetization of the FM layer and the thick black arrow represents the direction of the injected current, $\vec{I}$.

[3] This is why SOT devices generally have heavy metals (HM) in their structure.

As a result, two qualitatively different torques are created on the magnetization of the ferromagnetic layer: a Damping-Like (DL) torque, $\vec{T}_D$, and a Field-Like (FL) torque, $\vec{T}_{FL}$. If we inject an electric current ($\vec{I}$ or current density $\vec{J}_e$) along the $\hat{x}$ axis, the symmetry of the DL torque will be:

$$\vec{T}_D \approx \vec{m}\times(\vec{y}\times\vec{m})$$

Equation 2.16

and the symmetry of the FL toque will be:

$$\vec{T}_{FL} \approx \vec{m}\times\vec{y}$$

Equation 2.17

But, since the torque can be expressed as the cross product between the magnetic moment and the magnetic field, $\vec{\tau} = \vec{m}\times\mu_0\vec{H}$, we can discuss the current induced torques by means of their effective fields (Figure 2.8). We therefore have:

$$\vec{H}_D \approx \vec{m}\times\vec{y}$$

Equation 2.18

for the DL effective field, and for the FL effective field:

$$\vec{H}_{FL} \approx \vec{y}$$

Equation 2.19

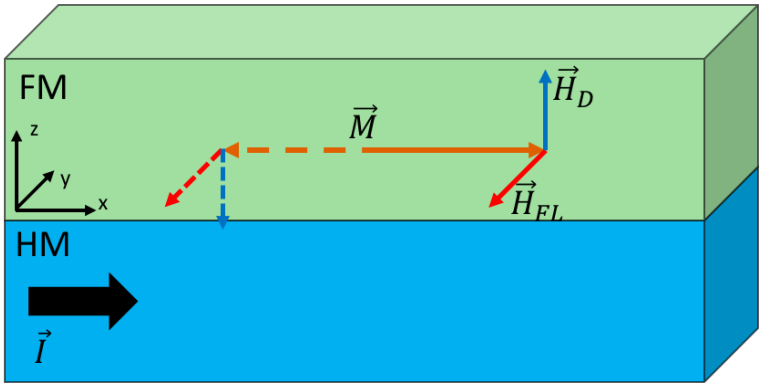

Figure 2.8: Schematic representation of the Damping-Like and Field-Like effective fields showing their dependence on the orientation of the magnetization. $\vec{H}_D$ is the Damping-Like effective magnetic field, $\vec{H}_{FL}$ is the Field-like effective magnetic field and $\vec{M}$ is the magnetization of the FM layer. The thick black arrow represents the direction of the injected current, $\vec{I}$.

The names of the two torques are not arbitrary. The DL effective field, $\vec{H}_D$, lies in the plane created by the SIA axis, in our case the $\hat{z}$ axis, and the current direction, in our case the $\hat{x}$ axis, and it is perpendicular to $\vec{M}$. As a consequence, this torque will change sign when $\vec{M}$ changes sign. For samples with in-plane magnetic anisotropy, when $\vec{M}$ is perpendicular to the

$\vec{I}$, this torque is opposed to the Gilbert damping[4]. As such, it is also called Damping-Like torque (or Slonczewski-Like torque as its expression is similar to the STTs).

The FL effective field, $\vec{H}_{FL}$, is perpendicular to the current direction and its sign is independent of $\vec{M}$. It acts like an applied magnetic field, hence its name. Figure 2.8 shows a schematic of the described situation.

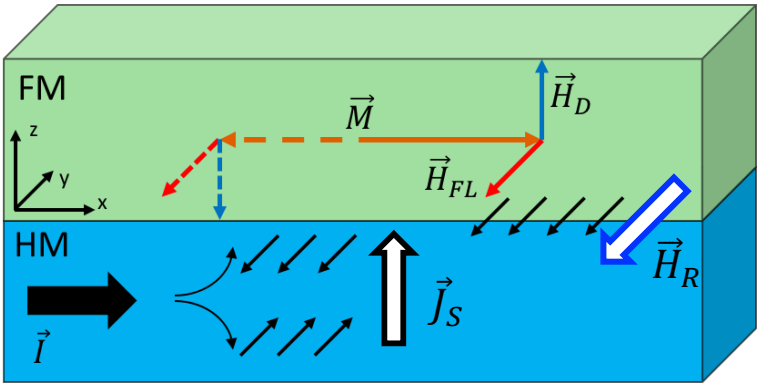

Figure 2.9: Schematic showing the generation of SOTs by the SHE and Rashba effects. $\vec{J}_S$ is the spin current from the Spin Hall Effect and $\vec{H}_R$ is the Rashba field.

An important question that we need to ask is "Where do these torques come from?". There are two mechanisms at work that address this question:

i) the Spin Hall Effect (SHE) and

ii) the Rashba effect[5]

The first mechanism is a bulk effect originating in the HM: when we inject an in-plane current, the SHE in the HM creates a spin current density, $\vec{J}_S$, incident to the FM. These spins couple with $\vec{M}$ and through the s – d exchange interaction create the torques [38], [39].

The second mechanism is an interface effect. Because of the SIA, the crystal field at Each of the two FM interfaces are not equal, which results in a net electric field. Therefore, conduction electrons will feel the effects of a magnetic field, called Rashba field, perpendicular to the injected current density, $\vec{J}_e$, and the asymmetry axis, $\hat{z}$. It causes the conduction electrons' spins to re-align at the interface and again, through the s-d exchange interaction create a torque on $\vec{M}$ [21], [22].

---

[4] The Gilbert damping is a dissipative term in the LLG equation of magnetization dynamics, $\frac{\partial \vec{m}}{\partial t} = \gamma_0 \vec{H}_{eff} \times \vec{m} + \alpha \vec{m} \times \frac{\partial \vec{m}}{\partial t}$. Here, γ_0 is the gyromagnetic ratio, $\vec{H}_{eff}$ is an effective field that takes into account the magnetocrystalline anisotropy, Zeeman energy, exchange interaction and magnetostatic interaction energies, $\vec{m} = \frac{\vec{M}}{M_S}$ and α is the Gilbert damping coefficient.

[5] The notions of Rashba Effect and SHE will be discussed in sections 2.3.2 and 2.3.3.

Both mechanisms make use of the SOI to create a non-equilibrium spin accumulation that eventually creates torques on $\vec{M}$ via the s-d exchange interaction between conduction electrons in the HM and electrons responsible for $\vec{M}$ in the FM [21], [40]. Zhang et. al. [9] show in a mathematical framework how, by considering this exchange interaction between the magnetization of a FM layer and a spin current perpendicular to said layer, one can demonstrate the existence of both an effective field and a torque that contribute to the current driven control of $\vec{M}$.

Distinguishing between these two mechanisms is one of the most important questions in the scientific community. In the following sections, we will look, in more detail, at each of the two mechanisms as well as at the non-equilibrium spin accumulation.

2.3.2 Rashba Effect (Inverse Spin Galvanic Effect)

An easy way of envisioning the Rashba effect is by looking at thin film structures that have SIA, such is the case of HM/FM/NM heterostructures. Conduction electrons in the FM will feel the effects of asymmetric crystal fields from the different interfaces, which give rise to an uncompensated electric field, $\vec{E}$. We can transform this electric field into a net effective magnetic field, $\vec{B} = \frac{\vec{v}\times\vec{E}}{2c^2}$, by considering the electron's rest frame.

This effective magnetic field we call Rashba field, $\vec{H}_R$ and its orientation is perpendicular to the direction of motion of the electrons, i.e. perpendicular to the direction of the injected current (Figure 2.10).

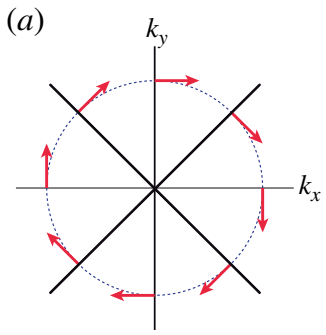

Figure 2.10: Orientation of the Rashba magnetic field (red arrows) with respect to the current direction (black lines). From [26]

When we inject an electric current ($\vec{I}$ or current density $\vec{J}_e$), the spins of the conduction electrons will interact with $\vec{H}_R$ and will reorient themselves parallel to it's direction. The Rashba effect thus creates a non-equilibrium spin density perpendicular to the current flow

and to the asymmetry axis. It is this spin density that interacts with the magnetization of the adjacent FM layer, by means of the s – d exchange interaction, creating a torque (Figure 2.11).

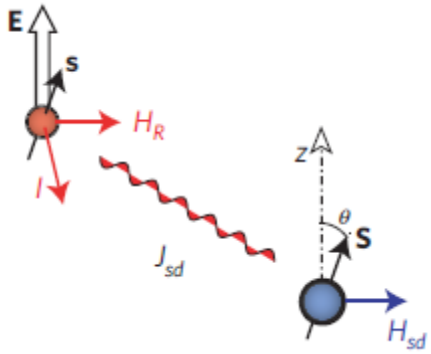

Figure 2.11: Schematic showing the s – d exchange interaction between the spin density and the local magnetization. The spins of the conduction electrons, $\vec{s}$, exert a torque on the local magnetization, $\vec{S}$, by means of the exchange interaction. From [19]

Taking the Rashba interaction into account, we can write the total Hamiltonian for a 2D electron gas system as [19], [21], [26], [36]:

$$\mathcal{H} = \frac{\hbar^2 k^2}{2m_e^*} + \alpha_R(\vec{k}\times\hat{z})\vec{\sigma}$$

Equation 2.20

where m_e^* is the effective electron mass and α_R is a material dependent parameter that is proportional to the strength of the SOI. The Rashba term in this expression is the same as the SOI interaction for SIA shown in Equation 2.15; so, we can see the Rashba effect as a consequence of the SOI interaction in a 2D electron gas system with SIA.

To see how this leads to the creation of a non-equilibrium spin density perpendicular to the current flow and to the asymmetry axis we look at the Fermi surfaces for the majority and minority carriers in our FM. Manchon and Zhang [21] provide a theoretical calculation of this spin density as well as an intuitive picture. Figure 2.12 shows the Fermi surfaces at equilibrium. When we apply an electric field (i.e. inject an electric current density), the Fermi surface shifts along the opposite direction. The dashed circles represent the shift of the Fermi surface under an applied electric field.

If we neglect the Rashba interaction, Figure 2.12 a), the spins of the conduction electrons are all aligned parallel and antiparallel to the local magnetization. There is no net spin density created by the shift for either spin population.

If we take into account the Rashba interaction however, Figure 2.12 b), the spins of the conduction electrons are all aligned with the Rashba field, perpendicular to the asymmetry

axis and to the current flow. In this case, each spin population gains a net spin density of different sign and, because their radii are different, the system gains a net spin density, proportional to the applied electric field (i.e. the current density). However, without considering also the exchange interaction there is no means by which this net spin density can interact with the local magnetization. Adding the exchange interaction into the mix, Figure 2.12 c), the net spin density created by the Rashba interaction is coupled with the local magnetization thus exerting a torque on $\vec{M}$ in the adjacent FM layer [19], [21], [22], [26], [35]. If the injected current is strong enough, this torque can be used to manipulate the direction of $\vec{M}$. Also, by reversing the current we can change the direction the the SOTs, thus having reversible control of the magnetization.

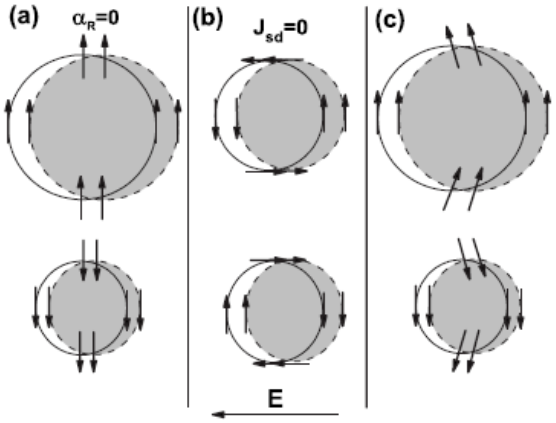

Figure 2.12: Schematic showing the Fermi surface for majority up (top) and down (bottom) electrons for a ferromagnet, corresponding to zero Rashba SOI (a), non-zero Rashba SOI (b), and non-zero Rashba SOI combined with exchange interaction (c). The dashed circles represent the shift of the Fermi surface under an applied electric field. From [21]

2.3.2.1 Field-Like Torque

Combining the effects of the Rashba interaction and the exchange interaction, we can write the Hamiltonian of our 2D electron gas system as [26]:

$$\mathcal{H} = \frac{\hbar^2 k^2}{2m_e^*} + \alpha_R\left(\vec{k}\times\hat{z}\right)\vec{\sigma} + J\frac{\vec{M}}{M_S}\vec{\sigma}$$

Equation 2.21

where M_S is the saturation magnetization, J is the exchange constant and $\vec{\sigma}$ is the net spin density created by the current flow. We can write the effective field acting on the local $\vec{M}$ as [21], [22], [26], [35]:

$$\vec{B}_{SO} = J\frac{\langle\delta\vec{\sigma}\rangle}{M_S} = -\frac{m_e^*\alpha_R}{e\hbar M_S}Pj(\hat{z}\times\vec{j})$$

Equation 2.22

which, in terms of torque yields:

$$\vec{T}_{SO} = \frac{\vec{M}}{M_S}\times J\langle\delta\vec{\sigma}\rangle = \frac{m_e^*\alpha_R}{e\hbar}Pj\left[\vec{M}\times(\hat{z}\times\vec{j})\right]$$

Equation 2.23

We call this torque Field-Like Toque and its associated effective field Field-Like or Rashba field.

2.3.2.2 Damping-Like Torque

We have seen how, in a HM/FM heterostructure, the Rashba interaction coupled with the exchange interaction lead to the Field-Like effective field acting on the magnetization creating the Field-Like torque.

Now we will look at how the same interaction gives rise to a second torque acting on the magnetization, perpendicular to the Field-Like torque. It is a more complicated picture.

For this, we look at the Rashba model of a 2D electron gas system with SIA [41]. We have seen that injecting an electric current along the $\hat{x}$ axis will induce a spin accumulation at the interface equivalent to an effective magnetic field, $\vec{H}_{FL} \approx \vec{y}$. The question is how does a spin accumulation along the $\hat{z}$ axis, capable of creating an effective magnetic field on the magnetization, appear?

Kato *et. al.* [42] showed that in InGaAs semi-conductor thin films, when there is a magnetic field component parallel to the injected current a second spin accumulation, along the $\hat{z}$ axis, will exist. This spin accumulation would be capable to create a Damping-Like torque on the magnetization. Engel *et. al.* [43] gave a theoretical model of this effect for a Rashba 2D electron gas system. According to their theory, the perpendicular spin accumulation, $\vec{\sigma}_z$, arises from the combined effects of $\vec{B}_R$, the Rashba field, and anisotropic spin dependent conductivity. Figure 2.13 shows a simplified schematic of this effect.

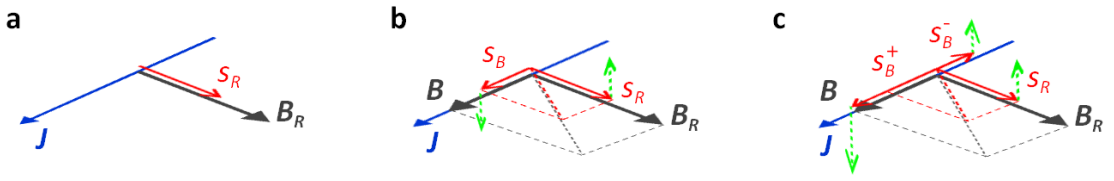

Figure 2.13: Schematic showing the $\vec{H}_{FL}$ effective field with the associated spin accumulation $\vec{\sigma}_y$ (a), the longitudinal spin accumulation, $\vec{\sigma}_x$, induced by the external field, $\vec{H}$, (b), and the two different torques corresponding to $\vec{\sigma}_x^+$ and $\vec{\sigma}_x^-$ that produce a net out of plane torque. From [20].

When the Rashba interaction is considered, an injected in-plane current along the $\hat{x}$ axis creates a spin accumulation along the $\hat{y}$ axis, $\vec{\sigma}_y$, oriented along the direction of $\vec{B}_R$. When we add an in-plane external magnetic field along the $\hat{x}$ axis, $\vec{B}$, another spin accumulation will be created, independent of the first and oriented along the direction of the field, $\vec{\sigma}_x$. The two spin accumulations will now precess, $\vec{\sigma}_y$ around $\vec{B}$ and $\vec{\sigma}_x$ around $\vec{B}_R$ giving rise to two torques, $\vec{B}\times\vec{\sigma}_y$ and $\vec{B}_R\times\vec{\sigma}_x$. But, since the two spin accumulations are proportional to their respective fields, the two torques will be equal and cancel each other out [20]. This is an ideal case. In reality, $\vec{B}_R$ is an effective magnetic field created by a difference in spin dependent electron mobility. If we consider $\vec{\sigma}_x$ as the sum of two components $\vec{\sigma}_x = \vec{\sigma}_x^+ + \vec{\sigma}_x^-$, with different mobility, $\vec{\sigma}_x^+$ and $\vec{\sigma}_x^-$ will precess around $\vec{B}_R$ at different speeds. The corresponding torques will also be different and will no longer cancel out the $\vec{B}_R\times\vec{\sigma}_x$ torque [20]. Taking into account spin relaxation, Engel et. al. [43] show that this leads to a net perpendicular spin accumulation, $\vec{\sigma}_z \approx \vec{B}_R\times\vec{B}$.

In the case of a FM, it is the magnetization, $\vec{M}$, that induces a spin accumulation parallel to the current direction, $\vec{j}$, giving rise to a $\vec{\sigma}_z \approx \vec{B}_R\times\vec{M}$ perpendicular spin accumulation by means of the mechanism described above [20]. The corresponding torque has the symmetry of the Damping – Like torque and can achieve magnetization switching. The associated effective field, called Damping – Like effective field, will be:

$$\vec{H}_D \approx \vec{m}\times\vec{y}$$

Equation 2.24

Other authors [44] propose a framework based on the intrinsic Berry curvature mechanism (initially used to explain the AHE in FM semiconductors [45]). Based on this model, the authors show that there is an intrinsic SOT, similar to the Damping-Like torque (the SHE effect is excluded by design since they study (Ga,Mn)As thin films with no HM).

2.3.3 Spin Hall Effect

In the previous section, we have seen how the two SOTs arise from the Rashba interaction at the interface between a HM and a FM, in the presence of strong SOI and SIA. But there is another mechanism that could be responsible for the generation of SOTs, based on the Spin Hall Effect (SHE) originating in the bulk of the heavy metal [37].

The Spin Hall Effect was predicted by Dyakonov and Perel [46] in 1971. It is a consequence of the SOI and consists in the creation of a spin current proportional and transverse to a charge current flowing within a heavy metal conductor. This current leads to the formation of spin accumulations at the edges of the conductor. The orientations of the spin accumulations are opposite at opposing edges. Figure 2.14 shows a schematic of the spin accumulation for a thin film and a cylindrical conductor.

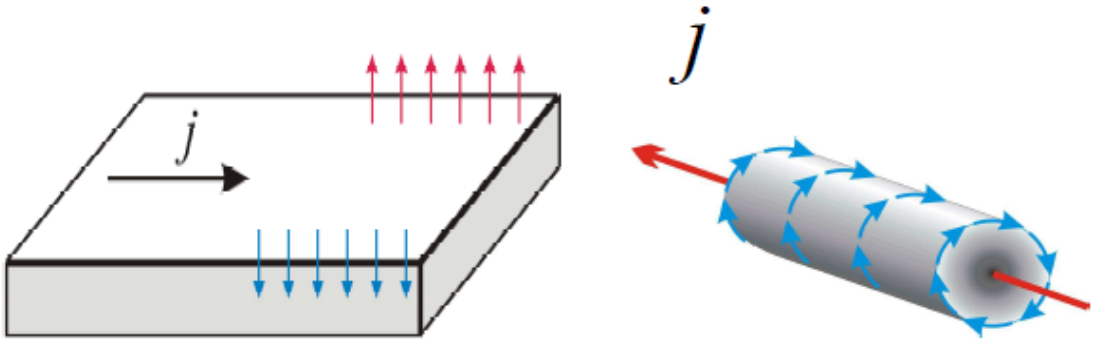

Figure 2.14: Schematic of the Spin Hall Effect. For a thin film, an injected electrical current induces spin accumulation at the edges of the sample. For a wire the spins wind up around the surface, similar to the magnetic field created by the current itself. From [38]

The term itself, Spin Hall Effect, was introduced in 1999 by Hirsch [47] due to its similarity with the Hall Effect which results in charge accumulation at the edges of a conductor. In the case of the SHE, when an electric current passes through a heavy metal, conduction electrons will suffer spin dependent scattering, giving rise to a spin current, $\vec{J}_s$, transversal to the current direction. There will be no net charge current, since there will be the same number of spin up and spin down electrons being scattered in opposite directions, but there will be a spin imbalance [38]. The SHE is present in non-magnetic and semiconductor materials and allows the generation of a spin current without the need of a FM material or magnetic field.

The origin if the SHE can be extrinsic and intrinsic. For the extrinsic SHE, the mechanisms involved in the scattering process are skew-scattering and side-jump [48]–[50]. The skew-scattering mechanism, or Mott effect [51], [52], can be explained by considering the electron's movement through the electric field created by an impurity (Figure 2.15). Because

of the presence of the impurity, the crystal field in the vicinity will no longer be homogeneous. Through the SOI, the conduction electron feels the effect of a magnetic field, $\vec{B} \approx \frac{\vec{v}\times\vec{E}}{2}$, perpendicular to the electrons trajectory. From the cross product, $\vec{v}\times\vec{E}$, we see that, as the velocity vector changes with the trajectory upon scattering, the orientation of $\vec{B}$ will depend on the scattering. It will be opposite for electrons scattered to the right than it is for electrons scattered to the left. Therefore, spin up electrons will be scattered to the right and spin down electrons will be scattered to the left, giving rise to the Spin Hall Effect [38], [53], [54].

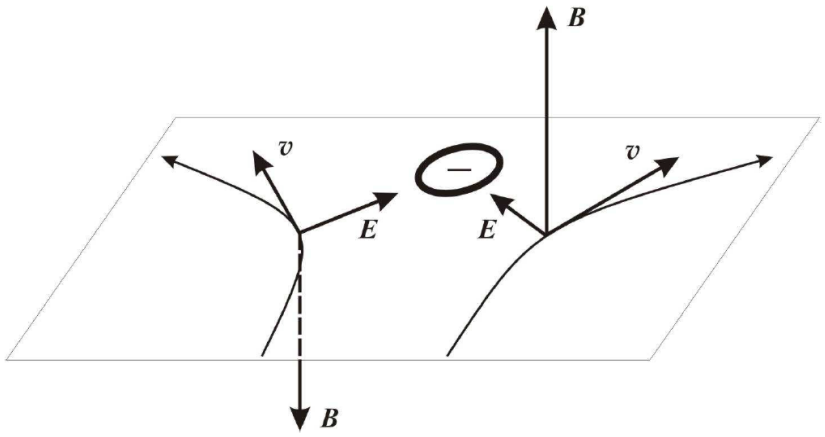

Figure 2.15: Schematic of the skew-scattering mechanism. The electron moving in the central potential of the impurity feels the effect of a magnetic field perpendicular to the crystal field and the electron's velocity. This magnetic field has opposing orientations for electrons scattered to the right and for electrons scattered to the left, causing spin up electrons to be scattered to the right and spin down electrons to the left. From [38]

The second mechanism, the side-jump, was introduced by Berger [55]. In his work, the conduction electron is viewed as a wave packet. Let us consider current injection along the $\hat{x}$ axis and an impurity creating a central potential. Upon scattering on the impurity, the center of mass of the wave packet suffers a deviation transversal to the current direction which, in the case of non-magnetic metals, is spin dependent (Figure 2.16). The ensemble of such scattering events leads to the formation of spin accumulations at the edges of the conductor. As in the previous case, the orientation of the spin accumulations is opposite at opposite edges [49].

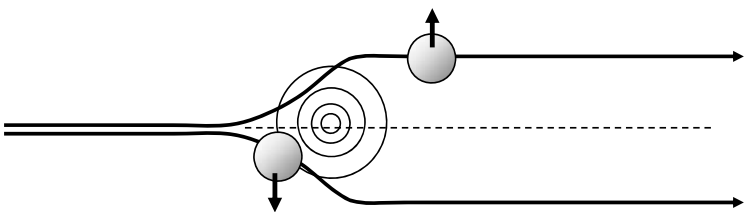

Figure 2.16: Schematic showing the side-jump scattering mechanism. From [49]

A third mechanism, giving rise to what is known as intrinsic SHE. It is called "intrinsic" because it is independent of impurity scattering. This effect was first predicted by Murakami *et. al.* [56] for p-type semiconductors and by Sinova *et. al.* [57] for a 2DEG with Rashba-type SOI. The Intrinsic SHE has been extensively studied by Kontani *et. al.* [58]–[61]. What happens is that electrons with spin up and spin down will get distributed in different d orbitals as they change atomic sites. This is in order to comply with Hund's third rule[6]. As spin up and spin down electrons turn anti-clockwise and clockwise respectively, they get scattered in opposite directions, thus creating a transverse spin current transversal to the current direction.

The combination of extrinsic and intrinsic SHE, regardless of the dominant scattering mechanism, leads to the formation of a spin current, $\vec{J}_s$, transversal to the current direction. This spin current is proportional to the charge current, $\vec{J}_e$, and can be expressed as:

$$\vec{J}_s = \frac{\hbar}{2e}\theta_H \vec{J}_e$$

Equation 2.25

where $\theta_H = \frac{\sigma_{SHE}}{\sigma}$ is the so-called Spin Hall Angle (SHA), a parameter which gives the ratio of spin current being created to electric current being injected. It is an intrinsic material dependent parameter and it can take positive and negative values. In the case of a HM thin film, $\vec{J}_s$ oriented along the $\hat{z}$ axis, thus it creates two spin accumulations, with opposite orientations, at the top and bottom interfaces of the HM, with the form $\delta\vec{s} = \vec{j}\times\hat{n}$, where $\hat{n}$ is a unitary vector normal to the surface.

In addition to the Spin Hall Angle, the amplitude of the spin current, and therefore the spin accumulation, also depends on the thickness of the HM. When the thickness of the HM is smaller than the spin diffusion length, $t_{HM} < \lambda_{SF}$, through diffusion the spin accumulation at the interfaces will decrease as spins will diffuse back into the "bulk" of the layer.

The SHA and spin diffusion length in heavy metals like Pt, Ta and W have been extensively studied in literature, however the values reported vary depending on sample system and measurement technique used (see section 3.2).

When a FM is put in contact with the HM, conduction electrons at the interface are influenced both by the SHE in the HM and by the magnetization of the FM layer. The spin

[6] Hund's third rule states that the total kinetic moment, J, is $J = |L - S|$ for an atom with it's valence shell less than half filled and $J = |L + S|$ for an atom with its valence shell more than half filled [7]. It thus dictates whether the orbital and spin magnetic moments are parallel or antiparallel.

accumulation created at the HM interface through the SHE can diffuse into the FM. Then, through the s-d exchange interaction, it interacts with the localized d electrons responsible for the magnetization of the FM giving rise to torques acting on the magnetization. Using a semi-classical drift-diffusion model, Manchon [62] shows that these, as in the case of the Rashba Effect, the torques arising from the SHE are of the form $\vec{T}_{DL} \sim \vec{m} \times \hat{y}$ and $\vec{T}_{FL} \sim \vec{m} \times (\hat{y} \times \vec{m})$.

To propose a unified approach to the SOTs, based both on Rashba Effect and SHE, Haney et. al. [39] used a diffusive model to theoretically calculate the SOTs created by the SHE on the magnetization, by considering that the transversal component of the spin current is completely absorbed at the interface and neglecting the side-jump mechanism. To describe the spin transport at the interface, a parameter called "Spin Mixing Conductance" is used. This parameter, introduced by Brataas et. al. [63] is relevant for spin transport at the interface between layers with non-collinear magnetizations. It takes into account the rotation of the spins around the magnetization of the FM layer.

We can express the Field-Like torque as:

$$\vec{T}_{FL} \approx \frac{\theta_H \hbar j_0}{2e\mu_0 M_S t_{FM}} \left(\vec{M} \times \hat{y}\right)$$

Equation 2.26

and the Damping-Like torque as:

$$\vec{T}_{DL} \approx \frac{\theta_H \hbar j_0}{2e\mu_0 M_S t_{FM}} \left(\vec{M} \times \left(\vec{M} \times \hat{y}\right)\right)$$

Equation 2.27

where j_0 is the electric current density, θ_H is the SHA, t_{FM} is the thickness of the FM layer and M_S is the saturation magnetization of the FM layer.

Theoretically it has been demonstrated that both the Field-Like effective field and the damping-Like effective field can arise theoretically from either the Rashba Effect or the SHE [21], [22], [39], [62]. To further complicate the matter, both effects can occur at the same time in the sample structures needed to achieve SOTs. According to theoretical studies, it is generally expected that the SHE provides a stronger contribution to the Damping-Like torque than the Rashba effect, which in turn provides a stronger contribution when it comes to the Field-Like torque [62], [64], [65].

The fact that we find the same SOT components, with the same symmetry arising both from the Rashba effect as well as from the SHE, has sparkled a long debate regarding the origin of the SOTs.

2.3.4 Anomalous and Planar Hall Effect – tools to measure the SOTs

The Hall Effect [66] consists in the creation of a voltage, called Hall voltage, transverse to the direction of an electric current flowing inside an electrical conductor when an external magnetic field is applied transversal to the current. For an electric current flowing along the $\hat{x}$ axis and an applied magnetic field along the $\hat{z}$ axis, we can write the transverse or Hall resistivity as

$$\rho_H = -\rho_{xy} = R_0 H$$

Equation 2.28

where R_0 is the Hall coefficient.

As early as 1881[7], 2 years after its discovery [66], it has been observed that in the case of FM materials, the Hall Effect was substantially larger.

This phenomenon is known as the Anomalous Hall Effect (AHE). In the case of FM materials, the transverse resistivity includes an additional component, which is non-zero even in zero field, and which depends on the FM's magnetization. Empirically, we can write the transverse resistivity as:

$$\rho_{xy} = R_0 B_z + \mu_0 R_S M_z$$

Equation 2.29

where R_S is the anomalous Hall coefficient and M_z is the magnetization component along the $\hat{z}$ axis [48].

The origin of the AHE rests on the same mechanisms as in the case of the SHE [48], [49], namely skew-scattering [51], [52], side-jumping [55] and intrinsic effects [58]–[61], [67].

As in the case of a HM, the SOI creates a transverse spin current in a FM material. Only this time, because of the magnetization of the FM, spin up and spin down electrons have different mobilities. As shown in Figure 2.17, in the case of a FM, spin up and spin down electrons have different densities of states at the Fermi level. This makes electrons with one

[7] E. Hall, Philos. Mag. 12, 157-160 (1881)

spin orientation (in this case down) more susceptible to scattering events, and thus having a lower mobility than the other orientation (in this case up).

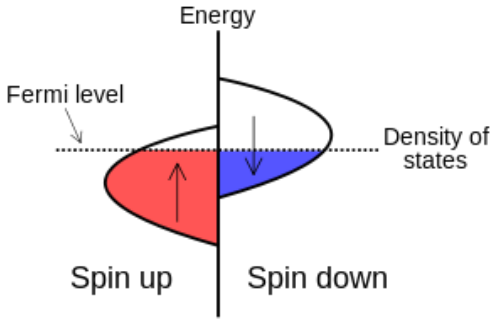

Figure 2.17: Schematic showing the density of states at the Fermi level for spin up and spin down electrons in a FM.

Having different mobilities means that the spin current created will be accompanied by a charge current as well, leading to a transverse voltage that depends on the perpendicular component of the magnetization, and can be expressed as:

$$V_H \sim R_{AHE} \frac{M_z}{M_s} \sim I R_{AHE} \cos\theta$$

Equation 2.30

where θ is the angle between $\vec{M}$ and the normal to the surface and I the injected current.

Another component to the transverse resistivity, which depends on the angle of the in-plane component of the magnetization, M_{xy}, with respect to the direction of the injected current is given by the Planar Hall Effect (PHE, or transverse AMR[8]) [68], [69]. Empirically, the PHE component of the transversal resistivity can be expressed as [70][9]:

$$\rho_{trans} \sim (\rho_{\parallel} - \rho_{\perp}) \sin\varphi \cos\varphi$$

Equation 2.31

and the corresponding transverse voltage as:

$$V_H \sim I R_{PHE} \sin^2\theta \sin 2\varphi$$

Equation 2.32

where θ is the polar angle of the magnetization, φ is the angle between the magnetization and the current, $\rho_{\perp}$ and $\rho_{\parallel}$ are the longitudinal and transverse resistivities corresponding to $\varphi = 0°$ and $\varphi = 90°$ respectively.

[8] Anisotropic Magnetoresistance

[9] There will also be a longitudinal component of the resistivity corresponding to the longitudinal AMR, which can be expressed as: $\rho_{long} \sim \rho_{\perp} + (\rho_{\parallel} - \rho_{\perp}) \cos^2\varphi$ [70].

By using the AHE dependence on the perpendicular component of the magnetization, M_z, and the PHE on the in-plane component of the magnetization M_{xy}, one can follow the changes in the magnetization's position induces by external factors such as the SOTs. In section 3.3 as well as in chapter 4 we will discuss at length about how the AHE and PHE are used to observe and quantitatively measure the SOTs.

3 State of the art

3.1 Spin Orbit Torque Manifestations

In this chapter I will try to give an overview of the current directions in the quantitative analysis of SOTs. The purpose of this it, is not to give an exhaustive review of the work done in this field, but rather to emphasize the most significant results in the context of this manuscript.

In the first section, we will briefly look at two important, and intimately connected, applications that SOTs make possible: Magnetization Switching and current induced magnetic Domain Wall (DW) motion.

3.1.1 Magnetization Switching

After the first experiments demonstrating current induced bipolar switching by SOTs [20], [37], the idea became that three terminal MRAM devices based on SOTs could be implemented. Current induced SOT switching has therefore been studied extensively in HM/FM/MgO samples, which are representative for the lower electrode of Magnetic Tunnel Junction (MTJ) devices[10].

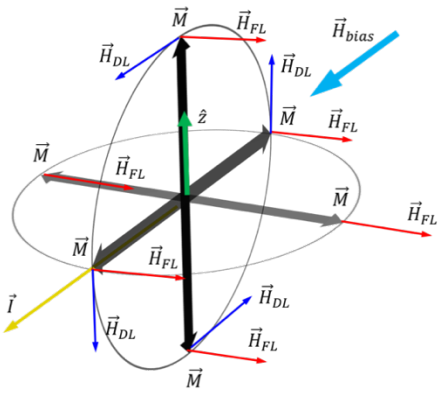

Figure 3.1: Schematic showing effective fields corresponding to the current induced SOTs acting on the magnetization $\vec{M}$, (black arrows), for a system with SIA along the $\hat{z}$ axis (green arrow). Red arrows represent the Field-Like effective field and blue arrows represent the Damping-Like effective field for different possible orientations of the magnetization. The FL always points in the same direction while the DL rotates with the magnetization and disappears when $\vec{M}$ is perpendicular to the current, $\vec{I}$ (yellow arrow) and in-plane. An applied bias field (light blue arrow) will destabilize one orientation of $\vec{M}$ (up/down) and stabilize the other (down/up).

[10] Three terminal MTJ based devices provide a means to "write" information by using in-plane current injection to change the orientation of the magnetization of a "free" magnetic layer. Using Tunnel Magnetoresistance, the written information stored can be "read" in terms of the relative orientation of the magnetization of the "free: layer and a "fixed" reference layer. As such, MTJ based devices form the basis of spintronics devices.

We can understand how current induced SOT magnetization switching works by looking at the symmetry of the SOTs and consider a typical system with SIA (ex. HM hall cross with a FM dot at its center, as shown in Figure 3.6 (a)). Figure 3.1 shows a schematic of the SOTs' symmetry in this situation.

Considering the situation described in Figure 3.1, for a system with PMA, the magnetization, $\vec{M}$ will be oriented either up or down. Let's say up. When an in-plane current, $\vec{I}$, is injected, let's say along the $\vec{x}$ axis, the two components of the SOTs, the FL and Dl effective fields are created. We notice that, since it always points in the same direction (along the $\hat{y}$ axis), the FL effective field cannot be responsible for the switching. At most, it could align $\vec{M}$ along the $\hat{y}$ axis. The DL effective field however, is always perpendicular to $\vec{M}$ and lies in the plane created by $\vec{M}$ and $\vec{I}$. Since it always changes direction, it will cause $\vec{M}$ to rotate. Here is where the bias field comes into play. In one situation, when $\vec{M}$ points up, it will add-up to the DL effective field, destabilizing the up orientation. When $\vec{M}$ points down, it opposes the DL field, stabilizing the down orientation. We now have up/down switching. Changing the direction of the current and the bias filed will result in down/up switching.

Switching measurements have been conducted in Pt/Co/AlO_X [71], Pt/Co/MgO [72], Ta/CoFeB/MgO [73], [74], Ta/CoFeB/TaO_X [75] Pt/Co/IrMn [76], W/CoFeB/MgO [77] samples with PMA and SIA. As switching speed is a very important parameter for applications, studies have also been conducted in the sub ns timescale. It has been demonstrated that deterministic ultrafast SOT switching in Pt/Co/AlO_X and Ta/CoFe/MgO/CoFeB samples with PMA is possible for current pulses of 180 and 400 ps respectively [78], [79]. Another important parameter is the critical current density required to achieve switching – the lower the better. In this context, Bi *et. al.* [80] showed that, for Pt/Co/AlO_X samples, the critical current density can be significantly lower in the case of thermally assisted SOT.

Cubukcu *et. al.* [81] demonstrated a proof of concept of a perpendicularly magnetized SOT-MRAM cell based on a CoFeB/MgO/CoFeB MTJ deposited on a Ta current line. The read/write operations, essential to a memory device, are achieved by magnetization reversal by in-plane current injection in the Ta current line and the subsequent reading of the TMR signal, just like in the case of STT-MRAM. Other studies show three terminal device switching by in-plane current injection in CuIr/CoFeB/MgO [82]. SOT-MRAM devices are not limited to perpendicular magnetization. Fukami *et. al*. [83] demonstrated SOT magnetization switching

in Ta/CoFeB/MgO based MTJs with the easy axis parallel to the current injection direction. Recent experiments have also demonstrated that SOT switching can also occur in AFM[11]/FM structures such as PtMn/[Co/Ni]/Co/MgO [84] and topological insulator based structures such as (Bs,Sb)Te [85].

Current induced magnetization switching is one of the most important manifestations of the SOTs. It is fundamental to the development of fast, non-volatile SOT based data storage devices. The ability to switch the magnetization over very short time scales makes SOT-based devices a very promising candidate for ultra-fast recording applications.

[11] Antiferromagnet

3.1.2 Domain Wall Motion

Another important manifestation of the SOTs is their influence on current induced DW motion, most importantly by allowing DW motion at very high speeds.

Remark

Theoretically, current induced DW motion as a consequence of STTs was predicted by Berger [16] in 1974. Initial theories [3], [86], [87] have considered the adiabatic torque, $\vec{T}_A$ (see section 2.1) to be responsible for DW motion. However, these theories could not account for the much lower critical currents observed experimentally [17], [88], [89]. It was Zhang and Li [13] that introduced the idea of the non-adiabatic torque, $\vec{T}_{NA}$, which acts on the DW like an easy axis effective magnetic field. It is $\vec{T}_{NA}$ that allows for current induced domain wall motion [14]. It induces an in-plane rotation of the magnetization, $\vec{M}$, inside the DW, which in turn creates a demagnetizing field, $\vec{H}_D$, perpendicular to the DW. The torque associated to $\vec{H}_D$, $\vec{T}_D$, will be oriented out-of-plane, parallel to $\vec{T}_A$. The combined effect of $\vec{T}_A$ and $\vec{T}_D$ is what drives the DW motion (Figure 3.2). A complete review of current induced DW motion is given by Boulle at. al. in [8].

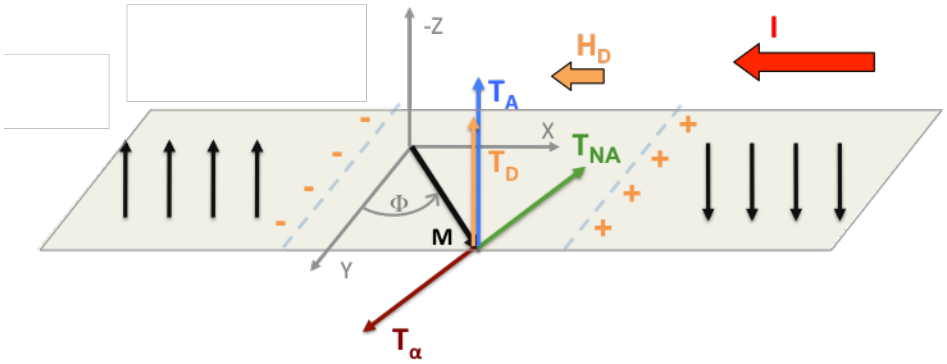

Figure 3.2: Schematic of current induced magnetic Domain Wall motion. $\vec{H}_D$ and $\vec{T}_D$ are the demagnetizing field perpendicular to the DW, and its associated torque, $\vec{T}_{NA}$ is the non-adiabatic torque, $\vec{T}_A$ is the adiabatic torque and $\vec{T}_\alpha$ is a dissipative term. From [90].

Initially, very fast DW motion (up to $400\,m/s$) has been observed in Pt/Co/AlO_X samples with PMA and SIA [91]. These observations were interpreted as an increase in the efficiency of the STT induced by the Rashba Effect [92]. Later, the experimental observation of the Field-like and Damping-Like SOTs [19], [20], has led to the conclusion that a more

complex mechanism is involved and that the Damping-Like torque plays an essential role in DW motion.

In 2011, Miron *et. al.* [93] showed that, in the same sample system as their previous experiment [19], Pt/Co/AlO_X with PMA and SIA, DW movement speeds up to $400\ m/s$ are possible. Their results show that, even for large current densities, no Walker breakdown[12] is observed, and the DW velocity varies linearly with the current density, consistent with the flow regime.

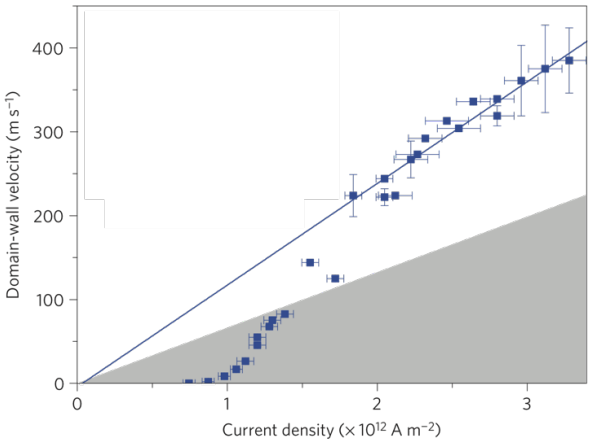

Figure 3.3: DW velocity as a function of current density for Pt/Co/AlO_X samples with PMA and SIA. At low current densities DW motion is in the creep regime, followed by strong depinning, and, for higher current densities, the flow regime is observed, where DW velocity is linear with current density. The grey area corresponds to DW velocities in the turbulent regime. From [93].

In order to explain these findings, we consider the presence of the Field-Like and Damping-Like SOTs in their system. First, the Damping-Like effective magnetic field acting on $\vec{M}$ inside the DW is oriented out-of-plane, along the easy magnetization axis. Thus, it acts like the non-adiabatic effective field, $\vec{H}_{NA}$, from the STT (see Remark 1) and participates directly to the DW motion. Secondly, the Field-Like effective magnetic field oriented along the $\hat{y}$ axis (assuming, as usual, current injection along the $\hat{x}$ axis) "stabilizes" the DW structure, delaying the onset of the Walker breakdown to higher current densities.

Micromagnetic calculations done by Thiaville *et. al.* [97] are very revealing in this context. The authors study the influence of DMI[13] on the DW in a thin film structure with PMA

[12] Field and current induced DW motion velocity depends on the strength of the applied magnetic field or current. In both cases, we can distinguish two separate linear velocity regimes, corresponding to viscous motion (creep regime) and stable DW structure. The two linearity regimes are separated by a complex transition regime which begins at a critical field called Walker field (or Walker-like critical current density). The transition is called Walker breakdown. In this regime, DW becomes oscillatory and the average velocity drops significantly [94]–[96].

[13] DMI (Dzyaloshinskii-Moriya interaction) is an antisymmetric exchange interaction present in low-symmetry systems (SIA) and it is another consequence of SOI [98]–[100]. It favors the existence of non-uniform magnetic structures (i.e. skyrmions) and the existence of Neel domain walls. [97], [101]–[103].

and SIA, similar to the experimental studies presented before. By considering the interface DMI energy, for very thin FM layers, they show that a Neel Wall (NW) configuration is more energetically favorable, above a critical DMI value, than a Bloch Wall configuration. Now, since very thin FM layers are also required in order to have PMA, NWs can be energetically favorable in most systems with PMA and SIA studied experimentally. By studying the dynamics of this DW structure under an applied easy axis magnetic field, the authors show that, indeed, the DMI extends the high velocity stationary DW motion regime to higher field values, delaying the onset of the Walker breakdown. The physics behind this is intuitive: as the DMI favors a Neel Wall domain structure, with a predetermined chirality, it is also responsible for stabilizing this structure. It makes the magnetization inside the DW less susceptible to precession around the applied field, thus extending the stationary regime to higher field values.

The influence of the DMI on current induced DW dynamics, alongside SOTs, is also shown to be responsible for the direction of DW motion (along current or electron flow) [102]. By tuning the sign of the DMI, one can effectively decide on the chirality of the DWs (since all NW created by the DMI will have the same chirality). This means than we can move multiple DWs in the same direction at the same time, a feature that is very important for applications (such as the race-track memory).

SOTs provide very interesting ways of controlling magnetization in HM/FM based devices. We can switch the orientation of $\vec{M}$ very fast, thus writing information in a device which can be later read through the TMR effect. We can move DW along a strip, with very high speeds, thus creating a shift register. We can use the shape of our devices to tune both switching and DW motion to suit a particular device application.

In the following sections, we will look at the first experimental evidence of the Field-Like and Damping-Like SOTs, we will discuss their origin and measurement techniques used for quantitative analysis

3.1 Experimental Observation of the SOTs

In this section, we will look at the first experimental evidence of the Field-Like and Damping-Like torques and their corresponding effective fields.

3.1.1 Field-Like torque

The first experimental evidence of the Field-Like torque was found in p-type FM semiconductors, by Chernyshov et. al. [23]. By injecting an in-plane current and measuring the transverse anisotropic magnetoresistance of a circular (Ga,Mn)As dot, the authors observe the effects of a current induced effective field, transversal to the current direction, and proportional to the current amplitude. They further show that, for current amplitudes above a critical value, this field is strong enough to switch the direction of the magnetization.

Later, Miron *et al.* [19] in Pt/Co/AlO_X found the first evidence of the Field-Like torque in FM metal systems with strong PMA as well as SIA along the normal direction. Their idea was to study the probability of magnetic domain nucleation under the action of an in-plane current, in the presence of an external in-plane transversal bias magnetic field.

The process of magnetic domain nucleation can be qualitatively described by the energy profile of the magnetization as a function of its orientation. The nucleation probability is given by the probability of the magnetization to overcome the energy barrier separating the two magnetization states (up and down in this case) due to thermal fluctuations. Figure 3.4 shows the energy profile of the magnetization for a system with PMA such as the ones studied in [19]. When there is no applied magnetic field, the energy profile is symmetric (black line in Figure 3.4). In this case, the energy barriers for up-down and down-up nucleation are equal. When an external transversal magnetic field is applied, the energy profile becomes asymmetric and the energy barriers are no longer equal. This means that nucleation will be favored in one direction (ex. up-down) while in the other direction will be suppressed.

Because of its symmetry, the Field-Like effective field will act as a transversal magnetic field, and, depending on the direction of the applied current, will either add to the bias field or diminish it. In this way, the presence of the Field-Like effective field will modify the height energy barriers (green and red lines in Figure 3.4).

By using wide field polar Kerr microscopy, on devices patterned in the shape of nanowires, the effects of single 100 ns current pulses of constant amplitude are studied.

Starting from a uniform magnetization state, these pulses produced nucleation in all wires, gradually making the transition to a demagnetized state. When the bias field is applied (perpendicular to the current direction), nucleation is observed to occur only for one direction of the current (positive). When the sign of the bias field is changed, nucleation is found to occur only when the direction of the current is also changed (negative). Figure 3.5 shows the differential Kerr images showing this asymmetry in nucleation. What this actually means is that when the bias field and the current induced field are parallel nucleation is favored. When they are antiparallel, nucleation is suppressed.

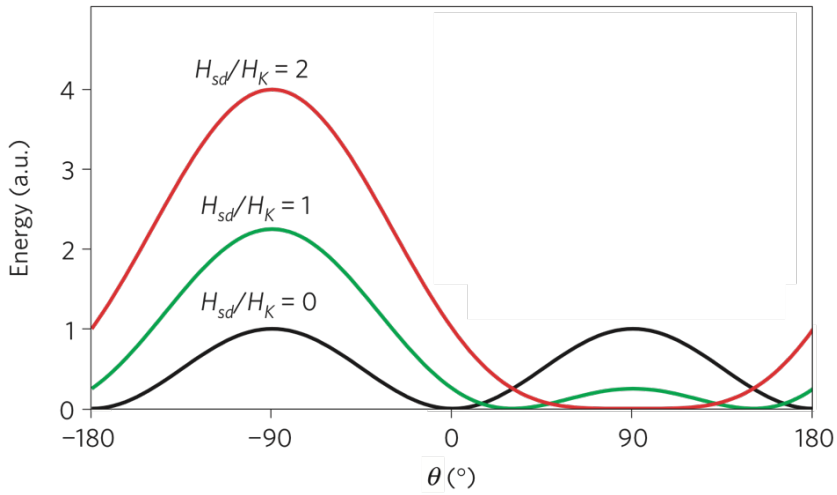

Figure 3.4: Energy profile of the magnetization as a function of its orientation, for a system with PMA, showing the energy barrier for different H_{FL}/H_K ratios. From [19].

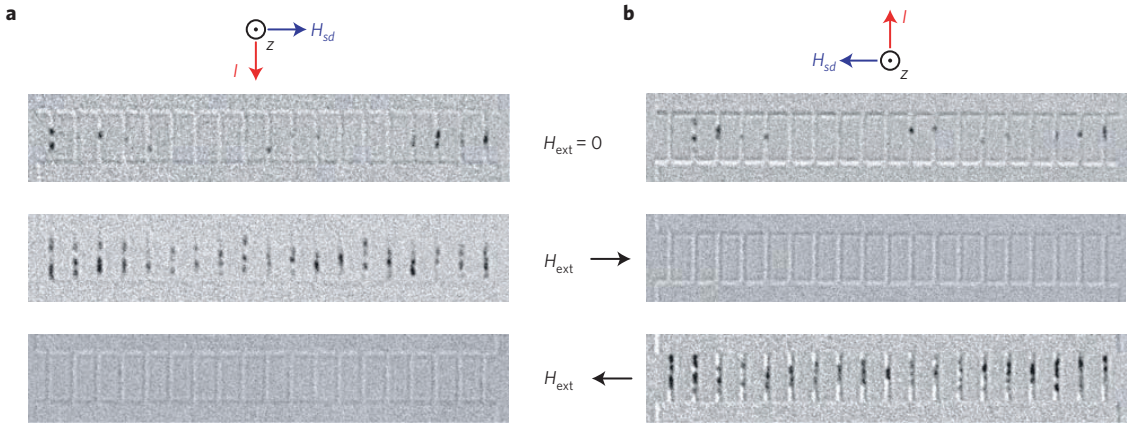

Figure 3.5: Differential Kerr microscopy images showing domain nucleation following current pulse injection of positive (a) and negative (b) sign, for an applied external field value of $0, \pm 47.5\ mT$. From [19].

The current density is constant throughout the measurements and thermal effects are excluded as a source of the nucleation asymmetry observed. Also excluded are artefacts from

misalignment of the the applied field since these would not depend on the direction of the applied current pulse.

To complete the study and investigate the role of the interface, the same experiment is performed on Pt/Co/Pt samples without SIA. In this case, no nucleation asymmetry is observed.

This asymmetry proves the existence of a current induced effective field that acts on the magnetization of the Co layer. This effective field is perpendicular to the current direction and to the SIA axis, which is this case is the normal to the interface. It also changes sign by reversing the current, is independent of the direction of the local magnetization and is uniform inside the device, all consistent with the symmetry properties predicted in theory [21], [22]:

$$\vec{H}_{FL} \approx \vec{y}$$

Equation 3.1

The value observed for the Field-Like effective magnetic field, $\vec{H}_{FL}$, was $(1 \pm 0.1) \cdot 10^{-8}\ Tcm^2A^{-1}$.

3.1.2 Damping-Like torque

Initial observations of a Damping-Like torque induced by in-plane current injection were made by Ando et. al. [104] in Py/Pt thin films with in-plane magnetic anisotropy. The authors investigate the modulation of the width of the FMR[14] spectra by the spin current created by the SHE in the Pt layer. Most notably, they observe that when the bias field and current are perpendicular, the modulation depends on the current polarity, indicating that magnetization relaxation depends on the current. Depending on the sign of the current, the angle of the magnetization precession around the bias field is either increased or decreased. They explain their findings in terms of the spin transfer induced by the SHE.

In another experiment, Miron *et. al.* [20] demonstrated the existence of the Damping-Like torque by showing that current induced bipolar magnetization switching can be achieved in a Pt/Co/AlO_X system with strong PMA and SIA, similar to their previous experiment [19], by injecting in-plane current pulses.

[14] FMR (Ferromagnetic Resonance) measurements will be discussed in section 3.3.2.

In this case, the samples were patterned in the shape of hall crosses with a Co dot in the center, and AHE measurements we used to follow the orientation of the magnetization[15]. Figure 3.6 (a) shows a schematic of the measured device. In their experiment, a magnetic field, $\vec{H}$, is applied in-plane, along the $\hat{x}$ axis, with a tilt of 2° ($\theta = 92°$) meant to avoid the formation of magnetic domains. The magnetic field is then swiped and at each field value positive and negative current pulses are injected, while measuring the out of plane component of the magnetization after each pulse. The field/current pulse steps are shown in Figure 3.6 (c).

The result is shown in Figure 3.6 (b). Black points represent the magnetization orientation after positive current pulses and red points after negative current pulses. It indicates the presence of deterministic switching of the magnetization direction from up to down and from down to up depending on the sign of the current pulse. The direction of this switching reverses as the external field changes sign, being thus bipolar both in current and field.

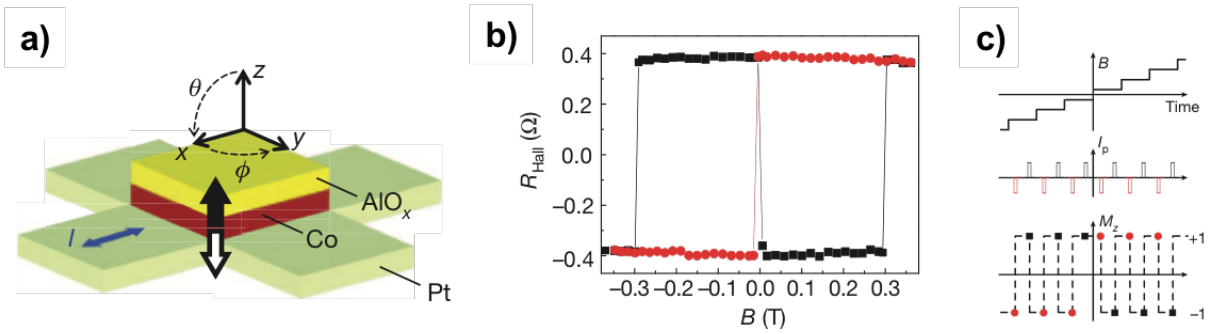

Figure 3.6: (a) Schematic representation of the device and coordinate system. Black and white arrows represent the up/down magnetization states. (b) Out of plane component of the magnetization, measured using the AHE, after the injection of positive (black squares) and negative (red circles) current pulses. (c) Schematic of the field/current pulse and measurement sequence as a function of time. From [20].

The study has been repeated for various field orientations, showing that the current induced torque responsible for the switching is maximum when the external field is parallel to the current direction, decreasing proportionally to $\sin\left(\varphi - \frac{\pi}{2}\right)$ [20].

The central result of this work is that the effect of the current on the magnetization has another component: another torque, which we call Damping – Like, perpendicular to both magnetization, $\vec{M}$, and current, $\vec{J}$, thus parallel to the $\vec{H}_{FL}$ which we have discussed previously. When the magnetization is saturated out of plane, along the $\pm\hat{z}$ axis, the effective field equivalent to this torque is parallel to the current direction, along the $\pm\hat{x}$ axis. Because of the

[15] We will discuss this measurement technique (as well as related measurements) in more detail in sections 3.3.1 and 4.2.

presence of this torque we can conclude that, through some mechanism, the current induces a second spin accumulation at the interface between the HM and the FM, oriented along the $\vec{H}_{FL} \times \vec{M}$ direction [20].

The value observed for the Damping-Like effective magnetic field, $\vec{H}_{DL}$, was $(80 - 90) \cdot 10^{-8}\ mTcm^2A^{-1}$.

In conclusion, the two SOTs predicted theoretically [21], [22], [35], Field-Like and Damping-Like, do exist and can be experimentally detected. But, as we have seen in section 2.3, both the Rashba Effect and the SHE allow for the same SOT components. This has sparked a debate in the scientific community as to the origin of the SOTs.

3.2 Rashba Effect or SHE?

3.2.1 Debate on the origin of the SOTs

In their initial paper, Miron *et. al.* [20] identified both the Rashba Effect and the SHE as possible sources of SOTs.

To verify the first hypothesis, the authors have studied samples with different PMA strengths, obtained by fabricating devices with different degrees of Al oxidation. At the same time, the strength of the Rashba Effect also depends on the oxidation [105]. The results showed that devices with a higher degree of oxidation switch at lower currents, even if the anisotropy is stronger. This shows strong dependence of the strength of the Damping-Like SOT on the strength of the Rashba Effect.

According to this hypothesis, the Damping-Like torque comes from an interface effect.

Regarding the second hypothesis, the Damping-Like torque arises from the absorption of spin current created by the SHE in the Pt layer. In contrast with the previous idea, this is a bulk effect. However, Miron *et. al.* [20] concluded that in their Pt/Co/AlO_X system the SHE induced effective field is five times too small compared to the observed effective field, and therefore it is unlikely to be responsible on its own for the SOT induced magnetization switching[16].

Later, in 2012, Liu *et. al.* measured the SHA for β-Ta by performing ST-FMR measurements [106] on in-plane magnetized CoFeB/Ta multilayers with in-plane magnetic anisotropy [37]. They report SHA values for Ta of $\theta_{SH}^{Ta} \approx 0.12 - 0.15$ [37], much larger and with opposite sign as for Pt. By comparison, SHA values for Pt reported in literature at the time range from $\theta_{SH}^{Pt} \approx 0.004 - 0.07$. However, the authors base their SHA estimation on the assumption that the measured ST-FMR signal only consists of the SHE contribution, which can result in overestimating the value. In the same context, they also show current induced bipolar magnetization switching of Ta/CoFeB/MgO/Ta samples with PMA and Ta/CoFeB/MgO/CoFeB/Ta/Ru samples with in-plane magnetic anisotropy. Their result is shown Figure 3.7. It is worth noting that, in accordance with the SHA, the polarity of the switching has opposite sign for Ta-based samples than for Pt-based samples. Similar to the SHA measurements, the authors consider that the SHE is the only effect responsible for the

[16] The authors have estimated the SHE induced effective field by using SHA and spin diffusion length values for Pt reported in literature at the time, namely $\theta_{SH} = 0.004 - 0.076$ and $\lambda_{SF} = 3 - 14\ nm$ [20].

current induced SOTs, ruling out both the torque created by the Oersted field (by symmetry considerations) and the torque created by the Rashba effect. Furthermore, they argue that the Field-Like component is so small that it practically cannot be measured, which is more evidence that the Rashba Effect plays no part in the generation of SOTs.

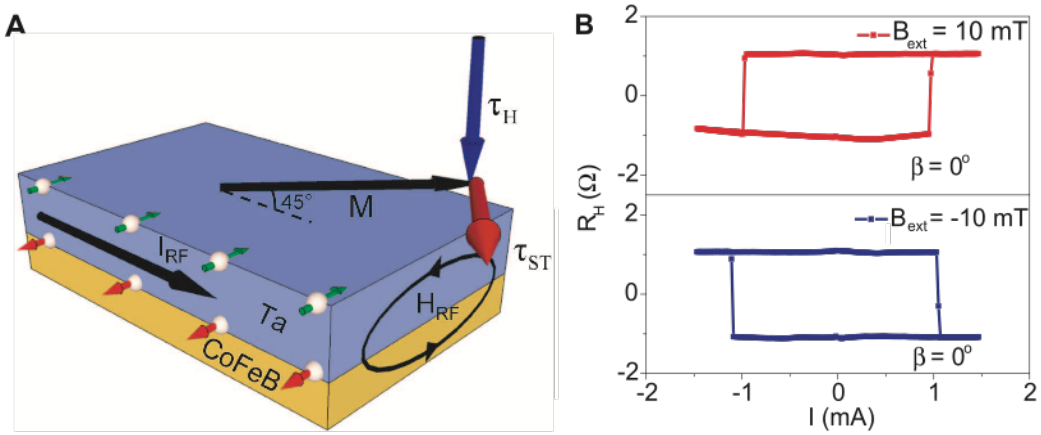

Figure 3.7: (a) Schematic representation of the sample geometry and ST-FMR measurement. (b) Current induced switching for external field parallel (top) and antiparallel (bottom) to the current direction. From [37].

Following these two results and their contradictory conclusions, a strong debate has sparked in the scientific community, whether to attribute the SOTs to interface effects (such as the Rashba Effect) or to bulk effects (mainly the SHE).

One of the common arguments for a SHE-only model for the origin of SOTs is that the current induced magnetization switching observed in HM/FM structures can be quantitatively explained by the SHE [107] and as such Rashba Effect contributions to the Damping-Like are ignored. But from simple torque measurements it is impossible to distinguish between the two, since both effects can give rise to the same torque components.

A second point in favor of this model is that in some experiments, most notably Liu *et. al.*'s first experiments, no important Field-Like torque is measured. The presence of the Field-Like torque is important, because theoretical models [21], [22], [71], [108] predict that a large spin accumulation along the $\hat{z}$ axis, which could contribute to the Damping-Like torque, created by the Rashba effect, will be accompanied by an even larger spin accumulation in the plane of the sample, which will result in a large Field-Like torque. As such, the absence of a measurable Field-Like torque could be considered as a sign of the absence of important interfacial contributions to the SOTs.

Since the early experiments, however, important Field-Like torque values have been reported[17]. Oftentimes these values are even larger than the Damping-Like torque values. By the previous reasoning, this contradicts a SHE-only approach.

A third argument brought forth for a SHE-only model is the fact that current induced magnetization switching by SOTs has been observed in HM/FM heterostructures using various FM materials, for various thicknesses and for different capping layers (eg. [107]: Pt(30)/Co(5)/Ni(10)/Ta(10), Pt(30)/Co(5)/Ni(10)/Au(10), Pt(30)/CoFeB(10)/MgO(16) – thickness in parenthesis, given in Angstroms). This has led some authors to conclude that the SHE inside the HM layer is responsible for the SOTs, and that the interfaces play no part. One can argue this point by considering the origin of the Rashba effect. It does not depend on a specific HM/FM material combination, but on a combination of large SOI and SIA along the normal direction to the interface, which can be achieved in many HM/FM/capping layer systems and it is not dependent on one particular material on its own [see section 2.3.2].

The origin of the SOTs remains one of the most important unanswered questions to date. While some data seem to suggest a SHE-only model for the SOTs, others point towards a combined contribution of the bulk (SHE) and interface (Rashba) effects. However, distinguishing between SHE and Rashba Effect by simply measuring the SOTs is not trivial, as we have no means of directly distinguishing between the two possible sources from simple torque measurements. At the same time, many studies start with a SHE only hypothesis and do not consider interfacial effects. Furthermore, there are not so many systematic studies on the effects of interfaces.

3.2.2 Strength of the SHE

Apart from the arguments presented in the previous section, another aspect that has generated significant discussion in the scientific community is the strength of the SHE. This is very important in the discussion about the origin of SOTs, since it is the strength of the SHE reported by various groups that has led to a SHE-only model.

Quantifying the strength of the SHE in a material comes down to measuring two parameters: the SHA and the spin diffusion length. However, even for Ta and Pt, materials

[17] We will discuss these measurements in the next sections.

that have been studied extensively both in the context of SOTs and SHE, neither the SHA nor the spin diffusion length are precisely known.

Remark

As discussed in 2.3.3, the SHA parameter governs the efficiency with which the injected charge current is converted into a transversal spin current. It gives a measure of the strength of the SHE in a material and it is also a measure of the amplitude of the spin accumulation potentially created at the HM/FM interface. In a SHE only model it is this spin accumulation that creates the SOTs. But a spin current will get slowly depolarized by diffusion and spin-flip phenomena. The Spin Diffusion Length, $\boldsymbol{l_{sf}}$, is the characteristic length of this phenomena. It is usually larger than the electrons mean free path inside the material, $\boldsymbol{\lambda = \tau v_F}$, depending both both on $\boldsymbol{\lambda}$ and on the mean free path between two spin-flip events, $\boldsymbol{\lambda_{sf} = \tau_{sf} v_F}$. We can express $\boldsymbol{l_{sf}}$ as $\boldsymbol{l_{sf} = \sqrt{\lambda_{sf}\lambda/6}}$ [109], [110]. By means of the Spin Diffusion Length, the spin current will also depend on the thickness of the HM. As a consequence, the spin current that can effectively be the source of the SOTs can only "come" from maximum $\boldsymbol{l_{sf}}$ away from the HM/FM interface. This makes any estimation of the SHA and the effective current density that much harder. Furthermore, to thin a HM layer will also be detrimental to the current induced SOTs as the two spin accumulations created by the SHE will be too close to each other and by means of diffusion their amplitude greatly reduced.

For example, Emori *et. al.* [111] used a cavity-based spectrometer to perform resonance measurements of the Damping-Like field and the SHA on Ta/FeGaB samples, a technique initially developed by Ando et. al. [104] for Pt/Py samples. Their measurements show SHA values of 0.09 for Ta, much smaller than what Liu *et. al.* have reported. Furthermore, the SHA measurements have been shown to be highly dependent on the measurement parameters as well as thickness of the HM and FM layers. SHA measurements as a function of HM and FM layer thickness in Pt/CoFe and Pt/Py samples [112] have shown some striking results. Firstly, depending on whether a dc bias current, $\vec{I}_{bias}$, is applied or not during the measurements, the SHA will either increase with FM layer thickness or be constant.

Second, for the same HM layer (Pt in this case), the measured SHA value differs between Pt/CoFe and Pt/Py samples.

This inconsistency of SHA values is not uncommon. For example, in the case of Pt[18], SHA values vary from $\theta_{SHA} = 0.37\%$ to $\theta_{SHA} = 11\%$, and spin diffusion length vary from $\lambda_{sf} = 0.5\ nm$ to $\lambda_{sf} = 10\ nm$ [122].

And herein lies the problem: depending on the measurement method used and other factors such as sample fabrication, the values obtained for these parameters vary greatly, sometimes even up to one order of magnitude. This leads to a difficult interpretation of experimental data, sometimes with unrealistic results.

[18] Further studies on the SHE and its relevant parameters have been reported in heavy metals like Ta and Pt [113]–[115], Pd [116], [117], Au and Mo [114], W [118] and heavy metal based alloys like $CuIr_X$ [119], $CuBi_X$ [120], AuW [121].

3.3 Quantitative SOT measurements

In this section, we will look in more detail at the experimental work dedicated to the quantitative study of the SOTs themselves, their amplitude, symmetry and most importantly, their origin.

The techniques used in quantitative SOT measurements generally fall under two categories: i) quasi-static measurements and ii) resonance based measurements.

3.3.1 Quasi-static measurements

This type of studies focuses on measuring the current induced effective fields acting on the magnetization of a FM layer by comparing them to an applied external magnetic field. The effects of the current induced effective fields are followed by means of measuring magneto-resistive effects such as Anomalous Hall Effect, Planar Hall Effect and Anisotropic Magnetoresistance. Generally, for this type of measurements one uses devices patterned in shapes suited for Hall measurements (such as Hall crosses). During the measurement, an in-plane electric current is injected and the tilting angle of the magnetization of the FM layer is followed, by measuring the magnetoresistive response of the device. Since the tilting angle is proportional to the Field-Like and Damping-Like effective fields created by the current, these measurements can give a quantitative estimation of $\vec{H}_{FL}$ and $\vec{H}_{DL}$.

As opposed to the initial observations of SOTs by means of the Magneto-Optical Kerr-Effect (MOKE), this type of measurements allows for a more accurate quantitative analysis of the SOTs as well as studying their symmetry. As the name implies, these measurements are conducted at thermodynamic equilibrium.

The original method has been first proposed by Pi *et. al.* [123] by performing quasi-static Harmonic Hall voltage measurements in Ta/Pt/Co/AlO_X samples, and has been greatly improved and adapted in recent years. In order to account for both Field-Like and Damping-Like SOTs in samples with PMA as well as in-plane magnetic anisotropy Garello *et al.* [124] propose a similar quasi-static experiment to quantitatively measure both torque components as well as their angular dependencies. The authors use symmetry arguments to derive general expressions for the current induced SOTs, regardless of the orientation of the magnetization, and independent of specific physical models such as Rashba or SHE. They use harmonic analysis of the Hall voltage to perform three-dimensional measurements of the SOTs by

measuring 1st and 2nd harmonic components of the AHE and PHE. They are able to show a self-consistent way of quantitatively measuring both the Field-Like and the Damping-Like torque amplitudes as well as their orientation. Hayashi *et. al.* [125] provide a thorough mathematical framework for the Harmonic Hall voltage analysis and derive analytical expressions for both torques. They compare the analytical results with numerical calculations based on the macrospin model both for systems with out-of-plane magnetization as well as in-plane magnetization.

It is important to note that magneto-resistance based measurements rely on an accurate measurement of a Hall voltage (Anomalous Hall voltage, Planar Hall voltage, AMR voltage) in order to calculate the SOTs. Therefore, the results are prone to being influenced by other effects that result in a voltage with the same symmetry as the Hall voltage. In such a case, one will under- or over- estimate the amplitude of the SOTs. In the case of quasi-static measurements, the most notable influence comes from the Anomalous Nernst Effect (ANE) [126]–[128], which creates a voltage offset that leads to an overestimation of the Damping-Like effective field. Avci *et. al.* [129] and Kawaguchi *et. al.* [130] have both shown adequate methods of taking the ANE into account. This situation will be discussed in more detail in section 4.3.2.

In chapter 4, we will discuss at length the quasi-static harmonic Hall measurements that we have used to quantitatively measure SOTs in HM/FM heterostructures with in-plane magnetic anisotropy. We will also detail the intricate data analysis process needed to extract SOT values from the raw measurements.

3.3.2 Resonance based measurements

These experiments differ from the quasi-static measurements we have discussed in the previous section in that they are generally conducted in the rf regime. However, they are also magnetoresistance-based, in that in order to measure the current induced SOTs one must follow the magnetoresistive response of the magnetization to an applied excitation, albeit usually in the microwave regime. Widely used in this case are FMR based techniques.

FMR[19] is a spectroscopic technique that measures the magnetic of FM materials by probing the precession of the magnetization [131]. A constant amplitude external magnetic field, called bias field, causes the magnetization to precess around the field direction, until the damping causes the magnetization to align itself with the direction of the field[20]. To counter the damping, a "driving force", i.e. a transverse rf field is applied. When the rf frequency matches the precessional frequency, the resonance condition is achieved and rf power is absorbed by the sample. The LLG equation describes the motion of the magnetization in this situation:

$$\frac{\partial \vec{M}}{\partial t} = -\gamma\left(\vec{M}\times\vec{H}_{bias}\right) + \frac{G}{\gamma M_S^2}\left(\vec{M}\times\frac{\partial \vec{M}}{\partial t}\right)$$

Equation 3.2

where the first term describes the precession and the second term the damping, with G being the Gilbert damping constant and $\gamma = \frac{g\mu_B}{\hbar}$ the gyromagnetic ratio. The measured signal is usually the derivative of the absorption as a function of bias field amplitude, for a fixed rf frequency[21], resulting in a Lorentzian shaped resonance signal. The width of the resonance peak carries information about the relaxation process [131], [132].

Liu *et. al.* [106] showed that the spin current created by the SHE in a Pt layer can induce FMR in an adjacent FM layer by means of the current induced SOTs. In this situation, the "driving force" is provided by injecting a microwave frequency electric current in the plane of Pt/Py bilayers with in-plane magnetization. Through the SHE, an oscillating spin current is created transverse to the charge current and exerts an oscillating SOT on the magnetization of the Py layer that induces precession. The magnetization precession around the direction of a bias magnetic field is "driven" by means of current induced effective fields, hence the name – Spin Transfer FMR (ST-FMR).

When the ferromagnetic resonance condition is satisfied, the magnetization precesses around the direction of the bias field. Due to the AMR of the FM layer, the resistance of the

[19] FMR is closely related in principle to NMR (Nuclear Magnetic Resonance). The differences lie in the fact that the former measures the total magnetization of the magnetic moments of unpaired electrons, while the latter measures the magnetic moment of atomic nuclei which are generally screened by surrounding atomic or molecular orbitals.

[20] The magnetization will precess around the direction of the total local effective field, $\vec{H}_{eff}$, that takes into account any other local field contributions, such as demagnetizing field, anisotropy field. For simplicity, in the text we consider the direction of the bias field.

[21] Experimentally it is easier to change the amplitude of the bias field than it is to change the frequency of the rf field over a large interval.

sample oscillates as well, creating a transverse dc voltage which is then measured. The signal can be fitted by the sum of symmetric and antisymmetric Lorentzian curves. The symmetric component was linked to the Damping-Like torque while the antisymmetric component was linked to the torques created by the Oersted field[22] [37], [106].

A variation of this method, shown in [133], involves applying a dc bias electric current, $\vec{I}_{bias}$. Measurements of the transverse voltage are taken as a function of the amplitude of $\vec{H}_{bias}$, and then fitted with a Lorentzian curve[23]. The resonance properties allow for a quantitative measurement of the spin current absorbed by the FM. The ratio between the half-width at half-maximum and $\vec{I}_{bias}$ is used to quantify the Damping-Like [104], [106], [112]. The Field-Like torque is evaluated from the change it induces in the resonance field value, as it either adds to or opposes the bias field [134], [135]. Figure 3.8 shows a schematic of a typical ST-FMR measurement with dc bias current.

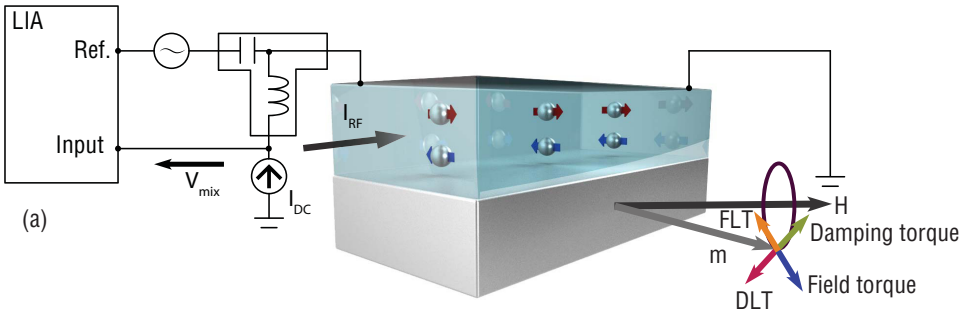

Figure 3.8: Schematic of the ST-FMR measurement setup, showing the applied $\vec{H}_{bias}$ and $\vec{I}_{bias}$, as well as the symmetry of the SOTs acting on the magnetization. The use of a bias-Tee allows both the microwave and the dc current to be applied, as well as the signal measurement. For the detection, a lock-in amplifier is used. From [133]

Similarly, Spin Pumping measurements also make use of magnetic resonance phenomena. By applying an rf magnetic field to a HM/FM multilayer, one can induce precession of the magnetization in the FM layer. When the resonance condition is achieved, the precession of the magnetization induces a spin current in the adjacent HM layer [136], [137]. Through the Inverse SHE (ISHE) [47], [138], a charge current, transversal to the spin current, is induced in the HM, which results in a measurable transversal voltage. This type of

[22] Since the initial ST-FMR measurements, the antisymmetric component has been used to measure the Field-Like effective field.

[23] The form of the Lorentzian curve used to fit the measured voltage, as given in [133], is $V_{STFMR} \approx S\frac{W^2}{\left(\mu_0 H-\mu_0 H_{FMR}\right)^2+W^2}+A\frac{W\left(\mu_0 H-\mu_0 H_{FMR}\right)}{\left(\mu_0 H-\mu_0 H_{FMR}\right)^2+W^2}$, where S and A are the symmetric and antisymmetric Lorentzian coefficients, W is the half-width at half-maximum and H_{FMR} is the resonance field. S is proportional to the ISHE and A is proportional to the AHE.

analysis allows for ISHE and interface conductivity measurements. In a sense, ST-FMR and spin pumping can be viewed as reciprocal phenomena, like SHE and ISHE.

As resonance-based measurements are beyond the scope of this manuscript, I will no longer focus on the specifics of the ST-FMR and spin pumping measurements, but rather talk about the more interesting results obtained.

3.3.3 SOT measurements

Following up on the first evidence of the Field-Like effective field in FM metals given by Miron *et. al.* [19], in that same year Pi *et. al.* [123] confirmed the existence of the Field-Like component by means of quasi-static Harmonic Hall voltage measurements. However, for the same Pt/Co/AlO_X system with PMA and SIA, they report a much lower $\vec{H}_{FL}$ value, namely $2.9 \cdot 10^{-9}\ Tcm^2A^{-1}$. Using a similar method, the existence of the current induced Field-Like torque is confirmed in Ta/CoFeB/MgO samples by Suzuki *et. al.* [139] and Kim et. al. [140]. They measure a $\vec{H}_{FL}$ value of $\sim 1900\ Oe$ for a current density of $10^8\ Acm^{-2}$. It is worth noting that the sign of $\vec{H}_{FL}$ for Ta based samples is opposite that of Pt based samples. The authors agree that, although bulk contributions cannot be excluded, the Rashba Effect plays an important role in the generation of SOTs.

In contrast, by using resonance-based measurements [37], [101], [106], [141], [142] as well as quasi-static measurements [107], other groups do not measure any Field-Like components in similar systems (such as Ta/CoFeB/Mgo/Ta [37], Pt/Co/AlO_X [107] and W/CoFeB/MgO/CoFeB/Ta/Ru [142]). However, they report large Spin Hall Angle values, 0.15 for Ta and 0.33 for W. Consistent with theoretical models, both Ta and W have SHA with opposite sign from Pt. The lack of measured Field-Like components especially in Ta based samples, coupled with the large SHA values has lead the authors attribute the Damping-Like SOT solely to the SHE in the HM, considering it as proof of the absence of an important Rashba-type interface effect.

A common characteristic of resonance-based measurements, so far, is that a large proportion of them is focused almost exclusively on studying the Damping-Like torque and material parameters related to the SHE, such as the Spin Hall Angle (SHA), θ_{SH}, Spin Hall Conductivity, σ_{SH}, and the Spin Diffusion Length, l_{sf}. There are fewer studies that report on

the Field-Like torque, and among those that do, some find it to be negligible while others find Field-Like values larger than for the Damping-Like.

These differences seem to raise questions regarding the reliability of measurement techniques used. In their analysis, Garello *et. al.* [124] take into account not just the AHE, but the PHE as well. They use harmonic analysis of the Hall voltage to measure both the Damping-Like and Field-Like components in in Pt/Co/AlO_X and Ta/CoFeB/MgO samples with PMA and SIA. Figure 3.9 shows the Field-Like (a) and Damping-Like (b) as a function of magnetization position (θ angle). The PHE is found to be extremely important in the measurement of the Field-Like effective field component. In addition, the authors conclude that the PHE was not taken into account in previous experiments, where no Field-Like effective field component is measured. This opens up the question whether or not the Field-Like was in fact present in said experiments and just overlooked in the data analysis. Using a similar method, Hayashi *et. al.* [125] report a Field-Like effective field value three times larger than the Damping-Like, in Pt/CoFeB/MgO samples. They measure a Damping-Like value of $44\ Oe$ for a current density of $10^8\ Acm^{-2}$ (much smaller than Garello *et. al.* [124], who measure a value of $\sim 690\ Oe$, albeit for Pt/Co/AlO_X). This FL to DL torque ratio is further confirmed in [140].

Now, on one hand these measurements prove the existence of the Field-Like torque, and on the other they support the general theoretical expectations of the Field-Like torque being larger than the Damping-Like torque. But while these results are in general agreement with both Rashba and SHE models, no clear distinction can be made between the two.

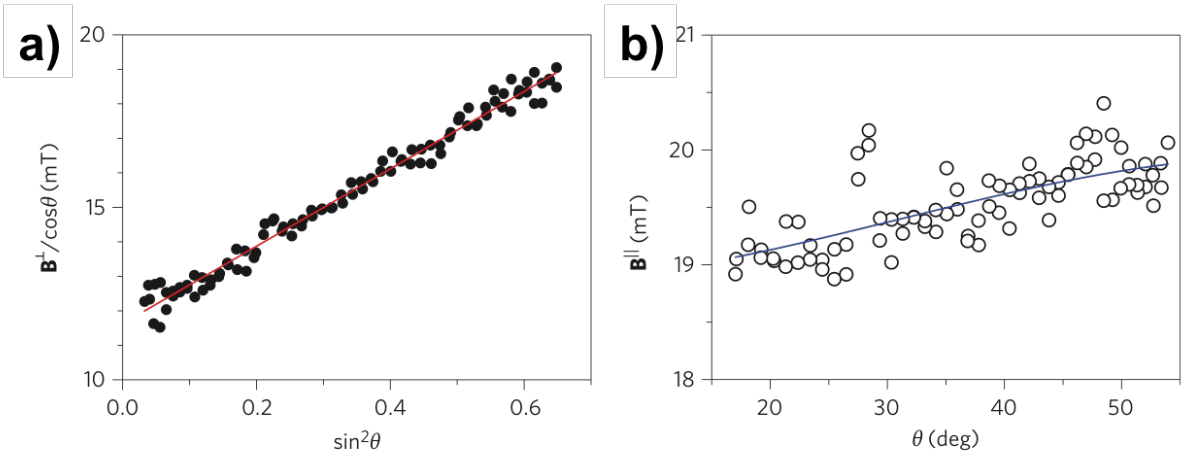

Figure 3.9: (a) Field-Like effective field normalized by $cos\ \theta$ and (b) Damping-Like effective field as a function of $sin^2\ \theta$ and θ, for a *Pt/Co/AlO_X* sample. From [124].

In this context, the study of Nan *et. al.* [133] is very interesting. The authors studied the effect of interfaces on the SOTs and spin pumping, by ST-FMR measurements on Pt/Py

samples, with in-plane magnetic anisotropy, by inserting a Cu layer at the HM/FM interface. In their hypothesis, they also considered the SHE as the sole mechanism responsible for the Damping-Like torque. By parameterizing the Damping-Like torque with an "effective spin hall angle", θ_{DL}, proportional to θ_{SH}, they show that, both the Damping-Like torque and spin pumping, are reduced by a comparable factor after the insertion of the Cu layer. The authors argue that the reciprocity between the Damping-Like torque and the spin pumping measured by the ISHE, all the while being consistent with a diffusive transport model of spins at the interface, points towards the SHE being the dominant source of Damping-Like torque. However, contrary to previous ST-FMR measurements, in this case there is also a significant Field-Like torque, that follows the same dependence as the Damping-Like torque, suggesting that it too originates in the SHE. Field-Like torque values of $0.2 \pm 0.002\ mT/mA$ for the Pt/Py interface and $0.1 \pm 0.002\ mT/mA$ for the Pt/Cu/Py interface are reported (while no Damping-Like values are shown directly).

In a further attempt to distinguish between the Rashba Effect and the SHE, several groups perform SOT measurements on various sample systems with PMA and SIA, as a function of layer thickness, structural, electrical and magnetic properties. The goal was to look at the dependence of the SOT components as a function of bulk and interfacial properties of the samples.

In this context, Kim *et. al.* [140], perform measurements of current induced SOTs in perpendicularly magnetized Ta/CoFeB/MgO as a function of Ta and CoFeB thicknesses. They show that the amplitudes of both torques vary with varying Ta thickness, and even change sign at low Ta thicknesses. However, in terms of CoFeB thickness dependence, only the Field-Like effective field shows a variation in amplitude. Figure 3.10 shows the Field-Like (a, b) and Damping-Like (c, d) effective fields, normalized by the applied voltage, as a function of Ta and CoFeB thicknesses.

The authors attribute these dependencies to a combination of Rashba Effect and a much stronger SHE.

The physics behind their findings can be explained intuitively. As the Ta thickness decreases, there is less current flowing in the Ta layer and therefore the SHE is smaller, which results in both the Damping-Like torque and Field-Like torque going to zero. This behavior is consistent with the SHE being the main source of SOT in their system. Furthermore, the thickness interval over which this decrease happens is of the order of magnitude of the spin

diffusion length in Ta. Now, when the Ta thickness becomes very small, the observations become even more interesting: both Damping-Like and Field-Like torques change sign. Because we expect that the SHE will be very small at very low Ta thicknesses, the observed sign change can be explained by the Rashba Effect. As the SHE becomes smaller, the relative contribution of the Rashba Effect to the SOTs becomes greater, and it can therefore be detected below a certain HM thickness value.

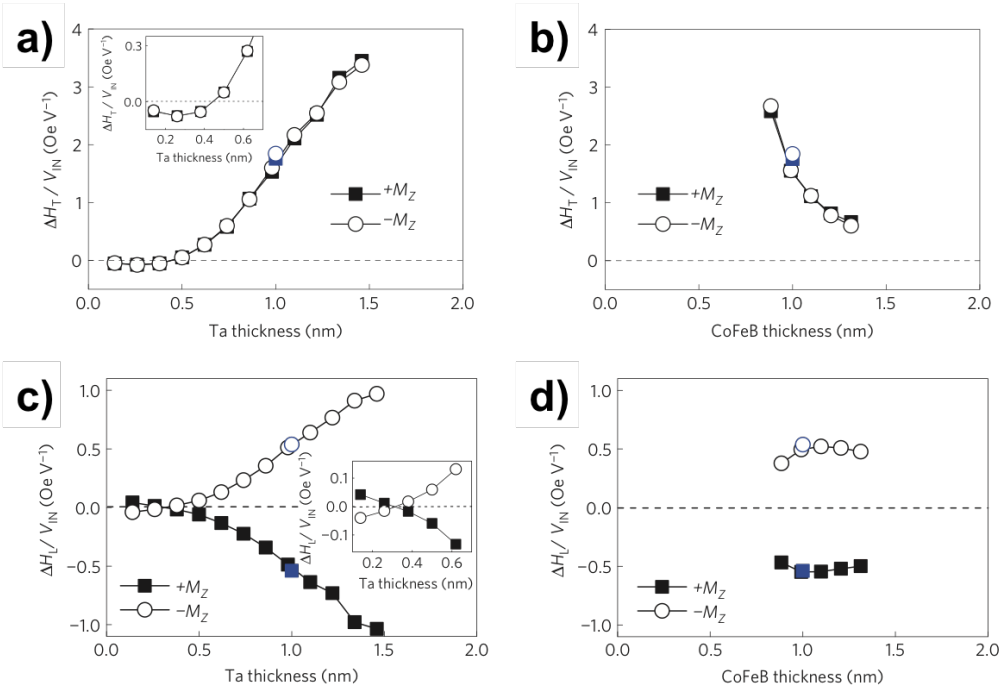

Figure 3.10: Ta and CoFeB thickness dependence of the Field-Like effective field (a, b) and the Damping-Like effective field (c, d), normalized by the applied voltage. From [140].

Aside from changing layer thickness, another way of trying to separate between bulk and interface contributions to the SOTs, is to follow the temperature dependence of the two torques. What is very interesting in this case, and cannot be reconciled with a SHE only model, is the fact that Field-Like and Damping-Like torques show opposite dependencies for the two torques, namely the FL component of the SOTs increases while the DL component decreases with increasing temperature. These results are shown in a follow-up study, on similar Ta/CoFeB/MgO samples [143]. Temperature measurements are taken at a Ta layer thickness large enough so that any thickness dependence of the torques is saturated [140].

This points out to interfacial contributions from the Rashba Effect to the SOTs. However, the authors [143] propose a simplified model to account for the temperature dependence solely based on the SHE, by assuming negative spin mixing conductance

components[24]. But such values are, as the authors themselves ultimately acknowledge, unrealistic. However, they do not provide any reasoning for this assumption, concluding that effects other than spin diffusion into the magnetic layers (Rashba Effect, magnon excitation or other interface contributions) need to be taken into account to accurately describe SOTs in ultrathin magnetic heterostructures.

A third idea, that can help distinguishing between bulk and interface effects, goes a little further than temperature dependent torque measurements. In this case, one can try modifying the structural, electrical and magnetic properties of the samples system through annealing, and follow the evolution of the SOTs accordingly. Based on this idea, Avci *et. al.* [74] investigate the correlation between the current induced SOTs and annealing temperature in Ta/CoFeB/MgO samples with strong PMA and SOI.

Their results also show opposite dependence of the Field-Like and Damping-Like torques, this time as a function of evolving annealing temperature (as opposed to just measurement temperature). The Field-Like torque is found to increase with annealing temperature while the Damping-Like decreases, consistent with the findings in [143]. Furthermore, as in previous studies, the Field-Like is also found to be much larger than the Damping-Like.

Stepping away from trying to tune bulk and interface contributions to the SOTs by modifying material properties of the samples as done in previous studies, R.H. Liu *et. al.* [64] show that, while SHE contribution to the Damping-Like torque is larger, the Rashba effect contribution is considerable. They do this by studying the effect of electric gating[25] on the SOTs in Pt/Co layers with PMA. The authors use Harmonic Hall measurements to evaluate both the Damping-Like and the Field-Like torques while applying a "gating" voltage along the normal direction to the sample.

The common conclusion among these studies is three-fold:

i) The Field-Like effective field is present and it is larger than the Damping-Like effective field, therefore it's supposed absence cannot be a valid argument towards a SHE-model for the SOTs;

[24] The spin mixing conductance is a parameter that governs spin transport at the interfaces.
[25] An interesting conclusion of this study was that, being significantly affected by the gating voltage, the Rashba contribution allowed for electric modulation of the SOT.

ii) Different dependencies of the DL and FL components as a function of sample properties seem to point towards different origins for the two SOTs, or, at least, towards different dominating mechanisms;

iii) There is no clear distinction between the Rashba Effect and the SHE as sources of SOTs, as experimental data points towards a combined effect of interface and bulk.

3.4 Our approach

In order to understand the origin of the SOTs and to clearly distinguish between SHE and interface contributions, one needs to systematically study the influence of the interface on the SOTs.

One possible approach to this question is to study a large variety of HM/FM interfaces by simply changing the materials.

Another possibility, is to change the bulk to interface effect ratio, and follow their influence on the SOTs. Firstly, the torques from the SHE will depend on the thickness of the HM layer. Secondly, the strength of interfacial effects on the magnetization of the FM will depend on the thickness of the FM layer. Therefore, to achieve our goal, in our studies we have independently varied the thickness of the HM and FM layers, and measured the SOTs as a function of said thicknesses.

To further change the properties of the HM/FM interface and to follow its effects on the SOTs, we have also changed the layer order and inserted buffer layers.

3.4.1 Perpendicular and In-Plane Magnetic Anisotropy

The majority of the quasi-static measurements have been conducted on samples with PMA. But having PMA brings some restrictions to material choices, and especially on material thicknesses. In the absence of significant interfacial anisotropy contributions, for a thin film the energetically favorable magnetization state is to be in plane. This minimizes the demagnetizing energy [7]. To achieve PMA in a multilayered structure, the out of plane component of the anisotropy has to come from the interfaces, both HM/FM and FM/capping layer. Furthermore, the interfacial anisotropy has to be larger than the bulk anisotropy in the FM. This limits the thickness of the FM layer to vary small values. For example, typical Co layer thicknesses in samples with PMA are around $0.6\ nm$ to $1\ nm$.

By fabricating samples with in-plane magnetic anisotropy, we are afforded several degrees of freedom for studying the effects of interfaces on the SOTs. Since we no longer need a dominant interfacial contribution to the anisotropy, we can study a wider range of materials and, equally important, a much wider range of thicknesses, which means we can tune the ratio between bulk and interface effects, to distinguish between two the two possible sources of

SOTs. This is particularly useful since we can deliberately study samples with layer thicknesses larger than the spin diffusion length, in order to suppress the effects of the SHE.

Another benefit is that by measuring thicker FM layers we can improve the signal-to-noise ratio and improve the accuracy of the measurement.

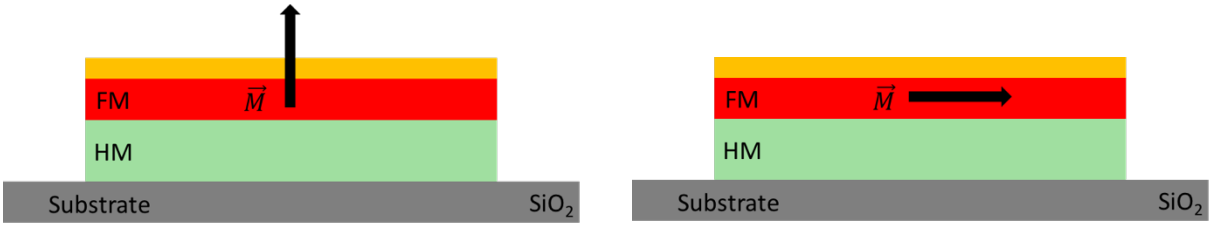

Figure 3.11: Schematic showing PMA and in-plane magnetization systems

After laying the theoretical background regarding the SOT and discussing the current open question regarding the origin of the SOTs, in the following chapter we will present, in detail, the experimental technique used to quantitatively characterize the SOTs in our devices. We will further look at the nanofabrication process used for our devices as well as at the most important difficulties specific to our measurements.

4 Quasi – Static Spin – Torque Measurements

4.1 Sample preparation

One of the main questions regarding the SOTs is whether they arise from bulk effects such as the SHE, from interface effects such as the Rashba Effect, or both. In order to study the nature of the SOTs and their origin, we have explored two avenues. First, several HMs were used in combination with CoFeB and Co FMs, namely Pt, Ta and W; all are HMs with high SOI and are widely used in the study of spintronics related phenomena and MRAMs. Second, we have studied several layer thicknesses both for the FM and for the HM layers. As discussed in 3.4.1, due to the in-plane magnetic anisotropy of our samples, we are afforded more material choices for the HMs and a significantly larger thickness interval for the FM as compared with PMA samples.

Two main sample systems have been studied: CoFeB-based and Co-based, both of which are FM materials with strong in-plane magnetic anisotropy (over the range of thicknesses that we studied).

Our samples were thin films, consisting of Heavy Metal (HM), Ferromagnetic Metal (FM) and Non-Magnetic Metal (NM) multilayers with in-plane magnetic anisotropy. The sample stacks were deposited on thermally oxidized Si/SiO_2 wafers by d.c. magnetron sputtering, in the ACTEMIUM chamber at the Plateforme Technologique Amont (PTA), Grenoble and at the Department of Physics, at UTCN Cluj-Napoca, Romania, as part of a collaboration with SPINTEC. As needed, a 2 nm Al capping layer was deposited on top of the multilayers to prevent the oxidation of the FM layer and to create Structural Inversion Asymmetry (SIA). The capping layer was naturally oxidized, the 2 nm thickness being enough to ensure a metallic interface between the FM layer and the Al layer. Unlike in the case of metal-oxide interfaces with AlO_x capping layers obtained by oxidizing the Al layer using low power r.f. oxygen plasma [144], [145], the metallic interface does not induce Perpendicular Magnetic Anisotropy (PMA).

AHE measurements were used to measure the magnetic hysteresis loops of the samples to check that the desired in-plane magnetic anisotropy is achieved. Figure 4.1 shows a typical hysteresis loop for a Pt/Co/Al sample, with the magnetic field perpendicular to the sample plane. The measurement is consistent with a perpendicular magnetization hard axis.

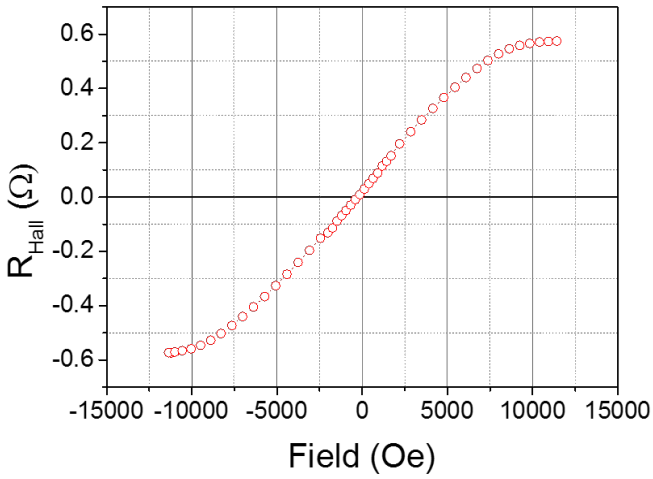

Figure 4.1: AHE measurement for a $Pt_{(30)}/Co_{(20)}/Al_{(20)}$ sample with the applied magnetic field along the $\hat{z}$ axis, showing a magnetization hard axis.

To be able to measure the current induced SOTs, a patterning process is required to build suitable devices. The devices of choice are Hall crosses. Using this geometry, we can pass a current through one of the branches and follow the current induced SOTs by measuring the Hall voltage transversal and/or longitudinal to the injected current (see section 2.3.4 for details). Figure 4.2 shows a schematic of the patterning process.

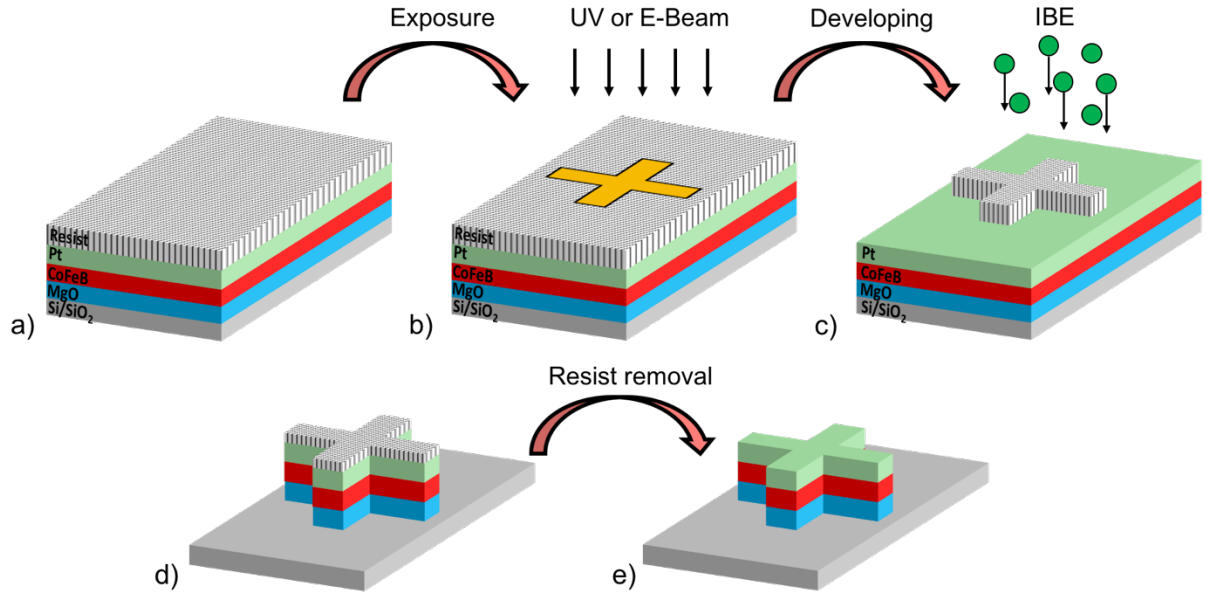

Figure 4.2: Schematic showing the patterning process used for the nanofabrication of the Hall cross devices: a) initial stack, as deposited, with the resist spin-coated on top; b) the desired pattern transferred to the resist by UV or E-Beam lithography; c) Ion Beam Etching of the developed stack, with the resist acting as an etching mask; d) the etched device having the Hall cross shape; e) the device after removing the resist.

The samples are patterned by e-beam or UV lithography and Ion Beam Etching (IBE) following the protocols developed at the PTA. The thin films of the desired composition are covered with AZ 1512HS resist (for UV) and ZEP520A resist (for E-beam) by spin coating,

typically for 60 s at 2000 rpm, followed by a baking process which is resist dependent (Figure 4.2 (a)). The device pattern is then defined in the resist either by e-beam or by UV lithography (Figure 4.2 (b)). After the lithography step, the resist is developed and then removed by a chemical process, defining the mask for the IBE process. Using a negative resist eliminates the need of depositing an IBE mask (which would typically involve the deposition of a Ti layer followed by chemical lift-off), as the resist itself will double as an IBE mask (Figure 4.2 (c)). The etching process is monitored in-situ by Secondary Ion Mass Spectroscopy (SIMS) that detects the atomic species being etched and allows us to stop the process when the desired etching is achieved (Figure 4.2 (d)). The left-over resist is then removed by a chemical stripping step (Figure 4.2 (e)).

At the end of this process, the samples are made of Hall crosses or double Hall crosses of desired dimensions, suitable for the study of SOTs.

4.2 Measurement technique

In this section, we will look in more detail at the quasi-static Harmonic Hall measurements that we used to characterize the SOTs in our systems, in the limit of small oscillations of the magnetization.

4.2.1 Quasi-Static measurements

One way of characterizing SOTs in a HM/FM multilayer is to compare their effect on the magnetization to that of an applied external magnetic field. It is the basic principle of a quasi-static measurement: we create a perturbation with an unknown torque and then compare it with a similar perturbation from a reference torque. Here, it all comes down to measuring the angular deviation of the magnetization from its equilibrium position, caused by the SOTs created by an electrical current passing through the plane of the sample, and comparing it against the angular deviation created by a known external magnetic field.

The condition for equilibrium is that the vector sum of all torques (or corresponding effective magnetic fields) acting on the magnetization must be zero. In the absence of field and current, the magnetization will lie in the plane of the sample. The combined effect of the current induced SOTs, the external applied magnetic field and the anisotropy field defines a new equilibrium position of the magnetization, parallel to a total effective field, defined as the vector sum of all the magnetic fields acting on the magnetization:

$$\vec{M} \parallel \vec{H}_{total}$$

Equation 4.1

where:

$$\vec{H}_{total} = \vec{H}_K + \vec{H}_{ext} + \vec{H}_{SOT}(I)$$

Equation 4.2

$\vec{H}_K$ is the anisotropy field, and takes into account both the magneto-crystalline anisotropy, and the demagnetizing field caused by the shape anisotropy of the thin film. $\vec{H}_{ext}$ is the applied external magnetic field whose direction is always known during the measurement. $\vec{H}_{SOT}(I)$ is the total effective magnetic field corresponding to the current induced SOTs. Figure 4.3 shows a detailed schematic of the coordinate system as well as the direction of the magnetization, current and applied field. The direction of the magnetization is given by the angles θ, defined

with respect to the normal to the plane of the sample, and φ, defined with respect to the $\hat{x}$ axis (if $\vec{H}_{ext} = \vec{H}_{SOT}(I) = 0$, then $\theta = 90°$).

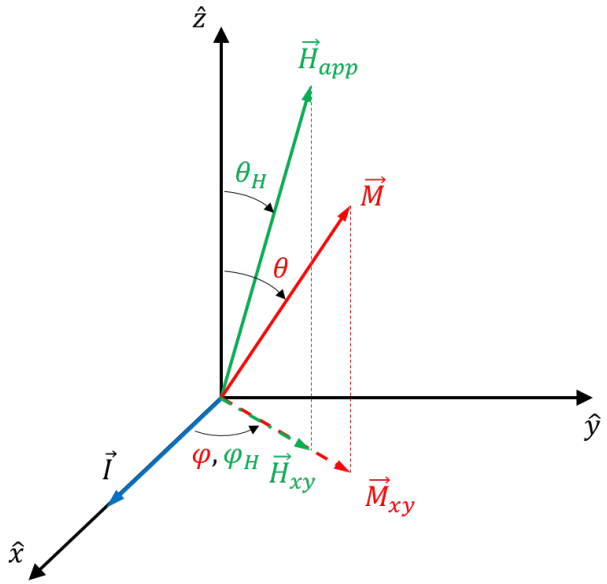

Figure 4.3: Coordinate system and relevant angles; θ and θ_H are the angles of the magnetization and the external applied magnetic field with respect to the $\hat{z}$ axis respectively; φ and $\varphi_H$are the angles between the direction of the current (along the $\hat{x}$ axis) and the planar components of the magnetization and the applied field respectively; due to the small in-plane anisotropy of our samples (Co, CeFeB, Py…), in most samples $\varphi = \varphi_H$ for external field values above 100 Oe.

If we were to apply only an external magnetic field, $H_{ext}(\theta_H, \varphi_H)$, the magnetization would reach equilibrium at a position $M(\theta_0, \varphi_0)$, defined by the direction of the total magnetic field acting on it, $\vec{H}_{total} = \vec{H}_K + \vec{H}_{ext}$. In a spherical coordinate system, $\vec{M}$ and $\vec{H}_{ext}$ are:

$$\vec{M} = M_S \begin{pmatrix} \sin(\theta_0)\cos(\varphi_0) \\ \sin(\theta_0)\sin(\varphi_0) \\ \cos(\theta_0) \end{pmatrix}$$

Equation 4.3

$$\vec{H}_{ext} = \begin{pmatrix} H_x \\ H_y \\ H_z \end{pmatrix} = H_{ext} \begin{pmatrix} \sin(\theta_H)\cos(\varphi_H) \\ \sin(\theta_H)\sin(\varphi_H) \\ \cos(\theta_H) \end{pmatrix}$$

Equation 4.4

A change in the applied field, ΔH_{ext}, will lead to a corresponding change in the equilibrium position, $M(\theta_0 + \Delta\theta, \varphi_0 + \Delta\varphi)$. Now if we are to inject a d.c. electric current, through the presence of the current-induced SOTs ($\vec{H}_{SOT}(I)$), we will again get a change in the equilibrium position of the magnetization, $M(\theta_0 + \Delta\theta', \varphi_0 + \Delta\varphi')$. When the two angular deviations are equal, the effective magnetic field corresponding to the current induced SOTs, $\vec{H}_{SOT}(I)$, is

equal to the applied external magnetic field. Figure 4.4 shows a schematic of our quasi-static measurement principle.

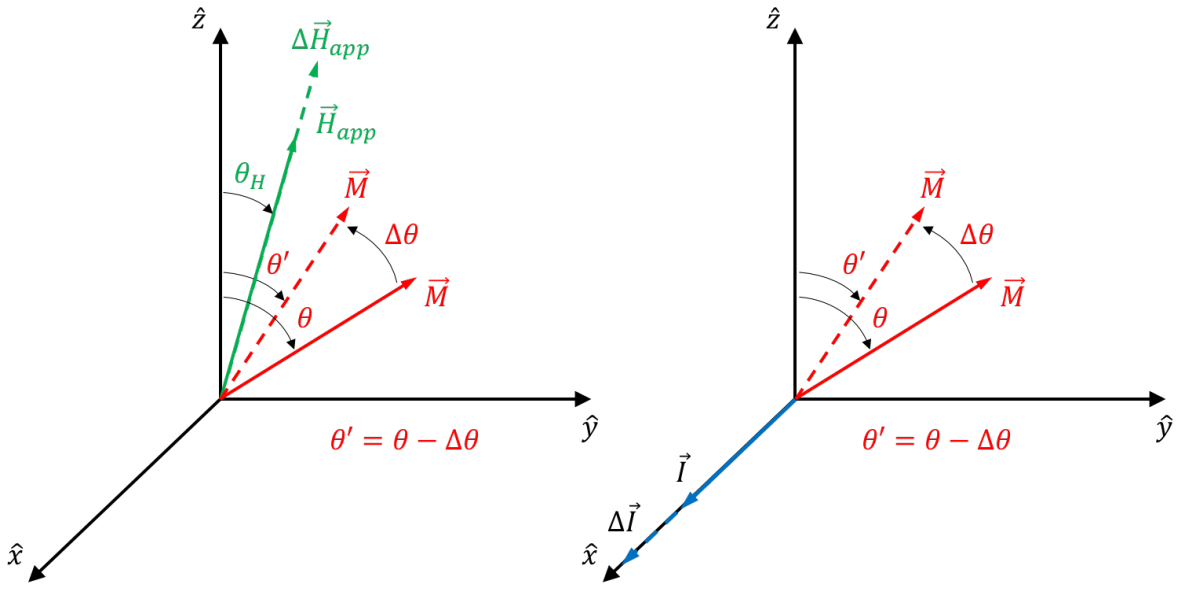

Figure 4.4: Comparison between the effect of a $\Delta\vec{H}_{app}$ and a $\Delta\vec{I}$ on the magnetization, $\vec{M}$. For simplicity, in the schematic, we assumed that the magnetization and the field are contained in the (yz) plane.

The position of the magnetization as a function of the current induced SOTs and the external field is measured by means of the Hall Voltage, V_H, which is measured transversal to the injected current. For a d.c. current, V_H reads:

$$V_H = IR_H = IR_{AHE}\cos\theta + IR_{PHE}sin^2\theta\sin 2\varphi$$

Equation 4.5

where I is the applied current, R_{AHE} and R_{PHE} are the AHE and PHE resistances respectively[26], and θ and φ are the polar and azimuthal angles of the magnetization, as shown in Figure 4.3. Through the AHE, the first term in Equation 4.5, V_H depends on the out-of-plane component of the magnetization, $\vec{M}_z$, and therefore on the θ angle. Through the PHE, the second term in Equation 4.5, V_H depends on the planar component of the magnetization, $\vec{M}_{xy}$, and therefore on the φ angle. This makes it possible to use Hall Voltage measurements to determine the position of the magnetization. The Hall cross geometry of our samples allows us to inject an electric current through one of the branches and to measure the Hall voltage transversal to the current. By performing longitudinal measurements on double Hall Cross devices, we can measure the AMR signal, V_{MR}, which provides complementary information about the position

[26] We left out the contribution from the ordinary Hall effect, since it is negligible in ferromagnetic materials.

of the magnetization, and, consequently, about the SOTs. Figure 4.5 shows a schematic representation of the current injection and measurement geometry on a Hall Cross device.

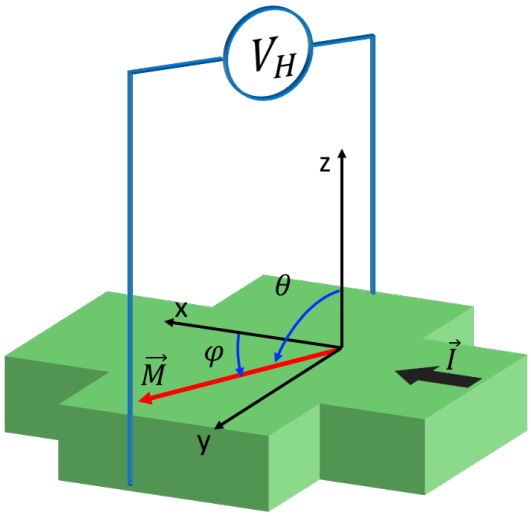

Figure 4.5: Schematic representation of the sample shape and the measurement geometry.

By applying a large out-of-plane magnetic field perpendicular to the sample plane, $\theta_H = 0°$ and φ_H is no longer defined, the magnetization will be almost completely saturated in the out-of-plane direction, $\theta_0 = \theta_H = 0°$. In this situation, the second term in Equation 4.5, vanishes and the measured Hall signal is proportional to the polar angle, θ: $V_H = V_{AHE} = IR_{AHE}\cos\theta$, that is to say proportional to $\vec{M}_z$. In the limit of small variations[27], for $\Delta H_{ext} \ll H_{ext}$, the angular displacement of the magnetization, $\Delta\theta$, caused by ΔH_{ext} is proportional to the change in the measured AHE voltage, ΔV_{AHE}. By sweeping the external magnetic field amplitude between large enough values to saturate the magnetization along the $\pm\vec{z}$ directions, ($\pm H_{ext}$), measuring the Hall resistance at each field step, we can calculate the polar angle of the magnetization at equilibrium for each field value, as:

$$\theta_0 = acos\left(\left|\frac{R_{AHE}(H_{ext})}{R_{AHE}^S}\right|\right)$$

Equation 4.6

where R_{AHE}^S is the Hall resistance value at saturation, and $R_{AHE}(H_{ext})$ is the Hall resistance corresponding to each field step value.

By fitting the measured Hall signal we can also extract the anisotropy field, $\vec{H}_K$:

[27] Linear variations

$$R_{AHE}(H_{ext}) = R_{AHE}^{S} \frac{\vec{H}_{ext}}{\sqrt{\vec{H}_{ext}^2 + \vec{H}_k^2}}$$

Equation 4.7

The azimuthal angle is much easier to evaluate: due to the low in-plane anisotropy of Co, CoFeB and Py, $\varphi_0 = \varphi_H$ even for relatively small external magnetic field values ($\vec{H}_{xy}$~$100\ Oe$).

4.2.2 Harmonic Analysis of the Hall Voltage

To measure the SOTs in our samples, we inject an a.c. current, $I = I_0 \sin(\omega t)$, of moderate frequency, $f = 10\ Hz$ and follow the magnetization dynamics through the harmonic analysis of the Hall voltage [124]. Through the current induced SOTs, the a.c. current will induce small time-dependent oscillations of the magnetization around its equilibrium position, $M(\theta_0, \varphi_0)$, defined by $\vec{H}_{total} = \vec{H}_K + \vec{H}_{ext}$, as shown in Figure 4.6.

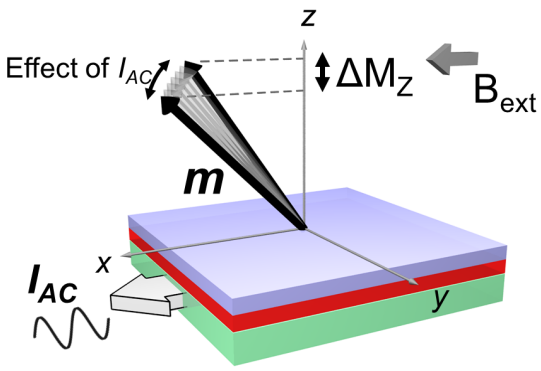

Figure 4.6: Effect of an a.c. current, $I_{a.c.} = I\ sin(\omega t)$, on the magnetization position. From [74].

These oscillations are in phase with the current and can be written as:

$$\theta = \theta_0 + \Delta\theta(I)$$

Equation 4.8

and

$$\varphi = \varphi_0 + \Delta\varphi(I)$$

Equation 4.9

Because the Hall resistance, R_H, depends on the position of the magnetization, these oscillations will modulate R_H which will oscillate with the same frequency as the current:

$$R_H(t) = R_H^0 \sin(\omega t)$$

Equation 4.10

A first order Taylor expansion of the Hall resistance, $R_H(t)$, around the equilibrium position, $M(\theta_0, \varphi_0)$, gives:

$$R_H = R_H^0(\theta_0, \varphi_0) + \frac{\partial R_H}{\partial I} I_0 \sin(\omega t)$$

Equation 4.11

where $R_H^0(\theta_0, \varphi_0)$ is related to the equilibrium position of the magnetization, independent of the a.c. current and $\frac{\partial R_H}{\partial I}$ is the current modulated Hall resistance, linked to the oscillations of the magnetization. Now, it is important to note that the analysis is valid in the limit of small oscillations. In our case, these oscillations are with respect to the current and not the time, therefore it is important to take the derivative of the Hall resistance with respect to the current and not the time. $R_H^0(\theta_0, \varphi_0)$ is given by:

$$R_H^0(\theta_0, \varphi_0) = R_{AHE} \cos(\theta_0) + R_{PHE} \sin^2(\theta_0) \sin(2\varphi)$$

Equation 4.12

Next, calculating the derivative[28] of R_H with respect to the current, we get:

$$\frac{\partial R_H}{\partial I} = [R_{AHE} - 2R_{PHE} \sin(2\varphi_0)] \frac{d \cos(\theta)}{dI}\bigg|_{\theta_0} + R_{PHE} \sin^2(\theta_0) \frac{d \sin(2\varphi)}{dI}\bigg|_{\varphi_0}$$

Equation 4.13

We see that the current modulated signal has static parameters, Equation 4.12, which are independent of the current induced SOTs, and dynamic parameters, which are current dependent, Equation 4.13.

Experimentally, we will be measuring the Hall voltage, given by Equation 4.5. Taking into account that $I = I_0 \sin(\omega t)$, and substituting R_H with Equation 4.11, we see that the different terms in the Hall voltage corresponding to static and dynamic components are in fact harmonic components of the Hall voltage:

$$\begin{aligned} V_H(t) = {} & I_0 [R_{AHE} \cos(\theta_0) + R_{PHE} \sin^2(\theta_0) \sin(2\varphi_0)] \sin(\omega t) \\ & + I_0 \left[I_0 (R_{AHE} - 2R_{PHE} \cos(\theta_0) \sin(2\varphi_0)) \frac{d \cos(\theta)}{dI}\bigg|_{\theta_0} \right. \\ & \left. + I_0 R_{PHE} \sin^2(\theta_0) \frac{d \sin(2\varphi)}{dI}\bigg|_{\varphi_0} \right] \sin^2(\omega t) \end{aligned}$$

Equation 4.14

[28] While calculating the derivative we need to take into account that both θ and φ depend on I.

Making the substitution:

$$\sin^2(\omega t) = \frac{1}{2} - \frac{1}{2}\cos(2\omega t)$$

Equation 4.15

we get:

$$V_H = I_0\left[\frac{1}{2}R_H^0 + R_H^f \sin(\omega t) + \frac{1}{2}R_H^{2f}\cos(2\omega t)\right]$$

Equation 4.16

where

$$\begin{cases} R_H^0 = I_0(R_{AHE} - 2R_{PHE}\cos(\theta_0)\sin(2\varphi_0))\left.\frac{d\cos(\theta)}{dI}\right|_{\theta_0} + I_0 R_{PHE} sin^2(\theta_0)\left.\frac{d\sin(2\varphi)}{dI}\right|_{\varphi_0} \\ R_H^f = R_{AHE}\cos(\theta_0) + R_{PHE} sin^2(\theta_0)\sin(2\varphi_0) \\ R_H^{2f} = I_0(R_{AHE} - 2R_{PHE}\cos(\theta_0)\sin(2\varphi_0))\left.\frac{d\cos(\theta)}{dI}\right|_{\theta_0} + I_0 R_{PHE} sin^2(\theta_0)\left.\frac{d\sin(2\varphi)}{dI}\right|_{\varphi_0} \end{cases}$$

Equation 4.17

Here R_H^f is the first harmonic Hall resistance component and R_H^{2f} is the second harmonic Hall resistance component.

R_H^0 is a static, rectifying term linked to the R_H^{2f}. It also contains information about the SOTs, however, in practice it is much more difficult to accurately measure a constant offset than it is to measure a variation. Furthermore, there are many different other sources of constant offsets that add to the measured signal, making R_H^0 even harder to determine. It is therefore preferred to use R_H^{2f} to calculate the SOTs.

Comparing Equation 4.5 and Equation 4.17 we see that R_H^f is equivalent to the Hall resistance in d.c. measurements and it gives the equilibrium position of the magnetization. It is independent of the current induced SOTs. On the other hand, $R_H^{2f}(I)$ is current dependent and is related to the modulation of the Hall resistance by the a.c. current. It is a measure of the magnetization's susceptibility to the current induced SOTs. By performing an FFT analysis of the measured Hall signal, one can get both the first harmonic, R_H^f, and the second harmonic, R_H^{2f}.

The two derivatives in Equation 4.17, $\frac{d\cos(\theta)}{dI}$ and $\frac{d\sin(2\varphi)}{dI}$, carry the information about the two effective fields, $\vec{H}_{FL}$ and $\vec{H}_{DL}$, corresponding to the two current induced SOTs, FL and DL torques. The dependence on $\cos(\theta)$ of $R_H^{2f}(I)$ (and R_H^0) comes from the AHE and the

dependence on $\sin(2\varphi)$ from the PHE. We will see in the next section how we link the second harmonic to the SOTs.

4.2.3 Field-Like and Damping-Like torques

Equation 4.17 allows us to calculate the current induced SOTs. R_H^{2f} depends explicitly on the current. The a.c. current acts on the magnetization by means of a current induced effective magnetic field, $\vec{H}_I$. To be able to calculate the SOTs we need to write the current dependence of R_H^{2f} in terms of the current induced effective field dependence. In the general case, we have:

$$\vec{H}_I = \vec{H}_{\parallel} + \vec{H}_{\perp} + \vec{H}_{Oe}$$

Equation 4.18

or

$$\vec{H}_I = \vec{H}_{FL} + \vec{H}_{DL} + \vec{H}_{Oe}$$

Equation 4.19

where $\vec{H}_{Oe}$ is the Oersted field created by the injected current.

The derivatives in Equation 4.17 carry the current dependence of R_H^{2f} so we need to rewrite them in terms of $\vec{H}_I$, taking into account that only the polar component of the current induced field can induce an oscillation in θ, while only the azimuthal component of the current induced field can induce an oscillation in φ:

$$\frac{d\cos(\theta)}{dI} = \frac{d\cos(\theta)}{d\vec{H}_I} \cdot \frac{d\vec{H}_I}{dI} = \frac{d\cos(\theta)}{dH_I^{\theta}} h_I^{\theta}$$

Equation 4.20

and

$$\frac{d\sin(2\varphi)}{dI} = \frac{d\sin(2\varphi)}{d\vec{H}_I} \cdot \frac{d\vec{H}_I}{dI} = \frac{d\sin(2\varphi)}{dH_I^{\varphi}} h_I^{\varphi}$$

Equation 4.21

where H_I^{θ} and H_I^{φ} are the polar and azimuthal components of the current induced field, $\vec{H}_I$, while h_I^{θ} and h_I^{φ} respectively are their derivatives with respect to the current, I. We should note that the third component of $\vec{H}_I$, namely the radial component, H_I^r, has no effect on the motion of the magnetization around its equilibrium position and it is therefore left out of this

discussion. Figure 4.7 shows the polar, azimuthal and radial components of the applied field with respect to the magnetization.

The field dependence of R_H^{2f} is independent of the nature of the magnetic field, that is to say θ and φ variations are independent of the origin of the magnetic field, so we can use the external field as a reference. Therefore, we can replace the polar and azimuthal components of $\vec{H}_I$ (the unknown field) with those of $\vec{H}_{ext}$ (the reference field):

$$dH_I^{\theta} \rightarrow dH_{ext}^{\theta} = H_{ext} d\sin(\theta - \theta_H)$$

Equation 4.22

and

$$dH_I^{\varphi} \rightarrow dH_{ext}^{\varphi} = H_{ext}\sin(\theta_H)\, d\sin(\varphi - \varphi_H)$$

Equation 4.23

Here, $\theta - \theta_H$ is the angle between the applied field and the magnetization. The polar component of the applied field acting on the magnetization will then be $H_{ext}^{\theta} = H_{ext}\sin(\theta - \theta_H)$. Similarly, the azimuthal component will be $H_{ext}^{\varphi} = H_{ext}\sin(\theta_H)\sin(\varphi - \varphi_H)$.

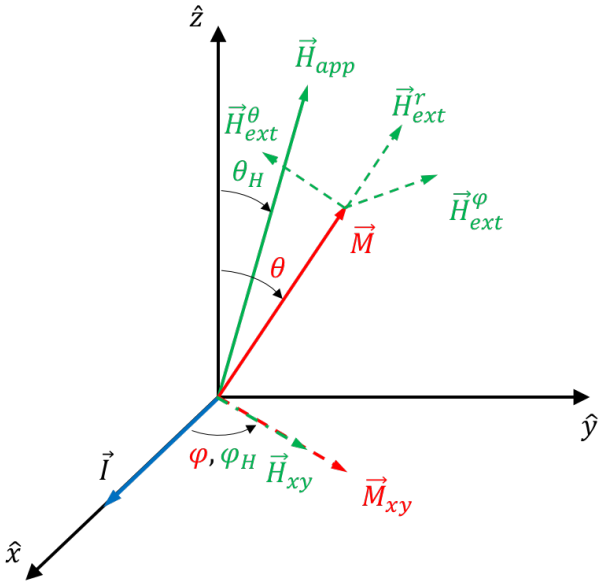

Figure 4.7: Polar, azimuthal and radial components of the applied external magnetic field.

We can thus write the field dependence of R_H^{2f} in terms of the applied external magnetic field. It is important to note that the two derivatives in question must be calculated with respect to the variable that is actually being changed during the experimental measurements. Here we can distinguish two situations:

i. Field Scan: in which an external magnetic field is applied along a known fixed direction, $H_{ext}(\theta_H, \varphi_H = \varphi)$, and its amplitude its being scanned with a controlled step between $\pm H_{ext}$;

ii. Angle Scan: in which the applied external field has a constant amplitude, H_{ext}, and its direction is scanned with a controlled step along the polar or azimuthal angle.

In the first case, where the variable that is being changed is the amplitude of the external field, we will have:

$$\frac{d\cos(\theta)}{d\vec{H}_I^{\theta}} \cdot h_\theta = \frac{d\cos(\theta)}{dH_{ext}} \frac{h_I^{\theta}}{\cos(\theta_0 - \theta_H)\, H_{ext}}$$

Equation 4.24

$$\frac{d\sin(2\varphi)}{d\vec{H}_I^{\varphi}} h_I^{\varphi} = \frac{d\sin(2\varphi)}{dH_{ext}} \frac{h_I^{\varphi}}{H_{ext}\sin(\theta_H)} \approx \frac{2\cos(2\varphi)}{H_{ext}\sin(\theta_H)} h_I^{\varphi}$$

Equation 4.25

Replacing the derivatives in Equation 4.17 we have:

$$R_H^{2f}(I) = I(R_{AHE} - 2R_{PHE}\cos(\theta_0)\sin(2\varphi_0)) \left.\frac{d\cos(\theta)}{dH_{ext}}\right|_{\theta_0} \frac{h_I^{\theta}}{\cos(\theta_0 - \theta_H)\, H_{ext}}$$
$$+ IR_{PHE} sin^2(\theta_0) \left.\frac{d\sin(2\varphi)}{dH_{ext}}\right|_{\varphi_0} \frac{h_I^{\varphi}}{H_{ext}\sin(\theta_H)}$$

Equation 4.26

In the case of Angle Scan measurements, the variable that we are changing is the position of the external field, not it's amplitude. Here we will have:

$$\frac{d\cos(\theta)}{d\vec{H}_I^{\theta}} \cdot h_\theta = \frac{d\cos(\theta)}{d\theta} \frac{h_I^{\theta}}{\cos(\theta - \theta_H)\, H_{ext}}$$

Equation 4.27

$$\frac{d\sin(2\varphi)}{d\vec{H}_I^{\varphi}} h_I^{\varphi} = \frac{d\sin(2\varphi)}{d\varphi} \frac{h_I^{\varphi}}{H_{ext}\sin(\theta_H)\cos(\varphi - \varphi_H)}$$

Equation 4.28

In this case, R_H^{2f} is:

$$R_H^{2f}(I) = I(R_{AHE} - 2R_{PHE}\cos(\theta_0)\sin(2\varphi_0))\left.\frac{d\cos(\theta)}{d\theta}\right|_{\theta_0}\frac{h_I^\theta}{\cos(\theta_0-\theta_H)\,H_{ext}}$$
$$+ IR_{PHE}sin^2(\theta_0)\left.\frac{d\sin(2\varphi)}{d\varphi}\right|_{\varphi_0}\frac{h_I^\varphi}{H_{ext}\sin(\theta_H)\cos(\varphi-\varphi_H)}$$

Equation 4.29

During our angle scan measurements, we apply the external field, H_{ext}, in the plane of the sample, at $\theta_H = 90°$, and we scan the field position along the azimuthal angle, φ. Because our samples have easy-plane anisotropy, the following will hold: $\theta_H = \theta_0 = 90°$ and $\varphi_H = \varphi$. Equation 4.29 then becomes:

$$R_H^{2f}(I) = IR_{AHE}\left.\frac{d\cos(\theta)}{d\theta}\right|_{\theta_0}\frac{h_I^\theta}{H_{ext}} + IR_{PHE}\left.\frac{d\sin(2\varphi)}{d\varphi}\right|_{\varphi_0}\frac{h_I^\varphi}{H_{ext}}$$

Equation 4.30

We can now write the derivatives in terms of the first harmonic of the Hall resistance, which is a quantity that we directly measure in our experiment. We will therefore have:

$$\frac{dR_H^f}{d\theta} = R_{AHE}\frac{d\cos(\theta)}{d\theta}$$

Equation 4.31

and

$$\frac{dR_H^f}{d\varphi} = R_{PHE}\frac{d\sin(2\varphi)}{d\varphi}$$

Equation 4.32

Making the substitution, Equation 4.30 becomes:

$$R_H^{2f} = \frac{dR_H^f}{d\theta}\frac{h_I^\theta}{H_{ext}} + \frac{dR_H^f}{d\varphi}\frac{h_I^\varphi}{H_{ext}}$$

Equation 4.33

At this point, what is missing from our analysis is directly linking R_H^{2f} to the SOTs. From the symmetry of the SOTs [19], [20], we can write the symmetry of the corresponding effective fields as $\vec{H}_D = H_D(\vec{m}\times\vec{y}) \approx H_D\cos(\varphi)\,\hat{\theta}$ and $\vec{H}_{FL} = H_{FL}[\vec{m}\times(\vec{m}\times\vec{y})] \approx H_{FL}\cos(\varphi)\,\hat{\varphi}$. Using this information, we can write H_D and H_{FL} in terms of the polar and azimuthal components of the current induced field, as $h_I^\theta = H_D\cos(\varphi)$ and $h_I^\varphi = H_{FL}\cos(\varphi)$. Making the substitutions in Equation 4.33 we get:

$$R_H^{2f} = \frac{dR_H^f}{d\theta}\frac{H_D\cos(\varphi)}{H_{ext}} + \frac{dR_H^f}{d\varphi}\frac{H_{FL}\cos(\varphi)}{H_{ext}}$$

Equation 4.34

Equation 4.34 shows two components of the measured R_H^{2f}. The first term contains the contribution from the Damping-Like torque, while the second term contains the contribution from the Field-Like torque[29]. We note here that both Damping-Like and Field-Like components are inversely proportional to the external field, H_{ext}. At the same time, through $\frac{dR_H^f}{d\theta}$ and $\frac{dR_H^f}{d\varphi}$, the two components are proportional with the variation of the AHE and PHE with respect to the θ and φ angles. For samples with in-plane magnetic anisotropy, $\frac{dR_H^f}{d\varphi}$ depends on the position of the in-plane oscillation of the magnetization. This oscillation is induced by the Field-Like SOT and it is being opposed by the applied field, H_{ext}. On the other hand, $\frac{dR_H^f}{d\theta}$ depends on the position of the out-of-plane oscillation of the magnetization around the $\theta = 90°$ position. This oscillation is induced by the Damping-Like SOT, and it is being countered by the applied field, H_{ext}, as well as by the demagnetizing field, H_{dem}. Any perpendicular magnetic anisotropy components, induced by the interfaces, will act to reduce the effective demagnetizing field, which is calculated for each sample as $H_{dem} \approx \mu_0 M_S$, where M_S is the saturation magnetization.

Separating these contributions and taking into account the individual field dependencies will give us direct access to the effective fields corresponding to the SOTs.

[29] There are other contributions to R_H^{2f}, from the Oersted field and thermoelectric effects, which we will discuss in later sections.

4.3 Angle Scan Measurements and Analysis

4.3.1 Separating Damping-Like and Field-Like torques

We have seen in the previous section that the second harmonic signal of the Hall Resistance, R_H^{2f}, contains contributions both from the Damping-Like and Field-Like torques. Looking at the symmetry of the SOTs, for a current flowing in the $\hat{x}$ direction, we have the Damping – Like torque, $\vec{T}_D \sim \vec{m}\times(\vec{y}\times\vec{m})$, and the Field-Like torque, $\vec{T}_{FL} \sim \vec{m}\times\vec{y}$ [19], [20], [124], [140], [146], where $\vec{m}$ is the magnetization unit vector and $\vec{y}$ the Cartesian axis perpendicular to the current flow. For samples with in-plane magnetic anisotropy, where the magnetization lies in the plane of the sample, the effect of $\vec{T}_D$ can be seen as the effect of an effective out-of-plane field, $\vec{H}_D = H_D(\vec{m}\times\vec{y})$, and that of the $\vec{T}_{FL}$ as the effect of an effective in-plane field, $\vec{H}_{FL} = H_{FL}[\vec{m}\times(\vec{m}\times\vec{y})]$. With the injection of an in-plane a.c. current, $I = I_0 \sin(\omega t)$, $\vec{T}_D$ will cause the magnetization to oscillate out-of-plane, while the $\vec{T}_{FL}$ will cause the magnetization to oscillate in-plane. The effect of $\vec{T}_{FL}$ will add to that of $\vec{T}_{Oe}$ created by the Oersted field which also lies in-plane and has the same current dependence as the Field-Like effective field, $\vec{H}_{FL}$. Figure 4.8 shows a schematic of the effects of the SOTs on the magnetization.

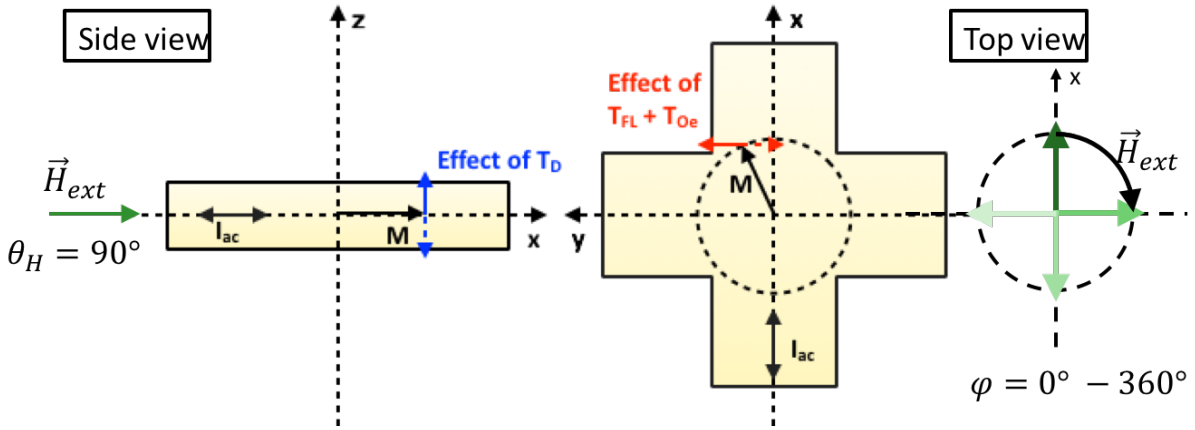

Figure 4.8: Schematic showing the effects of the Damping-Like and Field-Like torques on the magnetization of a sample with in-plane magnetic anisotropy when an in-plane a.c. current is injected. $\vec{T}_D$ causes out-of-plane oscillations of the magnetization, while $\vec{T}_{FL}$ and $\vec{T}_{Oe}$ both cause in-plane-oscillations.

During the measurements, these contributions add up and are measured at the same time (Figure 4.9 e)). In order to properly calculate the value of the current induced SOTs, we need a way of separating each contribution from the measured R_H^{2f} signal.

Simulations of the R_H^f and R_H^{2f} signals, done by Garello *et. al.* (Figure 4.9 a) – c)), of the transversal Hall resistance, due to $\vec{T}_D$ and $\vec{T}_{FL}$ respectively, show different angular dependency of the corresponding R_H^{2f} signal components. Details about the simulations are shown in [129]. Consistent with Equation 4.17, for samples with in-plane magnetic anisotropy when the external magnetic field lies in-plane, $\theta_H = \theta_0 = 90°$, the first harmonic signal of the Hall resistance consists only of the PHE, with a $R_H^f \approx \sin(2\varphi)$ angular dependency. In the case of the second harmonic signal, R_H^{2f}, the angular dependency is more complicated. The R_H^{2f} component due to the $\vec{T}_D$ has a $R_{DL}^{2f} \approx \cos(\varphi)$ dependence and the R_H^{2f} component due to the $\vec{T}_{FL}$ has a $R_{FL+Oe}^{2f} \approx 2\cos^3(\varphi) - \cos(\varphi)$ dependence [129]. This means that, when we perform an angle scan between $\varphi = 0° \; and \; 360°$, for $\varphi = 45°, 135°, 225°$ and $315°$ the R_H^{2f} signal component due to $\vec{T}_{FL}$ will be zero. If we fit a cosine function that passes through the R_H^{2f} values at $\varphi = 45°, 135°, 225° \; and \; 315°$ and subtract the fit from the measured R_H^{2f} signal we can separate the contributions from the two SOTs (Figure 4.9 f) and g)).

We can therefore write the expressions of the Damping-Like and Field-Like torques in terms of the R_{DL}^{2f} and R_{FL+Oe}^{2f} components of the measured R_H^{2f} signal:

$$H_D = (H_{ext} + H_{dem}) \frac{1}{\cos(\varphi)} \frac{R_{DL}^{2f}}{\frac{dR_H^f}{d\theta}}$$

Equation 4.35

and

$$H_{FL} = H_{ext} \frac{1}{\cos(\varphi)} \frac{R_{FL}^{2f}}{\frac{dR_H^f}{d\varphi}}$$

Equation 4.36

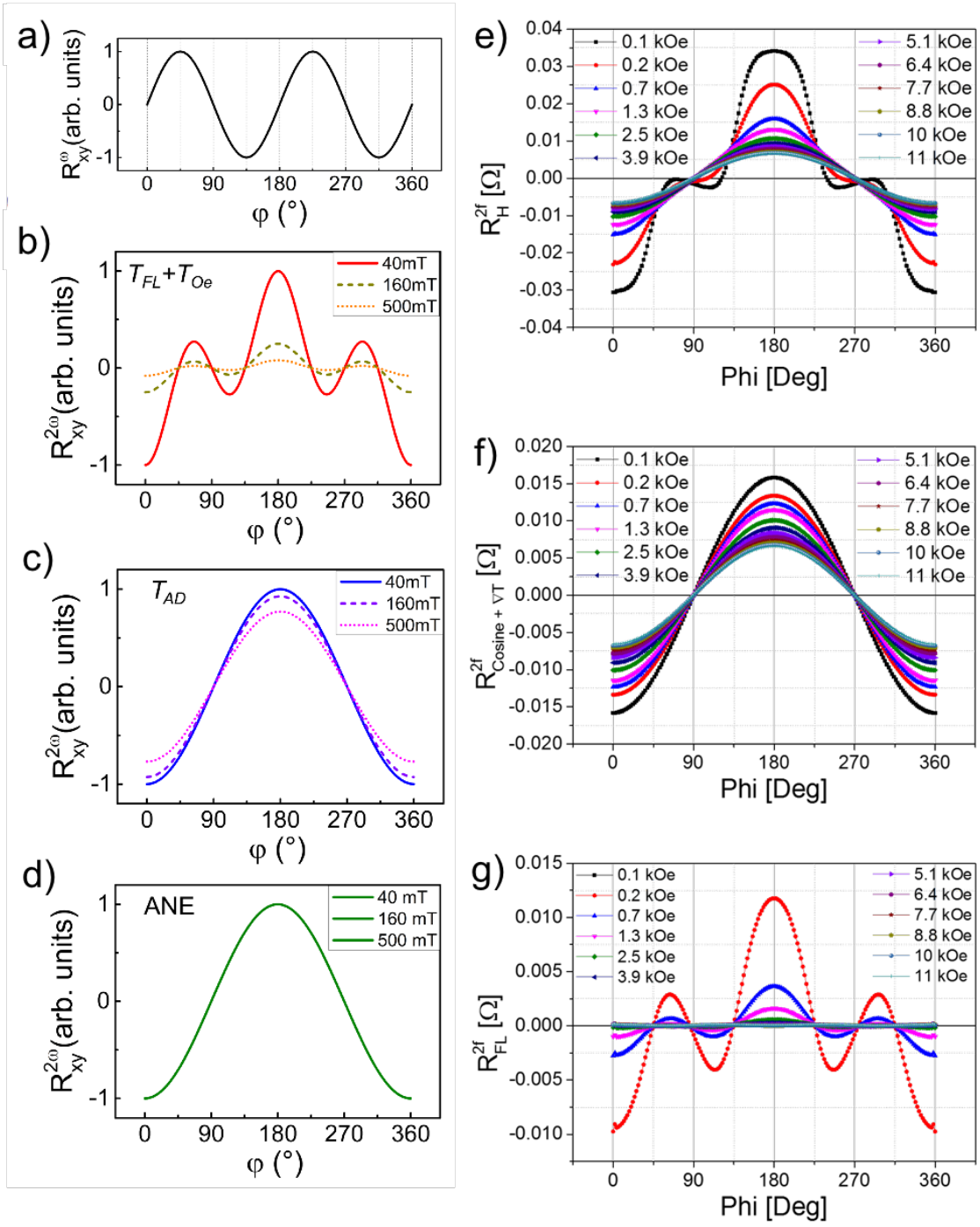

Figure 4.9: Simulations of the a) first harmonic, R_H^f , and second harmonic R_H^{2f} due to b) the Field-Like torque, $\vec{T}_{FL}$, c) the Damping-Like torque, $\vec{T}_D$, and d) the ANE of the transversal Hall resistance. From [129]; Angle scan measurements of the second harmonic signal, R_H^{2f}, of the Hall resistance for a $Cu_{10}/Co_{20}/Pt_{45}$ sample showing e) contributions from the Damping-Like and Field-Like torques, f) the separated the $\approx cos(\varphi)$ contribution from the Damping-Like torque and g) the separated $2\,cos^3(\varphi) - cos(\varphi)$ contribution from the Field-Like torque.

4.3.2 Separating thermoelectric effects

Previous work of Garello *et. al.* [124] and Avci *et. al.* [129] also showed that the measured R_H^{2f} signal also contains contributions from thermoelectric effects, most notably the Anomalous Nernst Effect (ANE), which can lead to an overestimation of the SOTs if not properly taken into account. In this section we will look at how to separate the thermoelectric component in the R_H^{2f} signal from the SOTs components.

As we perform the measurements, the injected current causes Joule heating. This heating creates a thermal gradient, $\vec{\nabla}T$, in the sample, which generates thermoelectric effects such as ANE and/or SSE (Spin Seebeck Effect). In ferromagnetic materials (or in the presence of a local magnetization) when a temperature gradient is present, the ANE creates a voltage transversal to the magnetization and to the said temperature gradient [126]–[128], [147], [148]:

$$V_{ANE} = \vec{\nabla}T \times \vec{m}$$

Equation 4.37

Because the thermal conductivity of the substrate is much higher than that of the contact leads, the $\vec{\nabla}T$ will be oriented along the $\hat{z}$ axis. The implication is two fold: first, V_{ANE} will have a non zero component along the $\hat{y}$ axis that will be detected by our Hall measurements; second, V_{ANE} voltage will have a $\approx \cos(\varphi)$ angular dependence (Figure 4.9 d)). As the thermal gradient does not depend on the sign of the injected a.c. current, the ANE voltage will have a second order dependence on the current and therefore will add to the R_H^{2f} signal, more precisely it will add to the Damping-Like component of the R_H^{2f} signal:

$$\left.\begin{matrix} R_{DL}^{2f} \approx \cos(\varphi) \\ R_{\vec{\nabla}T}^{2f} \approx \cos(\varphi) \end{matrix}\right\} \implies R_{cos}^{2f} \approx \cos(\varphi)$$

Equation 4.38

Equation 4.35 therefore needs to be corrected for the ANE offset:

$$H_D = (H_{ext} + H_{dem}) \frac{1}{\cos(\varphi)} \frac{R_{DL}^{2f}}{\frac{dR_H^f}{d\theta}} = (H_{ext} + H_{dem}) \frac{1}{\cos(\varphi)} \frac{R_{cos}^{2f} - R_{\vec{\nabla}T}^{2f}}{\frac{dR_H^f}{d\theta}}$$

Equation 4.39

Figure 4.10 shows a schematic of the thermal gradient with respect to the sample plane and current injection direction as well as the direction of the ANE voltage.

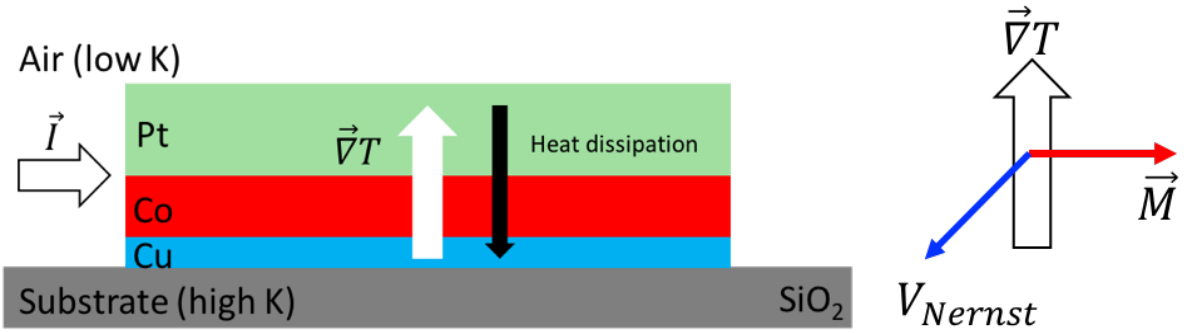

Figure 4.10: a) Schematic showing the direction of the thermal gradient with respect to the sample plane ; b) ANE voltage perpendicular to the thermal gradient and magnetization.

To separate R_{DL}^{2f} and $R_{\vec{\nabla}T}^{2f}$ from the measured R_{cos}^{2f} we can perform current dependent measurements [130] or field dependent measurements [129]. The R_{DL}^{2f} contribution to the measured signal is the result of the magnetizations oscillations around its equilibrium position. As we increase the strength of the applied field however, the magnetization will be more strongly aligned with the field direction and its susceptibility to the SOTs decreases. In the limit of very high field, where the magnetization's susceptibility to the SOTs goes to zero, the Damping – Like component, R_{DL}^{2f}, of the measured R_{cos}^{2f} signal vanishes. On the other hand, the $R_{\vec{\nabla}T}^{2f}$ contribution to the measured signal depends only on the magnetization's direction and is independent of the applied field amplitude[30]. By performing measurements at different external field values and plotting the amplitude of the R_{cos}^{2f} as a function of the inverse of the total field opposing the magnetization's oscillations, $H_{ext} + H_{dem}$, we get a linear dependency that we can fit with a linear function. In the limit of high fields, the intercept corresponds to the linear offset induced by the ANE signal. The slope of the fit function corresponds to the field dependent signal due to the Damping-Like torque (Figure 4.11).

[30] As long as the magnetization is saturated.

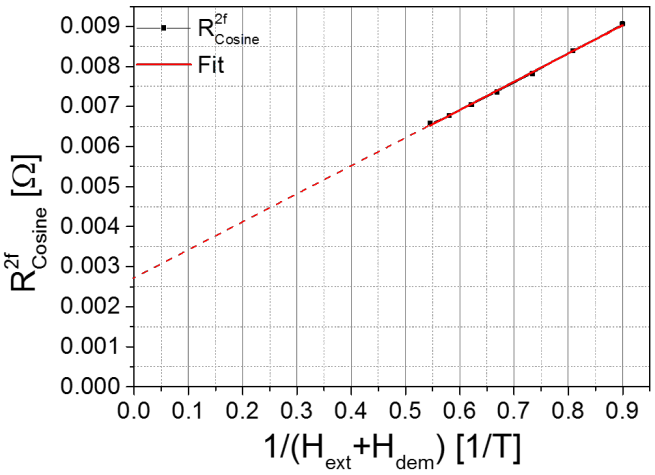

Figure 4.11: Linear dependence of the amplitude of the R_{cos}^{2f} as a function of the inverse of the total magnetic field opposing the magnetization's out of plane oscillation for a $Cu_{10}/Co_{20}/Pt_{45}$ sample. In the limit of high fields, the intercept corresponds to the ANE signal and the slope corresponds to the Damping-Like torque signal.

4.3.3 Calculating Damping-Like and Field-Like effective fields

Using the linear fit of the R_{cos}^{2f} signal amplitude vs the inverse of the total field acting on the magnetization, $\frac{1}{H_{ext}+H_{dem}}$, shown in Figure 4.11, we can write R_{cos}^{2f} as:

$$R_{cos}^{2f} = a + b\frac{1}{H_{ext} + H_{dem}}$$

Equation 4.40

where a is the intercept and b is the slope of the fitting function. From Equation 4.39 we can also write R_{cos}^{2f} as:

$$H_D = (H_{ext} + H_{dem})\frac{1}{\cos(\varphi)}\frac{R_{cos}^{2f} - R_{\vec{\nabla}T}^{2f}}{\frac{dR_H^f}{d\theta}} \Leftrightarrow R_{cos}^{2f} = R_{\vec{\nabla}T}^{2f} + H_D\cos(\varphi)\frac{dR_H^f}{d\theta}\frac{1}{H_{ext} + H_{dem}}$$

Equation 4.41

By simply identifying the coefficients in the equations above, we have:

$$a = R_{\vec{\nabla}T}^{2f}$$

Equation 4.42

and

$$b = H_D\cos(\varphi)\frac{dR_H^f}{d\theta}$$

Equation 4.43

This gives us a direct and easy way of evaluating the Damping-Like effective field, H_D, from our R_{cos}^{2f} measurements as a function of angle, at different field amplitudes, regardless of the type and magnitude of the thermoelectric offsets, or any other field independent offsets present:

$$H_D = \frac{b}{\cos(\varphi)\frac{dR_H^f}{d\theta}}$$

Equation 4.44

A similar reasoning is followed for the calculation of the Field-Like effective field, H_{FL}, as well. We plot the amplitude of the R_{FL}^{2f} signal as a function of the inverse of the external field, H_{ext}, and we fit the data with a linear function. In the limit of high fields, when the susceptibility of the magnetization to the current induced SOTs is zero, the R_{FL}^{2f} signal vanishes and the data goes to zero (i.e. the intercept of the fitting function is 0). We can therefore write R_{FL}^{2f} as:

$$R_{FL}^{2f} = k\frac{1}{H_{ext}}$$

Equation 4.45

where k is the slope of the fitting function. Using Equation 4.36 we can also write R_{FL}^{2f} as:

$$H_{FL} = H_{ext}\frac{1}{\cos(\varphi)}\frac{R_{FL}^{2f}}{\frac{dR_H^f}{d\varphi}} \Leftrightarrow R_{FL}^{2f} = H_{FL}\cos(\varphi)\frac{dR_H^f}{d\varphi}\frac{1}{H_{ext}}$$

Equation 4.46

Again, by identifying the coefficients in the equations above, we have:

$$k = H_{FL}\cos(\varphi)\frac{dR_H^f}{d\varphi}$$

Equation 4.47

This gives us a direct and easy way of evaluating the Field-Like effective field, H_{FL}, from our R_{FL}^{2f} measurements as a function of angle, at different field amplitudes:

$$H_{FL} = \frac{k}{\cos(\varphi)\frac{dR_H^f}{d\varphi}}$$

Equation 4.48

It is important to note that both R_{cos}^{2f} and R_{FL}^{2f} are symmetrical with respect to $\varphi = 180°$ and any antisymmetric component in the measured signal has to be corrected for, in order for our analysis to hold. There are a number of potential sources for antisymmetric components in the measured signal such as sample misalignment in the field, thermal gradients within the plane due to hot spots, misalignment of the Hall branches due to the lithography process that create AMR signals, misalignment along the θ angle.

4.3.3.2 Additional measurements – Out-of-Plane Field scans

In order to evaluate $\frac{dR_H^f}{d\theta}$ and the demagnetizing field, H_{dem}, which are needed to calculate H_D, we need additional measurements. For this we perform Field Scans with the external field perpendicular to the sample, that is $\theta_H = 0°$. As seen in section 4.2.1, in this situation the measured R_H^f signal will be proportional to $\approx \cos\theta$. By sweeping the external magnetic field amplitude between large enough values to saturate the magnetization along the $\pm\vec{z}$ directions, ($\pm H_{ext}$), and measure the Hall resistance at each field step, we will get a magnetic hysteresis loop in terms of R_H^f as a function of H_{ext} (see Figure 4.1 for an example). We obtain the effective demagnetizing field, H_{dem}, as the H_{ext} value at which the magnetization is completely saturated out-of-plane. This way, we also take into account any anisotropy field induced by the sample interfaces that can modify the demagnetizing field.

Using Equation 4.6 we calculate the polar angle of the magnetization at equilibrium, θ_0, for each field value, and we plot R_H^f as a function of θ_0 (Figure 4.12). It will show a linear variation around $\theta_0 = 90° \pm \Delta\theta$, corresponding to the magnetization being in- or slightly out-of-plane. If we fit the data around $\theta_0 = 90° \pm \Delta\theta$ with a linear function, the slope of the fit will give us the variation of R_H^f with respect to θ:

$$n = \frac{dR_H^f}{d\theta}$$

Equation 4.49

where n is the slope of the linear fit.

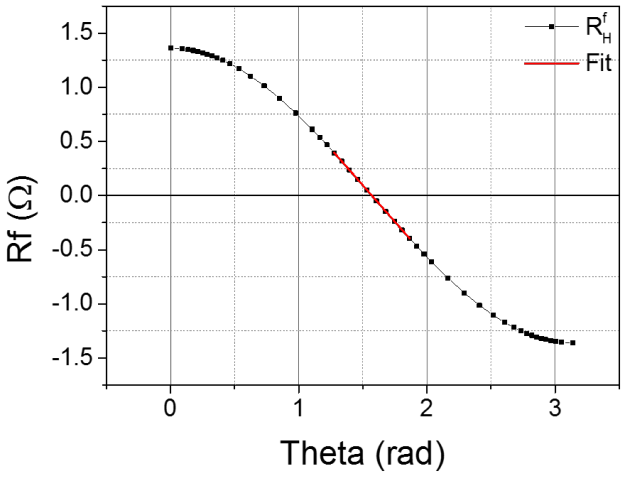

Figure 4.12: R_H^f as a function of θ for a Cu10/Co20/Pt30 sample. The red solid line represents a linear fit around the in-plane position ($\theta = 90°$). The slope of the fit is a measurement of $\frac{dR_H^f}{d\theta}$.

4.4 Experimental Setup

In order to perform the SOT measurements using the technique described in the previous sections, we mount the devices on a non-magnetic sample holder using a non-magnetic adhesive. The sample holder has Cu contact pads onto which we connect each of the terminals of our Hall cross devices by micro-bonding with 30 µm diameter Al wire. A low frequency a.c. current is injected across two of the contacts while a data acquisition system measures the Hall voltage across the other two contacts. To extract and compare the harmonic components of the Hall signal we perform an FFT analysis on the measured signal.

The experimental setup consists of an electromagnet, that can generate a magnetic field up to 2 T, connected to a bipolar power supply. The poles of the electromagnet are flat so that the field will be homogeneous over a large area and the sample holder is placed and centered in between the poles. Depending on the configuration of the sample holder, we can rotate the sample, inside the magnetic field, around θ or φ angles. The rotation is ensured by a Standa motorized rotation stage with a resolution of 0.01 degrees. Figure 4.13 shows a schematic of the measurement configuration and the two rotation geometries.

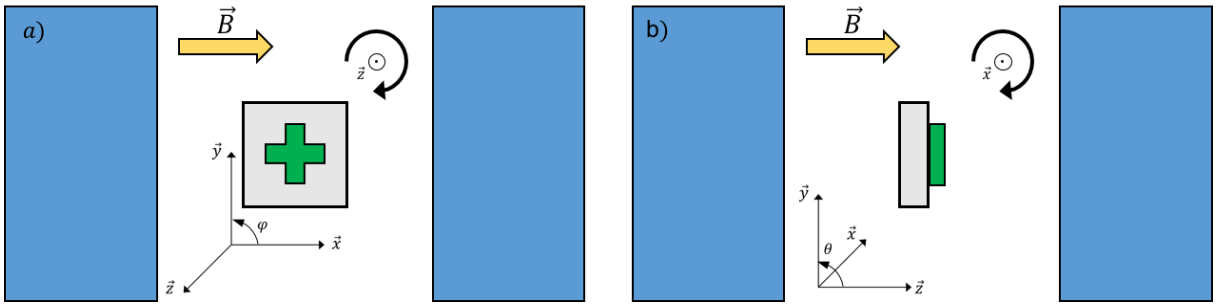

Figure 4.13: Schematic of the measurement configuration showing a) φ angle rotation and b) θ angle rotation of the sample under the external magnetic field, $\vec{B}$, created by the electromagnet.

This setup also poses a few challenges. First, good alignment of the sample within the applied field is important to minimize any error coming from an inhomogeneous field. However, the sample size is small relative to the electromagnet's poles (which, being flat create a homogeneous field over a large volume), rendering such errors minimal.

Second, mounting the sample on the sample holder can be affected by small misalignments: i) with respect to the center of the sample holder (xy plane), as well as ii) in the form of a φ angle rotation. In the first case, because the sample rotates inside a homogeneous field and the misalignments are very small, any errors induced this way are

negligible. In the second case, the φ angle misalignment induces an offset between the real φ angle and the angle readout during the measurement. It is easily corrected by applying the corresponding angle correction to the measured angle values within each data set.

Furthermore, when the plane of the sample and that of the sample holder are not parallel, because of the adhesive used, a misalignment in the θ angle is created. Figure 4.14 shows a schematic of the most likely situations. Because of this, the applied external magnetic field, $\vec{H}_{ext}$, will have two components: i) a planar component, $\vec{H}_{xy} = \vec{H}_{ext}\sin(\theta) \approx \vec{H}_{ext}$, which creates the PHE signal, and ii) an OOP component, $\vec{H}_z = \vec{H}_{ext}\cos(\theta)$, which creates an additional AHE signal. However, the two signals have different angular dependency and are easy to separate (Figure 4.15).

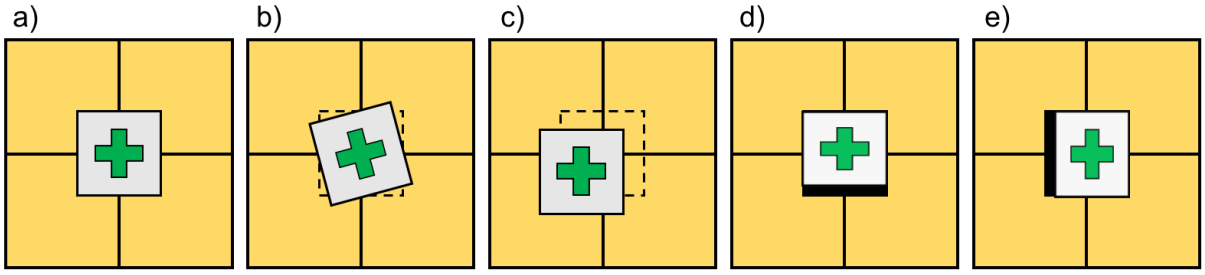

Figure 4.14: Potential problems linked to sample mounting on the sample holder: a) ideal position, b) φ angle misalignment, c) (xy) misalignment, d) and e) sample and sample holder planes are not parallel leading to θ angle misalignment.

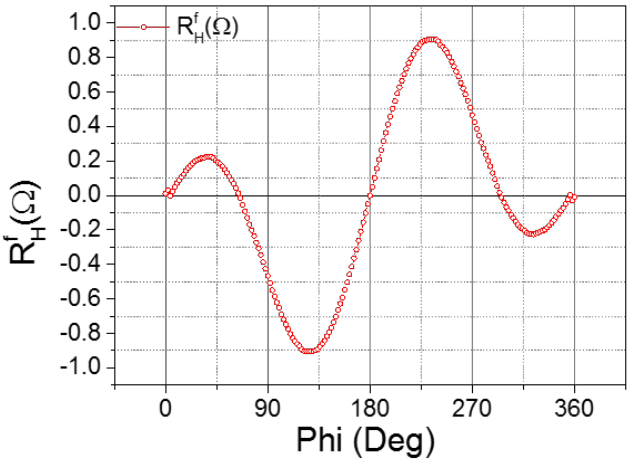

Figure 4.15: First harmonic signal consisting of the PHE signal with a $sin(2\varphi)$ angular dependency and the AHE contributions due to θ angle misalignment with a $cos(\theta)$ angular dependency.

For the current generation as well as signal measurement and magnetic field control we use a National Instruments PXI system. To control the applied magnetic field, we have connected the bipolar power supply to the output of a PXIe-6363 card set on a 10 V range. This allows us to perform measurements at constant field as well as sweeping the field across

a desired interval with a desired step. The field value is measured by means of a Hall probe placed between the poles of the electromagnet and connected to one of the inputs of a PXIe-4462 card.

For the a.c. current generation we used the output of a PXIe-4461 card, with a sampling frequency of 204.8 kS/s and a 24-bit resolution over a voltage range from ±316 mV to ±10 V. The error due to the data acquisition card is of the order of a few tens of nV. Using the two inputs of the same card we are measuring the injected current as well as the Hall voltage. The electric circuitry used for the measurements is shown schematically in Figure 4.16.

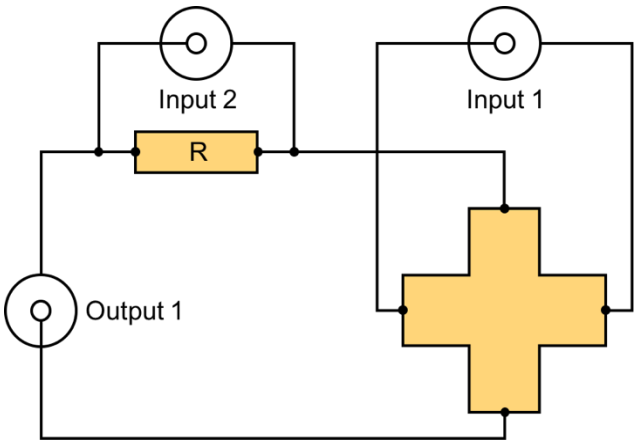

Figure 4.16: Schematic of the electric circuitry used in the measurement system. The a.c. current on the sample is applied from Output 1, the Hall voltage is measured at Input 1 while the current is measured at Input 2.

At each field or angle value an FFT analysis is done to extract the fundamental and harmonic components of the Hall signal. Their respective amplitudes are afterwards divided by the injected current to give the first and second harmonic components of the Hall resistance.

Since the measurements need to be in the quasi-static regime, the current frequency needs to be much lower than the relaxation time of the magnetization. Another point to consider is the noise of the a.c. current supplied by the power grid at 50 Hz and 220 V. Therefore, the frequency we are using is 10 Hz, which is lower than the frequency of the power grid current and much lower than the relaxation time of the magnetization. During the measurements, the sampling frequency is set to 40 kS/s while the number of samples points for each field or angle step varies between 44000 and 404000, which translates to between 1.1 and 10.1 seconds per step. We start the measurements by skipping one period, to ensure that the phase of the analyzed signal is zero. The entire measurement system, field and angle steps, data acquisition and FFT analysis, is controlled by a LabVIEW program developed “in-house”.

5 SOTs in HM/FM heterostructures with in-plane magnetic anisotropy

5.1 Objectives

As we have discussed in Chapters 2 and 3, one of the fundamental questions regarding the SOTs concerns their physical origin, namely the SHE (bulk) or the Rashba Effect (interface). The main focus of this study is to investigate the origin of SOTs and to differentiate between bulk and interface effects as dominant SOTs sources in HM/FM heterostructures. But, by simply measuring the SOTs, we have no means of distinguishing between these two effects, so instead, we will be modifying the interface/bulk effect ratio in our samples.

Traditionally, in the study of SOTs, HM/FM/Oxide multilayers are the representative sample system. Using HMs with high SOC allows for strong bulk contributions to the SOTs through the SHE, while the SIA created by the dissimilar HM/FM and FM/Oxide interfaces allows for strong interfacial contributions through the Rashba Effect.

One of the HM that has been studied most extensively is Pt, due to its low resistivity and high SOI. However, as we have discussed in section 3.2.2, even in the case of Pt, there is a high degree of discrepancy when it comes to its properties, such as SHA and spin diffusion length [122]. And these properties are essential when it comes to discussing the origin of the SOTs. We therefore conducted an extensive study on the influence of bulk and interface effects on the SOTs, in Pt based samples with in-plane magnetic anisotropy.

In order to modify the interface/bulk effect ratio in our samples, we explored several avenues:

i. First, we varied the thickness of the HM. The thickness of the HM layer directly affects the influence of the SHE on the amplitude of the SOTs. Because of spin diffusion, the amplitude of the SOTs due to the SHE is expected to decrease. It therefore allows us to “isolate” and study the effect of the interface. We also looked at different interfaces, by changing the HM/FM combination to study how different interfaces affect the SOTs. Finally, we changed the position of the Pt layer with respect to the FM layer, to study the SOTs coming from both the top and bottom interface.
ii. Second, we studied the influence of the HM’s crystalline structure on the SOTs, by growing epitaxial/textured Pt layers, with different orientations and coupling them with different FM layers. Our goal is to study how the DL and FL torques evolve for different HM crystal structure orientations, and how this affects the torques in different FM layers.

iii. Finally, we further modified the interface by oxidizing the samples.

We used the method described in Chapter 4, to follow the evolution of the Damping-Like and the Field-Like torques in each of the three cases. To be able to compare, in a meaningful way, the measured SOT values across the sample systems we have studied, as well as with values reported in literature we followed the evolution of magnetic and electric properties.

This chapter presents our experimental studies and proposes a discussion of our results, in the context of the “interface vs. bulk” debate regarding the origins of the SOTs.

5.2 Influence of top Pt layer thickness on the SOTs

5.2.1 Sample Stacks

To study the relative strength of interface and bulk effects on the SOTs, we have deposited $MgO_{(20)}/FeCoB_{(20)}/Pt_{(10\text{-}100)}$ layers with in-plane magnetic anisotropy and SIA, by dc magnetron sputtering on thermally oxidized Si/SiO_2 (1 µm), at the ACTEMIUM deposition chamber at SPINTEC. Pt/CoFeB/MgO based systems have been studied extensively at SPINTEC, in the context of perpendicular TMR junctions for STT-MRAM applications, and therefore we have experience in producing good quality layers. In our case, we want to investigate the evolution of SOTs as a function of the thickness of the top Pt layer. The MgO/FeCoB/Pt system is well suited for our purpose. First, the MgO layer allows for good CoFeB growth, ensuring continuous layers for the thickness interval we are interested in. It also helps create the SIA without contributing directly neither to the SOTs (no SHE), nor to the electrical conductivity of our samples. Second, FeCoB shows strong in-plane magnetic anisotropy for thicknesses above 1 nm. Third, Pt has a relatively low resistivity, compared to other heavy metals. This makes it an interesting material, from an applications perspective, as it reduces losses through Joule heating. We further made several design choices:

i. The FeCoB layer thickness of 20 Å has been chosen to ensure strong in-plane magnetic anisotropy, uniform layers without discontinuities and good susceptibility of the magnetization to the SOTs (thicker layers would result in much lower signal as it would be harder for the SOTs to “move” more magnetic moments).

ii. We place the Pt layer on top to ensure that the FeCoB/Pt interface is the same, regardless of the Pt layer thickness. What can happen, when increasing the thickness of the Pt layer, is that the growth direction of the Pt changes. When we deposit a FeCoB layer (or any other material for that matter) on top, it will grow differently depending on the thicknesses of the Pt layer underneath, hence the interface will be different. Since our goal is to study the effects of the interface on the SOTs, this can introduce errors when comparing our results. Placing the Pt layer on top solves this issue.

iii. Instead of fabricating stacks with different Pt layer thickness, our stacks are deposited with a Pt thickness gradient. This makes it easier to study a large range of thicknesses and, it also ensures that all samples are grown in the exact same conditions.

Figure 5.1 shows a schematic of the sample system (c), as well as the direction of the thickness gradient with respect to the wafer (b). We have kept the same orientation for all the samples that contain thickness gradients.

Now, using thickness gradients instead of stacks with nominal thicknesses raises another issue: we need to know the thickness of the Pt layer for each sample. For this, we used a thick Pt gradient (Figure 5.1 (a)), between 50 and 200 Å, as a reference, to calibrate the Pt thickness in our sample stacks.

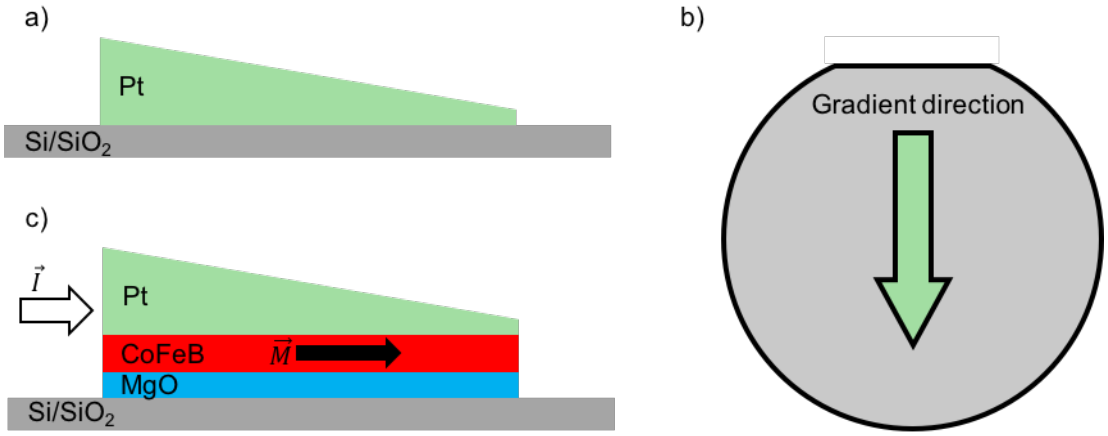

Figure 5.1: Schematics of a) the Pt gradient sample used to calibrate the thickness of the Pt layer as a function of position of the wafer; b) the direction of the thickness gradient with respect to the Si/SiO_2 wafer and c) the MgO(20 Å)/FeCoB(20 Å)/Pt(gradient) sample system with in-plane magnetic anisotropy and SIA. The thickness of the layers is not represented to scale.

To grow the gradients, the desired material is deposited by sputtering "off-axis". This means that the center of the wafer is horizontally shifted towards the side of the deposition chamber by a set amount, depending on the desired gradient. In our case, the wafer is shifted by 50 mm. We then cut the wafer into equal strips, 3 mm by 26 mm in size, with their length perpendicular to the gradient (Figure 5.3), and use 4-point resistivity measurements to measure the resistance of the Pt. Figure 5.2 (b) shows the inverse of the resistance as a function of position on the wafer. Because of the horizontal shift (50 mm) and the flat edge of the wafer (5 mm), the thickest part of the gradient is found at 55 mm, while the thinnest is found at 150 mm (Figure 5.2 (b) inset). We then use values of the resistivity of on-axis deposited thick Pt layers, to calculate the corresponding thickness. The result is shown in Figure 5.2 (c). All the samples with Pt thickness gradients in our study are deposited in the same conditions. This means that fitting the thickness vs position curve for the reference layer gives us a fit function that we can use to calculate the thickness of the Pt layer, as a function of position, for all the samples.

To verify our calibration, we deposited several Pt layers of nominal thicknesses, and carried out 4-point resistance measurements on identical strips. Figure 5.2 (d) shows the inverse of the resistance as a function of calculated Pt thickness (black squares), alongside the inverse of the resistance as a function of Pt thickness for nominal sample stacks (red triangles). The plot shows good agreement between the two data sets, indicating that our method of calculating the thickness is correct.

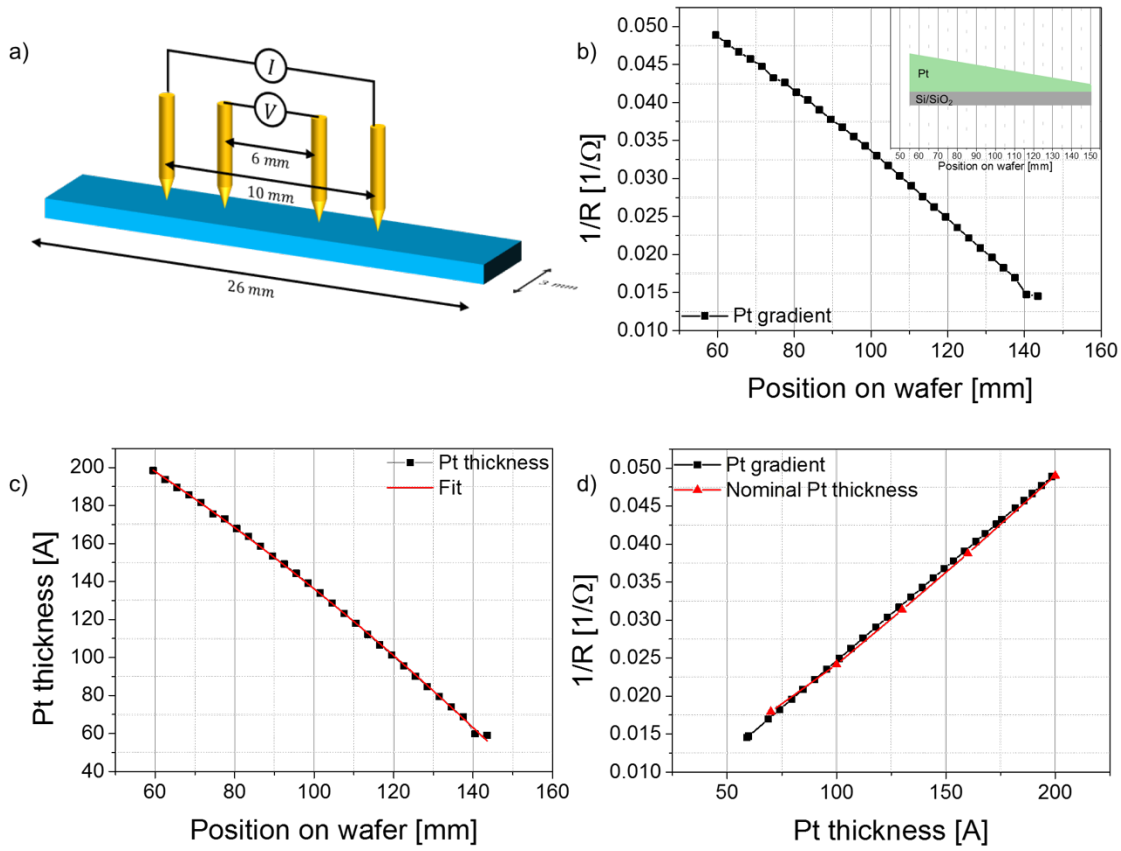

Figure 5.2: a) Schematic of the 4-point resistance measurement system along with the dimensions of the strips; b) The inverse of the resistance, $1/R$, as a function of position for the reference Pt layer; c) The calculated thickness of the reference Pt layer as a function of position. The red line represents the fit function; d) $1/R$ as a function of Pt thickness for the gradient (black squares) and for nominal samples (red triangles).

The $MgO_{(20)}/FeCoB_{(20)}/Pt_{(10\text{-}100)}$ layers are then cut in half, along the gradient. One half of the wafer is patterned into Hall cross devices, with both branches $5\ \mu m$ wide, as described in section 4.1. The other half is cut into identical strips, perpendicular to the gradient, as shown in Figure 5.3. For each line of devices, we have a corresponding strip, of equal Pt thickness, on which we perform VSM and 4-point resistance measurements.

The 10-100 Å Pt gradient was split between two different stacks: 10-40 Å and 30-100 Å. This allows us to verify the consistency of our findings, across different, independent sample stacks.

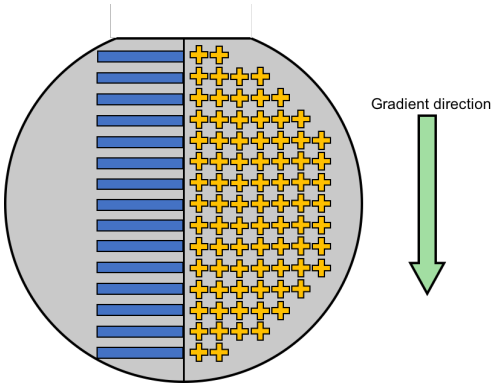

Figure 5.3: Schematic showing the two halves of the wafer, one patterned into Hall cross devices, and one cut into identical strips. Horizontal lines correspond to constant Pt thickness. Also shown is the direction of the thickness gradient. The devices and strips are not shown to scale.

Since our objective is to distinguish between bulk and interface effects as sources of SOTs, we also need to look at different interfaces. The first thing to do, is to place the Pt gradient beneath the FM. Doing so, we will no longer have an identical Pt/FM interface across the entire thickness gradient, because the structure of the Pt layer changes with its thickness. It also allows us to look at the importance of the position of the Pt layer (top vs bottom). For this, we have prepared $Pt_{(gradient)}/Co_{(20)}/Al_{(20)}$ samples, with in-plane magnetic anisotropy and SIA (Figure 5.4).

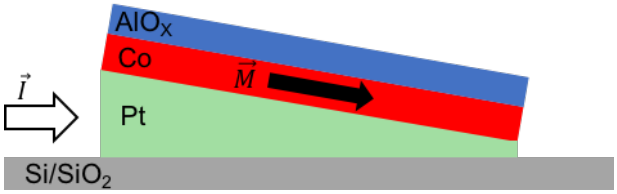

Figure 5.4: Schematic of the Pt(gradient)/Co(20 Å)/AlO_x(20 Å) sample system. The thickness of the layers is not represented to scale.

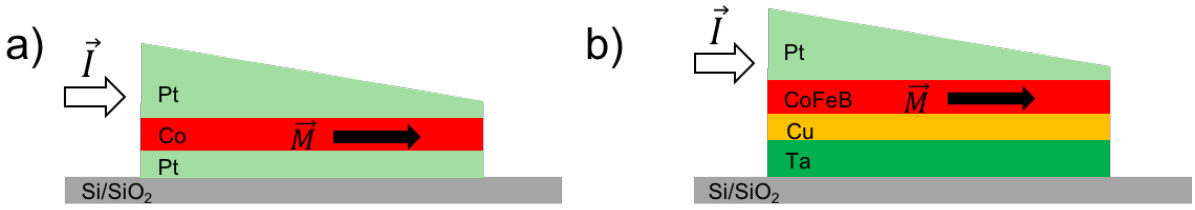

Figure 5.5: Schematics showing the a) $Pt_{(30)}/Co_{(20)}/Pt_{(gradient)}$ and b) $Ta_{(30)}/Cu_{(10)}/CoFeB_{(20)}/Pt_{(gradient)}$ with in-plane magnetic anisotropy and SIA. The thickness of the layers is not represented to scale.

Next, to study the evolution of the SOTs over a wider range of interfaces, we also studied $Pt_{(30)}/Co_{(20)}/Pt_{(gradient)}$ and $Ta_{(30)}/Cu_{(10)}/CoFeB_{(20)}/Pt_{(gradient)}$ samples (Figure 5.5). In the first case, the SIA is only due to the thickness variation of the Pt layer. It allows us to better isolate the effects of the thickness gradient on the SOTs. The second system serves to compare the effects of different bottom interfaces on the SOTs. The Ta buffer layer ensures good

quality growth of the Cu layer. However, because its resistivity is much larger than that of the Pt and Cu layers, it will not influence the SOTs.

In the following sections, we will present, and discuss, the results of our study of the electrical and magnetic properties as well as the evolution of the SOTs, for these sample systems.

5.2.2 Characterizing electric properties

To evaluate the effects of the Pt layer thickness on the SOTs, we first need to measure the resistivity of the samples. Knowing the resistivity as a function of Pt thickness allows us to calculate the current density in the Pt layer. We will later use this value to normalize the values of the SOTs in our samples, and compare the effects of different Pt thicknesses.

As in the previous case, we used 4-point resistance measurements on identical strips (Figure 5.3) to measure the resistance of our $MgO_{(20)}/FeCoB_{(20)}/Pt_{(10\text{-}100)}$ samples as a function of Pt thickness (Figure 5.6 (b)). The inverse of the resistance as a function of Pt thickness, shown in Figure 5.6 (c), allows us to calculate the resistivity, by taking into account that:

$$\frac{1}{R} = \frac{1}{R_0} + \frac{\omega t}{\rho L}$$

Equation 5.1

where L is the length of the measured strip (distance between inner contacts in Figure 5.2 (a)), ω the width of the strip (3 mm in our case), t the thickness of the Pt layer and ρ its resistivity. R_0 is the resistance of our stack, in the limit of an infinitely thin Pt layer. It therefore corresponds to the resistance of the $MgO_{(20)}/FeCoB_{(20)}$ stack.

Should the resistivity of the Pt layer be constant, the inverse of the resistance would show a linear dependence with thickness. However, as the Pt layer becomes thinner, conduction electrons suffer more collisions and scattering at the interfaces (Figure 5.6 (a)), and the resistivity increases. Truly, our measurements show that the resistance increases significantly at lower Pt thicknesses (Figure 5.6 (b)), which can be linked to an increase in resistivity. At the same time, we see that the $1/\mathrm{R}$ vs thickness plot is not linear (Figure 5.6 (c)). To take into account the evolution of the resistance we fit our data to a Fuchs-Sondheimer model [70], which, assuming that the thickness of the Pt layer is larger than the mean free path, λ, can be written as:

$$\rho(t) = \rho_0 \left(1 + \frac{3}{8}\frac{\lambda}{t}\right) L$$

Equation 5.2

which, replacing in Equation 5.1, gives us the fitting function:

$$\frac{1}{R} = \frac{1}{R_0} + \frac{\omega t}{\rho_0 \left(1 + \frac{3}{8}\frac{\lambda}{t}\right) L}$$

Equation 5.3

The fitted $1/\mathrm{R}$ vs thickness plot is shown in Figure 5.6 (d). The fitting parameters we obtain are $\rho_0 = 18.63\ \mu\Omega cm$, $\lambda = 11.8\ nm$ and $R_0 = 1\ k\Omega$. The $R_0 = 1\ k\Omega$ value corresponds to the $MgO_{(20)}$/$FeCoB_{(20)}$ bilayer of constant thickness. Next, we notice that the mean free path is larger than the thickness of the Pt layer, which can impact the fitting parameters obtained. However, our analysis still holds, since the model fits very well the experimental data. More so, the resistivity value, $\rho_0 = 18.63\ \mu\Omega cm$, is consistent with values reported in literature for similar Pt layers (between 10 and $20\ \mu\Omega cm$). Using the fitted parameters, we calculate the corresponding variation of the resistance and resistivity of the Pt layer as a function of its thickness. The results are shown in Figure 5.6 (e) and (f) respectively.

What the resistivity variation at low Pt thickness tells us, is that the SOT values, measured as a function of Pt thickness, need to be calculated as a function of current density in the Pt layer. A normalization in terms of the applied voltage would only be accurate in the case of constant resistivity or constant layer thickness. To calculate the current density in the Pt layer, as a function of thickness, we use the resistivity values calculated previously and the effective voltage applied on the sample. This effective voltage is calculated as the product between the measured resistance value and the injected current through the sample.

It is also worth noting the discontinuity in the measured values for the two gradients. As we will see further, this discontinuity is consistent with changes in the properties of the CoFeB layer, caused most likely during deposition. It is an indication that the CoFeB layer has a lower resistivity in the case of the second sample, perhaps due to better deposition of the layer. This hypothesis is confirmed by the lower R_0 value obtained for the second gradient (720 Ω).

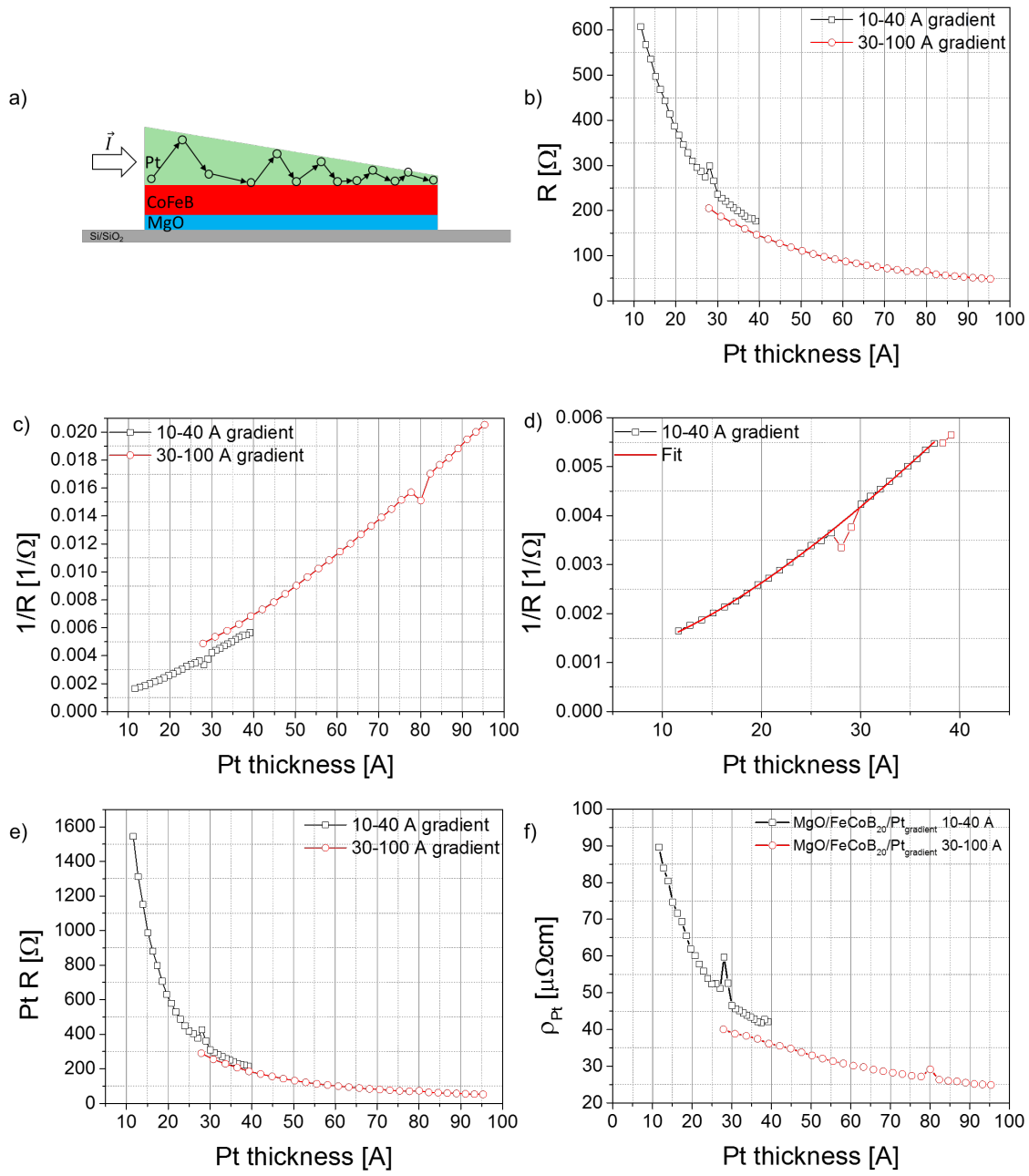

Figure 5.6: a) Schematic representation of the scattering of conduction electrons at the interfaces, for the Pt thickness gradient; 4-point measurements on $MgO_{(20)}/FeCoB_{(20)}/Pt_{(10\text{-}100)}$ samples, showing: b) Resistance measurements as a function of Pt layer thickness; c) Inverse of the resistance as a function of Pt layer thickness; d) Fuchs-Sondheimer model fit to the measured inverse resistance as a function of Pt layer thickness; e) Calculated resistance values of the Pt layer as a function of its thickness; f) Calculated Pt layer resistivity as a function of its thickness.

Next, we performed a similar analysis on the $Pt_{(gradient)}/Co_{(20)}/Al_{(20)}$ samples. Figure 5.7 shows 4-point resistance measurements and inverse resistance as a function of bottom Pt layer thickness. For the bottom Pt gradient, the inverse resistance plot does not show any significant deviations from linearity, like in the case of the top Pt layer. Fitting the data (Figure 5.7 (b)) with Equation 5.1, we obtain $\rho_0 = 26.45\ \mu\Omega cm$ and $R_0 = 746\ \Omega$

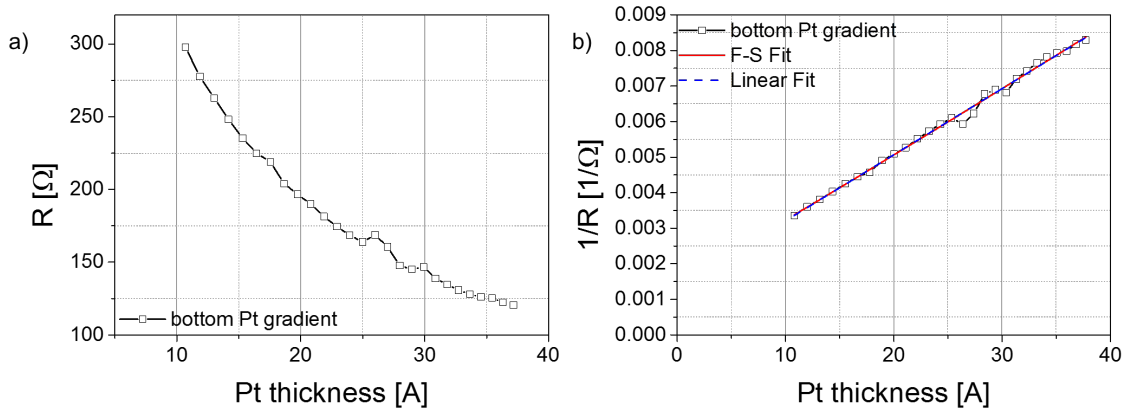

Figure 5.7: a) Resistance measurements as a function of Pt layer thickness for Pt(gradient)/Co(20 Å)/AlO_X(20 Å) samples; b) Inverse of the resistance as a function of Pt layer thickness for Pt(gradient)/Co(20 Å)/AlO_X(20 Å) samples. The solid lines represent fits to the experimental data.

This appears to support the conclusion that, in the case of the bottom gradient, the resistivity of the Pt layer is constant as a function of its thickness.

But the resistivity of the Co layer is much closer to that of the Pt layer than the resistivity of the CoFeB was in the previous samples. This means that changes in the resistivity of the Co layer will have a bigger impact on the overall resistivity of the device for Pt/Co layers, than changes in CoFeB resistivity had for CoFeB/Pt devices. The Co layer, having a nominal thickness of 20 Å, is deposited "on-axis". As a result, the thickness of the layer is smaller towards the edges of the wafer. This results in a decrease in the resistivity of the devices located towards the edges of the wafer. On the other hand, the resistivity of the Pt layer increases with decreasing thicknesses. Now, the two effects can balance each other, resulting in what appears to be a linear dependence of $1/R$ with the thickness of the Pt layer. This questions the assumption that the resistivity of the Pt layer is constant.

In order to account for this, we used 4-point resistance measurements to follow the evolution of the resistivity as a function of the position on the wafer, for various thin films of constant thickness, deposited "on-axis". In such a way, the variations in resistivity are only due to the variation of the layer thickness towards the edges of the wafer. We have indeed found that, this thickness variation results in a measurable variation of the resistance, that can be fitted with a simple polynomial function (Figure 5.8 (a)). Since this variation is isotropic, we use the fitting function to correct the resistivity measurements along the Pt gradient in our samples. Figure 5.8 (b) shows the inverse resistance as a function of the bottom Pt layer thickness, for the $Pt_{(gradient)}/Co_{(20)}/AlO_{X(20)}$ samples, after applying the correction. We see that the inverse resistance plot is no longer linear, and closely resembles the behavior of the top

Pt gradient. This is an indication that, like for the samples with a top Pt gradient, the resistivity of the Pt is not constant. We then fit the data with Equation 5.3 (red line in Figure 5.8 (b)), and obtain the fitting parameters $\rho_0 = 17.83\ \mu\Omega cm$, $R_0 = 340\ \Omega$ and $\lambda = 8.7\ nm$, consistent with the values obtained for the $MgO_{(20)}/FeCoB_{(20)}/Pt_{(gradient)}$ samples. The lower R_0 value we obtain for the bottom gradient can be explained by the much lower resistivity of the Co/Al bilayer than that of the MgO/FeCoB.

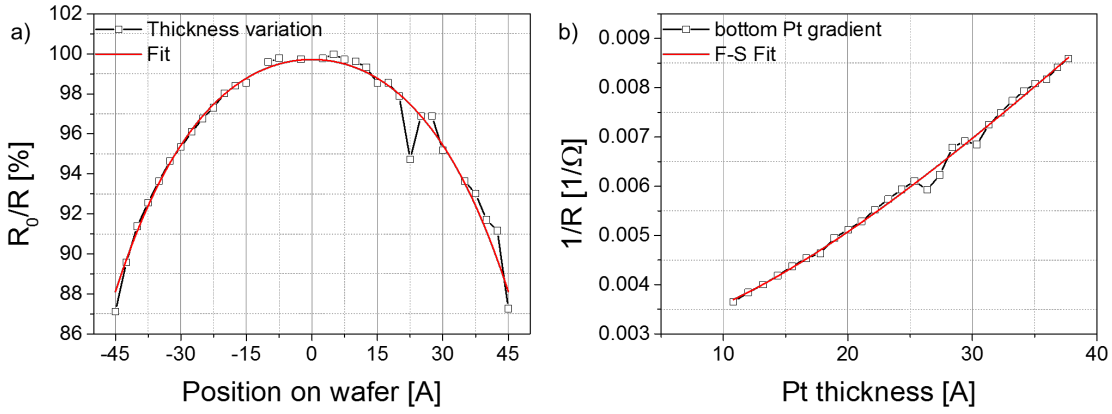

Figure 5.8: a) Variation of the resistance as a function of distance from the center of the wafer, caused by the thickness decrease towards the edges of the wafer. The curve was measured on a W layer with a thickness value of 700 Å at the center. b) Inverse of the resistance as a function of Pt layer thickness for $Pt_{(gradient)}/Co_{(20)}/AlO_{x(20)}$ samples after correcting for the variations induced by the variation of the Co layer thickness towards the edges of the wafer. The solid lines represent fits to the experimental data.

The amplitude of the correction is chosen so as, for high Pt thicknesses (above 25 Å), the inverse resistance data points are all linear as a function of Pt thickness (Figure 5.9).

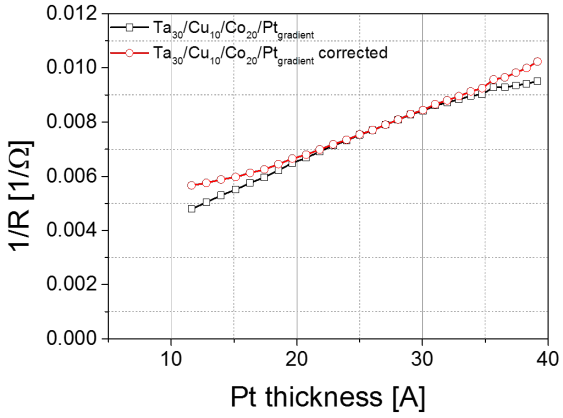

Figure 5.9: Inverse of the resistance as a function of Pt layer thickness for $Ta_{(30)}/Cu_{(10)}/Co_{(20)}/Pt_{(gradient)}$ samples, before and after correcting for the variations induced by the variation of the Co layer thickness towards the edges of the wafer (black squares and red circles respectively). For the corrected data set, for high Pt thicknesses (above 25 Å), the inverse resistivity data points are all linear as a function of Pt thickness.

The inverse resistance as a function of Pt thickness, for $Ta_{(30)}/Cu_{(10)}/CoFeB_{(20)}/Pt_{(gradient)}$, $Ta_{(30)}/Cu_{(10)}/Co_{(20)}/Pt_{(gradient)}$, $Ta_{(30)}/Cu_{(20)}/Co_{(20)}/Pt_{(gradient)}$ and $Pt_{(30)}/Co_{(20)}/Pt_{(gradient)}$ is shown in

Figure 5.10 (a) and (b). After applying the same correction, we once again arrive at the thickness dependent resistivity of the Pt layer, following a Fuchs-Sondheimer model. The fitting parameters, obtained by fitting the data with Equation 5.3 are summarized in Table 2. The fitting parameters are very sensitive to the value of R_0, which in turn is determined by the resistivity values at low Pt thicknesses. For the $Pt_{(30)}/Co_{(20)}/Pt_{(gradient)}$ samples these points proved more difficult to fit, therefore we have fitted the data for two different R_0 values to provide an upper and lower boundary for ρ_0 and λ.

Sample stack	ρ_0 $[\mu\Omega cm]$	R_0 $[\Omega]$	λ $[nm]$
$Ta_{(30)}/Cu_{(10)}/CoFeB_{(20)}/Pt_{(gradient)}$	18.5	374.5	9.1
$Ta_{(30)}/Cu_{(10)}/Co_{(20)}/Pt_{(gradient)}$	18.5	206	10.1
$Ta_{(30)}/Cu_{(20)}/Co_{(20)}/Pt_{(gradient)}$	19.3	117	7.7
$Pt_{(30)}/Co_{(20)}/Pt_{(gradient)}$	18.9 - 22.9	117 - 120	6.1 - 10.1

Table 2: Fitting parameters for the inverse resistivity as a function of Pt thickness, for $Ta_{(30)}/Cu_{(10)}/CoFeB_{(20)}/Pt_{(gradient)}$, $Ta_{(30)}/Cu_{(10)}/Co_{(20)}/Pt_{(gradient)}$, $Ta_{(30)}/Cu_{(20)}/Co_{(20)}/Pt_{(gradient)}$ and $Pt_{(30)}/Co_{(20)}/Pt_{(gradient)}$ samples, before and after oxidation, obtained using a Fuchs-Sondheimer model.

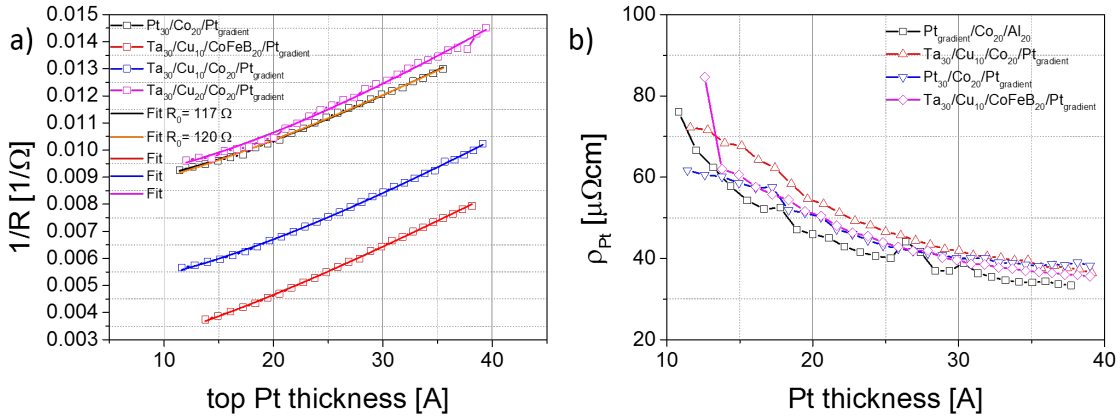

Figure 5.10: a) Inverse of the resistance as a function of Pt layer thickness for $Ta_{(30)}/Cu_{(10)}/CoFeB_{(20)}/Pt_{(gradient)}$, $Ta_{(30)}/Cu_{(10)}/Co_{(20)}/Pt_{(gradient)}$, $Ta_{(30)}/Cu_{(20)}/Co_{(20)}/Pt_{(gradient)}$ and $Pt_{(30)}/Co_{(20)}/Pt_{(gradient)}$ samples after correcting for the variations induced by the change in layer thickness towards the edges of the wafer. The solid lines represent fits to the experimental data; b) Corresponding Pt resistivity.

Analyzing the electrical properties of our samples reveals a very important aspect. The fact that the resistivity of the Pt layer is not constant, but rather thickness dependent, means that, if we want to normalize the SOT values by the current density, simply normalizing the SOT values by the value of the injected current, or even the applied voltage, may not give an accurate picture of the thickness dependence of the Damping-Like and Field-Like torques. In

both situations, regardless of the position of the Pt layer or the FM/Pt interface, the conclusion that can be drawn is the same:

i) The current density responsible for the generation of the SOTs is not as straight forward to evaluate, and the thickness dependence of the resistivity has to be taken into account.

ii) Depending on the fabrication process, it is possible that the thickness dependence of the resistivity of the Pt layer can be masked by other effects that can impact the resistivity measurements. In our case, we have shown that towards the edges of the wafer we encounter variations in the thickness of the layers, that have a significant influence on the resistivity measurements. By measuring these variations independently, and taking their effect into account, we can recover the thickness dependence of the resistivity of the Pt layer.

5.2.3 Evolution of SOTs with Pt thickness

5.2.3.1 SHE hypotheses

Using the method described in Chapter 4, we measured the evolution of the Damping-Like and Field-Like SOTs as a function of Pt thickness. In order to be able to compare the amplitudes of the measured torques across samples, it is essential to normalize the measured values. First, we will look at the SOTs in terms of amplitude per unit of applied electric field, E. Figure 5.11 shows the Damping-Like (a) and Field-Like (b) effective fields normalized by unit of applied electric field, as a function of Pt thickness, for $MgO_{(20)}/FeCoB_{(20)}/Pt_{(10\text{-}100)}$ samples. As the Pt thickness decreases, so does the amplitude of the Damping-Like effective field. The Field-Like effective field starts from positive values (in our sign convention) and changes sign for Pt thicknesses below 50 Å. This indicates that the Field-Like and the Oersted field generated by the charge current in the Pt layer have opposite signs. The reason for the Oersted field's influence of the Field-Like effective field measurements is that the two have the same symmetry, making it very difficult to separate during the measurement.

Generally, we have:

$$B_{Oe} = -\frac{\mu_0 (I_{Pt} - I_{bottom})}{2\omega}$$

Equation 5.4

where I_{Pt} is the current through the top Pt layer, I_{bottom} is the current through the bottom layers (below the FM layer) and ω is the width of the Hall cross branch through which the current is injected. Equation 5.4 assumes an infinite current strip. In the case of $MgO_{(20)}/FeCoB_{(20)}/Pt_{(10\text{-}100)}$ samples, I_{bottom} can be considered negligible due to the very high resistivity of the MgO and FeCoB layer. Therefore the Oersted field is only due to I_{Pt}. Figure 5.11 (c) shows the Field-Like effective with the Oersted contribution subtracted. The corrected Field-Like effective field shows a decrease in amplitude at low the Pt thicknesses, and no longer changes its sign.

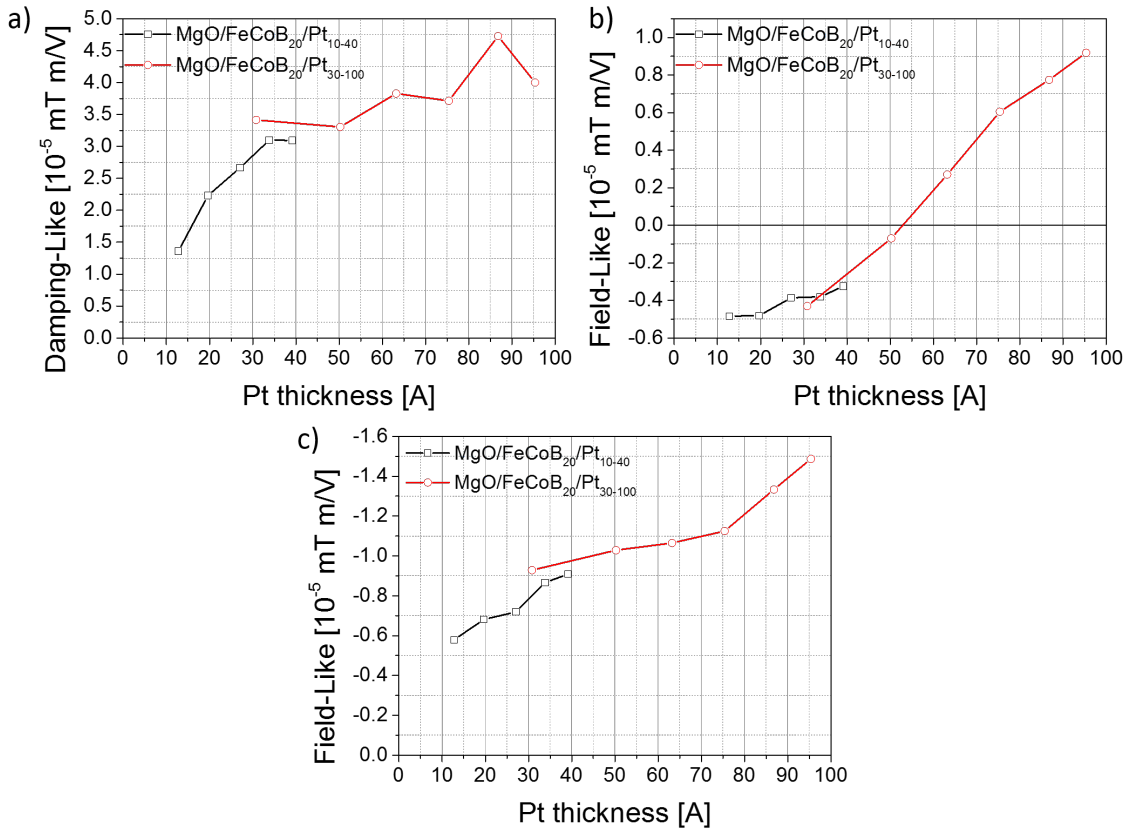

Figure 5.11: Damping-Like (a) and Field-Like (b) effective fields per unit of applied electric field, as a function of Pt thickness; c) Field-Like effective field with the Oersted field contribution subtracted, per unit of applied electric field, as a function of Pt thickness. The data is for $MgO/FeCoB_{(20)}/Pt_{(gradient)}$ samples.

As an exercise, we can use the measured PHE resistance values to verify the torque measurement. According to Onsager's reciprocal theorem to our system, the Damping-Like torque will create an additional "backflow" current component, I_b, proportional to the Damping-Like torque and parallel to the current that created the torque, similarly to the SMR (Spin Hall Magnetoresistance) effect [149], [150]. Now, whenever we perform electric current measurements in thin films with spin orbit interaction, this additional current contribution is always present, influencing the effective resistance of the HM layer (Pt in our case).

For CoFeB and FeCoB-based samples, the AMR contribution to the PHE is negligible, but not so for Co-based samples (due to their lower resistivity). The only remaining contribution to the PHE is therefore from the I_b creating a "torque magnetoresistance". We can thus express the total voltage as $V = I_{Pt}R + I_bR$, where R is the longitudinal resistance. In terms of the PHE resistance, the total voltage is given by $V = I_{Pt}R + I_{Pt}R_{PHE}$. Equating the two equations, and normalizing by the square of the longitudinal resistance, we get $\frac{I_b}{V_{eff}} = \frac{R_{PHE}}{R^2}$. Based on our assumption that I_b is proportional to the Damping-Like torque, our analysis translates to:

$$\frac{H_D}{E} \propto \frac{R_{PHE}}{R^2}$$

Equation 5.5

where H_D is the Damping-Like effective field and E is the applied electric field.

Figure 5.12 plots the amplitude of the Damping-Like effective field per unit of applied electric field, as a function of Pt thickness, together with the PHE resistance divided by the square of the longitudinal resistance. Their respective evolutions are exactly the same, to a proportionality factor, α, as expected from Equation 5.5, further confirming the correctness of our torque measurement.

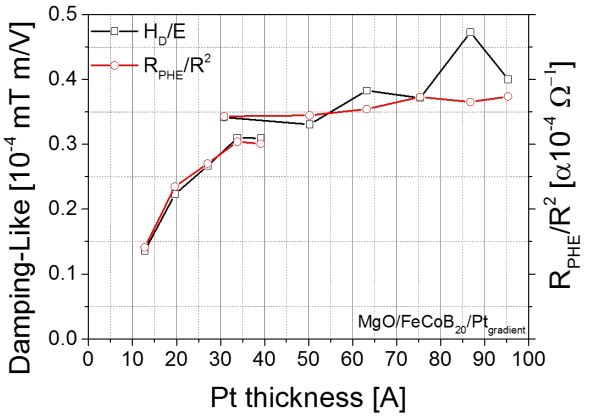

Figure 5.12: Damping-Like effective fields per unit of applied electric field (black squares) and the PHE resistance divided by the square of the longitudinal resistance (red circles), as a function of Pt thickness, for MgO/FeCoB$_{(20)}$/Pt$_{(gradient)}$.

Measurements on Pt/Co-based samples, albeit with PMA, reported by Nguyen *et. al.* in [151], show a similar behavior of the Damping-Like and Field-Like effective fields per unit of applied electric field as a function of Pt thickness. The evolution of the Damping-Like torque is shown in Figure 5.13 (a). The model proposed is based on assuming that the SHE is the only source for the Damping-Like torque, and analyzing the efficiency of the SOTs per unit of

applied electric field, $\xi_{DL}^{E}(t_{Pt}) = \frac{2e}{\hbar}\mu_0 M_S t_{FM}\frac{H_{DL}}{E}$, as a function of Pt thickness, which, in this model, is given by the functional form [151]:

$$\xi_{DL}^{E}(t_{Pt}) = \frac{2e}{\hbar}\sigma_{SH}\left[1 - \operatorname{sech}\left(\frac{t_{Pt}}{\lambda_{sf}}\right)\right]\left(1 + \frac{\tanh\left(\frac{t_{Pt}}{\lambda_{sf}}\right)}{2\lambda_{sf}\rho_{Pt}G_r}\right)^{-1}$$

Equation 5.6

where t_{Pt} is the Pt thickness, t_{FM} is the FM layer thickness, M_S is the saturation magnetization, E is the applied electric field, H_{DL} the measured amplitude of the Damping-Like effective field, σ_{SH} is the spin-hall conductivity, ρ_{Pt} is the resistivity of the Pt layer, λ_{sf} is the spin diffusion length and G_r is the real part of the spin mixing conductance. Using Equation 5.6, with theoretically calculated values of G_r and a fixed value of ρ_{Pt} corresponding to the resistivity of the bulk Pt, the authors are able to calculate $\lambda_{sf} = (2 \pm 0.1)\, nm$ and $\sigma_{SH} = (10.5 \pm 0.3)\times 10^5 \frac{\hbar}{2e}\Omega^{-1}m^{-1}$. Going beyond the constant ρ_{Pt} approximation, and taking into account the resistivity's dependence on t_{Pt}, the λ_{sf} given by the authors is just a lower boundary of the λ_{sf} value in the bulk of the Pt film.

We test our data against this model by applying the same analysis on our systems. Figure 5.13 (b) shows the efficiency of the Damping-Like effective field per unit of applied electric field, $\xi_{DL}^{E}(t_{Pt})$, as a function of Pt thickness, for $MgO_{(20)}/FeCoB_{(20)}/Pt_{(10\text{-}100)}$ samples, fitted with Equation 5.6. The effective spin diffusion length that we obtain is smaller, $\lambda_{sf} = 1.15\, nm$, and the spin hall conductivity is $\sigma_{SH} = 8.4 \times 10^{-5}\frac{\hbar}{2e}\Omega^{-1}m^{-1}$. We note that the theoretical model proposed is able to fit our experimental data, especially at low Pt thicknesses. However, at large Pt thicknesses, the model becomes less accurate.

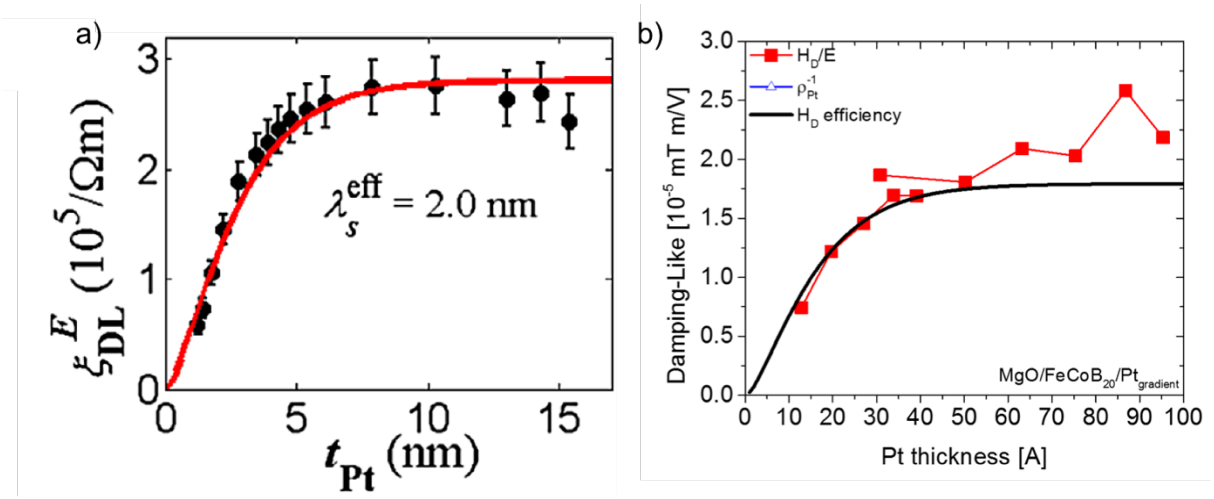

Figure 5.13: a) Damping-Like torque per unit of applied electric field (black squares) as a function of Pt thickness for $Ta_{(10)}/Pt_{(gradient)}/Co_{(10)}/MgO_{(20)}/Ta_{(10)}$. The solid red line represents the fit to *Equation 5.6* from which the effective spin diffusion length and spin conductivity parameters are calculated. From [151]. b) Damping-Like torque per unit of applied electric field (red squares) as a function of Pt thickness for $MgO/FeCoB_{(20)}/Pt_{(gradient)}$. The solid black line represents the fit to *Equation 5.6* from which the effective spin diffusion length and spin conductivity parameters are calculated.

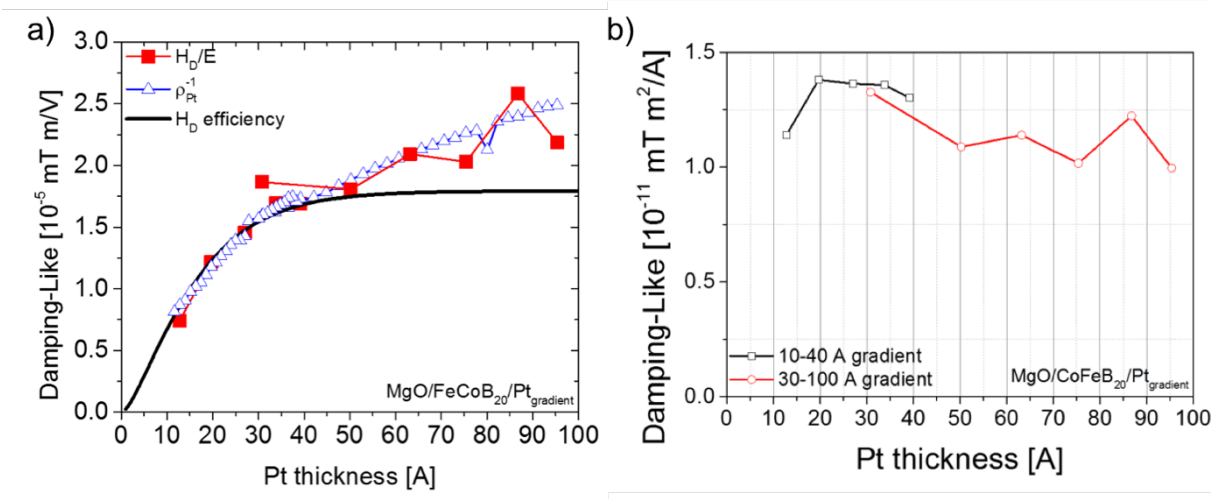

Figure 5.14: a) Damping-Like torque per unit of applied electric field (red squares) as a function of Pt thickness for $MgO/FeCoB_{(20)}/Pt_{(gradient)}$. The solid black line represents the fit to *Equation 5.6* from which the effective spin diffusion length and spin conductivity parameters are calculated. Blue triangles represent the inverse of the resistivity of the Pt layer, multiplied by a proportionality factor. b) Damping-Like torque per unit of applied current density as a function of Pt thickness for $MgO/FeCoB_{(20)}/Pt_{(gradient)}$.

An alternative way of analyzing the evolution of the Damping-Like effective field per unit of applied electric field as a function of Pt thickness, is to consider this evolution in terms of the current density through the Pt layer. This makes sense, since it is only the current density through the Pt layer that is responsible for the SOTs. The blue triangles in Figure 5.14 (a) represent the inverse of the resistivity of the Pt layer, multiplied by a proportionality constant, which accurately describes the evolution of the Damping-Like effective field, even at large Pt thicknesses, indicating that the torque scales exactly as the current density in the Pt layer. This means that the Damping-Like effective field per unit of current density should

be constant with respect to the thickness of the Pt layer, which indeed is the case, as shown in Figure 5.14 (b).

Such a behavior is not consistent with a SHE hypothesis. Now, we have to ask the following question: is this a coincidence or is this behavior systematic? To verify this, we perform this analysis on samples with different HM/FM/NM interfaces. Figure 5.15 shows the Damping-Like (a) and Field-Like (b) effective fields normalized by unit of applied electric field, as a function of Pt thickness, for $Ta_{(30)}/Cu_{(10)}/CoFeB_{(20)}/Pt_{(gradient)}$, $Ta_{(30)}/Cu_{(10)}/Co_{(20)}/Pt_{(gradient)}$, $Ta_{(30)}/Cu_{(20)}/Co_{(20)}/Pt_{(gradient)}$, $Pt_{(gradient)}/Co_{(20)}/Al_{(20)}$ and $Pt_{(30)}/Co_{(20)}/Pt_{(gradient)}$ samples. Globally, the dependence of the Damping-Like and Field-Like effective fields is the same across all samples. The amplitude of both effective fields decreases with decreasing Pt thickness and does not saturate at large t_{Pt} values (within the thickness interval studied). In the particular case of the $Pt_{(30)}/Co_{(20)}/Pt_{(gradient)}$ samples (pink triangles), due to the contribution to the SOTs from both the top and bottom Pt gradients, we see the presence of an offset in our data. The offset corresponds to the Damping-Like and Field-Like effective field value at 30 Å (where both top and bottom Pt layers have the same thickness and the torque contributions from each layer will cancel each other out). Another important point regarding the Field-Like measurements in Ta/Cu-based samples is that, because a non-negligible part of the injected current will flow through the Cu layers, I_{bottom}, there will be an additional component to the Oersted field (as described by Equation 5.4). Since we have not measured I_{bottom}, this means that the measured values are accurate in the limit of a constant offset. We also note that in the case of Co-based samples, the Field-Like effective field dependence is the same for both 10 and 20 Å Cu buffer layers (blue triangles and red circles in Figure 5.15 respectively), in the limit of an offset. This is an important point, as the only difference between the samples is the thickness of the Cu layer, and therefore the Oersted field contribution from the Cu layer. Now, since the Oersted field from the Cu layer is constant with the applied voltage, this indeed means that the only difference in the Pt thickness dependence of the Field-Like effective field for the two samples should be a constant offset. This behavior confirms that the current through the Pt layer, I_{Pt}, is correctly calculated.

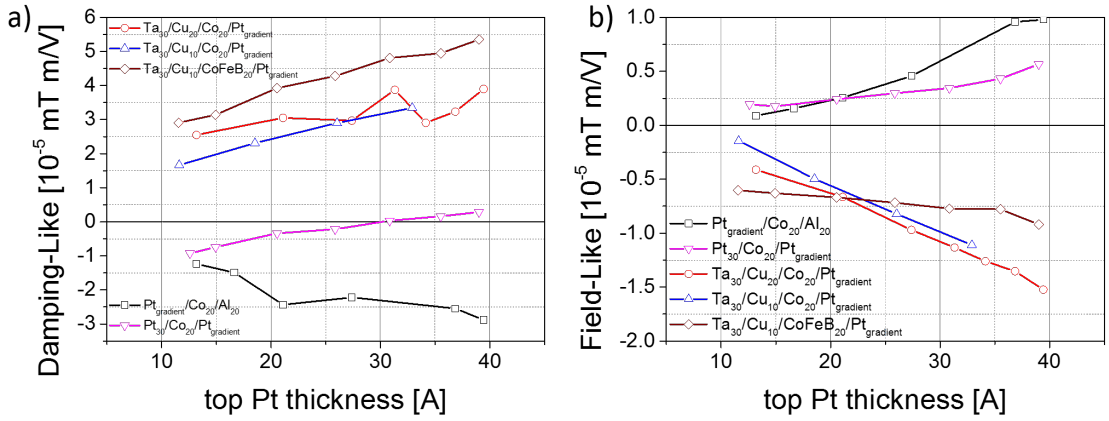

Figure 5.15: Damping-Like (a) and Field-Like (b) effective fields per unit of applied electric field, as a function of Pt thickness, for $Ta_{(30)}/Cu_{(10)}/CoFeB_{(20)}/Pt_{(gradient)}$, $Ta_{(30)}/Cu_{(10)}/Co_{(20)}/Pt_{(gradient)}$, $Ta_{(30)}/Cu_{(20)}/Co_{(20)}/Pt_{(gradient)}$, $Pt_{(gradient)}/Co_{(20)}/Al_{(20)}$ and $Pt_{(30)}/Co_{(20)}/Pt_{(gradient)}$ samples. The Field-Like effective field is corrected for the Oersted field contribution.

We performed the same verification of the correctness of the torque measurement by again plotting the amplitude of the Damping-Like effective field per unit of applied electric field, as a function of Pt thickness, together with the PHE resistance divided by the square of the longitudinal resistance, for $Ta_{(30)}/Cu_{(10)}/CoFeB_{(20)}/Pt_{(gradient)}$, and, as before, we observe a complete agreement between the two dependencies (Figure 5.16). Because of the much lower resistance of the Co, compared to the CoFeB and FeCoB layers, and the presence of a larger AMR, which also creates PHE, we cannot make the same analysis for Co-based samples.

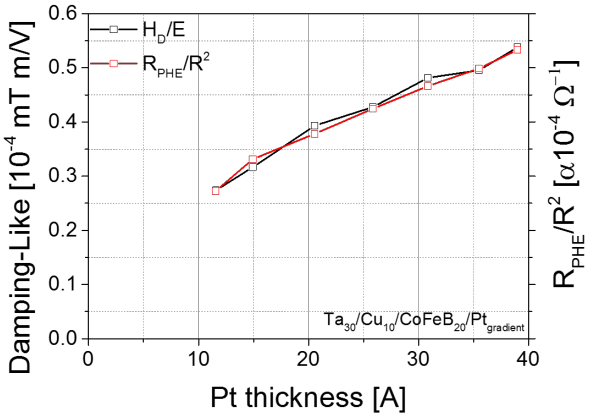

Figure 5.16: Damping-Like effective fields per unit of applied electric field (black squares) and the PHE resistance divided by the square of the longitudinal resistance (red circles), as a function of Pt thickness, for $Ta_{(30)}/Cu_{(10)}/CoFeB_{(20)}/Pt_{(gradient)}$.

Figure 5.17 shows $\xi_{DL}^{E}(t_{Pt})$ fitted to Equation 5.6, while λ_{sf} and σ_{SH}, calculated as best fit parameters, are shown in Table 3. We see that the SHE-like model, Equation 5.6, can somewhat fit the experimental data. However, this type of curve has enough fit parameters to be fitted to almost any experimental observation.

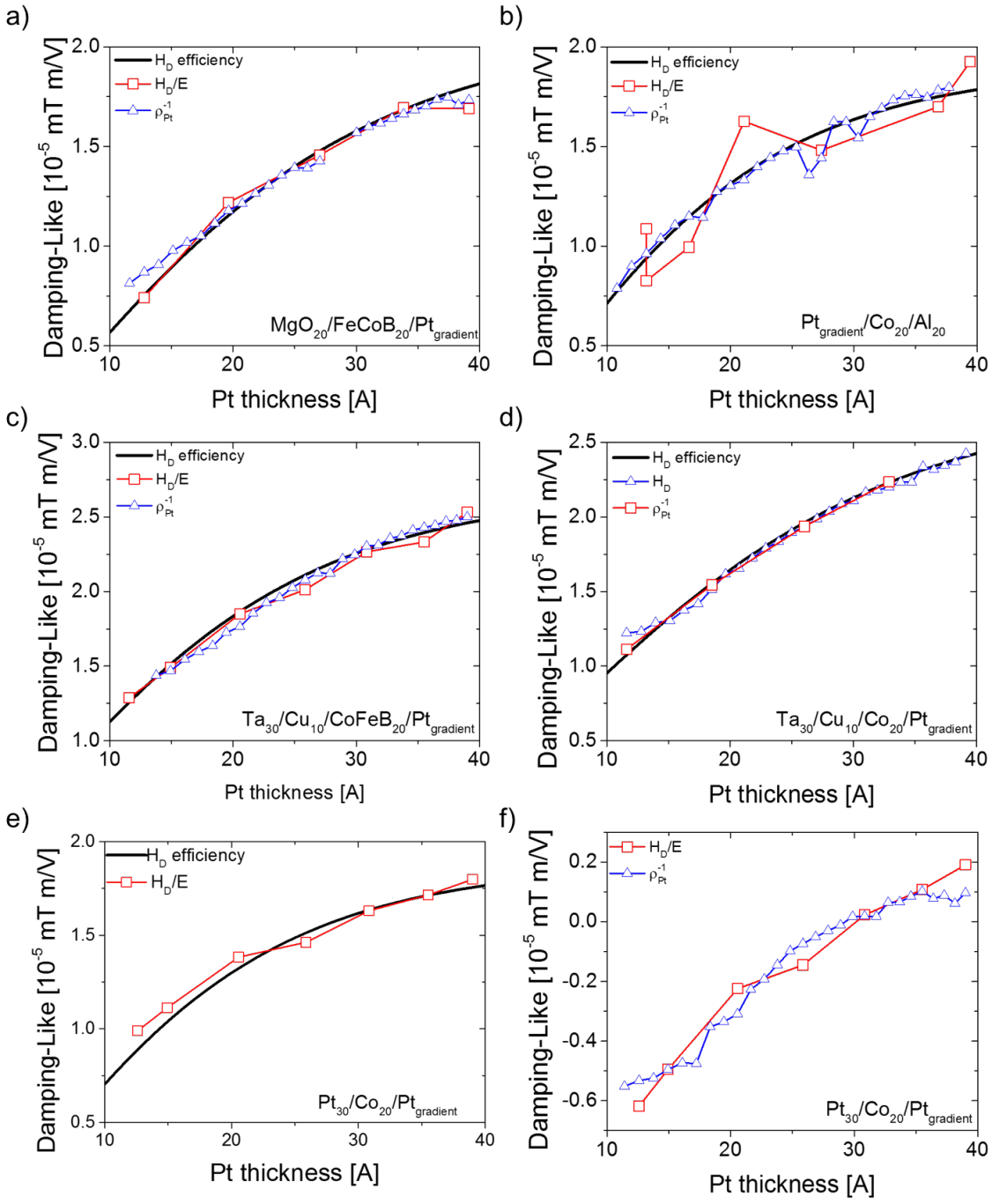

Figure 5.17: Damping-Like per unit of applied electric field (red squares) as a function of Pt thickness for a) $MgO/FeCoB_{(20)}/Pt_{(gradient)}$ (red squares), b) $Pt_{(gradient)}/Co_{(20)}/Al_{(20)}$ (red squares), c) $Ta_{(30)}/Cu_{(10)}/CoFeB_{(20)}/Pt_{(gradient)}$ (red squares), d) $Ta_{(30)}/Cu_{(10)}/Co_{(20)}/Pt_{(gradient)}$ (red squares), e) and f) $Pt_{(30)}/Co_{(20)}/Pt_{(gradient)}$ samples. The solid black lines represent the fits to *Equation 5.6* from which the effective spin diffusion length and spin conductivity parameters are calculated. Blue triangles represent the inverse of the resistivity of the Pt layer, multiplied by a proportionality factor.

As before, the blue triangles in Figure 5.17 represent the inverse of the resistivity in the Pt layer, multiplied by a proportionality constant. In all cases, the inverse of the resistivity of the Pt layer accurately describes the evolution of the Damping-Like effective field, up to a proportionality factor. This proportionality factor is the only fit parameter that changes from sample to sample. It indicates that, in all cases, the Damping-Like effective field scales exactly

as the current density in the Pt layer. Fitting the experimental data in this way only involves a single free fit parameter, unlike the SHE picture which involves many adjustable parameters, $\lambda_{sf}, \sigma_{SH}, \rho_{Pt}, G^{\uparrow\downarrow}$, that allow to change the shape of the curve. To illustrate this, Table 3 shows the SHE-model fit parameters calculated as best fit parameters for our samples. Firstly, σ_{SH} (spin-hall conductivity) should be constant, since all the samples are Pt-based. However, σ_{SH} as best fit parameter varies from sample to sample. Secondly, λ_{sf} (spin diffusion length) also shows a variation of up to 30% from sample to sample, even if all the samples are Pt-based. Together, these too parameters give the shape of the fit-curve, and to some degree can compensate each other, thus weakening the quality of the fit. Thirdly, $G^{\uparrow\downarrow}$ (spin mixing conductance), although an interface dependent parameter, does not show any variation with different interfaces. This points towards incompatibilities with the established SHE-model. At the same time, we observe that the Damping-Like torque per unit of applied current density is constant with the thickness of the Pt layer, down to 1 nm, for all samples, both for top and bottom Pt layers.

Sample Stack	λ_{sf} $[nm]$	σ_{SH} $[\times 10^{-5} \frac{\hbar}{2e} \Omega^{-1} m^{-1}]$	$G^{\uparrow\downarrow}$ $[\times 10^{15}\ \Omega^{-1} m^{-2}]$	C $[\times 10^{-6}]$
$MgO_{20}/FeCoB_{20}/Pt_{10\text{-}100}$	1.5	8	0.59	7.3
$Pt_{gradient}/Co_{20}/Al_{20}$	1.15	8.5	0.59	6
$Pt_{30}/Co_{20}/Pt_{gradient}$	1.15	8.8	0.59	6.5
$Ta_{30}/Cu_{10}/CoFeB_{20}/Pt_{gradient}$	1.3	9.8	0.59	7.3
$Ta_{30}/Cu_{10}/Co_{20}/Pt_{gradient}$	1.6	9	0.59	7.3

Table 3: Effective spin diffusion length and spin conductivity parameters, for $MgO_{(20)}/FeCoB_{(20)}/Pt_{(10\text{-}100)}$, $Ta_{(30)}/Cu_{(10)}/CoFeB_{(20)}/Pt_{(gradient)}$, $Ta_{(30)}/Cu_{(10)}/Co_{(20)}/Pt_{(gradient)}$ $Pt_{(30)}/Co_{(20)}/Pt_{(gradient)}$ and $Pt_{(gradient)}/Co_{(20)}/Al_{(20)}$ samples, calculated from the corresponding fits to *Equation 5.6*.

In this section, we explored a hypothesis based on considering the SHE as the only source of the Damping-Like torque. We have seen however, that our experimental data cannot be accurately described by such a model. In the following section, we will look at a different hypothesis, that takes into account interface effects, such as the Rashba Effect or interfacial SHE, as sources of Damping-Like torque.

5.2.3.2 Interface effects hypothesis

As we have shown in the previous section, the Damping-Like torque per unit of applied current density remains constant with decreasing thickness of the Pt layer (Figure 5.14 (b) and

Figure 5.18 (a)). This is compatible with the theoretical model proposed by Stiles *et. al.* [152] for SOTs originating in the Rashba Effect (Figure 5.18 (c)). Plotting the amplitude of the SOTs per unit of applied current density in the Pt layer, as a function of Pt thickness, shows that the data no longer follows a SHE model (Figure 5.18 (d)).

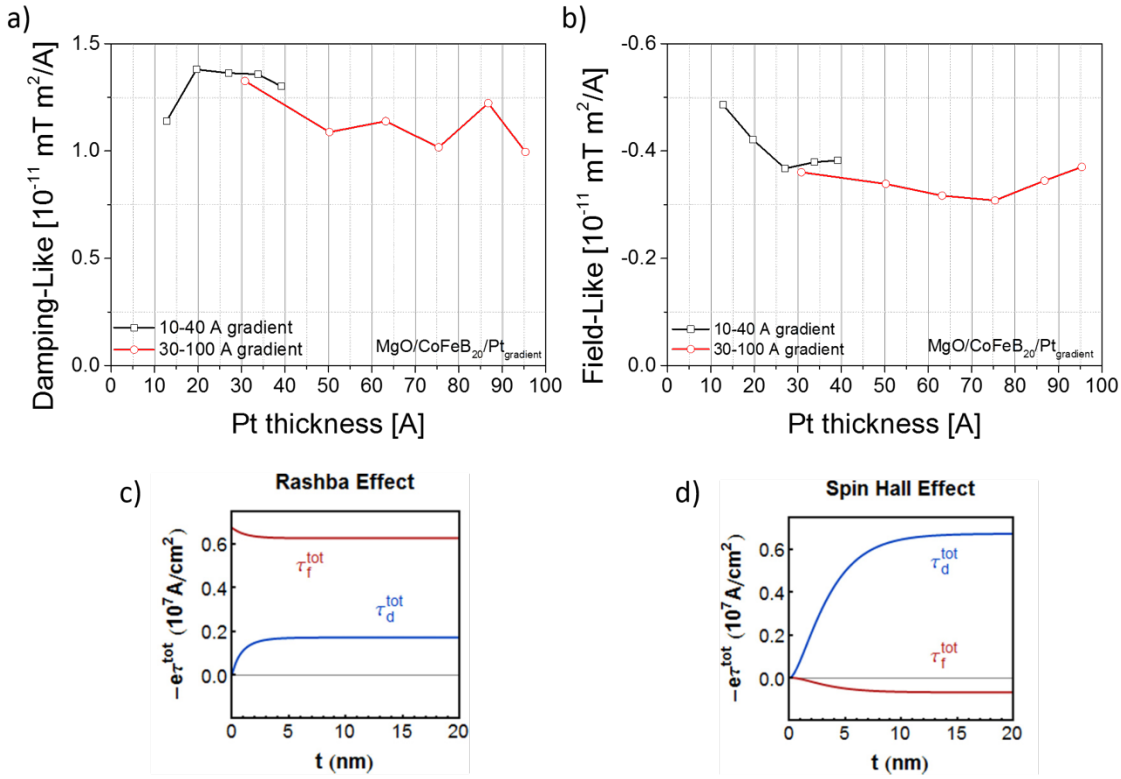

Figure 5.18: a) Damping-Like effective field as a function of Pt layer thickness, normalized by current density in the Pt layer; b) Field-Like effective field as a function of Pt layer thickness, normalize by the same current density; c) Theoretical model for the Damping-Like (blue lines) and Field-Like (red lines) torques per unit of current density, as a function of heavy-metal thickness, originating in the Rashba Effect and d) in the bulk SHE. From [152].

The Damping-Like effective field values corresponding to the second gradient (red circles in Figure 5.18 (a)), are lower. Because the Pt gradient is spread across two different wafers, this can be associated to differences in the properties of the FM layer, such as R_0 and H_{dem} (Figure 7.1 (b)).

The Field-Like effective field normalized by the current density in the Pt layer, with the correction for the Oersted field applied, is shown in Figure 5.18 (b).

Figure 5.18 (c) and (d) show the theoretically calculated evolution of the Damping-Like and Field-Like torques per unit of current density, as a function of HM thickness, originating in the Rashba Effect and bulk SHE respectively [152]. In (d) we find once again the expected behavior of the SOTs as originating only in the SHE, with both Damping-Like and Field-Like

decreasing rapidly at low Pt thicknesses, below 10 Å, and saturating at larger Pt thicknesses, as described by Equation 5.6, and in disagreement with our experimental data.

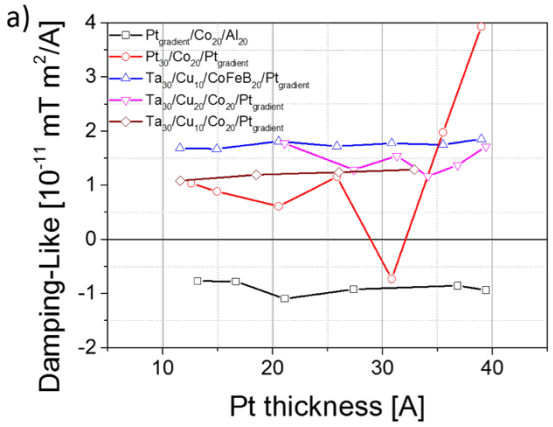

Figure 5.19: a) Damping-Like effective field, as a function of Pt thickness, for $Pt_{(gradient)}/Co_{(20)}/Al_{(20)}$ (black squares), $Ta_{(30)}/Cu_{(10)}/CoFeB_{(20)}/Pt_{(gradient)}$ (blue triangles) and $Pt_{(30)}/Co_{(20)}/Pt_{(gradient)}$ (red circles) samples, normalized by the current density in the Pt layer.

We continued our analysis for all our sample systems. Figure 5.19 shows the measured SOTs Damping-Like (a) and Field-Like (b), normalized by the current density in the Pt layer, for $Pt_{(gradient)}/Co_{(20)}/Al_{(20)}$, $Ta_{(30)}/Cu_{(10)}/CoFeB_{(20)}/Pt_{(gradient)}$, $Ta_{(30)}/Cu_{(10)}/CoFeB_{(20)}/Pt_{(gradient)}$, $Ta_{(30)}/Cu_{(20)}/CoFeB_{(20)}/Pt_{(gradient)}$ and $Pt_{(30)}/Co_{(20)}/Pt_{(gradient)}$ samples, as a function of Pt thickness. As in the previous case, we once again see the same striking result, that the amplitude of the Damping-Like torque is constant across the entire thickness range of the Pt layer (Figure 5.19 (a)), in agreement with the theoretical model proposed in [152]. The effective field values shown are not multiplied by the corresponding M_S values, but since the magnetization of the FM layers does not change, they are accurate in the limit of a multiplicative constant.

A particular case is the $Pt_{(30)}/Co_{(20)}/Pt_{(gradient)}$ stack, in which both top and bottom Pt layers contribute to the SOTs. Their respective contributions however, have opposite signs. As the thickness of the top Pt layer becomes smaller, the corresponding current density increases, while the current density in the bottom Pt layer will not. When the two current densities are equal, for $t_{Pt}^{top} = t_{Pt}^{bottom} = 30\text{Å}$, their respective contributions to the SOTs are equal and the total torque is zero. Using this, we are able to estimate the contribution from the bottom Pt layer, and therefore by subtracting it we can isolate only the contribution coming from the current density in the top Pt layer. Above 30 Å, where the torque contributions from the two Pt layers are very similar, the measured signal due to the total

SOTs is very small while the noise is very high, thus the measurements are not reliable. Below 30 Å, the Damping-Like torque is constant.

It is important to note that, the evolution of the Damping-Like torques with Pt thickness that we present in our analysis, is not specific to a particular FM/HM combination. On the contrary, we have seen the same global dependence of the SOTs as a function of Pt thickness across different FM materials, with both top and bottom SOT generating HM layer. The experimental data also shows that differences arise due to the interfaces. Because the thickness of all the FM layers studied is significantly larger than the distance over which the spin current gets absorbed, we could expect that the effects of the top and bottom interfaces are independent. However, comparing the Damping-Like effective field measurements for the Co-based samples, we see that the amplitudes change for different bottom interfaces. When the Pt/Co interface is coupled with a Cu/Co interface, the Damping-like effective field is larger than when coupled with an Oxide/Co interface. The same is true for CoFeB/FeCoB-based samples. Also, the amplitude of the Damping-Like effective field for Pt/CoFeB interfaces is larger than for Pt/Co interfaces. This is consistent with differences in saturation magnetization between Co and CoFeB-based samples.

The evolution with Pt thickness of the SOTs, that we measure experimentally, is not consistent with a SHE-only hypothesis, but rather, it points towards important interface contributions to the SOTs. Furthermore, a recent study into the SHE and ISHE in Pt/Py bilayers, by Wang et. al. [153], that takes into account interfacial contributions to the spin Hall current has a very interesting result, in that is shows that the SHA due to the interface is 25 times larger than the one due to the bulk. This implies that, even in a SHE approach to the SOTs, interface contributions cannot be neglected, especially in the case of the Damping-Like torque, which is often times assumed to be only due to bulk effects.

It is also important to discuss the main sources of error in our measurements. One potential source of errors is the misalignment of the devices inside the external magnetic field (as shown in Figure 4.14). However, these errors are easily accounted for, by using the symmetry of the measured Hall signals, which we know, and that of the measurement method, as described in Chapter 4. Errors due to in-plane misalignment can be corrected by using the symmetry of the measured Hall signal (comprising both first and second harmonics), which gives us the position (in degrees) of the zeroes. Using the symmetry of the

measurement ($0 - 360°$), it is a simple matter of shifting the position scale with the corresponding offset. Errors due to out-of-plane misalignment are corrected by fitting the measured signal with a function that takes into account contributions from the PHE (φ dependent) and the AHE (θ dependent).

Systematic errors can also be introduced by the variation in the width of the Hall Cross as a result of the nanofabrication process and the distribution of the current density inside the Hall Cross, which is not homogeneous. However, such errors do not affect the shape of the curves, but only introduce noise in the measurements that can be averaged out.

5.2.4 Discussion

We have studied the evolution of the Damping-Like and Field-Like effective fields as a function of the Pt layer thickness, for samples with top and bottom Pt gradients, and different FMs.

The situation is most interesting. In a first attempt to explain our findings, we have compared our data to a SHE-only model of the SOTs and found that although the model can, to some extent, describe the evolution of the SOTs in our samples, due to the large number of free parameters it uses, it is not accurate.

We have seen that, after taking into account the thickness dependence of the resistivity of the Pt layer, and calculating the current density through it accordingly, the amplitude of the Damping-Like effective field per unit of current density remains constant with decreasing Pt layer thickness. This behavior differs from the SHE model of the SOTs, but it is however consistent with strong contributions to the SOTs arising from the FM/Pt interface. Measurements on comparable stacks, Ta/CoFeB/MgO, but with PMA, show a similar, constant behavior of the Damping-Like as a function of Ta thickness only below 5 Å [140] (see Figure 3.10). In our case, however, this constant behavior extends across the entire range of thicknesses studied, up to approximately 40 and 100 Å, depending on the samples.

It is very unlikely that the SHE in the Pt layer could vary so much as a function of Pt thickness or Pt/FM interface, so as to account for the thickness dependence of the Damping-Like and Field-Like effective fields observed experimentally. This supports the presence of an additional contribution to the SOTs, different than the SHE and independent of the Pt layer thickness.

Another important point is related to the calculation of the current density in the Pt layer. Because the Pt layers in our samples were deposited as thickness gradients instead of layers of constant thickness, we had to study samples from the entire wafer, not just its center. We therefore needed to take into account the variation of layer thickness towards the edges of the wafer, due to the deposition process, which can influence the resistivity measurements. This influence was larger in the case of Co-based samples, because of the rather similar resistivity values of the Pt and Co layers, and even for CoFeB-based samples which contain a Cu buffer layer. We had to preform additional resistivity measurements to accurately calculate the current density in the Pt layer, in order to compensate for these variations. Not doing so, results in an inaccurate value of the current density, which has a significant impact on the normalized SOT values. This leads to an inaccurate picture of the SOTs' evolution with Pt thickness. One could also, in theory, use resistivity measurements on an identical stack, without the Pt layer, say for example MgO/CoFeB or Ta/Cu/CoFeB, as a reference to calculate the resistivity of the Pt gradient. However, this approach is inherently flawed, since it would completely omit the influence of the FM/Pt interface on the resistivity.

In this section, we studied different FM/Pt interfaces. We also changed the interface to bulk effects ratio by changing the thickness of the Pt layer, effectively diminishing the strength of the SHE, while keeping the interface between the CoFeB, Co and Pt unchanged. Next, we will look at how the crystallographic structure of the interface influences the SOTs.

5.3 Influence of Pt layer structure on the SOTs

5.3.1 Sample Stacks

In the second part of our study, we have prepared sample stacks with Pt [001] and Pt [111] layers. We then investigated the influence of the crystalline structure of the Pt layer on the evolution of the SOTs in Pt/Co and Pt/CoFeB-based devices, by measuring the Damping-Like and Field-Like torques as a function of the angle between the current direction and the crystal axis of the Pt layer. At the same time, this approach allows us to study the effects of structurally different interfaces on the SOTs.

To be able to have [001] growth of the Pt layers, we used a MgO substrate and a Cr buffer layer. For the [111] growth we used a Ta buffer layer and a standard Si/SiO_2 substrate, which results in [111] textured Pt. The sample structures have been grown by sputter deposition at the Faculty of Physics at the Technical University of Cluj-Napoca. We have prepared four sample systems, shown schematically in Figure 5.20: a) $Cr_{(20)}/Pt\text{-}001_{(30)}/Co_{(20)}/Al_{(20)}$, b) $Cr_{(20)}/Pt\text{-}001_{(30)}/CoFeB_{(20)}/Al_{(20)}$, c) $Ta_{(20)}/Pt\text{-}111_{(30)}/Co_{(20)}/Al_{(20)}$ and d) $Ta_{(20)}/Pt\text{-}111_{(30)}/CoFeB_{(20)}/Al_{(20)}$.

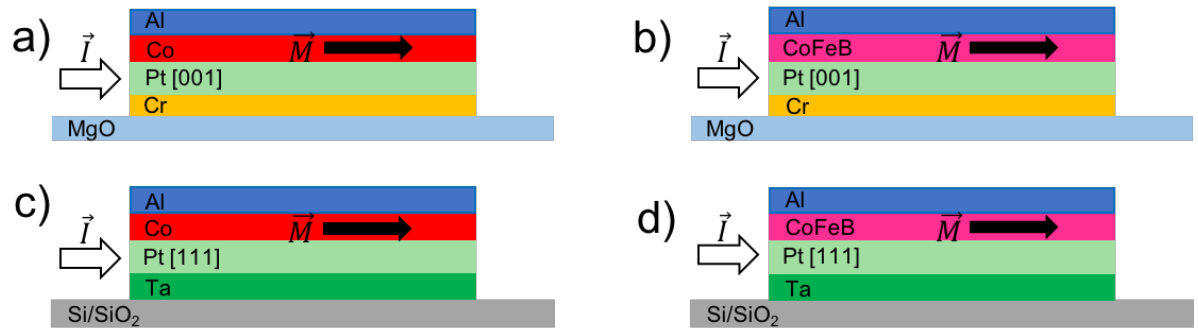

Figure 5.20: Schematics of: a) $Cr_{(20)}/Pt\text{-}001_{(30)}/Co_{(20)}/Al_{(20)}$, b) $Cr_{(20)}/Pt\text{-}001_{(30)}/CoFeB_{(20)}/Al_{(20)}$, c) $Ta_{(20)}/Pt\text{-}111_{(30)}/Co_{(20)}/Al_{(20)}$ and d) $Ta_{(20)}/Pt\text{-}111_{(30)}/CoFeB_{(20)}/Al_{(20)}$ sample systems. The thickness of the layers is not represented to scale.

The samples are then patterned into Hall cross devices, with both branches 5 μm wide, as described in section 4.1. To be able to control the angle between the crystallographic axes and the current, we have patterned our samples in such a way that the current injection lines are rotated with respect to one-another by 30°, 45° and 60° (as shown in Figure 5.21). This allows us to inject the current at 0°, 30°, 45°, 60° and 90°, and study the evolution of the SOTs as a function of this angle.

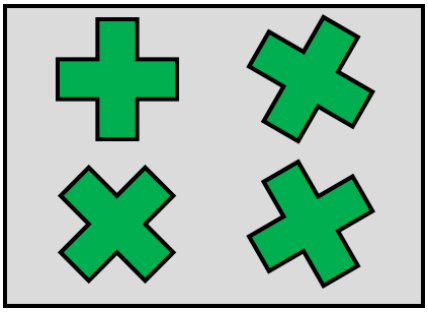

Figure 5.21: Schematic showing the distribution of Hall cross devices, rotated with respect to each other by 30°, 45° and 60°. This distribution allows for current injection at 0°, 30°, 45°, 60° and 90° with respect to the crystal axes.

In the following sections, we will present, and discuss, the results of our study of these sample systems.

5.3.2 Structural and Magnetic Properties

First, to verify the growth of the Pt layers, the crystalline structure of our samples is analyzed by X-ray diffraction and lattice parameters are calculated. The measurements have been done at the Department of Physics and Chemistry, at the Technical University of Cluj-Napoca, using a Cu anode with a characteristic wavelength $\lambda = 0.15418\, nm$, and a 2θ/ω measurement geometry. Figure 5.22 shows the diffraction spectra for the four sample systems studied.

The XRD analysis shows that the Pt has a FCC (Fm3m) structure. We see good [001] growth of the Pt layer on the MgO//Cr buffer layer (Figure 5.22 (a) and (b)), evidenced by the presence of the diffraction peak at $2\theta = 46°$. This is true for both Co and CoFeB samples. The diffraction peaks from the Co and CoFeB layers are not seen, because of their low intensity. The CoFeB layer, however, as we will discuss in the following paragraphs, shows a weak [001] textured growth on the Pt layer.

In the case of the SiO_2//Ta buffer layer (Figure 5.22 (c) and (d)), the XRD analysis shows the presence of the diffraction peak at $2\theta = 38°$. In addition, we also see the diffraction peak at $2\theta = 86°$. Again, this is true for both Co and CoFeB samples. Unlike in the previous case, here we also see [111] textured growth of the Co layer on top of the Pt layer, evidenced by the presence of the diffraction peak at $2\theta = 44°$, corresponding to diffraction on the planes of Co. In the case of the CoFeB layer, the XRD analysis shows a possible [011] textured growth. Also seen in both cases, is the diffraction peak corresponding to the β-Ta phase.

Using the Bragg formula, we calculate the lattice parameter for the Pt layer, in both in-plane and out-of-plane geometries. We get $0.3908 \pm 4 \cdot 10^{-4}\ nm$ (for out-of-plane) and $0.391 \pm 2 \cdot 10^{-3}\ nm$ (for in-plane), consistent with the average value reported in literature ($0.392\ nm$).

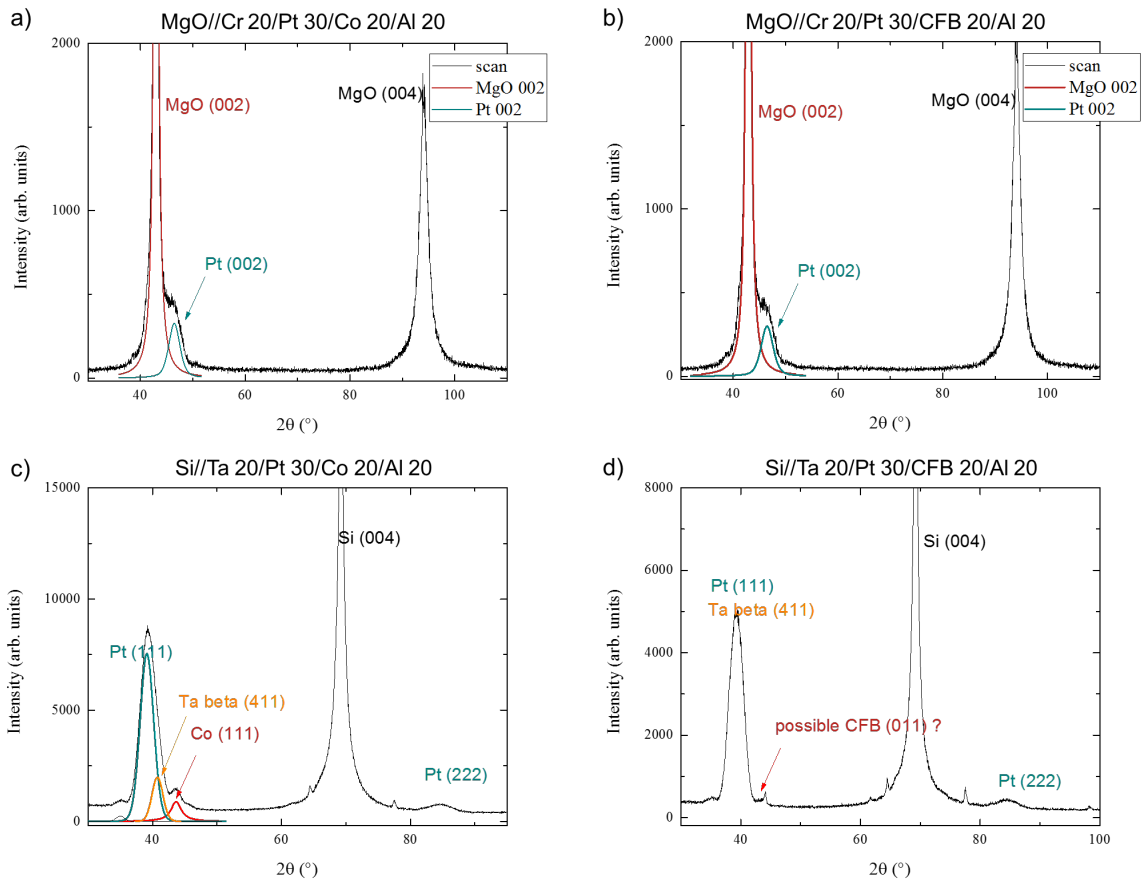

Figure 5.22: X-ray diffraction spectra for a) Cr/Pt-001/Co/Al, b) Cr/Pt-001/CoFeB/Al, c) Ta/Pt-111/Co/Al and d) Ta/Pt-111/CoFeB/Al samples.

Before we measure and compare the values of the SOTs, as a function of the angle between current direction and crystallographic axes, we also need to take a look at the magnetic properties.

Figure 5.23 shows VSM measurements of the in-plane magnetic hysteresis loops for our sample systems. To study the dependence of the magnetic properties on the crystal structure, we have measured several hysteresis loops as a function of the direction of the applied magnetic field.

In the case of the Co layers grown on either Pt-[001] or Pt-[111], we see no clear in-plane easy axis. The anisotropy of the CoFeB layer, however, shows a weak in-plane four-fold character, when grown on Pt-[001]. This can be a sign of a [001] texturing of the layer, as

mentioned earlier. When grown on Pt-[111], the CoFeB layer shows a weak in-plane uniaxial anisotropy, consistent with the possible [011] texturing of the layer.

In terms of saturation magnetization, we can see from the VSM measurements that the growth of the Pt layer has no effect. The calculated M_S values are as shown in Table 4.

Pt layer growth	Co M_S $\left[\frac{emu}{cm^3}\right]$	CoFeB M_S $\left[\frac{emu}{cm^3}\right]$
[001]	1085 ± 100	776 ± 100
[111]	1095 ± 100	735 ± 100

Table 4: Saturation magnetization, M_S, values for Co and CoFeB as a function of Pt layer texturing.

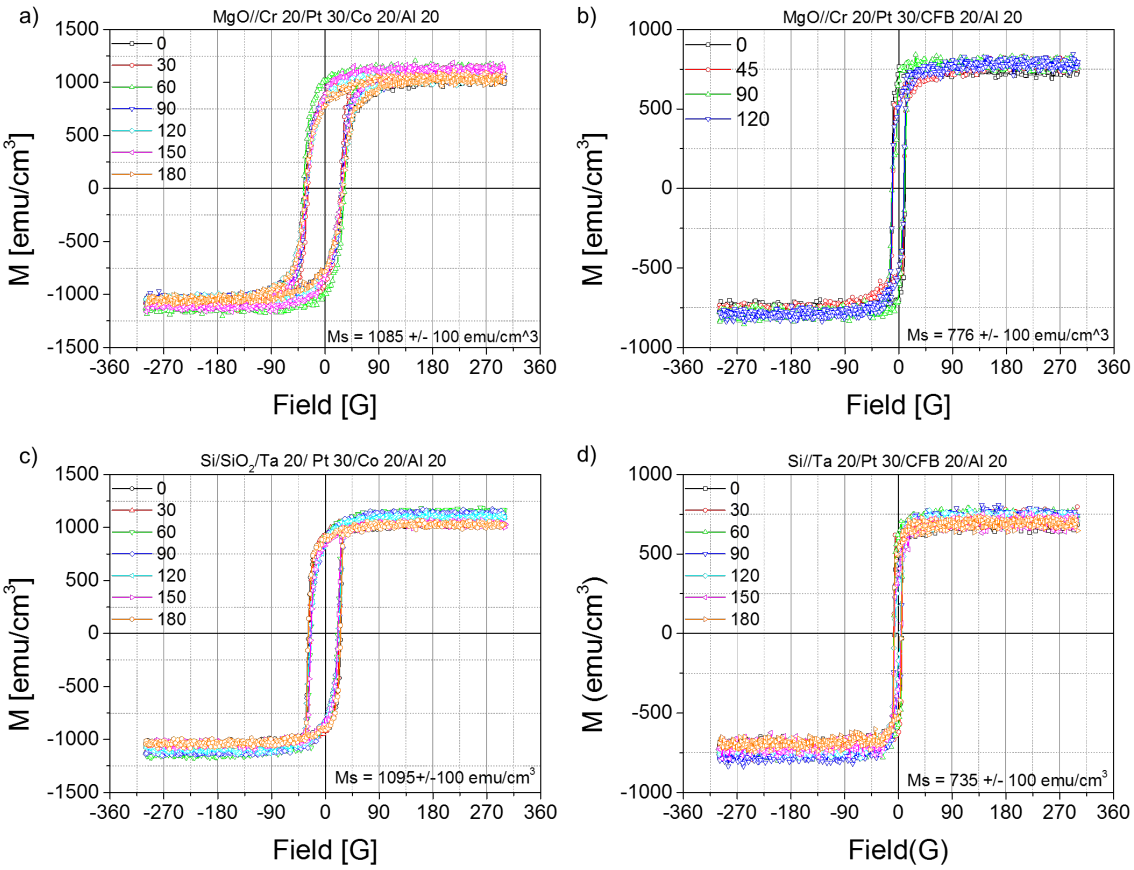

Figure 5.23: VSM measurements of the magnetic hysteresis loops for a) Cr/Pt-001/Co/Al, b) Cr/Pt-001/CoFeB/Al, c) Ta/Pt-111/Co/Al and d) Ta/Pt-111/CoFeB/Al samples, for the magnetic field applied at different in-plane angles.

Our samples thus have the structural and magnetic properties we are looking for. Having textured Pt layers allows us to control the angle between the current direction and the crystallographic axes in a consistent way. This allows us to study the influence of the Pt/FM layer interface type on the generation of SOTs. In the following section, we will present the results of our analysis of the SOTs in these conditions.

5.3.3 Evolution of the SOTs and Discussion

Taking advantage of the samples, we injected the current at five different angles with the crystallographic axes, and we measured the SOTs. Figure 5.24 shows the Damping-Like and Field-Like effective fields, as a function of current injection angle, for Co and CoFeB-based samples, both for Pt-001 and for Pt-111. In this case, because the samples have the same nominal thicknesses, we can normalize the effective field values by the total injected current.

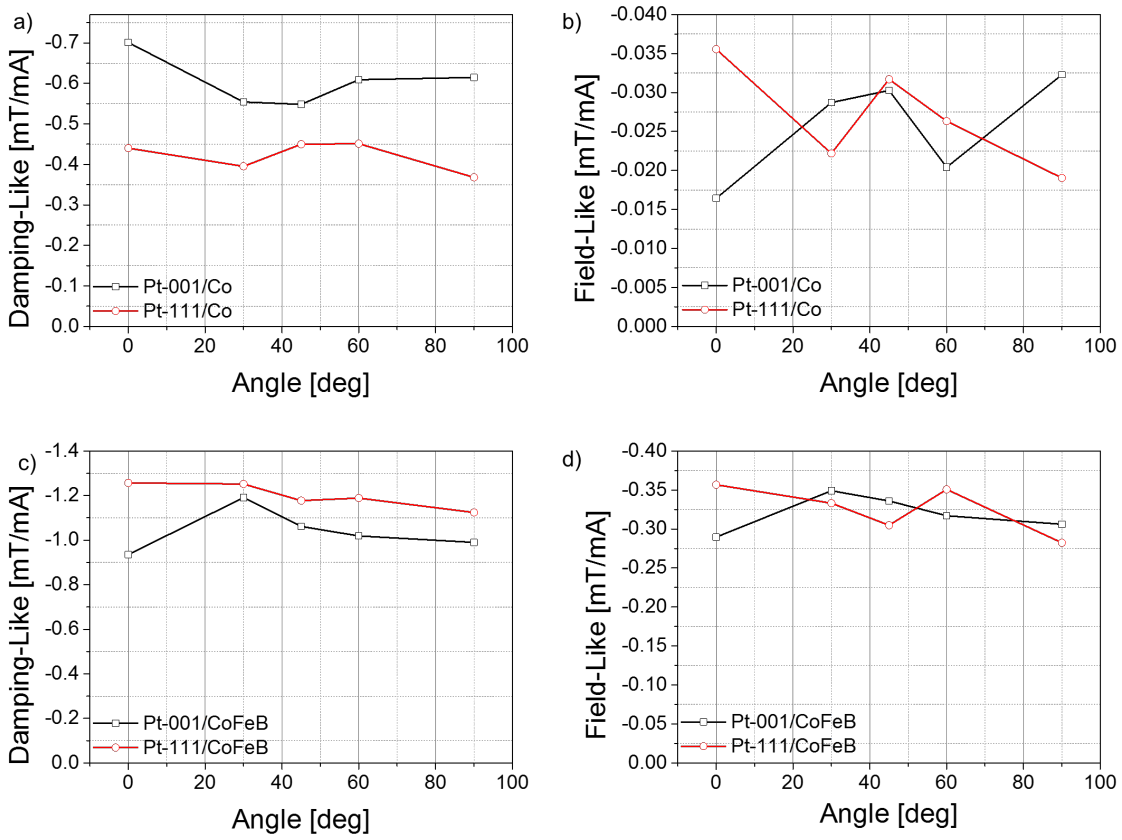

Figure 5.24: Damping-Like and Field-Like effective fields as a function of the angle between the current direction and the crystallographic axes, for Pt-001 (black squares) and Pt-111 (red circles) interfaces with Co (a and b) and CoFeB (c and d).

The effects we observe are interesting. First, we observe that the structure of the Pt layer influences the amplitude of the Damping-Like effective field, without having any impact on that of the Field-Like effective field. For the Field-Like effective field there is no noticeable amplitude difference between Pt-001/FM and Pt-111/FM interfaces, while for the Damping-Like effective field there is a clear difference in amplitude between the two interfaces. Second, neither the Damping-Like nor the Field-Like effective fields are affected by the angle between the crystallographic axes and the current injection direction. In both cases, the amplitude of the effective fields is constant with respect to the current injection angle.

The Damping-Like effective field per unit of applied electric current, for the CoFeB-based samples is significantly larger than for Co-based samples. We further note that the behavior of the Damping-Like effective field also changes when we change the FM layer. In the case of Co-based samples, the Damping-Like effective field per unit of applied electric current is larger for the Pt-001 interface than it is for the Pt-111 interface, while the opposite is true for the CoFeB-based samples. This is also correlated with the relative strength of the anisotropy field, H_{dem}, for Co and CoFeB-based samples, for Pt-001 and Pt-111 interfaces: samples with a larger Damping-Like amplitude have a smaller H_{dem} values (H_{dem} values are shown in Table 5). This is important, because as H_{dem} is a measure of the interface anisotropy.

Pt layer growth	Co H_{dem} $[kOe]$	CoFeB H_{dem} $[kOe]$
[001]	4.5	20
[111]	6.4	5.8

Table 5: Measured values of the demagnetizing field (also containing the contributions from the anisotropy field), H_{dem}, for Co and CoFeB-based samples, for Pt-001 and Pt-111 interfaces.

Figure 5.25 shows the Damping-Like effective fields per unit of applied electric field, as a function of the angle between the current direction and the crystallographic axes for Pt-001 (black squares and blue triangles) and Pt-111 (red circles and pink triangles) interfaces with Co (black squares and red circles) and CoFeB (blue triangles and pink triangles). In this case, the effective field values are also normalized by the saturation magnetization of the devices (see Table 4 and Figure 5.23), according to $\xi_{DL}^{E}(t_{Pt}) = \frac{2e}{\hbar}\mu_0 M_S t_{FM}\frac{H_{DL}}{E}$. In this case, we observe that for Pt-111 interfaces, the amplitude of the Damping-Like effective field is the same Co and CoFeB-based samples. This is consistent with our previous samples. For Pt-001 interfaces, however, we see a large difference in Damping-Like effective field amplitude for Co and CoFeB-based samples. While in the case of CoFeB-based samples, the normalized Damping-Like effective field values are similar with the values obtained for Pt-111 interfaces, for Co-based samples, these values are significantly larger.

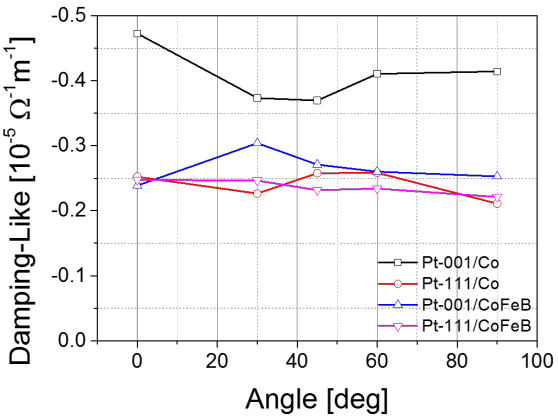

Figure 5.25: Damping-Like effective fields per unit of applied electric field, as a function of the angle between the current direction and the crystallographic axes, for Pt-001 (black squares and blue triangles) and Pt-111 (red circles and pink triangles) interfaces with Co (black squares and red circles) and CoFeB (blue triangles and pink triangles). The effective field values are normalized by the saturation magnetization of the device.

The overall behavior of the Damping-Like effective field (normalized by the applied electric current or by the applied electric field and saturation magnetization), shows that the FM/Pt interface has a strong influence on its amplitude.

5.4 Influence of top Pt layer oxidation on the SOTs

5.4.1 Sample Stacks

We have shown in section 5.2 that, in the case of a top Pt gradient, the Damping-Like torque is constant as a function of Pt thickness. This points out to significant interface effects that become important at low Pt thicknesses. To better understand the influence of interface and bulk effects on the SOTs, we decided to further change the properties of the HM/FM interface, on similar samples systems, with top Pt gradient.

For this part of our study, we began by preparing two sample systems, $Cu_{(10)}/Co_{(20)}/Pt_{(gradient)}$ and $Ta_{(30)}/Cu_{(10,\ 20)}/Co_{(20)}/Pt_{(gradient)}$, by dc. magnetron sputtering on thermally oxidized Si/SiO_2 (1 µm) at the ACTEMIUM deposition chamber at SPINTEC.

We kept the same design choices as in the previous study. First, the Cu layer creates SIA. We have decided on studying Cu layers of 10 and 20 Å, in order to minimize its effect on the resistivity of the device. Second, the thickness of the Co layer, 20 Å, ensures strong in-plane magnetic anisotropy, uniform layers without discontinuities and good susceptibility to the SOTs. Third, the top Pt gradient ensures identical Co/Pt interfaces across Pt thicknesses (for the same reasons discusses in section 5.2.1). Figure 5.26 shows the schematics of the sample systems.

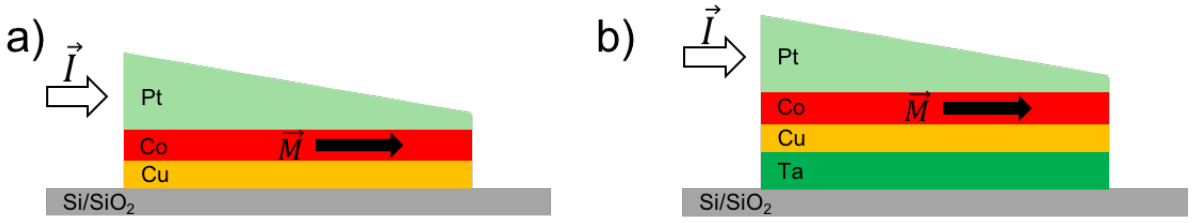

Figure 5.26: Schematics showing the a) $Cu_{(10)}/Co_{(20)}/Pt_{(gradient)}$ and b) $Ta_{(30)}/Cu_{(10,\ 20)}/Co_{(20)}/Pt_{(gradient)}$ samples with in-plane magnetic anisotropy and SIA. The thickness of the layers is not represented to scale.

As we will discuss further (Figure 5.35), one of the problems we have encountered during our analysis, is that due to the small thicknesses of the Cu layer (10 and 20 Å), layer growth is characterized by the formation of islands, and thus not uniform. This effect is especially strong for the 10 Å Cu layer. Since increasing the Cu layer thickness is not an option, because it will significantly decrease the amplitude of the SOTs, to correct this, we have deposited samples with a Ta buffer layer, in order to ensure good growth of the Cu layer. By

comparison with the Pt and Cu layers, the Ta resistivity is much larger, therefore it will not influence the SOTs.

The Pt gradients are grown in the same manner described in section 5.2.1 and the layers are cut into strips and patterned into Hall cross devices with $5\ \mu m$ wide branches, according to Figure 5.3 and the procedure described in section 4.1.

Now, to change the properties of the Co/Pt interface, we oxidized the samples, strips and devices, by exposing them to an O_2 plasma for 3 minutes. We then measured the SOTs as a function of the top Pt layer thickness, in order to study the effects of the oxidation, on both oxidized and non-oxidized samples. The degree of oxidation was controlled by the thickness of the Pt layer and studied by XPS measurements.

In the following sections, we will present, and discuss, the results of our study of the evolution of the SOTs with the thickness of the Pt layer, in these samples systems, as a function of the oxidation process. The first step is to study the oxidation of the Pt and Co layer, to confirm that the oxidation does reach the Pt/Co interface. Next, we need to study the electric and magnetic properties of our samples, in order to be able to normalize and compare the SOT values, and also to be able to understand and explain the evolution of the SOTs.

5.4.2 Studying the oxidation of Pt layer

First, to study the oxidation of the Pt and Co layers, we performed pARXPS (parallel Angle Resolved X-ray Photoemission Spectra) measurements on several devices, with different Pt thickness, before and after the O_2 plasma was applied. The measurements were done at LTM Grenoble, using a customized Thermo Fisher Scientific Theta 300 pARXPS, with a monochromatic Al X-ray source, at 1486.6 eV, in ultra high vacuum at $3 \cdot 10^{-9}\ mbar$.

In XPS measurements, a soft X-ray beam (around 1 keV) is focused on the sample surface. This causes photoelectrons to be emitted, whose kinetic energy is measured. An energy spectrum is thus created, plotting the peak intensity in terms of counts per unit of time (like an XRD pattern) against the binding energy of the emitted electron. The said binding energy is calculated as:

$$E_{binding} = E_{incident} - (E_{kinetic} + \phi)$$

Equation 5.7

where $E_{incident}$ is the energy of the incident X-rays, $E_{kinetic}$ is the kinetic energy of the emitted electron and ϕ is a correction factor dependent on the spectrometer. Each material gives out a specific set of peaks, corresponding to their electron configuration. The intensity of the peaks is proportional to the amount of material present in the sample. From the energy spectra it is possible to identify the materials present in the sample, as well as their states. XPS is a surface technique, giving us information about only 10 nm depth, but since our samples are ultra thin films, it is a well suited technique.

First, to get a reference measurement of the oxidation of the Pt and Co layers, we analyzed a sample with a thin layer of Pt, 15 Å in this case, before the O_2 plasma was applied. Should any oxidation of the Pt or Co layer, due to "natural" causes, occur, it would be visible in the low Pt thickness region of the sample stack. However, the XPS spectra for the $Ta_{(30)}/Cu_{(10,\ 20)}/Co_{(20)}/Pt_{(15)}$ sample, shown in Figure 5.27, shows no traces of oxidation.

We then selected several samples, with different Pt thicknesses, namely 14, 16 and 24 Å, in order to cover the thin portion of our Pt gradient. Analyzing the sample stacks after the O_2 plasma was applied shows a different situation. We will look at this analysis in the following paragraphs.

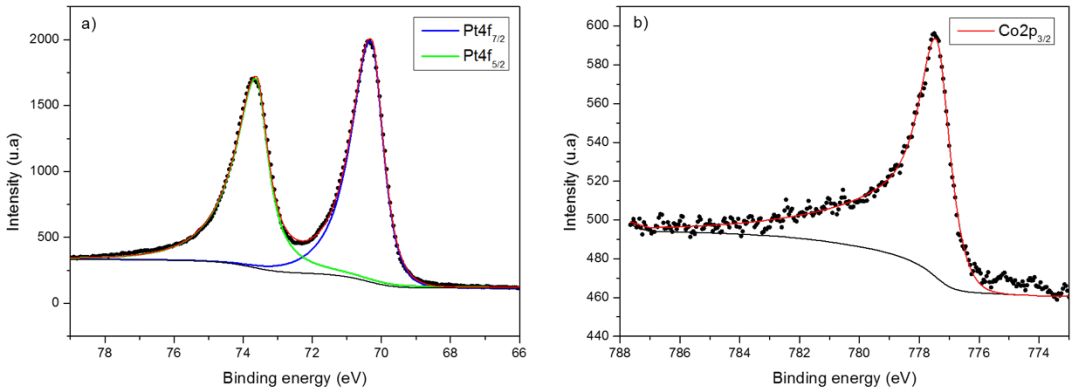

Figure 5.27: XPS spectra on $Ta_{(30)}/Cu_{(10)}/Co_{(20)}/Pt_{(gradient)}$ sample, before O_2 plasma was applied, for the a) Pt 4f and b) Co 2p3/2 peaks, showing no oxidation of neither Pt nor Co layers.

The XPS spectra on the $Ta_{(30)}/Cu_{(10)}/Co_{(20)}/Pt_{(14)}$ sample, for the Pt 4f peak shows the presence of four doublets, corresponding to the presence of Pt^{0+}, Pt^{2+}, Pt^{3+} and Pt^{4+} oxidation states. This is clear evidence of the oxidation of the Pt layer by the applied O_2 plasma. Measurements as a function of the emission angle show that at higher angles the peak intensity corresponding to the Pt^{2+}, Pt^{3+} and Pt^{4+} states increases, while for the Pt^{0+} state decreases (Figure 5.28 (a) and (b)). Furthermore, calculations show that the content of Pt

oxide represents 40% and 65% of the total Pt at 23.75° and 75.25° emission angle respectively. This result implies that the Pt layer is not homogenous, and that the percentage of Pt oxide is more important close to the surface of the Pt layer than at the Pt/Co interface. This finding is consistent with the oxidation method we used.

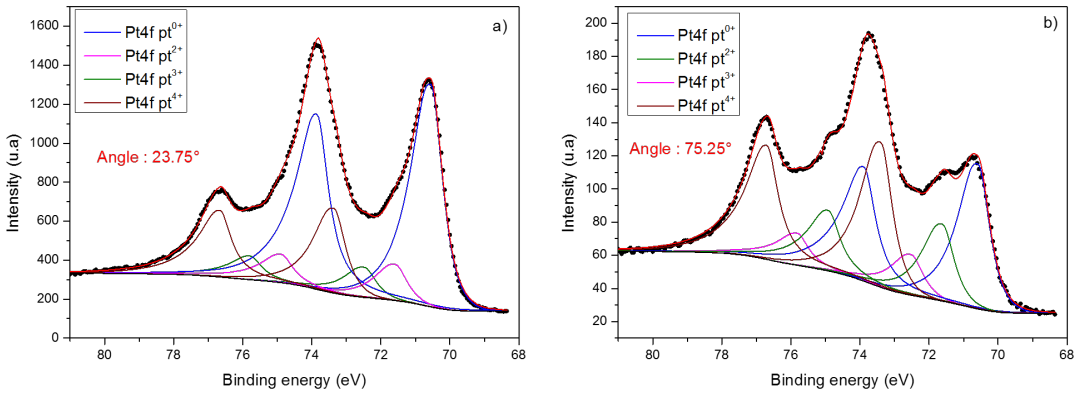

Figure 5.28: XPS spectra of $Ta_{(30)}/Cu_{(10)}/Co_{(20)}/Pt_{(14)}$ sample, after O_2 plasma was applied, for the Pt 4f peak, at a) 23.75° and b) 75.25° emission angles. The presence of peaks corresponding to Pt^{0+}, Pt^{2+}, Pt^{3+} and Pt^{4+} oxidation states indicates the presence of Pt oxide.

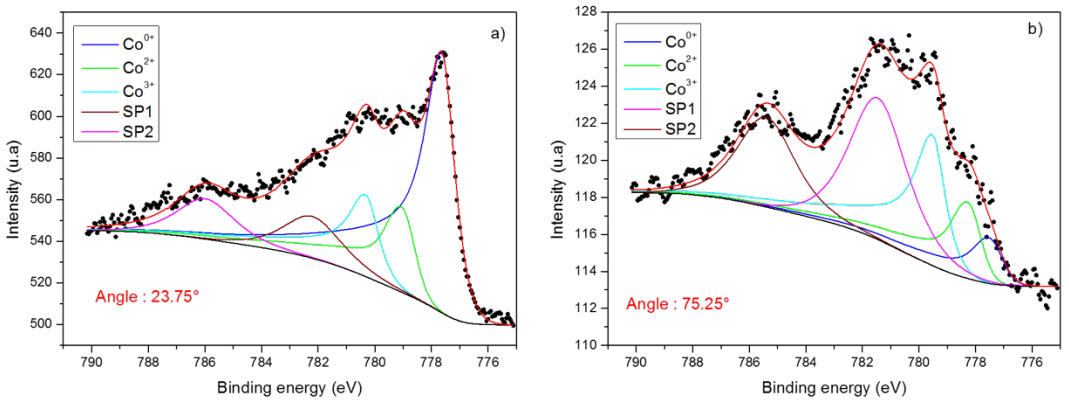

Figure 5.29: XPS spectra of $Ta_{(30)}/Cu_{(10)}/Co_{(20)}/Pt_{(14)}$ sample, after O_2 plasma was applied, for the Co 2p peak, at a) 23.75° and b) 75.25° emission angles. The presence of peaks corresponding to Co^{0+}, Co^{2+} and Co^{3+} oxidation states indicates the presence of Co oxide. SP1 and SP2 are associated to satellite peaks.

The same analysis on the $Ta_{(30)}/Cu_{(10)}/Co_{(20)}/Pt_{(14)}$ sample, for the Co 2p3/2 peak shows the presence of Co^{0+}, Co^{2+} and Co^{3+} oxidation states (Figure 5.29 (a) and (b)), which is a strong indication of the oxidation of the Co layer. Like for the Pt layer, the intensity of the Co^{2+} and Co^{3+} peaks increases while the intensity of the Co^{0+} peak decreases, indicating that the oxidation of the Co layer is more important at the Pt/Co interface (top of the layer) than at the Cu/Co interface (bottom of the layer).

Continuing the XPS analysis on the $Ta_{(30)}/Cu_{(10)}/Co_{(20)}/Pt_{(24)}$ sample, for the Pt 4f peak, shows the same trend, with Pt^{0+}, Pt^{2+}, Pt^{3+} and Pt^{4+} oxidation states being present (Figure 5.30 (a) and (b)). The peak intensity follows the same evolution with the emission angle, showing an increase in peak intensity for Pt^{2+}, Pt^{3+} and Pt^{4+} states and a decrease for the Pt^{0+} state. The findings are therefore consistent, as in both cases we see more Pt oxidation at the surface of the layer than at the bottom interface. However, in this case, no oxidation of the Co layer is detected (Figure 5.30 (c)). This is due to the much thicker layer of Pt that protects the Co layer from the applied O_2 plasma.

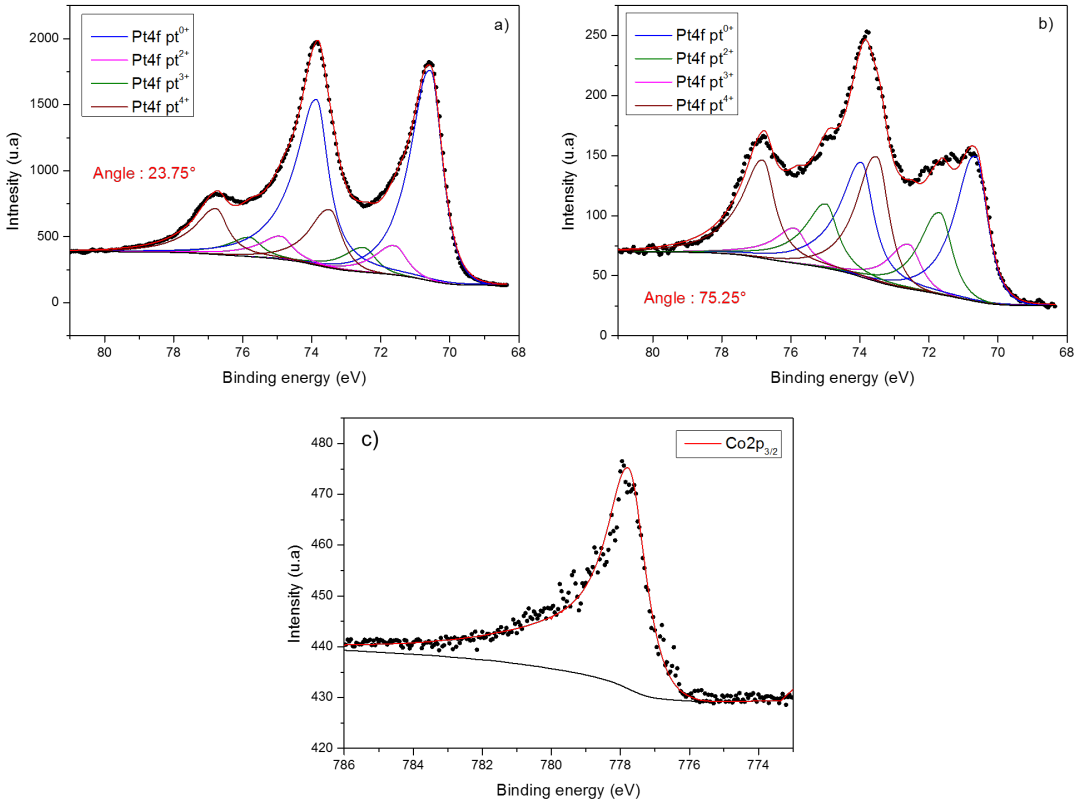

Figure 5.30: XPS spectra of $Ta_{(30)}/Cu_{(10)}/Co_{(20)}/Pt_{(24)}$ sample, after O_2 plasma was applied, for the Pt 4f peak, at a) 23.75° and b) 75.25° emission angles and c) for the Co 2p3/2 peak. The presence of peaks corresponding to Pt^{0+}, Pt^{2+}, Pt^{3+} and Pt^{4+} oxidation states indicates the presence of Pt oxide, while no oxidation of the Co layer is present.

The third sample we have analyzed by XPS, $Ta_{(30)}/Cu_{(10)}/Co_{(20)}/Pt_{(16)}$, shows a consistent behavior. We see the presence of Pt^{0+}, Pt^{2+}, Pt^{3+} and Pt^{4+} peaks, which confirm the existence of Pt oxide. Like in the previous cases, the evolution of the intensity of the peaks as a function of the emission angle indicates that the concentration of Pt oxide is more important at the top of the layer than at the bottom. Calculating the content of Pt oxide shows that it represents 50% and 75% of the total Pt at 23.75° and 75.25° emission angle respectively. It also seems

that, by comparison with the sample with 14 Å of Pt, in this case the oxidation is more important. The XPS spectra is shown in Figure 5.31 (a) and (b).

In Figure 5.32 we show the XPS spectra of the Co 2p3/2 peak, at 23.75° (a) and 75.25° (b) emission angle. We again see the presence of Co^{0+}, Co^{2+} and Co^{3+} oxidation states, indicating the presence of Co oxide. Like in the previous case, for the sample with 14 Å of Pt, the intensity of the Co^{2+} and Co^{3+} peaks increases at higher emission angles, while the intensity of the Co^{0+} peak decreases. However, the Co^{0+} peak remains dominant. This is an indication of a much weaker oxidation of the Co layer. This is consistent with the presence of a thicker Pt layer, that partially protects the Co layer from the applied O_2 plasma.

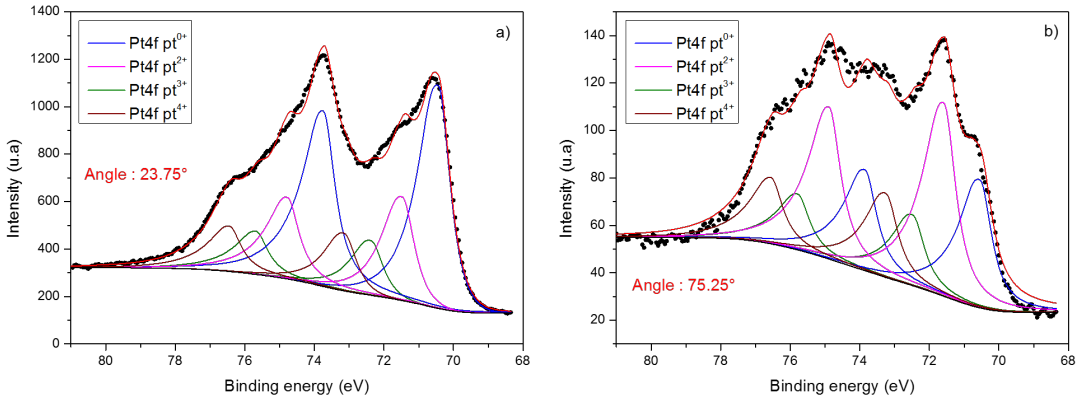

Figure 5.31: XPS spectra of $Ta_{(30)}/Cu_{(10)}/Co_{(20)}/Pt_{(16)}$ sample, after O_2 plasma was applied, for the Pt 4f peak, at a) 23.75° and b) 75.25° emission angles. The presence of peaks corresponding to Pt^{0+}, Pt^{2+}, Pt^{3+} and Pt^{4+} oxidation states indicates the presence of Pt oxide.

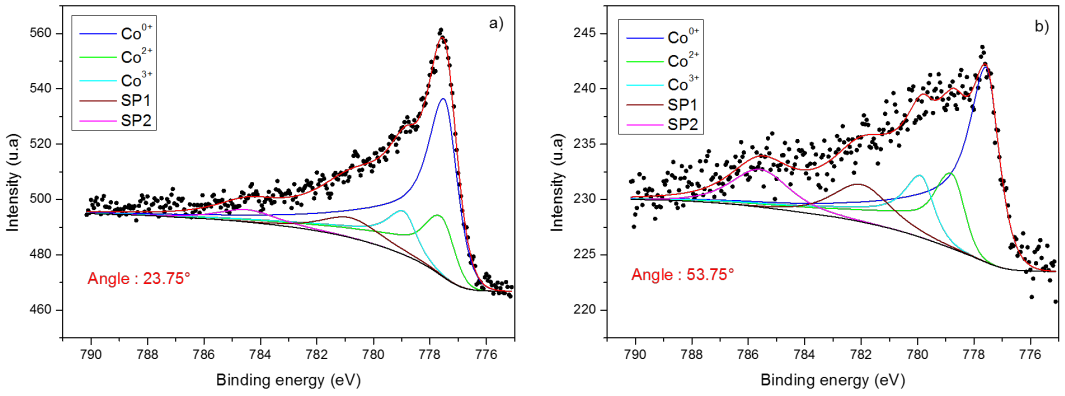

Figure 5.32: XPS spectra of $Ta_{(30)}/Cu_{(10)}/Co_{(20)}/Pt_{(16)}$ sample, after O_2 plasma was applied, for the Co 2p peak, at a) 23.75° and b) 75.25° emission angles. The presence of peaks corresponding to Co^{0+}, Co^{2+} and Co^{3+} oxidation states indicates the presence of Co oxide. SP1 and SP2 are associated to satellite peaks.

Our analysis shows that both the Pt and the Co layers get oxidized. The thickness of the Pt layer dictates the degree to which the Co layer is oxidized. In all cases, the oxidation is

found to be more important at the top of the layers, indicating that the degree of oxidation inversely proportional to the distance from the sample surface. It is important to note that the Co layer retains its full magnetization (Figure 5.33). The variations seen are within the confidence interval of our VSM measurements. They are probably due to uncertainties in sample positioning. Together with the data from the XPS measurements, this indicates only superficial oxidation of the Co layer. In the following sections, it is our objective to study the evolution of the SOTs as a function of Pt layer thickness and oxidation. For this, we will begin by studying the electric and magnetic properties of our systems.

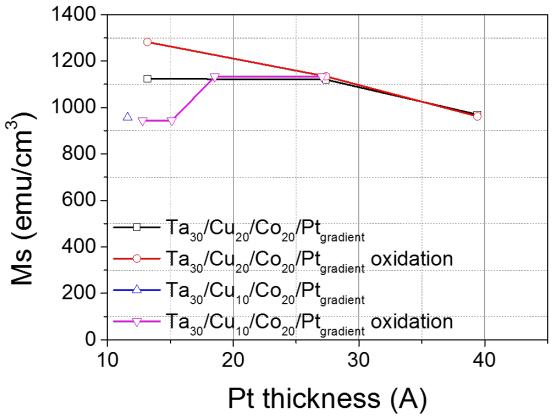

Figure 5.33: Saturation magnetization as a function of Pt layer thickness for $Ta_{(30)}/Cu_{(10,\ 20)}/Co_{(20)}/Pt_{(gradient))}$ samples, before and after oxidation.

5.4.3 Electrical Properties

As before, we used 4-point resistance measurements, to measure the resistance of our $Cu_{(10)}/Co_{(20)}/Pt_{(gradient)}$ and $Ta_{(30)}/Cu_{(10,\ 20)}/Co_{(20)}/Pt_{(gradient)}$ samples. Figure 5.34 shows the inverse resistance measurements as a function of Pt thickness, before and after oxidation, for samples without the Ta buffer layer, (a), and with the Ta buffer layer, (b).

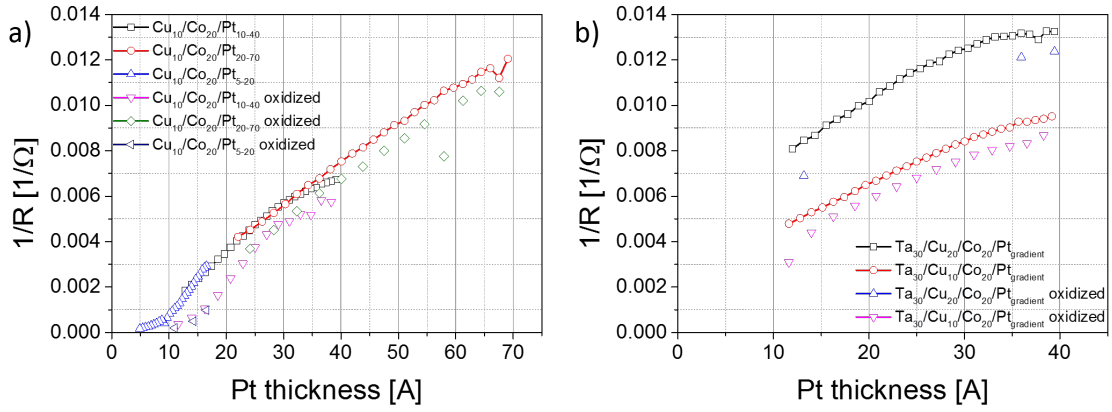

Figure 5.34: Measurements of the inverse resistance as a function of Pt thickness for a) $Cu_{(10)}/Co_{(20)}/Pt_{(gradient)}$ and b $Ta_{(30)}/Cu_{(10,20)}/Co_{(20)}/Pt_{(gradient)}$ samples, before and after oxidation.

First, let's look at the samples without the Ta buffer layer. The large Pt thickness range that we studied for the $Cu_{(10)}/Co_{(20)}/Pt_{(gradient)}$ system was spread across three different gradients (Figure 5.34 (a)). Although it allows us to verify the consistency of our results across different, independent, samples, it poses some difficulties as well. Because all the layers of constant thickness are deposited "on-axis", their thickness will vary slightly towards the edges of the wafer from the nominal value. For the ultra thin Cu layer in our samples (10 Å), this change in thickness brings a significant resistivity variation towards the edges of the wafer, corresponding to the thin and thick parts of the Pt gradient. In this case, the resistance of the samples increases and the inverse resistance vs thickness curves would show a downward concave-like shape. This deviation from linearity can mask the effect of the thickness dependent resistivity of the Pt layer, making the analysis more difficult. It is the same effect we observed in the case of the $Pt_{(gradient)}/Co_{(20)}/Al$ samples. We notice that it is more pronounced in the case of the 10-40 Å gradient. This can be understood this by considering that this effect on the resistivity, caused by the thinning effect at the edges of the wafer, is constant across all samples, and independent of the Pt gradient on top. Therefore, in the case of a thicker gradient (red circles in Figure 5.34 (a)), this effect is relatively too weak to influence the overall resistivity of the sample (compared to the large influence a thick Pt layer has). At the other end of the thickness gradient (blue triangles in Figure 5.34 (a)), the Pt layer is too thin and no longer continuous, causing large resistivity variations, which are difficult to analyze.

The oxidized samples show a similar inverse resistance variation with Pt thickness, characterized by a constant offset. This offset is consistent with an increase in resistance due to the oxidation of the Pt layer.

A second difficulty that arises with the $Cu_{(10)}/Co_{(20)}/Pt_{(gradient)}$ samples is that, because it is very thin (10 Å), the Cu layer is not continuous, but rather is characterized by the formation of islands. Because of this, the Co layer that is grown on top fills in the gaps between these islands, resulting in a Cu/Co mixture. Figure 5.35 shows a mapping of the distribution of Cu and Co in a $Cu_{(10)}/Co_{(20)}/Pt$ sample, using X-EDS analysis. We see how the Cu (yellow) and Co (red) layers are actually mixed, only the top most part of the Co layer being Cu free. This has an impact both on the electric and the magnetic properties of the samples, rendering the analysis of the SOTs more difficult.

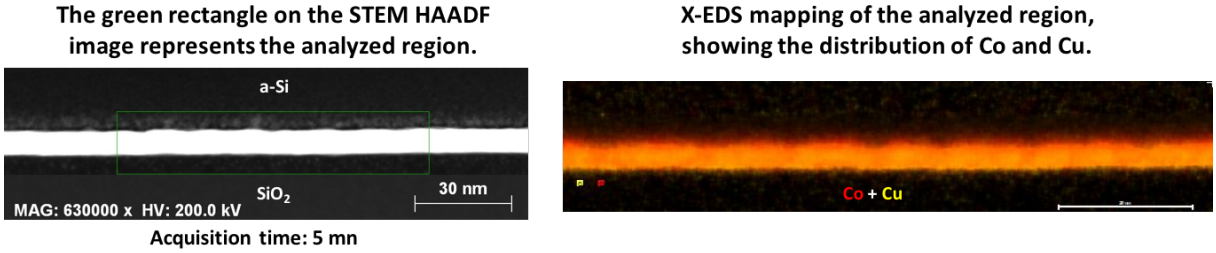

Figure 5.35: X-EDS mapping of a $Cu_{(10)}/Co_{(20)}/Pt$ sample showing the distribution of Co (red) and Cu (yellow). We see that the two layers are intermixed, due to the Cu layer not being continuous. This allows the Co layer to fill in all the gaps, resulting in a discontinuous growth of the Co layer as well. The analyzed section corresponds to the green rectangle on the STEM HAADF image on the right.

To tackle this problem, we use a 30 Å Ta buffer layer that facilitates the deposition of Cu, allowing for continuous layers. Figure 5.36 shows a mapping of the distribution of Cu and Co for a $Ta_{(30)}/Cu_{(10)}/Co_{(20)}/Pt_{(gradient)}$ sample, using X-EDS analysis. We see how, in this case, the Cu (red) and Co (yellow) layers are no longer mixed. The Ta buffer layer also lowers the resistance of the samples (Figure 5.34 (b)), indicating that indeed the Cu layer is continuous. However, this causes part of the current to be short circuited through the Cu layer, which leaves less current participating in the generation of SOTs, considerably decreasing their amplitude. For the thicker, 20 Å Cu layer, the decrease in torque amplitude is even larger.

Throughout our study we will therefore focus on the samples with 10 Å Cu layer and a Ta buffer layer. We will however show measurements for samples with a 20 Å Cu layer to serve as comparison.

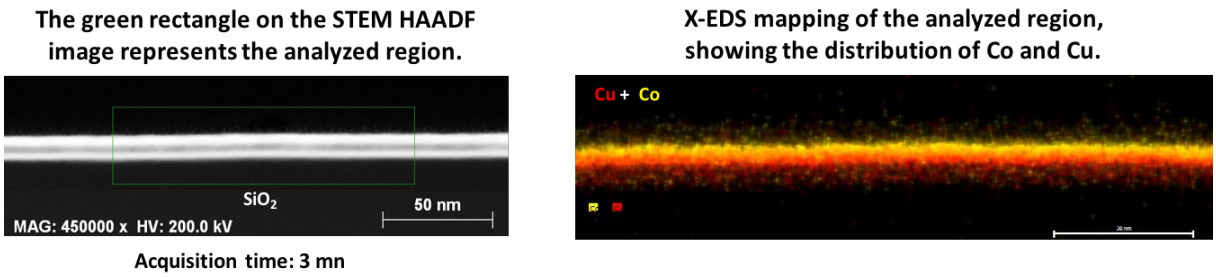

Figure 5.36: X-EDS mapping of a $Ta_{(30)}/Cu_{(10)}/Co_{(20)}/Pt_{(gradient)}$ sample showing the distribution of Co (yellow) and Cu (red). We see that using a Ta buffer layer greatly improves the deposition of the Cu layer. Cu and Co layers are no longer intermixed. The analyzed section corresponds to the green rectangle on the STEM HAADF image on the right.

Another consequence of the current being short circuited through the Cu layer is that the influence that the thickness dependence of the resistivity of the Pt layer has on the overall resistivity of the samples is harder to detect. This makes the analysis of the current density in the Pt layer more difficult.

As we did with the samples presented in section 5.2.2, we used 4-point resistivity measurements to follow the evolution of the resistance as a function of the distance from the center of the wafer, perpendicular to the Pt gradient. We then fitted the data with a symmetric polynomial function and used it to apply a correction to the resistance measurements taken along the Pt gradient. This correction takes into account the variations in resistivity that appear for devices, towards the edges of the wafer, as a result of "on-axis" deposition (see Figure 5.8 (a) and section 5.2.2). Figure 5.37 shows the inverse resistance as a function of Pt thickness for $Ta_{(30)}/Cu_{(10\text{-}20)}/Co_{(20)}/Pt_{(gradient)}$ samples before and after oxidation ((a) and (b) respectively), after applying the correction. We again see that the resistivity of the Pt layer is not constant with decreasing thickness. Therefore, we can fit the data to a Fuchs-Sondheimer model, using Equation 5.3. The fitting parameters for the samples with a $Cu_{(10)}$ layer, before and after oxidation, are summarized in Table 6. For the un-oxidized samples, ρ_0 and R_0 are consistent with the values we previously obtained, during the course of this work, for Pt layers. For the oxidized samples, both ρ_0 and R_0 values increase, as expected. Using the fitted parameters, we can then calculate the current density in the Pt layer, for each Pt thickness value, and normalize the SOT amplitudes by it.

$Ta_{(30)}/Cu_{(10)}/Co_{(20)}/Pt_{(gradient)}$	$\rho_0\ [\mu\Omega cm]$	$R_0\ [\Omega]$	$\lambda\ [nm]$
Before oxidation	18.53	206	10.1
After oxidation	24	250	5.5

Table 6: Fitting parameters for the inverse resistivity as a function of Pt thickness, for $Ta_{(30)}/Cu_{(10)}/Co_{(20)}/Pt_{(gradient)}$ samples, before and after oxidation, obtained using a Fuchs-Sondheimer model.

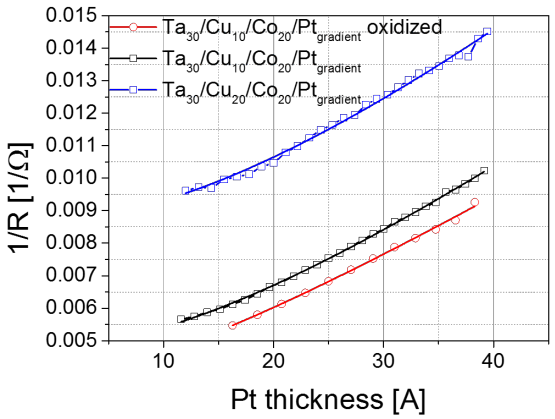

Figure 5.37: Inverse of the resistance as a function of Pt layer thickness for $Ta_{(30)}/Cu_{(10\text{-}20)}/Co_{(20)}/Pt_{(gradient)}$ samples after correcting for the variations induced by the change in layer thickness towards the edges of the wafer.

5.4.4 Evolution of SOTs and Discussion

The evolution of the SOTs, as a function of Pt thickness, is measured using the method described in Chapter 4. Figure 5.38 shows the Damping-Like field, as a function of Pt thickness, normalized by the effective voltage applied[31], V_{eff} (a), and by the current density in the Pt layer, J_{Pt}, (b), for $Ta_{(30)}/Cu_{(10\text{-}20)}/Co_{(20)}/Pt_{(gradient)}$ samples.

Looking first at the un-oxidized samples, the Damping-Like effective field per unit of applied voltage (and, in the limit of a multiplicative factor, applied electric field) as a function of Pt thickness shows the same global behavior presented in section 5.2.3.1. The amplitude of the Damping-Like effective field per unit of current density as a function of Pt thickness, is constant, also consistent with our previous findings (section 5.2.3.2).

Oxidizing the samples has an interesting effect on the SOTs. The amplitude of the Damping-Like effective field per unit of applied voltage, and also per unit of current density (blue triangles in Figure 5.38 (a) and (b) respectively) shows a remarkable increase at low Pt thicknesses, below 20 Å.

[31] The effective voltage is calculated using the longitudinal resistance of the stack and the total in-plane current injected.

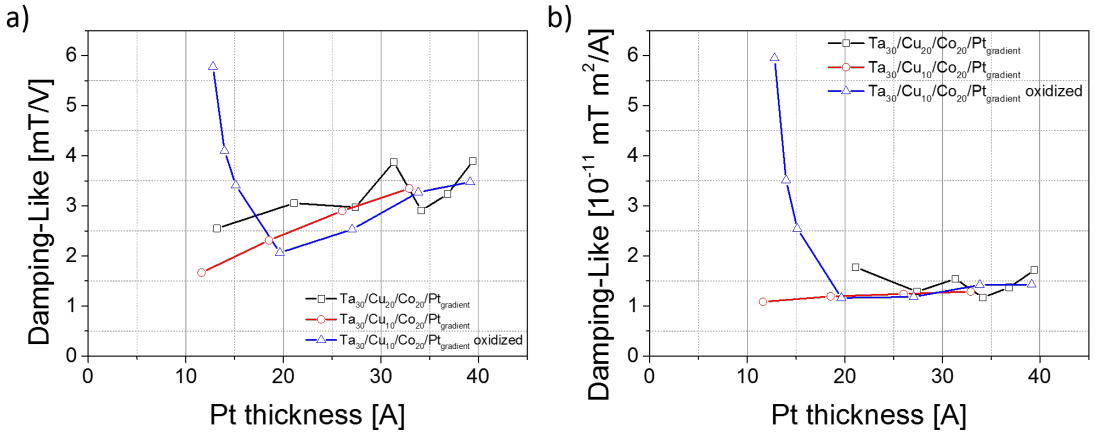

Figure 5.38: Damping-Like effective field as a function of Pt layer thickness, normalized by a) applied effective voltage and b) current density in the Pt layer.

An important aspect is that the Pt thickness interval over which the increase in Damping-Like effective field amplitude is observed, is consistent with the oxidation reaching the Pt/Co interface (see section 5.4.2). Furthermore, for Pt thicknesses over 20 Å, where the oxidation does not reach the interface, the Pt thickness dependence of the Damping-Like effective field is the same as for the non-oxidized samples, namely constant. This behavior is consistent the presence of very strong contributions to the SOTs, arising at the Pt/Co interface.

Although having poorer growth, $Cu_{(10)}/Co_{(20)}/Pt_{(gradient)}$ samples show an even larger increase of Damping-Like effective field amplitude at low Pt thicknesses, after oxidation (Figure 5.39). In this case, because the Cu layer is not continuous, we cannot use our previous method to calculate the current density in the Pt layer. However, this also means that most of the current flows through the Pt layer, instead of being short circuited through the Cu layer.

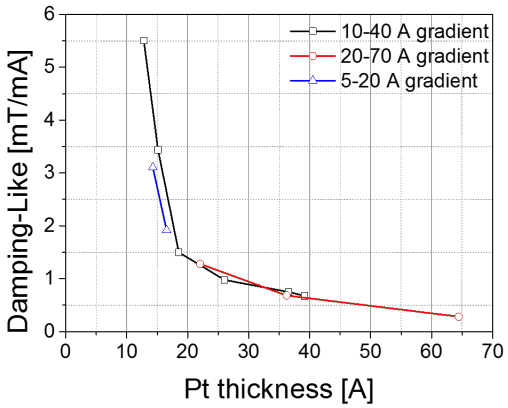

Figure 5.39: Damping-Like effective field as a function of Pt layer thickness, per unit of current density, as a function of Pt thickness, for $Cu_{(10)}/Co_{(20)}/Pt_{(gradient)}$ samples.

From an applications' perspective, the increase of the Damping-Like effective field amplitude is very interesting, as it potentially allows for devices to operate at lower current.

6 General conclusions

The main objective of this thesis was to explore one of the fundamental questions regarding the SOTs, question which concerns their physical origin, namely bulk effects (such as the SHE) or interfacial effects (such as the Rashba Effect or the Interfacial SHE) or both. Better understanding the origin of the SOTs is an essential first step in controlling and optimizing the SOTs for any kind of application. In order to do this, and to clearly distinguish between SHE and interface contributions, we aimed at conducting a systematic study of the influence of interfaces on the SOTs. Since by simply measuring the SOTs we have no means of distinguishing between bulk and interface effects as sources of SOTs, we explored three avenues:

i. First, we aimed at changing the interface/bulk effect ratio by changing the thickness of the HM. We have chosen Pt, because it is one of the most widely studied HM in Spintronics.
ii. Second, we explored different HM/FM/NM combinations, in order to study different interfaces and different interface and bulk contributions to the SOTs. We studied CoFeB/FeCoB and Co-based samples, paired with MgO, Al, Cu and Pt, all common materials in Spintronics.
iii. Third, we changed the properties of the interface either by textured growth of the HM layer or by oxidation.

To have the flexibility needed to complete our study, we investigated samples with in-plane magnetic anisotropy. By eliminating the need for interface-induced PMA, we were afforded more material choices and a wider range of thicknesses.

For the purpose of studying the SOTs, we developed an experimental setup to measure the SOTs in a quasi-static regime, based on the Harmonic analysis of the Hall voltage. The improvements brought to our setup allow for a fast and complete analysis of angular and field dependency of both SOT components, Damping-Like and Field-Like, in samples with both in-plane and out-of-plane magnetic anisotropy. The measurement technique and the experimental setup have been described at length in Chapter 4.

In the first part of our study, we varied the thickness of the Pt layer, both as a top and as a bottom layer, in $MgO/FeCoB_{(20)}/Pt_{(10\text{-}100)}$, $Pt_{(10\text{-}40)}/Co_{(20)}/Al_{(20)}$, $Pt_{(30)}/Co_{(20)}/Pt_{(10\text{-}40)}$, $Ta_{(30)}/Cu_{(10)}/Co_{(20)}/Pt_{(10\text{-}40)}$ and $Ta_{(30)}/Cu_{(10)}/CoFeB_{(20)}/Pt_{(10\text{-}40)}$ multilayers. We then followed the evolution of the SOTs as a function of Pt thickness for every sample system. We tested our experimental results against the SHE-only model of the SOTs, by looking at the efficiency of the Damping-Like effective field per unit of applied electric voltage, as a function of Pt thickness. We have seen that, in all cases, such a model does not accurately fit the experimental data. Furthermore, we have seen that, while the FM/Pt interface does not produce significant changes in the behavior of the torque, the nominally inactive NM/FM interface has significant impact.

We further show that the inverse of the resistivity of the Pt layer accurately describes the evolution of the Damping-Like effective field per unit of applied electric voltage, as a function of Pt thickness, for all the samples studied, up to a proportionality factor. This indicates that the amplitude of the torque scales exactly as the current density in the Pt layer. This is further supported by the evolution of the Damping-Like effective field per unit of applied current density in the Pt layer, which is constant with the thickness of the Pt. This behavior is in agreement with the theoretical model proposed by Stiles et. al. [152] for SOTs originating in the Rashba Effect, as well as with predictions by Wang et. al. [153] according to which interfacial contributions to the SOTs are 25 times larger than the bulk.

In the second part of our study, we changed the interface type by growing textured Pt layers. This way, we were able to study the evolution of SOTs in Co and CoFeB-based samples with Pt-001 and Pt-111 interfaces. The evolution of the SOTs shows that, while the interface type has no impact on the amplitude of the Field-Like effective field, it does have a significant influence on the amplitude of the Damping-Like effective field. This influence is further correlated, at a qualitative level, with the interfacial anisotropy of the samples.

In the third part of our study, we further modified the properties of the interface by oxidation. We then followed the evolution of the Damping-Like effective field per unit of applied current density and effective voltage as a function of Pt thickness, before and after oxidation, for $Ta_{(30)}/Cu_{(10)}/Co_{(20)}/Pt_{(10\text{-}40)}$ multilayers. In this case, the Pt thickness is also indicative of the degree of interface oxidation in the samples. What the experimental data

shows, is a remarkable increase in the amplitude of the Damping-Like effective field at low Pt thickness, corresponding to the oxidation of the Pt/Co interface. For the un-oxidized samples, as well as for the oxidized samples where the Pt layer is thick enough so as to protect the Pt/Co interface from oxidation, the behavior of the Damping-Like effective field is entirely consistent with our findings from the first part, indicating that this is a purely interfacial effect. This behavior is extremely interesting from an applications perspective, as it allows for devices operating at much lower currents.

Regarding the question we posed at the beginning of this thesis, the ensemble of observations gives a global view over the importance of interfacial effects in the generation of SOTs. Our experiments show the presence of a multitude of interfacial effects that have a significant impact on the amplitude of the Damping-Like effective field. It is therefore important that the experimental work be complemented by accurate theoretical studies that take into account interfacial contributions to the Damping-Like torque.

As future perspectives, it is very interesting of expanding the study on the influence of interface oxidation on the SOTs by investigating more FM/HM combinations. In accordance with this thesis, the first choices would be CoFeB/Pt and FeCoB/Pt, with MgO and Cu bottom interfaces. Next, a logical step would be the study of magnetization switching, for both oxidized and un-oxidized samples. This work is already under way.

7 Annexes

7.1 A: Characterization of magnetic properties

As part of the analysis, we need to look at the magnetic properties of our samples. First, we check the anisotropy of our samples. In Figure 7.1 (a) we plot the magnetization hysteresis loops, in terms of AHE resistance as a function of applied field, for the field applied along the $\hat{z}$ axis, for $MgO_{(20)}/FeCoB_{(20)}/Pt_{(gradient)}$. Indeed, from the shape of the hysteresis loops, we see that the $\hat{z}$ axis is a hard magnetization axis and that the stacks have in-plane magnetic anisotropy.

The evolution of the demagnetizing field, H_{dem}, as a function of Pt thickness, is shown in Figure 7.1 (b). It also takes into account the anisotropy field, and we notice that there is no variation with Pt thickness. This is an indication that changing the thickness of the Pt layer does not induce significant changes at the Pt/FeCoB interface.

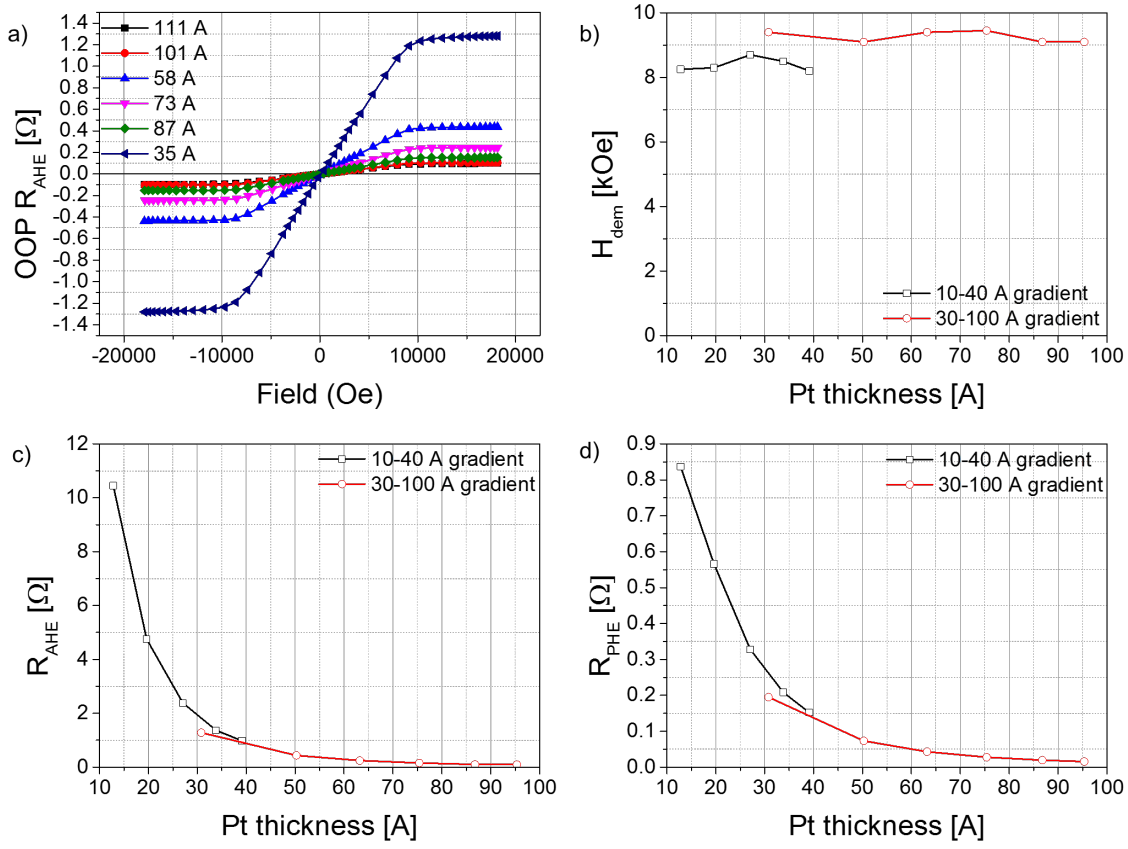

Figure 7.1: a) Out-of-plane AHE measurements for $MgO_{(20)}/FeCoB_{(20)}/Pt_{(gradient)}$ samples, for different Pt thicknesses, showing that the out-of-plane axis is a hard magnetization axis; b) The demagnetizing field, H_{dem}, also containing the anisotropy field contribution, as a function of Pt thickness; c) AHE and d) PHE resistances as a function of Pt layer thickness for $MgO_{(20)}/CoFeB_{(20)}/Pt_{(gradient)}$ samples.

We again note a discontinuity in the measured values for the two gradients. Consistent with our initial hypothesis, the higher H_{dem} values of the second gradient indicate a larger magnetization. This is also reflected by the AHE and PHE values that are larger in the case of the second gradient, for the same Pt thickness (Figure 7.2 (a) and (b)).

The evolutions of the Anomalous and Planar Hall effects as a function of the Pt thickness are shown in Figure 7.1 (c) and (d). Now, as we increase the thickness of the Pt layer, two effects occur. First, the current through the "active" part of the Pt layer, i.e. the current that participates to the AHE, decreases. Second, the Pt layer short-circuits the AHE voltage (see the following Remark). In order to account for these two effects, the AHE and PHE resistances need to be normalized by the square of the longitudinal resistance, R^2. The normalized values are shown in Figure 7.2 (a) and (b). The normalized AHE resistance is constant with respect to the Pt thickness. This is further indication that the CoFeB layer is largely unaffected by the thickness of the Pt layer and its magnetization remains unchanged. We can argue that, for thin Pt layers, below 20 Å, a small variation in the normalized AHE signal can be seen. This can be due to the formation of a Pt/CoFeB alloy at the interface, that is reflected in the magnetic properties of the sample.

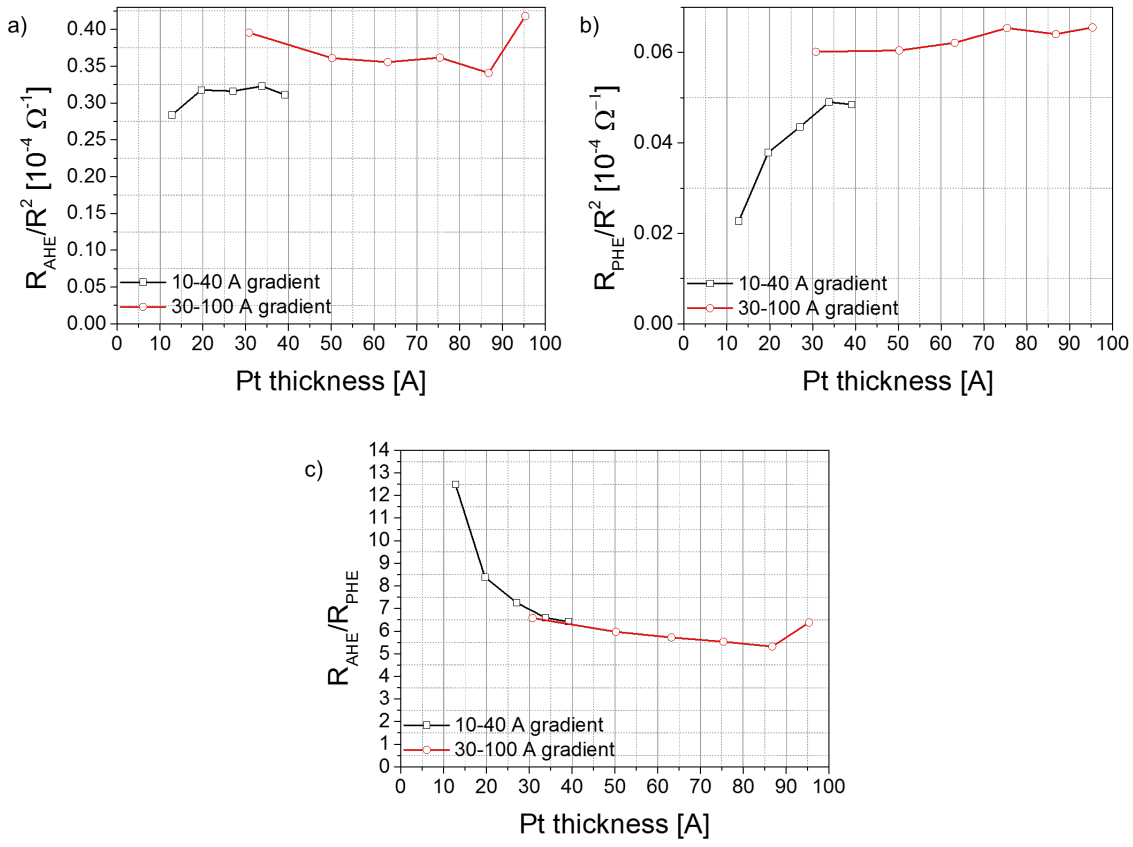

Figure 7.2: a) AHE and b) PHE resistances, normalized by the square of the longitudinal resistance of the system; c) The ratio between AHE and PHE as a function of Pt thickness.

The Planar Hall effect on the other hand, shows a significant variation with Pt thickness, below 40 Å. We can explain this, qualitatively, by considering the "torque magnetoresistance" mechanism discussed in section 5.2.3.1. The backflow current component, I_b, proportional to the Damping-Like torque, adds to the injected current and acts to increase or decrease the total current. This additional current contribution is always present, influencing the effective resistance of the Pt. The stronger the torque, the stronger this current will be. By the same mechanisms that create the PHE, another contribution to the magnetoresistive signal appears.

The AHE/PHE ratio increases significantly with decreasing Pt thickness. In accordance with their respective variation.

Remark

The current flowing through the devices can be considered as the sum of an active component, that flows through the "active" part of the Pt layer and contributes to the AHE, and a passive component that does not.

The active current can be expressed as $\boldsymbol{I_a = R/R_a}$, where $\boldsymbol{R}$ is the longitudinal resistance of the system and $\boldsymbol{R_a}$ that of the active part of the Pt layer. Now, because the AHE creates a voltage, $\boldsymbol{V_{AHE}}$ transverse to the current, $\boldsymbol{I_a}$, we will also have an associated transverse current, $\boldsymbol{I_{AHE}}$, created by $\boldsymbol{V_{AHE}}$, such that $\boldsymbol{I_{AHE} = (I_a \cdot R_{AHE})/R_a^t}$, where $\boldsymbol{R_{AHE}}$ is the AHE resistance and $\boldsymbol{R_a^t}$ is the transverse resistance of the active layer.

Continuing our reasoning, we see that this transverse current, $\boldsymbol{I_{AHE}}$, also creates a voltage by means of the AHE effect, $\boldsymbol{V'_{AHE}}$, transverse to itself but longitudinal to $\boldsymbol{I_a}$. As before, $\boldsymbol{V'_{AHE}}$ creates an associated current, transverse to $\boldsymbol{I_{AHE}}$ but opposite to $\boldsymbol{I_a}$. The resistance of the passive layer greatly reduces this effect. But as the Pt layer becomes thicker, so does the passive layer and its resistance decreases, and the "short-circuit" effect becomes larger. Our system behaves like an electric circuit with two parallel resistors, the active and the passive layers, and the measured AHE resistance will be proportional to $\boldsymbol{R^2}$. The PHE will behave in a similar fashion.

Figure 7.3 shows a similar analysis of the magnetic properties of the $Pt_{(gradient)}/Co_{(20)}/Al_{(20)}$ (black squares), $Pt_{(30)}/Co_{(20)}/Pt_{(gradient)}$ (red circles),

$Ta_{(30)}/Cu_{(10)}/CoFeB_{(20)}/Pt_{(gradient)}$ (blue triangles) $Ta_{(30)}/Cu_{(10)}/Co_{(20)}/Pt_{(gradient)}$ (pink triangles) and $Ta_{(30)}/Cu_{(20)}/Co_{(20)}/Pt_{(gradient)}$ (dark red stars) samples. The data shows no significant variations. The normalized Anomalous Hall Effect and Planar Hall Effect are a bit noisier than the AHE/PHE ratio because of device to device variations and resistance variations. The AHE variations are, very small and can be attributed to the formation of a Pt-Co alloy at the interface that modifies the magnetic properties of the Co layer. This can also explain why, for CoFeB-based samples, no such effect is observed. The AHE/PHE plots have less noise, since both values are measured on the same device. Furthermore, the AHE/PHE shows a significant variation for the CoFeB/FeCoB-based samples, reflecting mainly the variation of the torque magnetoresistance. The behavior of the $Pt_{(30)}/Co_{(20)}/Pt_{(gradient)}$ sample is most likely the result of the combined effects of top and bottom Pt gradients.

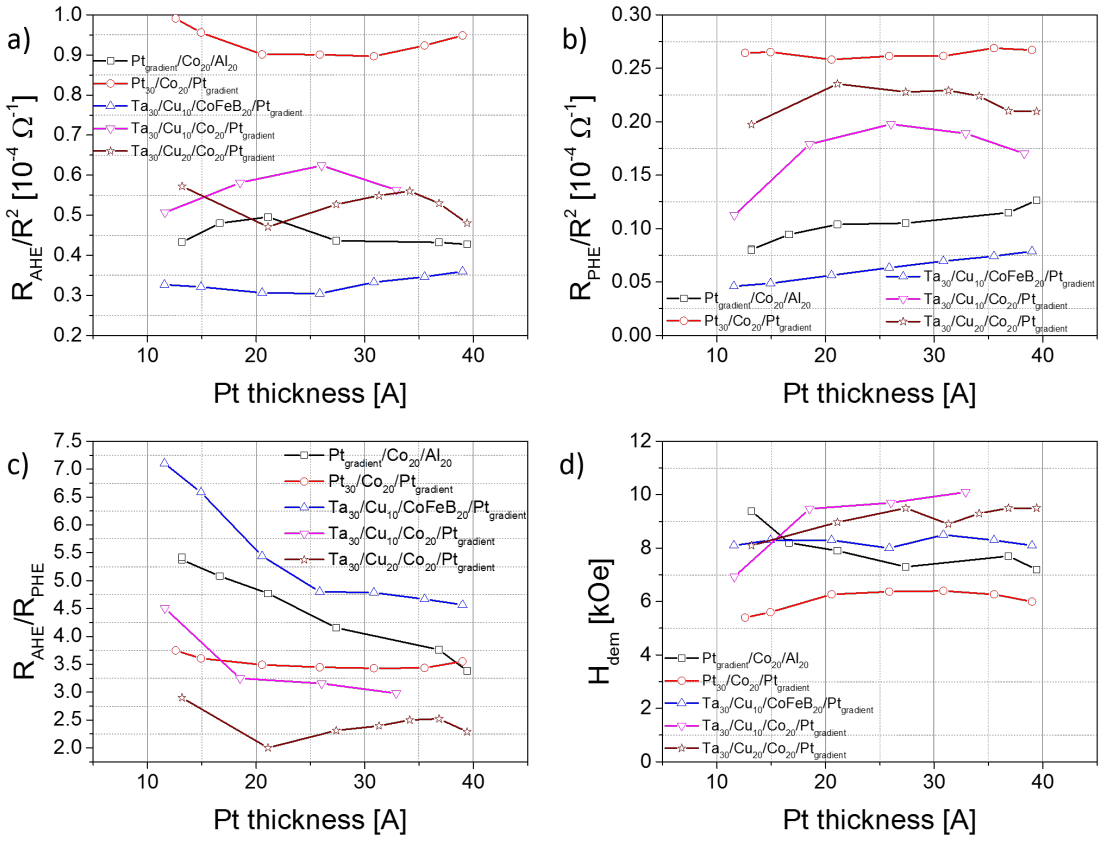

Figure 7.3: a) AHE and b) PHE resistances, normalized by the square of the longitudinal resistance, c) the AHE/PHE ratio and d) H_{dem}, as a function of Pt layer thickness, for $Ta_{(30)}/Cu_{(10)}/CoFeB_{(20)}/Pt_{(gradient)}$, $Ta_{(30)}/Cu_{(10)}/Co_{(20)}/Pt_{(gradient)}$, $Ta_{(30)}/Cu_{(20)}/Co_{(20)}/Pt_{(gradient)}$, $Pt_{(gradient)}/Co_{(20)}/Al_{(20)}$ and $Pt_{(30)}/Co_{(20)}/Pt_{(gradient)}$.

As a further exercise, we measured the saturation magnetization, M_S, along the easy axis, as a function of Pt thickness, using a VSM, for top and bottom Pt gradients ($MgO_{(20)}/CoFeB_{(20)}/Pt_{(10\text{-}100)}$ and $Pt_{(gradient)}/Co_{(20)}/Al_{(20)}$ samples). The results are shown in Figure

7.4. For the top Pt gradient (black squares), the saturation magnetization is constant, consistent with values expected for a thin CoFeB layer. The magnetization variations seen in the plots are of the order of $\pm 10\%$, which is also the confidence interval of our VSM measurements. This is probably due to uncertainties in sample positioning.

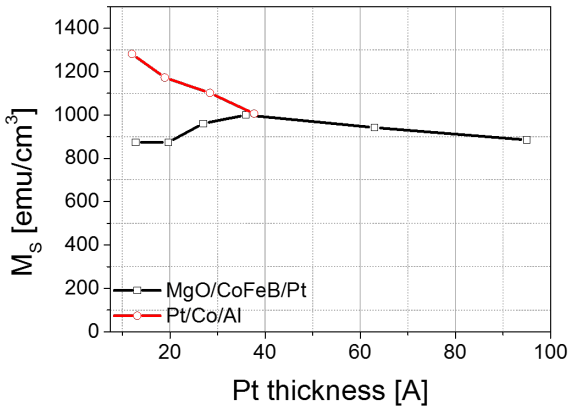

Figure 7.4: Saturation magnetization as a function of Pt layer thickness for $MgO_{(20)}/CoFeB_{(20)}/Pt_{(10\text{-}100)}$ (black squares) and $Pt_{(gradient)}/Co_{(20)}/Al_{(20)}$ (red circles) samples.

The effects of the oxidation on Ta/Cu/FM/Pt systems are followed by measuring the AHE and PHE resistances, as well as the demagnetizing field, H_{dem}. Figure 7.5 shows the evolution of the AHE and PHE resistances as a function of Pt thickness for $Ta_{(30)}/Cu_{(10\text{-}20)}/Co_{(20)}/Pt_{(gradient)}$ samples, with 10 and 20 Å Cu layers, before and after oxidation. We see that thicker Cu layer results in smaller AHE and PHE resistance values, as expected, since the current that passes through the Cu layer does not contribute to the AHE and PHE, nor to the SOTs. The normalized resistances are shown in Figure 7.6 (a) and (b) respectively, and their ratio in (c). The evolution of the normalized AHE resistance as a function of Pt thickness, before oxidation, is constant for samples with a 20 Å Cu layer (black squares in Figure 7.6 (a)), but its slightly decreasing with decreasing Pt thickness in the case of samples with a 10 Å Cu layer (green squares). This small variation can be attributed to the fact that a thinner Cu layer will result in more current passing through the Pt layer. This in turn, means that the thickness of the Pt layer has a larger impact on the resistance of the sample, than it would in the presence of a thicker Cu layer. Oxidizing the samples results in a decrease of the amplitude of the normalized AHE with decreasing Pt thicknesses, which is an indication that the oxidation process affects the magnetic/electronic properties of the Co layer. This effect is stronger for the samples with a thinner Cu layer, where a sharp decrease in amplitude is seen for Pt thicknesses below 20 Å. As our analysis of the oxidation has shown in section 5.4.2, this

thickness interval corresponds to the Co layer being strongly oxidized. Above 20 Å, the Pt layer "protects" the Co layer from oxidation.

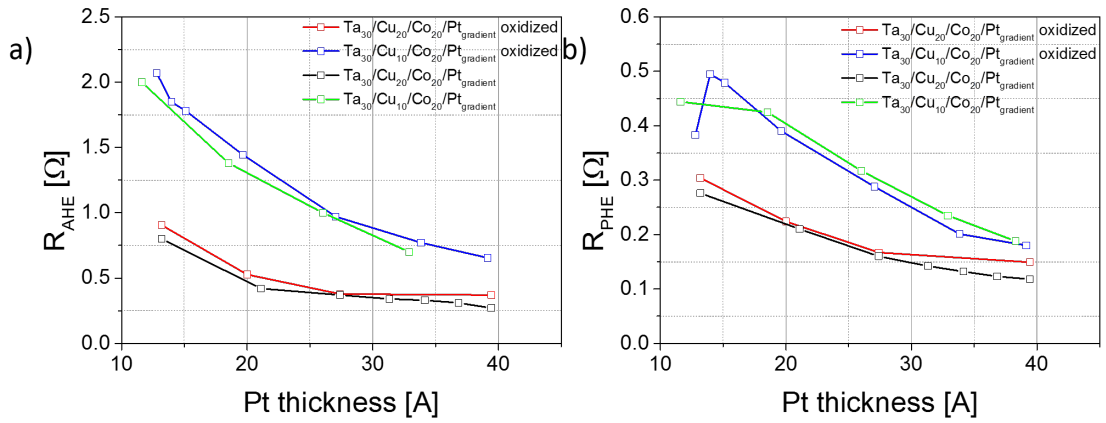

Figure 7.5: Measurements of the a) AHE and b) PHE resistances as a function of Pt thickness for Ta(30 Å)/Cu/Co(20 Å)/Pt(gradient) samples, before and after oxidation.

The demagnetizing field, H_{dem}, as a function of the Pt thickness is shown in Figure 7.6 (d). Its evolution is similar to that of the normalized AHE resistance: constant for un-oxidized samples with a thick Cu layer and sharply decreasing with decreasing Pt thickness for oxidized samples with a thin Cu layer. This is the result of the oxidation process inducing a perpendicular anisotropy component at the Co/Pt interface, effectively changing the properties of the interface. As the thick Pt layer protects the interface and the Co layer from oxidation, the decrease in H_{dem} is more important for Pt thicknesses below 20 Å.

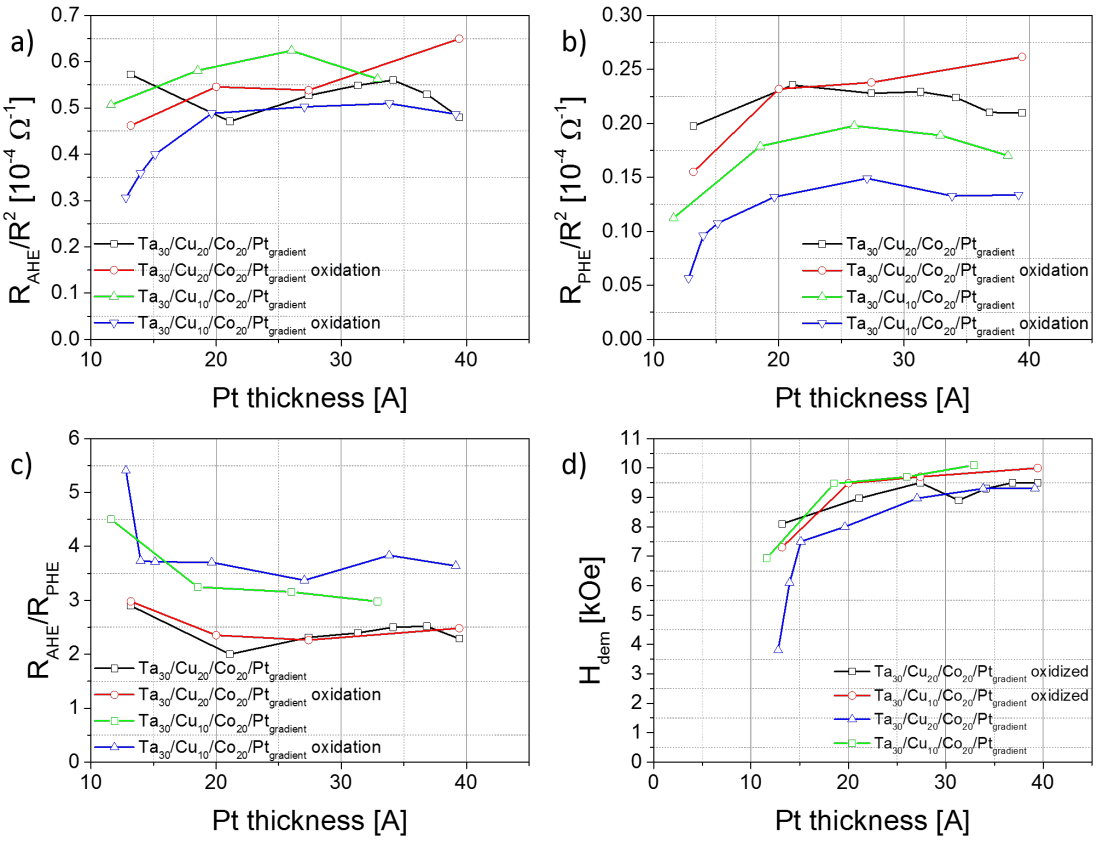

Figure 7.6: a) AHE and b) PHE resistances normalized by the square of the longitudinal resistance of the system, as a function of Pt layer thickness; c) AHE/PHE ratio as a function of Pt thickness; d) H_{dem} as a function of Pt thickness for Ta(30 Å)/Cu/Co(20 Å)/Pt(gradient) samples, before and after oxidation.

REFERENCES

[1] D. C. Ralph and M. D. Stiles, “Spin transfer torques,” *J. Magn. Magn. Mater.*, vol. 320, no. 7, pp. 1190–1216, Apr. 2008.

[2] L. Berger, “Emission of spin waves by a magnetic multilayer traversed by a current,” *Phys. Rev. B*, vol. 54, no. 13, pp. 9353–9358, Oct. 1996.

[3] J. C. Slonczewski, “Current-driven excitation of magnetic multilayers,” *J. Magn. Magn. Mater.*, vol. 159, no. 1–2, pp. L1–L7, Jun. 1996.

[4] A. Brataas, A. D. Kent, and H. Ohno, “Current-induced torques in magnetic materials,” *Nat. Mater.*, vol. 11, no. 5, pp. 372–381, 2012.

[5] M. D. Stiles and A. Zangwill, “Anatomy of spin-transfer torques,” *Phys. Rev. B*, vol. 66, p. 14407, 2002.

[6] “Wiley: Modern Magnetic Materials: Principles and Applications - Robert C. O’Handley.” [Online]. Available: http://eu.wiley.com/WileyCDA/WileyTitle/productCd-0471155667.html. [Accessed: 04-Mar-2016].

[7] J. M. D. Coey, *Magnetism and Magnetic Materials*. Cambridge University Press, 2010.

[8] O. Boulle, G. Malinowski, and M. Kläui, “Current-induced domain wall motion in nanoscale ferromagnetic elements,” *Mater. Sci. Eng. R Rep.*, vol. 72, no. 9, pp. 159–187, Sep. 2011.

[9] S. Zhang, P. M. Levy, and A. Fert, “Mechanisms of Spin-Polarized Current-Driven Magnetization Switching,” *Phys. Rev. Lett.*, vol. 88, no. 23, p. 236601, May 2002.

[10] Kittel, *INTRODUCTION TO SOLID STATE PHYSICS, 7TH ED*. Wiley India Pvt. Limited, 2007.

[11] S. Blundell, *Magnetism in Condensed Matter*. Oxford University Press, 2001.

[12] J. Xiao, “Spin-transfer torque for continuously variable magnetization,” *Phys. Rev. B*, vol. 73, no. 5, 2006.

[13] S. Zhang, “Roles of Nonequilibrium Conduction Electrons on the Magnetization Dynamics of Ferromagnets,” *Phys. Rev. Lett.*, vol. 93, no. 12, 2004.

[14] A. Thiaville, Y. Nakatani, J. Miltat, and Y. Suzuki, “Micromagnetic understanding of current-driven domain wall motion in patterned nanowires,” *Europhys. Lett.*, vol. 69, no. 6, pp. 990–996, Mar. 2005.

[15] I. Garate, “Nonadiabatic spin-transfer torque in real materials,” *Phys. Rev. B*, vol. 79, no. 10, 2009.

[16] L. Berger, “Prediction of a domain-drag effect in uniaxial, non-compensated, ferromagnetic metals,” *J. Phys. Chem. Solids*, vol. 35, no. 8, pp. 947–956, Jan. 1974.

[17] M. Kläui *et al.*, “Domain wall motion induced by spin polarized currents in ferromagnetic ring structures,” *Appl. Phys. Lett.*, vol. 83, no. 1, pp. 105–107, Jul. 2003.

[18] J. C. Slonczewski, “Electronic device using magnetic components,” 5695864.

[19] I. M. Miron *et al.*, “Current-driven spin torque induced by the Rashba effect in a ferromagnetic metal layer,” *Nat. Mater.*, vol. 9, no. 3, pp. 230–234, 2010.

[20] I. M. Miron *et al.*, “Perpendicular switching of a single ferromagnetic layer induced by in-plane current injection,” *Nature*, vol. 476, no. 7359, pp. 189–193, Aug. 2011.

[21] A. Manchon and S. Zhang, “Theory of spin torque due to spin-orbit coupling,” *Phys. Rev. B*, vol. 79, no. 9, p. 94422, Mar. 2009.

[22] A. Manchon and S. Zhang, “Theory of nonequilibrium intrinsic spin torque in a single nanomagnet,” *Phys. Rev. B*, vol. 78, no. 21, p. 212405, Dec. 2008.

[23] A. Chernyshov, M. Overby, X. Liu, J. K. Furdyna, Y. Lyanda-Geller, and L. P. Rokhinson, “Evidence for reversible control of magnetization in a ferromagnetic material by means of spin–orbit magnetic field,” *Nat. Phys.*, vol. 5, no. 9, pp. 656–659, Sep. 2009.

[24] J. Stohr and H. C. Siegmann, *Magnetism. From fundamentals to nanoscale Dynamics*. Springer, 2006.

[25] K. H. J. Buschow and F. R. de Boer, *Physics of Magnetism and Magnetic Materials*. Kluwer Academic Publishers, 2003.

[26] P. Gambardella and I. M. Miron, “Current-induced spin–orbit torques,” *Philos. Trans. R. Soc. Math. Phys. Eng. Sci.*, vol. 369, no. 1948, pp. 3175–3197, Aug. 2011.

[27] L. Thomas, “The Motion of the Spinning Electron,” *Nature*, vol. 117, p. 514, 1926.

[28] *Handbook of Magnetism and Advanced Magnetic Materials*. .

[29] R. Winkler, *Spin-orbit Coupling Effects in Two-Dimensional Electron and Hole Systems*. Berlin, Germany: Springer, 2003.

[30] H. A. Kramers, “Theorie generale de la rotation paramagnetique dans les cristaux,” *Proc Amst. Acad*, vol. 33, p. 959, 1930.

[31] G. Dresselhaus, “Spin-Orbit Coupling Effects in Zinc Blende Structures,” *Phys. Rev.*, vol. 100, no. 2, pp. 580–586, Oct. 1955.

[32] Y. A. Bychkov and E. I. Rashba, “Oscillatory effects and the magnetic susceptibility of carriers in inversion layers,” *J. Phys. C Solid State Phys.*, vol. 17, no. 33, p. 6039, 1984.

[33] İ. Adagideli, G. E. W. Bauer, and B. I. Halperin, “Detection of Current-Induced Spins by Ferromagnetic Contacts,” *Phys. Rev. Lett.*, vol. 97, no. 25, p. 256601, Dec. 2006.

[34] T. P. Pareek and A. M. Jayannavar, “Generation and measurement of nonequilibrium spin currents in two-terminal systems,” *Phys. Rev. B*, vol. 77, no. 15, p. 153307, Apr. 2008.

[35] A. Matos-Abiague and R. Rodríguez-Suárez, “Spin-orbit coupling mediated spin torque in a single ferromagnetic layer,” *Phys. Rev. B*, vol. 80, no. 9, Sep. 2009.

[36] A. Manchon and S. Zhang, “Theory of nonequilibrium intrinsic spin torque in a single nanomagnet,” *Phys. Rev. B*, vol. 78, no. 21, pp. 212405–212408, 2008.

[37] L. Liu, C.-F. Pai, Y. Li, H. W. Tseng, D. C. Ralph, and R. A. Buhrman, “Spin-Torque Switching with the Giant Spin Hall Effect of Tantalum,” *Science*, vol. 336, no. 6081, pp. 555–558, May 2012.

[38] M. I. Dyakonov, “Spin Hall Effect,” *arXiv:1210.3200*, Oct. 2012.

[39] P. M. Haney, H.-W. Lee, K.-J. Lee, A. Manchon, and M. D. Stiles, “Current induced torques and interfacial spin-orbit coupling: Semiclassical modeling,” *Phys. Rev. B*, vol. 87, no. 17, p. 174411, May 2013.

[40] Y. Tserkovnyak, A. Brataas, and G. E. W. Bauer, “Theory of current-driven magnetization dynamics in inhomogeneous ferromagnets,” *J. Magn. Magn. Mater.*, vol. 320, no. 7, pp. 1282–1292, Apr. 2008.

[41] Y. A. Bychkov and É. I. Rashba, “Properties of a 2D electron gas with lifted spectral degeneracy,” *Sov. J. Exp. Theor. Phys. Lett.*, vol. 39, p. 78, Jan. 1984.

[42] Y. K. Kato, R. C. Myers, A. C. Gossard, and D. D. Awschalom, “Current-Induced Spin Polarization in Strained Semiconductors,” *Phys. Rev. Lett.*, vol. 93, no. 17, p. 176601, Oct. 2004.

[43] H.-A. Engel, E. I. Rashba, and B. I. Halperin, “Out-of-Plane Spin Polarization from In-Plane Electric and Magnetic Fields,” *Phys. Rev. Lett.*, vol. 98, no. 3, p. 36602, Jan. 2007.

[44] H. Kurebayashi *et al.*, “An antidamping spin-orbit torque originating from the Berry curvature,” *Nat. Nanotechnol.*, vol. 9, no. 3, pp. 211–217, Mar. 2014.

[45] T. Jungwirth, Q. Niu, and A. H. MacDonald, “Anomalous Hall Effect in Ferromagnetic Semiconductors,” *Phys. Rev. Lett.*, vol. 88, no. 20, p. 207208, May 2002.

[46] M. I. Dyakonov and V. I. Perel, “Current-induced spin orientation of electrons in semiconductors,” *Phys. Lett. A*, vol. 35, no. 6, pp. 459–460, 1971.

[47] J. E. Hirsch, “Spin Hall Effect,” *Phys. Rev. Lett.*, vol. 83, no. 9, pp. 1834–1837, Aug. 1999.

[48] N. Nagaosa, “Anomalous Hall Effect –A New Perspective–,” *J. Phys. Soc. Jpn.*, vol. 75, no. 4, p. 42001, Apr. 2006.

[49] N. Nagaosa, J. Sinova, S. Onoda, A. H. MacDonald, and N. P. Ong, “Anomalous Hall effect,” *Rev. Mod. Phys.*, vol. 82, no. 2, pp. 1539–1592, May 2010.

[50] *The Hall Effect in Metals and Alloys | Colin Hurd | Springer*. .

[51] N. F. Mott, “The Scattering of Fast Electrons by Atomic Nuclei,” *Proc. R. Soc. Lond. Math. Phys. Eng. Sci.*, vol. 124, no. 794, pp. 425–442, Jun. 1929.

[52] “The theory of atomic collisions / by N.F. Mott and H.S.W. Massey. - Version details,” *Trove*. [Online]. Available: http://trove.nla.gov.au/version/17116406. [Accessed: 26-Nov-2016].

[53] J. Smit, “The spontaneous hall effect in ferromagnetics I,” *Physica*, vol. 21, no. 6, pp. 877–887, Jan. 1955.

[54] J. Smit, “The spontaneous hall effect in ferromagnetics II,” *Physica*, vol. 24, no. 1, pp. 39–51, Jan. 1958.

[55] L. Berger, “Side-Jump Mechanism for the Hall Effect of Ferromagnets,” *Phys. Rev. B*, vol. 2, no. 11, pp. 4559–4566, Dec. 1970.

[56] S. Murakami, “Intrinsic Spin Hall Effect,” *ArXivcond-Mat0504353*, vol. 45, pp. 197–209, 2005.

[57] J. Sinova, D. Culcer, Q. Niu, N. A. Sinitsyn, T. Jungwirth, and A. H. MacDonald, “Universal Intrinsic Spin-Hall Effect,” *Phys. Rev. Lett.*, vol. 92, no. 12, Mar. 2004.

[58] H. Kontani, M. Naito, D. S. Hirashima, K. Yamada, and J. Inoue, “Study of intrinsic spin and orbital Hall effects in Pt based on a (6s, 6p, 5d) tight-binding model,” *J. Phys. Soc. Jpn.*, vol. 76, no. 10, p. 103702, Oct. 2007.

[59] H. Kontani, T. Tanaka, D. S. Hirashima, K. Yamada, and J. Inoue, “Giant Intrinsic Spin and Orbital Hall Effects in ${\mathrm{Sr}}_{2}M{\mathrm{O}}_{4}$ ($M=\mathrm{Ru}$, Rh, Mo),” *Phys. Rev. Lett.*, vol. 100, no. 9, p. 96601, Mar. 2008.

[60] T. Tanaka *et al.*, “Study of Intrinsic Spin Hall Effect and Orbital Hall Effect in 4d- and 5d-Transition Metals,” *Phys. Rev. B*, vol. 77, no. 16, Apr. 2008.

[61] H. Kontani, T. Tanaka, D. S. Hirashima, K. Yamada, and J. Inoue, “Giant Orbital Hall Effect in Transition Metals: Origin of Large Spin and Anomalous Hall Effects,” *Phys. Rev. Lett.*, vol. 102, no. 1, p. 16601, Jan. 2009.

[62] A. Manchon, “Spin Hall effect versus Rashba torque: a Diffusive Approach,” *ArXiv12044869 Cond-Mat*, Apr. 2012.

[63] A. Brataas, Y. V. Nazarov, and G. E. W. Bauer, “Finite-Element Theory of Transport in Ferromagnet\char21{}Normal Metal Systems,” *Phys. Rev. Lett.*, vol. 84, no. 11, pp. 2481–2484, Mar. 2000.

[64] R. H. Liu, W. L. Lim, and S. Urazhdin, “Control of current-induced spin-orbit effects in a ferromagnetic heterostructure by electric field,” *Phys. Rev. B*, vol. 89, no. 22, p. 220409, Jun. 2014.

[65] X. Fan *et al.*, “Quantifying interface and bulk contributions to spin–orbit torque in magnetic bilayers,” *Nat. Commun.*, vol. 5, p. 3042, Jan. 2014.

[66] E. H. Hall, “On a New Action of the Magnet on Electric Currents,” *Am. J. Math.*, vol. 2, no. 3, pp. 287–292, 1879.

[67] R. Karplus and J. M. Luttinger, “Hall Effect in Ferromagnetics,” *Phys. Rev.*, vol. 95, no. 5, pp. 1154–1160, Sep. 1954.

[68] K. L. Yau and J. T. H. Chang, “The planar Hall effect in thin foils of Ni-Fe alloy,” *J. Phys. F Met. Phys.*, vol. 1, no. 1, p. 38, 1971.

[69] H. X. Tang, “Giant Planar Hall Effect in Epitaxial (Ga,Mn)As Devices,” *Phys. Rev. Lett.*, vol. 90, no. 10, 2003.

[70] T. McGuire and R. Potter, “Anisotropic magnetoresistance in ferromagnetic 3d alloys,” *IEEE Trans. Magn.*, vol. 11, no. 4, pp. 1018–1038, Jul. 1975.

[71] D. Wang, “Spin-orbit field switching of magnetization in ferromagnetic films with perpendicular anisotropy,” *Appl. Phys. Lett.*, vol. 100, no. 21, pp. 212405-212405–4, May 2012.

[72] C. O. Avci *et al.*, “Magnetization switching of an MgO/Co/Pt layer by in-plane current injection,” *Appl. Phys. Lett.*, vol. 100, no. 21, p. 212404, May 2012.

[73] L. You *et al.*, “Switching of Perpendicularly Polarized Nanomagnets with Spin Orbit Torque without an External Magnetic Field by Engineering a Tilted Anisotropy,” *ArXiv14090620 Cond-Mat*, Sep. 2014.

[74] C. O. Avci *et al.*, “Fieldlike and antidamping spin-orbit torques in as-grown and annealed Ta/CoFeB/MgO layers,” *Phys. Rev. B*, vol. 89, no. 21, p. 214419, Jun. 2014.

[75] G. Yu *et al.*, “Magnetization switching through spin-Hall-effect-induced chiral domain wall propagation,” *Phys. Rev. B*, vol. 89, no. 10, p. 104421, Mar. 2014.

[76] A. van den Brink *et al.*, “Field-free magnetization reversal by spin-Hall effect and exchange bias,” *ArXiv150908752 Cond-Mat*, Sep. 2015.

[77] Q. Hao and G. Xiao, “Giant Spin Hall Effect and Switching Induced by Spin-Transfer Torque in a $\mathrm{W}/{\mathrm{Co}}_{40}{\mathrm{Fe}}_{40}{\mathrm{B}}_{20}/\mathrm{MgO}$ Structure with Perpendicular Magnetic Anisotropy,” *Phys. Rev. Appl.*, vol. 3, no. 3, p. 34009, Mar. 2015.

[78] K. Garello *et al.*, “Ultrafast magnetization switching by spin-orbit torques,” *ArXiv13105586 Cond-Mat*, Oct. 2013.

[79] M. Cubukcu *et al.*, “Ultra-fast magnetization reversal of a three-terminal perpendicular magnetic tunnel junction by spin-orbit torque,” *ArXiv150902375 Cond-Mat*, Sep. 2015.

[80] C. Bi *et al.*, “Thermally assisted magnetic switching of a single perpendicularly magnetized layer induced by an in-plane current,” *Appl. Phys. Lett.*, vol. 105, no. 2, p. 22407, Jul. 2014.

[81] M. Cubukcu *et al.*, “Spin-orbit torque magnetization switching of a three-terminal perpendicular magnetic tunnel junction,” *Appl. Phys. Lett.*, vol. 104, no. 4, p. 42406, Jan. 2014.

[82] M. Yamanouchi *et al.*, “Three terminal magnetic tunnel junction utilizing the spin Hall effect of iridium-doped copper,” *Appl. Phys. Lett.*, vol. 102, no. 21, p. 212408, May 2013.

[83] S. Fukami, T. Anekawa, C. Zhang, and H. Ohno, “A spin–orbit torque switching scheme with collinear magnetic easy axis and current configuration,” *Nat. Nanotechnol.*, vol. 11, no. 7, pp. 621–625, Jul. 2016.

[84] S. Fukami, C. Zhang, S. DuttaGupta, and H. Ohno, “Magnetization switching by spin-orbit torque in an antiferromagnet/ferromagnet bilayer system,” *ArXiv150700888 Cond-Mat*, Jul. 2015.

[85] Y. Fan *et al.*, “Magnetization switching through giant spin–orbit torque in a magnetically doped topological insulator heterostructure,” *Nat. Mater.*, vol. 13, no. 7, pp. 699–704, Jul. 2014.

[86] L. Berger, “Low-field magnetoresistance and domain drag in ferromagnets,” *J. Appl. Phys.*, vol. 49, no. 3, pp. 2156–2161, Mar. 1978.

[87] L. Berger, “Exchange interaction between ferromagnetic domain wall and electric current in very thin metallic films,” *J. Appl. Phys.*, vol. 55, no. 6, pp. 1954–1956, Mar. 1984.

[88] A. Thiaville, Y. Nakatani, J. Miltat, and N. Vernier, “Domain wall motion by spin-polarized current: a micromagnetic study,” *J. Appl. Phys.*, vol. 95, no. 11, pp. 7049–7051, May 2004.

[89] M. Kläui, “Direct Observation of Domain-Wall Configurations Transformed by Spin Currents,” *Phys. Rev. Lett.*, vol. 95, no. 2, 2005.

[90] E. Jué, “Dynamique du déplacement de parois magnétiques dans les couches ultra-minces à forte interaction spin-orbite,” phdthesis, Université de Grenoble, 2013.

[91] T. A. Moore *et al.*, “High domain wall velocities induced by current in ultrathin Pt/Co/AlOx wires with perpendicular magnetic anisotropy,” *Appl. Phys. Lett.*, vol. 93, no. 26, p. 262504, Dec. 2008.

[92] I. M. Miron, P.-J. Zermatten, G. Gaudin, S. Auffret, B. Rodmacq, and A. Schuhl, “Domain Wall Spin Torquemeter,” *Phys. Rev. Lett.*, vol. 102, no. 13, p. 137202, Mar. 2009.

[93] I. M. Miron *et al.*, “Fast current-induced domain-wall motion controlled by the Rashba effect,” *Nat. Mater.*, vol. 10, no. 6, pp. 419–423, Jun. 2011.

[94] N. L. Schryer and L. R. Walker, “The motion of 180° domain walls in uniform dc magnetic fields,” *J. Appl. Phys.*, vol. 45, no. 12, pp. 5406–5421, Dec. 1974.

[95] G. S. D. Beach, C. Nistor, C. Knutson, M. Tsoi, and J. L. Erskine, “Dynamics of field-driven domain-wall propagation in ferromagnetic nanowires,” *Nat. Mater.*, vol. 4, no. 10, pp. 741–744, Oct. 2005.

[96] A. Mougin, M. Cormier, J. P. Adam, P. J. Metaxas, and J. Ferré, “Domain wall mobility, stability and Walker breakdown in magnetic nanowires,” *EPL Europhys. Lett.*, vol. 78, no. 5, p. 57007, 2007.

[97] A. Thiaville, S. Rohart, É. Jué, V. Cros, and A. Fert, “Dynamics of Dzyaloshinskii domain walls in ultrathin magnetic films,” *EPL Europhys. Lett.*, vol. 100, no. 5, p. 57002, Dec. 2012.

[98] I. E. Dzialoshinskii, “Thermodynamic theory of ‘weak’ ferromagnetism in antiferromagnetic substances,” *Sov Phys JETP*, no. 5, pp. 1259–1262, 1957.

[99] T. Moriya, “Anisotropic Superexchange Interaction and Weak Ferromagnetism,” *Phys. Rev.*, vol. 120, no. 1, pp. 91–98, Oct. 1960.

[100] A. Fert and P. M. Levy, “Role of Anisotropic Exchange Interactions in Determining the Properties of Spin-Glasses,” *Phys. Rev. Lett.*, vol. 44, no. 23, pp. 1538–1541, Jun. 1980.

[101] S. Emori, U. Bauer, S.-M. Ahn, E. Martinez, and G. S. D. Beach, “Current-driven dynamics of chiral ferromagnetic domain walls,” *Nat. Mater.*, vol. 12, no. 7, pp. 611–616, Jun. 2013.

[102] K.-S. Ryu, L. Thomas, S.-H. Yang, and S. Parkin, “Chiral spin torque at magnetic domain walls,” *Nat. Nanotechnol.*, vol. 8, no. 7, pp. 527–533, Jun. 2013.

[103] H. Yang, A. Thiaville, S. Rohart, A. Fert, and M. Chshiev, “Anatomy of Dzyaloshinskii-Moriya Interaction at Co/Pt Interfaces,” *Phys. Rev. Lett.*, vol. 115, no. 26, Dec. 2015.

[104] K. Ando *et al.*, “Electric Manipulation of Spin Relaxation Using the Spin Hall Effect,” *Phys. Rev. Lett.*, vol. 101, no. 3, p. 36601, Jul. 2008.

[105] O. Krupin, “Rashba effect at magnetic metal surfaces,” *Phys. Rev. B*, vol. 71, no. 20, 2005.

[106] L. Liu, T. Moriyama, D. C. Ralph, and R. A. Buhrman, “Spin-Torque Ferromagnetic Resonance Induced by the Spin Hall Effect,” *Phys. Rev. Lett.*, vol. 106, no. 3, p. 36601, Jan. 2011.

[107] L. Liu, O. J. Lee, T. J. Gudmundsen, D. C. Ralph, and R. A. Buhrman, “Current-Induced Switching of Perpendicularly Magnetized Magnetic Layers Using Spin Torque from the Spin Hall Effect,” *Phys. Rev. Lett.*, vol. 109, no. 9, p. 96602, Aug. 2012.

[108] X. Wang, C. O. Pauyac, and A. Manchon, “Spin-orbit-coupled transport and spin torque in a ferromagnetic heterostructure,” *Phys. Rev. B*, vol. 89, no. 5, Feb. 2014.

[109] J. Bass and W. P. P. Jr, “Spin-diffusion lengths in metals and alloys, and spin-flipping at metal/metal interfaces: an experimentalist’s critical review,” *J. Phys. Condens. Matter*, vol. 19, no. 18, p. 183201, 2007.

[110] T. Valet and A. Fert, “Theory of the perpendicular magnetoresistance in magnetic multilayers,” *Phys. Rev. B*, vol. 48, no. 10, pp. 7099–7113, Sep. 1993.

[111] S. Emori *et al.*, “Quantification of the spin-Hall anti-damping torque with a resonance spectrometer,” *ArXiv14116166 Cond-Mat*, Nov. 2014.

[112] A. Ganguly *et al.*, “Thickness dependence of spin torque ferromagnetic resonance in Co75Fe25/Pt bilayer films,” *Appl. Phys. Lett.*, vol. 104, no. 7, p. 72405, Feb. 2014.

[113] C. Hahn, G. de Loubens, O. Klein, M. Viret, V. V. Naletov, and J. Ben Youssef, “Comparative measurements of inverse spin Hall effects and magnetoresistance in YIG/Pt and YIG/Ta,” *Phys. Rev. B*, vol. 87, no. 17, p. 174417, May 2013.

[114] O. Mosendz, J. E. Pearson, F. Y. Fradin, G. E. W. Bauer, S. D. Bader, and A. Hoffmann, “Quantifying Spin Hall Angles from Spin Pumping: Experiments and Theory,” *Phys. Rev. Lett.*, vol. 104, no. 4, p. 46601, Jan. 2010.

[115] W. Zhang, V. Vlaminck, J. E. Pearson, R. Divan, S. D. Bader, and A. Hoffmann, “Determination of the Pt spin diffusion length by spin-pumping and spin Hall effect,” *Appl. Phys. Lett.*, vol. 103, no. 24, p. 242414, Dec. 2013.

[116] O. Mosendz *et al.*, “Detection and quantification of inverse spin Hall effect from spin pumping in permalloy/normal metal bilayers,” *Phys. Rev. B*, vol. 82, no. 21, p. 214403, Dec. 2010.

[117] V. Vlaminck, J. E. Pearson, S. D. Bader, and A. Hoffmann, “Dependence of spin-pumping spin Hall effect measurements on layer thicknesses and stacking order,” *Phys. Rev. B*, vol. 88, no. 6, p. 64414, Aug. 2013.

[118] C. He *et al.*, “Spin-torque ferromagnetic resonance measurements utilizing spin Hall magnetoresistance in W/Co40Fe40B20/MgO structures,” *Appl. Phys. Lett.*, vol. 109, no. 20, p. 202404, Nov. 2016.

[119] Y. Niimi *et al.*, “Extrinsic Spin Hall Effect Induced by Iridium Impurities in Copper,” *Phys. Rev. Lett.*, vol. 106, no. 12, p. 126601, Mar. 2011.

[120] Y. Niimi *et al.*, “Giant Spin Hall Effect Induced by Skew Scattering from Bismuth Impurities inside Thin Film CuBi Alloys,” *Phys. Rev. Lett.*, vol. 109, no. 15, p. 156602, Oct. 2012.

[121] P. Laczkowski *et al.*, “Experimental evidences of a large extrinsic spin Hall effect in AuW alloy,” *Appl. Phys. Lett.*, vol. 104, no. 14, p. 142403, Apr. 2014.

[122] J. Sinova, S. O. Valenzuela, J. Wunderlich, C. H. Back, and T. Jungwirth, “Spin Hall effect,” *ArXiv14113249 Cond-Mat*, Nov. 2014.

[123] U. H. Pi *et al.*, “Tilting of the spin orientation induced by Rashba effect in ferromagnetic metal layer,” *Appl. Phys. Lett.*, vol. 97, no. 16, pp. 162507-162507–3, Oct. 2010.

[124] K. Garello *et al.*, “Symmetry and magnitude of spin–orbit torques in ferromagnetic heterostructures,” *Nat. Nanotechnol.*, vol. 8, no. 8, pp. 587–593, Jul. 2013.

[125] M. Hayashi, J. Kim, M. Yamanouchi, and H. Ohno, “Quantitative characterization of the spin-orbit torque using harmonic Hall voltage measurements,” *Phys. Rev. B*, vol. 89, no. 14, p. 144425, Apr. 2014.

[126] M. Mizuguchi, S. Ohata, K. Uchida, E. Saitoh, and K. Takanashi, “Anomalous Nernst Effect in an L1$_{0}$-Ordered Epitaxial FePt Thin Film,” *Appl. Phys. Express*, vol. 5, no. 9, p. 93002, Aug. 2012.

[127] A. Slachter, F. L. Bakker, and B. J. van Wees, “Anomalous Nernst and anisotropic magnetoresistive heating in a lateral spin valve,” *Phys. Rev. B*, vol. 84, no. 2, p. 20412, Jul. 2011.

[128] K. Behnia, “The Nernst effect and the boundaries of the Fermi liquid picture,” *J. Phys. Condens. Matter*, vol. 21, no. 11, p. 113101, 2009.

[129] C. O. Avci *et al.*, “Interplay of spin-orbit torque and thermoelectric effects in ferromagnet/normal-metal bilayers,” *Phys. Rev. B*, vol. 90, no. 22, p. 224427, Dec. 2014.

[130] M. Kawaguchi *et al.*, “Extraction of the Anomalous Nernst Effect in the Electric Measurement of the Spin Orbit Torque,” *ArXiv151004363 Cond-Mat*, Oct. 2015.

[131] G. V. SKROTSKII and L. V. KURBATOV, “CHAPTER II - PHENOMENOLOGICAL THEORY OF FERROMAGNETIC RESONANCE A2 - VONSOVSKII, S.V.,” in *Ferromagnetic Resonance*, Pergamon, 1966, pp. 12–77.

[132] “FMR,” 20-Apr-2009. [Online]. Available: http://www.physik.fu-berlin.de/einrichtungen/ag/ag-kuch/research/techniques/fmr/index.html. [Accessed: 14-Dec-2016].

[133] T. Nan *et al.*, “Comparison of spin-orbit torques and spin pumping across NiFe/Pt and NiFe/Cu/Pt interfaces,” *Phys. Rev. B*, vol. 91, no. 21, p. 214416, Jun. 2015.

[134] S. Petit *et al.*, “Spin-Torque Influence on the High-Frequency Magnetization Fluctuations in Magnetic Tunnel Junctions,” *Phys. Rev. Lett.*, vol. 98, no. 7, p. 77203, Feb. 2007.

[135] A. R. Mellnik *et al.*, “Spin-transfer torque generated by a topological insulator,” *Nature*, vol. 511, no. 7510, pp. 449–451, Jul. 2014.

[136] Y. Tserkovnyak, A. Brataas, and G. E. W. Bauer, “Enhanced Gilbert Damping in Thin Ferromagnetic Films,” *Phys. Rev. Lett.*, vol. 88, no. 11, p. 117601, Feb. 2002.

[137] A. Azevedo, L. H. Vilela-Leão, R. L. Rodríguez-Suárez, A. F. Lacerda Santos, and S. M. Rezende, “Spin pumping and anisotropic magnetoresistance voltages in magnetic bilayers: Theory and experiment,” *Phys. Rev. B*, vol. 83, no. 14, p. 144402, Apr. 2011.

[138] E. Saitoh, M. Ueda, H. Miyajima, and G. Tatara, “Conversion of spin current into charge current at room temperature: Inverse spin-Hall effect,” *Appl. Phys. Lett.*, vol. 88, no. 18, p. 182509, May 2006.

[139] T. Suzuki *et al.*, “Current-induced effective field in perpendicularly magnetized Ta/CoFeB/MgO wire,” *Appl. Phys. Lett.*, vol. 98, no. 14, p. 142505, Apr. 2011.

[140] J. Kim *et al.*, “Layer thickness dependence of the current-induced effective field vector in Ta|CoFeB|MgO,” *Nat. Mater.*, vol. 12, no. 3, pp. 240–245, Mar. 2013.

[141] S. Emori, D. C. Bono, and G. S. D. Beach, “Interfacial current-induced torques in Pt/Co/GdOx,” *Appl. Phys. Lett.*, vol. 101, no. 4, p. 42405, Jul. 2012.

[142] C.-F. Pai, L. Liu, Y. Li, H. W. Tseng, D. C. Ralph, and R. A. Buhrman, “Spin transfer torque devices utilizing the giant spin Hall effect of tungsten,” *Appl. Phys. Lett.*, vol. 101, no. 12, p. 122404, Sep. 2012.

[143] J. Kim *et al.*, “Anomalous temperature dependence of current-induced torques in CoFeB/MgO heterostructures with Ta-based underlayers,” *Phys. Rev. B*, vol. 89, no. 17, p. 174424, May 2014.

[144] A. Manchon *et al.*, “Analysis of oxygen induced anisotropy crossover in Pt/Co/MOx trilayers,” *J. Appl. Phys.*, vol. 104, no. 4, p. 43914, Aug. 2008.

[145] S. Monso *et al.*, “Crossover from in-plane to perpendicular anisotropy in Pt/CoFe/AlOx sandwiches as a function of Al oxidation: A very accurate control of the oxidation of tunnel barriers,” *Appl. Phys. Lett.*, vol. 80, no. 22, pp. 4157–4159, Jun. 2002.

[146] P. M. Haney, H.-W. Lee, K.-J. Lee, A. Manchon, and M. D. Stiles, “Current induced torques and interfacial spin-orbit coupling: Semiclassical modeling,” *Phys. Rev. B*, vol. 87, no. 17, p. 174411, May 2013.

[147] C. M. Jaworski, J. Yang, S. Mack, D. D. Awschalom, J. P. Heremans, and R. C. Myers, “Observation of the spin-Seebeck effect in a ferromagnetic semiconductor,” *Nat. Mater.*, vol. 9, no. 11, pp. 898–903, Nov. 2010.

[148] H. Adachi, K. Uchida, E. Saitoh, and S. Maekawa, “Theory of the spin Seebeck effect,” *Rep. Prog. Phys.*, vol. 76, no. 3, p. 36501, 2013.

[149] Y.-T. Chen *et al.*, “Theory of spin Hall magnetoresistance,” *Phys. Rev. B*, vol. 87, no. 14, p. 144411, Apr. 2013.

[150] H. Nakayama *et al.*, “Spin Hall Magnetoresistance Induced by a Nonequilibrium Proximity Effect,” *Phys. Rev. Lett.*, vol. 110, no. 20, p. 206601, May 2013.

[151] M.-H. Nguyen, D. C. Ralph, and R. A. Buhrman, “Spin Torque Study of the Spin Hall Conductivity and Spin Diffusion Length in Platinum Thin Films with Varying Resistivity,” *Phys. Rev. Lett.*, vol. 116, no. 12, p. 126601, Mar. 2016.

[152] V. P. Amin and M. D. Stiles, “Spin transport at interfaces with spin-orbit coupling: Phenomenology,” *Phys. Rev. B*, vol. 94, no. 10, p. 104420, Sep. 2016.

[153] L. Wang, R. J. H. Wesselink, Y. Liu, Z. Yuan, K. Xia, and P. J. Kelly, “Giant Room Temperature Interface Spin Hall and Inverse Spin Hall Effects,” *Phys. Rev. Lett.*, vol. 116, no. 19, p. 196602, May 2016.

Résume en français

La loi de Moore est basée sur l'observation empirique qu'environ chaque deux années, le nombre de transistors dans des circuits denses intégrées double. Cette tendance s'est bien maintenue au cours des dernières décennies (années 1970 et suivantes). Cependant, la miniaturisation continue des transistors entraîne une augmentation significative des pertes d'énergie par le courant de fuite, ce qui augmente la consommation d'énergie de veille. Cette perte d'énergie est devenue un problème majeur dans la microélectronique pendant les dernières années, ce qui rend plus difficile le développement des nouvelles technologies. L'une des solutions est de placer des éléments mémoire non-volatile dans le puce, qui retiennent la configuration du transistor pendant la mise hors tension et permettent de le restaurer à la mise sous tension. Les Magnetic Random Access Memories (MRAM) sont considérées par l'ITRS comme un candidat crédible pour le remplacement potentiel de SRAM et de DRAM au-delà du nœud technologique de 20 nm. Bien que les exigences de base pour la lecture et l'écriture d'un élément de mémoire unique sont remplies, l'approche actuelle basée sur Spin Torque Transfer (STT) souffre d'un manque inné de la flexibilité. Le courant électrique entraine le retournement de l'aimantation de la couche ferromagnétique libre par le transfert du moment angulaire d'une couche ferromagnétique adjacent. Ainsi les éléments de mémoire basées sur STT ont deux terminaux dont les voies de courant pour « écriture » et « lecture » sont définies par la forme de «pillar». L'optimisation indépendant des paramètres d'écriture et de lecture reste, donc, très difficile. Au même temps, la densité de courant trop haute, nécessaire pour écrire, conduit à la vieillissement prématuré du jonction tunnel. En conséquence, l'intégration MRAM dans la technologie du semi-conducteur reste, donc, difficile.

Démonstrations récentes de reversement d'aimantation entrainées par l'injection d'un courant planaire dans des heterostructures métal lourd/ferromagnet ont attiré l'attention croissante sur les couples de spin basé sur le transfert du moment angulaire par l'effet Hall de spin et les effets d'interface. Contrairement à STT-MRAM, la SOT-MRAM a trois terminaux, dont les voies de courant pour « écriture » et « lecture » sont indépendantes. Cela permet d'améliorer les paramètres « écriture » et « lecture » de manière indépendante. Pour contrôler et optimiser les SOT il est nécessaire de comprendre très bien leur origine. Cela reste

l’une des plus importantes questions dont on n’a pas une réponse définitive. Dans ce contexte, plusieurs études ont conclu sur un modèle basé seulement sur l’effet Hall de spin, en même temps que d’autres ont suggéré un modèle basé sur une contribution combiné de l’effet Hall de spin et l’effet d’interface.

L’objectif de cette thèse est de réaliser une étude systématique sur les effets d’interface sur les SOT dans des heterostructures métal lourde/ferromagnet a base de Pt, avec aimantation planaire.

Dans ce but, cette thèse explore trois voies différentes. Premièrement nous avons modifié le rapport entre les effets d’interface et les effets bulk en changeant l’épaisseur de la couche de Pt et en suivant l’évolution des SOT. En deuxième nous avons exploré des différents empilements métal lourde/ferromagnet afin d’étudier différentes interfaces. Finalement, nous avons changé les propriétés des interfaces soit par changer la structure cristalline soit par oxydation. La technique de mesure, la méthode d’analyse de données associé et les aspects théoriques nécessaires pour l’interprétation des données sont aussi détaillés dans ce manuscrit.

Chapitre 2

Pour l'existence des SOT, il existe deux exigences générales : une forte interaction spin orbite (SOI) et brisure de la symétrie d'inversion au niveau de l’interface (SIA). Pour cette raison, la plupart des échantillons destinés à l'étude des SOT sont des multicouches de métaux lourds (HM) / Ferromagnetic (FM) / Non-magnétiques (NM), où le HM fournit le SOI et, en intercalant la couche FM entre des interfaces différentes, nous fournissons le SIA suivant la direction normale au plan d'échantillon.

Il a été théoriquement prédit et observé expérimentalement que, lorsque nous injectons un courant électrique dans le plan d’une telle structure, nous auront un transfert du moment angulaire du réseau cristallin à l'aimantation de la couche ferromagnétique. Deux couples de spin qualitativement différents sont créés : un couple d’amortissement (Damping-Like, DL), et un couple de champ (Field-Like, FL).

Théoriquement, il a été montré que les couples de champs et d’amortissement peuvent apparaître à partir de l'effet Rashba et de l’effet Hall de spin. Toutefois, les deux effets peuvent se produire au même temps dans nos échantillons et peuvent contribuer aux SOT.

Selon les études théoriques, on s'attend généralement à une contribution plus forte au couple d'amortissement apporté par le SHE que par l'effet Rashba, qui, en revanche, fournirait une contribution plus forte au couple de champ. Le fait que nous trouvions les mêmes composants SOT, avec la même symétrie résultant à la fois de l'effet Rashba et du SHE, a généré un long débat sur l'origine des SOT.

Chapitre 3

Dans ce chapitre, je vais essayer de donner un aperçu des orientations actuelles dans l'analyse quantitative des SOT. L'objectif de ce projet n'est pas d'examiner de manière exhaustive le travail effectué dans ce domaine, mais plutôt de souligner les résultats les plus significatifs dans le contexte de ce manuscrit.

Dans une première partie, nous examinerons brièvement deux applications importantes que les SOT permettent : Magnetisation Switching et le mouvement des parois de domaine magnétique (DW), induits par le courant électrique.

Le Magnetisation Switching induit par le courant électrique est l'une des manifestations les plus importantes des SOT. Il est fondamental pour le développement de dispositifs de stockage de données basés sur SOT rapides et non volatils. La possibilité de basculer l'aimantation sur des échelles de temps très courts, rend les dispositifs de mémoire basés sur les SOT comme des candidats très prometteurs pour des applications d'enregistrement ultra-rapides.

Une autre manifestation importante des SOT est leur influence sur le mouvement de DW induit par le courant, surtout en permettant des mouvements DW à des vitesses très élevées.

Les SOT fournissent des moyens très intéressants pour contrôler l'aimantation dans des dispositifs basés sur HM / FM. Nous pouvons changer l'orientation d'aimantation de manière très rapide, ce qui permet d'écrire des informations dans un dispositif de mémoire qui peut être lu plus tard par l'effet TMR. Nous pouvons déplacer le DW le long d'une bande, avec des vitesses très élevées, en créant ainsi un registre à décalage. Nous pouvons utiliser la forme de nos dispositifs pour régler la commutation et le mouvement du DW en fonction d'une application particulière.

Les techniques utilisées dans les mesures de SOT quantitatives appartiennent généralement à deux catégories : i) mesures quasi statiques et ii) mesures à base de résonance.

La conclusion commune parmi différents études est que i) les différentes dépendances des composants Damping - Like et Field - Like en fonction des propriétés de l'échantillon semblent indiquer différentes origines pour les deux SOT, ou, au moins, vers différents mécanismes dominants, et ii) il n'y a pas de distinction claire entre l'effet Rashba et le SHE en tant que sources de SOT, car les données expérimentales indiquent un effet combiné d'interface et de volume.

L'origine des SOT reste donc l'une des questions les plus importantes sans réponse à ce jour. Bien que certaines études semblent suggérer un modèle uniquement basé sur le SHE pour les SOT, d'autres indiquent une contribution combinée des effets de volume (SHE) et d'interface (Rashba). Cependant, la distinction entre SHE (volume) et Effet de Rashba (interface) en mesurant simplement les SOT n'est pas triviale, car nous n'avons aucun moyen de distinguer directement les deux sources possibles, par des mesures de couple simples. Au même temps, de nombreuses études commencent par une hypothèse de SHE comme la seule source de SOT, et ne considèrent pas les effets d'interface. En outre, il n'y a pas tellement d'études systématiques sur les effets d'interfaces.

Afin de comprendre l'origine des SOT et de distinguer clairement entre les contributions de l'interface et du volume (SHE), il faut étudier systématiquement l'influence de l'interface sur les SOT. Une approche possible de cette question est d'étudier une grande variété d'interfaces HM / FM en changeant simplement les matériaux. Une autre possibilité, est de modifier le rapport d'effet d'interface et de volume, et de suivre son influence sur les SOT. Premièrement, les couples du SHE dépendront de l'épaisseur de la couche HM. Deuxièmement, la force des effets d'interface sur l'aimantation du FM dépendra de l'épaisseur de la couche FM. Par conséquent, pour atteindre notre objectif, dans nos études, nous avons varié de manière indépendante l'épaisseur des couches HM et FM et nous avons mesuré les SOT en fonction de ces épaisseurs.

Chapitre 4

Afin d'étudier la nature des SOT et leur origine, nous avons exploré deux voies. Tout d'abord, plusieurs HM ont été utilisés en combinaison avec du CoFeB et Co : Pt, Ta et W; tous sont des HM avec une SOI élevée et ils sont largement utilisés dans l'étude des phénomènes liés à la spintronique et a MRAM. Ensuite, nous avons étudié plusieurs épaisseurs de couche à la fois pour le FM et pour les couches HM. En raison de l'anisotropie magnétique planaire de nos échantillons, nous avons un intervalle plus large des Hm et un domaine d'épaisseurs plus important pour le FM par comparaison aux échantillons avec l'anisotropie magnétique perpendiculaire.

Nous avons étudié deux systèmes d'échantillons principaux : à base de CoFeB et à base de Co, tous deux des matériaux FM avec une forte anisotropie magnétique planaire (sur la gamme des épaisseurs que nous avons étudiée).

Nos échantillons ont été sous forme de couches minces, constitués des multicouches de métaux lourds (HM), de métaux ferromagnétiques (FM) et de métaux non magnétiques (NM) avec une anisotropie magnétique planaire. Les couches ont été déposées sur des wafers de Si / SiO2 oxydés thermiquement, par pulvérisation cathodique (d.c. magnetron sputtering). Une couche de recouvrement de Al de 2 nm a été déposée au-dessus des multicouches pour empêcher l'oxydation de la couche FM et pour créer une asymétrie d'inversion structurale (SIA). La couche de recouvrement a été naturellement oxydée, l'épaisseur de 2 nm étant suffisante pour assurer une interface métallique entre la couche FM et la couche Al.

L'une des façons de caractériser les SOT dans une multicouche HM / FM est de comparer leur effet sur l'aimantation avec l'effet d'un champ magnétique externe appliqué. C'est le principe de base d'une mesure quasi-statique : nous créons une perturbation avec un couple inconnu, puis nous le comparons à une perturbation similaire à celle d'un couple de référence. Ici, tout se résume à mesurer la déviation angulaire de l'aimantation à partir de sa position d'équilibre, provoquée par les SOT créés par un courant électrique traversant le plan de l'échantillon et en le comparant à l'écart angulaire créé par un champ magnétique externe connu. Pour mesurer les SOT dans nos échantillons, nous injectons un courant alternatif, de fréquence modérée, et nous suivrons la dynamique de l'aimantation à travers de l'analyse harmonique de la tension Hall. Le courant alternatif induit de petites oscillations dépendant

du temps autour de la position d'équilibre de l'aimantation par les SOT induits par le courant. En mesurant ces oscillations, nous pouvons obtenir les SOT.

Chapitre 5

L'un des buts principaux de cette thèse est l'étude de l'origine physique des SOT dans des hétérostructures de type HM/FM (métal lourd/métal ferromagnétique). Plus particulièrement, nous sommes intéressés à distinguer entre les contributions des effets de « bulk » (l'effet Hall de spin - SHE) et des effets d'interface (l'effet Rashba) aux SOT. Dans ce sens, il faut trouver des moyennes pour faire varier le rapport de contribution entre ces deux sources et nous avons poursuivi plusieurs scenarios.

Dans un premier temps, l'épaisseur de la couche du métal lourd a été variée. Grace à la diffusion de spins, l'impact du SHE sur le couple spin-orbite devrait diminuer avec l'augmentation de l'épaisseur, permettant donc, pour les couches épaisses, d'isoler effectivement la contribution des effets de volume. Nous avons étudié aussi des différentes combinaisons des éléments de l'interface HM/FM et l'impact de la nature de ces éléments sur le SOT. A la fin, nous avons aussi étudié les différences entre les SOT provenant des interfaces supérieure et inférieure à la couche de Pt en mettant la couche ferromagnétique en dessous et au-dessus par rapport à celle-ci.

Deuxièmement, nous avons étudié l'influence de la structure cristalline du métal lourd sur les couples spin-orbites, en développant des couches de Pt en croissance épitaxiale / texturées, avec des orientations différentes et en les couplant avec des différentes couches FM. Notre objectif a été d'étudier comment les couples Damping-Like et Field-Like évoluent pour des différentes orientations de la structure cristalline du métal lourd et la façon dont cela affecte les couples dans des différentes couches FM.

Enfin, nous avons modifié l'interface en oxydant les échantillons.

Nous avons utilisé la méthode décrite précédemment pour étudier l'évolution des couples Damping-Like et Field-Like dans chacun de ces trois cas. Pour pouvoir comparer les valeurs des SOT mesurées pour les différents échantillons que nous avons étudiés, ainsi que de comparer ces valeurs avec celles rapportées dans la littérature, nous avons suivi l'évolution des propriétés magnétiques et électriques.

Ce chapitre présente nos études expérimentales et propose une discussion de nos résultats, dans le contexte du débat "interface par rapport à la masse" concernant les origines des SOT.

Nous avons étudié l'évolution des champs efficaces de type Damping-Like et Field-Like en fonction de l'épaisseur de la couche Pt, pour les échantillons avec des gradients Pt supérieur et inférieur et différents FM.

Les résultats sont très intéressants. Dans un premier essai d'explication de nos résultats, nous avons comparé nos données à un modèle SHE des SOT et nous avons constaté que bien que le modèle puisse, dans une certaine mesure, décrire l'évolution des SOT dans nos échantillons, en raison du grand nombre des paramètres gratuits qu'il utilise, il n'est pas précis.

Nous avons vu que, après avoir pris en compte la dépendance de l'épaisseur de la résistivité de la couche de Pt, et en calculant la densité de courant en conséquence, l'amplitude du champ Damping-Like effectif par unité de densité de courant reste constante avec une épaisseur de couche Pt décroissante. Ce comportement diffère du modèle SHE des SOT, mais il est toutefois conforme aux fortes contributions aux SOT découlant de l'interface FM / Pt. Les mesures sur des multi-couches comparables, Ta / CoFeB / MgO, mais avec PMA, montrent un comportement constant et constant du Damping-Like en fonction de l'épaisseur Ta seulement inférieure à 5 A. Dans notre cas, cependant, ce comportement constant s'étend sur toute la gamme d'épaisseurs étudiées, jusqu'à environ 40 et 100, selon les échantillons.

Il est très peu probable que le SHE dans la couche Pt puisse varier autant qu'une fonction de l'épaisseur Pt ou de l'interface Pt / FM, de manière à tenir compte de la dépendance à l'épaisseur des champs efficaces de type Damping-Like et Field-Like observés expérimentalement. Cela soutient la présence d'une contribution supplémentaire aux SOT, différente de la SHE et indépendamment de l'épaisseur de la couche Pt.

Un autre point important est lié au calcul de la densité actuelle dans la couche Pt. Parce que les couches de Pt dans nos échantillons ont été déposées sous forme de gradients d'épaisseur au lieu de couches d'épaisseur constante, nous avons dû étudier des échantillons de la pastille complète, pas seulement son centre. Nous avons donc dû tenir compte de la variation de l'épaisseur de la couche vers les bords de la plaquette, en raison du processus de dépôt, qui peut influencer les mesures de résistivité. Cette influence a été plus importante dans le cas des échantillons Co, en raison des valeurs de résistivité assez similaires des couches

Pt et Co, et même pour les échantillons à base de CoFeB qui contiennent une couche tampon de Cu. Nous avons dû préformer des mesures de résistivité supplémentaires pour calculer avec précision la densité de courant dans la couche Pt, afin de compenser ces variations. Ne le faire pas, entraîne une valeur inexacte de la densité actuelle, ce qui a un impact significatif sur les valeurs SOT normalisées. Cela conduit à une image inexacte de l'évolution des SOT avec une épaisseur de Pt. On pourrait aussi, en théorie, utiliser des mesures de résistivité sur une couche identique, sans la couche Pt, par exemple MgO / CoFeB ou Ta / Cu / CoFeB, comme référence pour calculer la résistivité du gradient Pt. Cependant, cette approche est intrinsèquement erronée car elle omettra complètement l'influence de l'interface FM / Pt sur la résistivité.

Dans la deuxième partie de notre étude, nous avons préparé des échantillons avec des couches Pt [001] et Pt [111]. Nous avons ensuite étudié l'influence de la structure cristalline de la couche de Pt sur l'évolution des SOT dans les dispositifs Pt / Co et Pt / CoFeB en mesurant les couples de type Damping-Like et Field-Like en fonction de l'angle entre les la direction du courant et l'axe cristalline de la couche Pt. Au même temps, cette approche nous permet d'étudier les effets d'interfaces structurellement différentes sur les SOT. Les effets que nous observons sont intéressants. Tout d'abord, nous observons que la structure de la couche Pt influe sur l'amplitude du champ effectif Damping-Like, sans avoir un impact sur le champ Field-Like effectif. Pour le champ Field-Like effectif, il n'y a pas de différence d'amplitude notable entre les interfaces Pt-001 / FM et Pt-111 / FM, alors que pour le champ Damping-Like effectif, il existe une nette différence d'amplitude entre les deux interfaces. Deuxièmement, ni les champs Damping-Like ni Field-Like effectifs sont affectés par l'angle entre les axes cristallographiques et le sens d'injection actuel. Dans les deux cas, l'amplitude des champs effectifs est constante par rapport à l'angle d'injection actuel.

Ensuite, pour modifier les propriétés de l'interface Co / Pt, nous avons oxydé les échantillons, les bandes et les dispositifs, en les exposant à un plasma d'O_2 pendant 3 minutes. Nous avons ensuite mesuré les SOT en fonction de l'épaisseur de la couche Pt supérieure, afin d'étudier les effets de l'oxydation, sur les échantillons oxydés et non oxydés. Le degré d'oxydation a été contrôlé par l'épaisseur de la couche de Pt et étudié par des mesures de XPS. L'oxydation des échantillons a un effet intéressant sur les SOT. L'amplitude du champ effectif Damping-Like par unité de tension appliquée, ainsi que par unité de densité de courant montre une augmentation remarquable à des épaisseurs de Pt faibles, inférieures à 20 A. Un

aspect important est que l'intervalle d'épaisseur Pt au cours duquel l'augmentation de l'amplitude effective du champ Damping-Like est conforme à l'oxydation atteignant l'interface Pt / Co. En outre, pour les épaisseurs de Pt supérieures à 20 A dont l'oxydation n'atteint pas l'interface, la dépendance de l'épaisseur de Pt du champ Damping-Like effectif est la même que pour les échantillons non oxydés, à savoir constante. Ce comportement est cohérent avec la présence de contributions très fortes aux SOT, issues de l'interface Pt / Co.

Conclusions

L'objectif principal de cette thèse a été d'explorer l'un des questions fondamentales concernant les couples de spin orbite (SOT), question qui concerne leur origine physique : les effets de volume (tel que SHE), les effets d'interface (tels que l'effet Rashba ou le SHE d'interface), ou tous les deux. Une meilleure compréhension de l'origine des SOT est une première étape essentielle pour contrôler et optimiser les SOT pour tout type d'application. Dans ce contexte, il faut être capable de faire une distinction claire entre les contributions de volume et de l'interface et nous avons visé à mener une étude systématique de l'influence des interfaces sur les SOTs.

En mesurant les SOTs, nous n'avons aucun moyen de distinguer entre les effets de volume et d'interface en tant que sources de SOT. Toutefois, pour pouvoir déterminer leur origine, nous avons donc exploré trois routes. Premièrement, nous avons cherché à modifier le rapport effet d'interface/effet de volume en modifiant l'épaisseur du métal lourde (HM). Nous avons choisi la Pt, car c'est l'un des métaux lourds le plus étudié dans la spintronique. La deuxième piste concerne l'étude des différentes combinaisons HM / FM / NM, afin d'étudier les différentes interfaces et les différentes contributions d'interface et de volume aux SOTs. Nous avons étudié des échantillons de type CoFeB / FeCoB et à base de Co, associés à MgO, Al, Cu et Pt, qui sont tous des matériaux communs dans la spintronique. Au final, nous avons modifié les propriétés de l'interface soit par croissance texturé de la couche HM, soit par oxydation.

Dans notre étude, nous avons investigué des échantillons avec une anisotropie magnétique planaire. En éliminant le besoin pour l'anisotropie perpendiculaire induite par l'interface, nous avons eu plus de choix des matériaux et un intervalle plus large d'épaisseurs.

Nous avons aussi développé une configuration expérimentale pour mesurer les SOT dans un régime quasi-statique, basé sur l'analyse harmonique de la tension Hall.
Les améliorations qu'ont été implémentées à notre configuration facilitent une analyse rapide et complète de la dépendance de la composante d'amortissement et de la composante de champ, les deux composantes du couple spin-orbite, en fonction de l'angle et du champ magnétique. En plus, cette dépendance peut être étudiée pour des échantillons avec une aimantation planaire, ainsi que pour ceux à l'aimantation perpendiculaire.

Dans la première partie de notre étude, nous avons modifié l'épaisseur de la couche de Pt, en tant que couche supérieure ou inférieure, dans les multicouches MgO/FeCoB(20)/Pt(10-100), Pt(10-40)/Co(20)/Al(20), Pt(30)/Co(20)/Pt(10-40), Ta(30)/Cu(10)/Co(20)/Pt(10-40) et Ta(30)/Cu(10)/CoFeB(20)/Pt(10-40). Après, nous avons suivi l'évolution des SOTs en fonction de l'épaisseur de la Pt pour tous cette série d'échantillons.

Nous avons ensuite étudié l'évolution des SOTs en fonction de l'épaisseur de Pt pour chaque échantillon. Nous avons comparé nos résultats expérimentaux aux prédictions du modèle de SOT généréés par le SHE, en examinant l'efficacité du champ effectif d'amortissement par unité de tension électrique appliquée en fonction de Pt épaisseur. Nous avons vu que, dans tous les cas, un tel modèle n'arrive pas à reproduire nos données expérimentales. En plus, nous avons vu que, bien que l'interface FM / Pt ne produise pas de changements significatifs dans le comportement du couple, l'interface NM / FM, normalement inactif, a un fort impact.

Nous montrons aussi que l'inverse de la résistivité de la couche Pt décrit avec une bonne précision (jusqu'à un facteur de proportionnalité) l'évolution du champ effectif d'amortissement par unité de tension électrique appliquée en fonction de l'épaisseur de Pt, pour tous les échantillons étudiés. Ceci indique que l'amplitude du couple évolue comme la densité du courant dans la couche Pt. Ceci est encore soutenu par l'évolution du champ effectif d'amortissement par unité de densité de courant appliquée dans la couche Pt, qui reste constante si l'épaisseur de couche de Pt ne change pas. Ce comportement est en accord avec le modèle théorique proposé par Stiles et al. Pour les SOTs provenant de l'effet Rashba, ainsi que sur les prédictions de Wang et al. Selon lequel les contributions d'interfaces aux SOTs sont 25 fois plus grandes que celles de volume.

Dans la deuxième partie de notre étude, nous avons changé le type d'interface en développant des couches de Pt texturées. De cette façon, nous avons pu étudier l'évolution des SOT dans les échantillons basés sur Co et CoFeB avec des interfaces Pt-001 et Pt-111. L'évolution des SOTs montre que, bien que le type d'interface n'ait aucun impact sur l'amplitude du champ effectif de champ, il influence fortement l'amplitude du champ effectif d'amortissement. Cette influence est corrélée, au niveau qualitatif, avec l'anisotropie d'interface des échantillons.

Dans la troisième partie de notre étude, nous avons modifié les propriétés de l'interface par oxydation. Nous avons ensuite suivi l'évolution du champ effectif d'amortissement par unité de densité de courant appliquée et de tension effective en fonction de l'épaisseur de Pt, avant et après l'oxydation, pour des multicouches de Ta (30) / Cu (10) / Co (20) / Pt (10-40). Dans ce cas, on s'attend que le degré d'oxydation de l'interface dans les échantillons décroisse avec l'augmentation de l'épaisseur de la couche de Pt. Nos données expérimentales montrent une augmentation remarquable de l'amplitude du champ effectif d'amortissement pour des faibles épaisseurs de Pt, correspondant à l'oxydation de l'interface Pt / Co. Pour les échantillons non oxydés, ainsi que pour les échantillons oxydés où la couche de Pt est assez épaisse afin de protéger l'interface Pt / Co de l'oxydation, le comportement du champ effectif d'amortissement reproduit nos résultats de la première partie, indiquant qu'il s'agit d'un effet purement d'interface. Ce comportement est extrêmement intéressant pour des potentielles applications, car il permettrait le fonctionnement des dispositifs dans un régime des courants beaucoup plus faibles.

En ce qui concerne la question posée au début de cette thèse, l'ensemble des observations effectués dans cet étude donne une vision globale sur l'importance des effets d'interface dans la génération des SOTs. Nos expériences montrent la présence d'une multitude des effets d'interface qui ont un impact significatif sur l'amplitude du champ effectif Damping - Like. Ensuite, il est important de compléter ces études par des modelés théoriques qui tiennent compte des contributions d'interface aux couple anti-amortisseur.

A titre d'avenir, il est très intéressant d'aborder l'étude de l'influence de l'oxydation de l'interface sur les SOT en étudiant plus de combinaisons FM / HM. En vue de cette thèse, les premiers choix seraient CoFeB / Pt et FeCoB / Pt, avec des interfaces inférieures de MgO et Cu. Ensuite, une autre étape concerne l'étude de la commutation de l'aimantation pour les échantillons oxydés et non oxydés. Ce travail est déjà en cours.